LIÈGE université
Sciences Appliquées

Towards rechargeable batteries with lower environmental impact via design optimization and innovative materials

A thesis submitted in partial fulfillment of the requirements
for the degree of Doctor of Philosophy (Phd) in Engineering Science

by

Berke Karaman

Supervisor: Nathalie Job

Doctoral college in Chemical Engineering

October 2024

To my mom, my dad and köpük

Acknowledgments

I would like to thank my supervisor, Prof. Nathalie Job, for her continuous support and patience. Apart from her scientific knowledge and her attention to detail, her mentorship was invaluable during the course of my doctoral studies. Prof. Job is a great scientist and a great mentor, I feel truly lucky to be her student.

I would like to thank Prof. Benoit Heinrichs and Dr. Alexandre Léonard from University of Liège for being a part of the jury for the thesis. I would also like to thank Prof. Michel Kinnaert from Université Libre de Bruxelles and Dr. Luis D. Couto from VITO for their guidance over the years of my doctoral studies as well as agreeing to be a part of the jury. Also, I would like to thank Dr. Camélia Ghimbeu from Université Haute-Alsace/CNRS in France for agreeing to also be a part of the jury for this thesis. I appreciate the time and energy you put into reviewing my work.

I would like to thank the F.R.S-FNRS for the research grant I was awarded for the studies in my thesis. That grant helped me to complete my studies and improve myself both scientifically and personally. I am grateful for their confidence on me and the project. I would also like to thank Prayon s.a. for supplying the needed samples to complete my studies.

I would like to also thank the other PhD students, researchers and technicians in the NCE lab whom most of them I can happily call friends. Even though I cannot name everyone here, your contribution to my studies has been immeasurable. More importantly, your friendship was able to help me get through these years easily and happily.

I would also like to thank Dr. Raphaël Janot, Dr. Da Huo, Dr. Hélène Tonnoir from Université de Picardie Jules Verne and Dr. Vanessa Fierro, Dr. Jimena Castro Gutiérrez and Prof. Alain Celzard from Université de Lorraine for their collaboration and Dr. Alexandre Léonard again for his guidance during my studies. Their contribution for improving my work has been greatly impactful.

Finally, I would like to thank my mom and dad for their extensive and immeasurable support. I hope you know all these would have been impossible without you. Also, I would like to thank my friends for making my life in Liège a great experience and truly enjoyable. Specifically, I would like to thank Maureen Beltrame and Ezgi Nur Güler for their continuous support and friendship. I hope you understand how important your presence in my life has been.

Abstract

In this thesis, different approaches to environmental-friendlier solutions for rechargeable batteries have been considered, both in their conception and final use. The first strategy was the use of water-based processes for the manufacturing of every single electrode produced. Indeed, a water-soluble organic binder, xanthan gum, was selected instead of common toxic binder/solvent pairs. Second, electrodes with different active material loadings and particle sizes were used for identification and validation of a model; the ultimate aim of that model was to orientate the overall battery design for optimal use of the materials. Finally, the third strategy concerned the development of new materials in view of decreasing the amount of critical raw resources used in current batteries. In that ambit, model hard carbons to be used in Na-ion batteries (NIBs) were produced and the impact of their physico-chemical features on the performance as negative electrode materials was studied. Those hard carbons were also used as a support material for silicon in lithium-ion batteries (LIBs) in order to improve the capacity as well as limiting the amount of graphite at the negative electrode.

In the first chapter, a dimensionless Single Particle Model with electrolyte (dSPMe) was developed. This model aimed at optimizing the design of a positive electrode ($LiFePO_4$ - LFP) in order to obtain the highest possible energy density from the half-cell. To verify and identify the model, developed by a research partner (ULB), a series of experiments was designed: galvanostatic charge/discharge (GCPL), galvanostatic intermittent titration technique (GITT) and electrochemical impedance spectroscopy (EIS). These methods were standardized in order to obtain results that were both reproducible and pertinent for the model. Using the data, a first sensitivity analysis was performed and the key parameters to energy density were found to be (i) the LFP particle radius, (ii) the electrode thickness and (iii) the electrode cross-sectional area. Finally, an adaptive particle swarm optimization was used to solve the optimal design problem: the optimal design of the electrode was found to be 310 µm thickness, 10 nm particle radius and 2×10^{-4} m^2 electrode cross-sectional area. This new design resulted in 250 Wh kg^{-1} energy density, which corresponds to an increase of 61 Wh kg^{-1} from the initial design obtained from literature.

The second chapter tries to optimize the electrode design in a different approach. The impact of both the LFP particle size and active material loading on the performance of the electrodes was studied experimentally. Electrodes with various LFP loadings (1.6 to 6.4 mg cm^{-2}) were prepared from two different LFP powders (0.24 µm and 0.84 µm particle size). Significant

differences were observed when the active material loading increases, especially in terms of rate capability. However, electrodes with the smaller particle size were less affected, meaning they could handle faster cycling with less capacity losses. EIS highlighted large differences of charge transfer resistances between the two different particle size groups, which explained the rate capability differences. Additionally, the electrode stability over long-term cycling was studied. Although it was observed that degradation takes place regardless of the particle size, electrodes with low material loadings and small LFP particle size get much less impacted. EIS showed that both internal and charge transfer resistances increased after long-term cycling.

In the 3rd and 4th chapters, carbon xerogels (CXs) with high specific surface area (A_{BET} ~ 600 $m^2 g^{-1}$) and various nodule size (50 nm to 2 µm) were used as negative electrode materials for NIBs. First, the effect of the nodule size was determined: its increase had a significant impact on the initial coulombic efficiency (ICE), which varied from 29% to 80% between the smallest and largest nodule size. This also shows that relating S_{BET}, measured by gas sorption, to the ICE, as often done in the literature, is not pertinent. In order to improve the performance, those materials were coated with a secondary carbon layer *via* Chemical Vapor Deposition (CVD) to close the micropores and reduce the surface accessible to the electrolyte. This carbon layer led to increasing the ICE as well as introducing/lengthening a plateau zone at low voltage, resulting in increased reversible capacity. Finally, since the importance and positive contribution of closed micropores was confirmed after CVD, CO_2 activation was used to first increase micropore volume of CXs; then, these micropores were masked by CVD. For the best material, ICE of 88% and capacity of 298 mAh g^{-1} was achieved while keeping a high rate capability, which is remarkable given the low maximum temperature used in carbon synthesis (<1000°C).

In the 5th chapter, silicon nanoparticles were deposited on a mesoporous CX *via* physical vapor deposition (PVD). The impact of deposition parameters such as surface pre-treatment by Ar^+ etching and use of bias voltage during coating were studied. It was observed that both pre-treatment and bias voltage significantly increase the amount of Si deposited on the CX scaffold. Additionally, both procedures led to decreasing the amount of oxygen in the final powder material, made of nano-sized (~15 nm) Si particles on CX. A high capacity around 1250 mAh g^{-1}, including both SEI (Solid Electrolyte Interface) formation and reversible capacity, was measured; it dropped to 560 mAh g^{-1} after the first cycle. After 30 cycles, reversible capacities of all samples decreased to 60% of their initial values, showing material degradation despite very small Si particle size. Degradation is attributed to continuous reaction with between the

Si nanoparticles and the electrolyte, which calls for strategies to avoid direct contact in the final electrode.

Résumé

Dans cette thèse, différentes approches pour obtenir des batteries rechargeables plus respectueuses de l'environnement ont été considérées, tant dans la conception des batteries que dans leur utilisation finale. La première stratégie a consisté en l'utilisation de procédés à base d'eau pour la fabrication de chaque électrode produite. En effet, un liant organique hydrosoluble, la gomme de xanthane, a été sélectionnée en remplacement de couples liant/solvant toxiques couramment utilisés. Deuxièmement, des électrodes avec différentes quantités de matière active et tailles de particules ont été utilisées pour l'identification et la validation d'un modèle, le but final de ce dernier étant d'orienter la conception globale de la batterie pour une utilisation optimale des matériaux. Enfin, la troisième stratégie a été consacrée au développement de nouveaux matériaux en vue de diminuer la quantité de matières premières critiques utilisées dans les batteries actuelles. Pour ce faire, des carbones durs modèles destinés à être utilisés dans les batteries Na-ion (NIBs) ont été produits et l'impact de leurs caractéristiques physico-chimiques sur les performances en tant que matériaux d'électrode négative a été étudié. Ces carbones durs ont également été utilisés comme matériaux support pour le silicium dans les batteries lithium-ion (LIBs) afin d'améliorer la capacité et de limiter la quantité de graphite dans l'électrode négative.

Dans le premier chapitre, un modèle de particule unique sans dimension avec électrolyte (dSPMe) a été développé. Ce modèle vise à optimiser la conception d'une électrode positive ($LiFePO_4$ - LFP) afin d'obtenir la densité d'énergie de la demi-cellule la plus élevée possible. Pour vérifier et identifier le modèle, développé par un partenaire de recherche (ULB), une série d'expériences a été conçue : charge/décharge galvanostatique (GCPL), technique de titrage intermittent galvanostatique (GITT) et spectroscopie d'impédance électrochimique (EIS). Ces méthodes ont été standardisées afin d'obtenir des résultats à la fois reproductibles et pertinents pour le modèle. À l'aide des données, une première analyse de sensibilité a été réalisée et les paramètres-clés de la densité d'énergie se sont avérés être (i) le rayon des particules de LFP, (ii) l'épaisseur de l'électrode et (iii) la section transversale de l'électrode. Enfin, une optimisation adaptative par essaim de particules a été utilisée pour résoudre le problème de conception optimale. La conception optimale de l'électrode s'est avérée être une épaisseur de 310 µm, un rayon de particule de 10 nm et une section transversale d'électrode de 2×10^{-4} m^2. Cette nouvelle conception a abouti à une densité énergétique de 250 Wh kg^{-1}, ce qui correspond à une augmentation de 61 Wh kg^{-1} par rapport à la conception initiale obtenue un utilisant des paramètres de fabrication issus de la littérature.

Le deuxième chapitre est consacré à l'optimisation de la conception des électrodes *via* une approche différente. L'impact de la taille des particules de LFP et de la quantité de matière active sur les performances des électrodes a été étudié expérimentalement. Des électrodes avec des quantités de LFP différentes (1,6 à 6,4 mg cm^{-2}) ont été préparées à partir de deux poudres de LFP différentes (granulométrie de 0,24 µm et 0,84 µm). Des différences significatives ont été observées lorsque la quantité de matière active augmente, notamment en termes de capacité en fonction de la vitesse de cyclage. Cependant, il a été remarqué que les électrodes avec des tailles des particules plus petites sont moins affectées, ce qui signifie que ces électrodes ont pu gérer des cycles plus rapides avec moins de pertes de capacité. L'EIS a mis en évidence de grandes différences de résistances au transfert de charge entre les deux groupes d'électrodes (avec des tailles de particules différentes), ce qui explique les différences de capacité à haute vitesse de cyclage. De plus, la stabilité des électrodes à long terme a été étudiée. Bien qu'une dégradation soit observée quelle que soit la taille des particules, les électrodes avec de faibles quantités de matériaux et une petite taille de particules de LFP sont beaucoup moins impactées. L'EIS a montré que les résistances internes et de transfert de charge augmentaient après un cyclage à long terme.

Dans les 3^e et 4^e chapitres, des xérogels de carbone (CX) avec une surface spécifique élevée (A_{BET} ~ 600 $m^2\ g^{-1}$) et différentes tailles de nodules (50 nm à 2 µm) ont été utilisés comme matériaux d'électrode négative pour les NIBs. Tout d'abord, l'effet de la taille des nodules a été déterminé : son augmentation a un impact significatif sur l'efficacité coulombienne initiale (ICE), qui varie de 29% à 80% entre la taille des nodules les plus petits et les plus grands. Cela montre également que relier la surface spécifique A_{BET}, mesurée par adsorption de gaz, à l'ICE, comme cela est souvent fait dans la littérature, n'est pas pertinent. Afin d'améliorer les performances, ces matériaux ont été recouverts par une seconde couche de carbone *via* un dépôt chimique en phase vapeur (CVD) pour fermer les micropores et réduire la surface accessible à l'électrolyte. Cette couche de carbone a conduit à l'augmentation de l'ICE ainsi qu'à l'introduction/élongation du plateau d'insertion-désinsertion du Na^+ à bas potentiel, entraînant une augmentation de la capacité réversible. Enfin, l'importance et la contribution positive des micropores fermés ont été confirmées après CVD. Une activation du carbone au CO_2 a d'abord été réalisée pour augmenter le volume des micropores des CXs. Par la suite, ces micropores ont été masqués par CVD. Une ICE de 88% et une capacité de 298 mAh g^{-1} ont été obtenus pour le meilleur matériau, tout en conservant une capacité à haute vistesse de cyclage relativement élevé. Ces propriétés sont remarquables compte tenu de la faible température maximale utilisée dans la synthèse du carbone (<1000°C).

Dans le 5^{e} chapitre, des nanoparticules de silicium ont été déposées sur un CX mésoporeux *via* un dépôt physique en phase vapeur (PVD). L'impact des paramètres du dépôt tels que le prétraitement de surface par décapage ionique à l’argon et l'application d'une tension de polarisation au substrat lors du revêtement a été étudié. Il a été observé que le prétraitement et la tension de polarisation augmentent considérablement la quantité de Si déposée sur le CX. De plus, les deux procédures ont conduit à la diminution de la quantité d’oxygène dans le matériau final, constitué de particules de Si de taille nanométrique (~15 nm) déposées sur le CX. Une capacité élevée d’environ 1250 mAh g^{-1}, incluant à la fois la formation de l’Interface Electrolyte-Solide (SEI) et la capacité réversible, a été mesurée ; cette dernière diminue jusqu’à à 560 mAh g^{-1} après le premier cycle. Après 30 cycles, les capacités réversibles de tous les échantillons ont diminué de 60 % par rapport à leurs valeurs initiales, indiquant une dégradation du matériau malgré la très petite taille de particules de Si. La dégradation est attribuée à une réaction continue entre les nanoparticules de Si et l'électrolyte, ce qui nécessite le développement de stratégies permettant d’éviter tout contact direct dans l'électrode finale.

Table of Contents

Introduction

I.1. Context

Industrial revolution has opened the doors of accelerated progress on scientific and technological areas and changed our life forever. First radio, first automobile, first television and first commercial plane all happened within a 50-year span. Therefore, with this kind of change in daily life, the needs of humankind also changed drastically. People moved from rural areas to cities in order to seek a better life by being a worker in factories. Under the capitalistic organisation of industrial society, they were working extensive hours (14 hours a day)[1] while earning much less than the minimum necessary for a decent life. This new life required many adjustments to their habits as well as their needs. Apart from all the social impacts, more in a materialistic way, a new increasing need emerged as well: energy. While for centuries the basic requirements for humankind were food and water, the need for energy, especially under electrical form, became as crucial as food and water as technological development moved on. The world we are living in is simply not liveable without energy. From the beginning, the main source of energy has been fossil fuels. However, it is now obvious that, although fossil fuels are a very reliable option as primary energy source, the toll of its intensive use was not anticipated or simply ignored[2]. Indeed, the greenhouse gasses released as a consequence of using fossil fuels as the source of energy brought us climate change[3].

Climate change now affects our lives drastically and it will only get worse unless we change the current course of events. The very first direct thing we need to do is to reduce the yearly amount of greenhouse gasses that are released to the atmosphere. Indeed, according to UNs, the world needs to cut down the CO_2 emissions by 45 percent by 2030, which roughly corresponds to yearly 22 gigatons of CO_2[4]. While almost every one of our actions causes CO_2 emissions, directly or indirectly, most of these come from electricity and heat production. Therefore, focusing on reducing the need for energy or/and changing the way to produce it seems like an obvious plan. Indeed, greenhouse gasses emission should be drastically reduced[5], namely, the energy production from non-renewable sources such as coal, oil and natural gas. Energy production must be switched to renewable sources such as wind, solar, hydroelectric and geothermal. However, global energy demand is still growing and with an average annual rate of 1.9% and this growth is met partly by fossil fuels[5]. Although new low carbon energy continues to improve, the pace is not fast enough to meet the increasing demand. With current rate, it would take 150 years to fully decarbonize the global energy system[5]. Therefore, reducing the energy demand should remain a primary focus on the battle against climate change.

Although the decrease of energy need is (or should be) at the agenda of many countries (mainly the more developed) and individuals, it is not possible or simply not the first concern for many others. Indeed, without mentioning the inequality, it is difficult to comprehend the CO_2 emissions. According to reports of OXFAM and the Stockholm Environment Institute, the richest 1% people of the world (63 million individuals) is responsible for 15% of the CO_2 emissions and it goes up to 52% of the emissions when the percentage of richest ones is increased to 10%[6]. Therefore, the reduction of energy consumption should be the concern of all, explicitly including the privileged people. However, when the CO_2 emissions by sectors are inspected, it can be seen that 73% of the entire CO_2 emissions are caused by energy production/usage in the sectors of industry (24%), transport (16%), and energy used in buildings (17.5%)[7]. Therefore, while reducing the energy consumption can stay as a focus, finding a better and cleaner way to match our need for energy looks to be a more direct approach. Indeed, converting the energy production to renewable sources instead of fossil fuels can be a way to reduce the greenhouse gas emissions. For example, coal and natural gas emit from 200 g_{CO2eq} per kWh^{-1} to more than 1000 g_{CO2eq} per kWh^{-1} over their life cycle depending on whether carbon capture and storage is used or not, respectively[8][9]. According to calculations that are accounting for life cycle of technologies (*i.e.* manufacturing of the plant to full operation and dismantling of the system), the CO_2 emissions are much lower for renewable sources: usually below 50 g_{CO2eq} kWh^{-1}, with a maximum of 100 g_{CO2eq} kWh^{-1}[8][9]. Therefore, using renewable sources clearly would help reducing the greenhouse gas emissions drastically. In the meantime, apart from the environmental upside of converting to renewable energy sources, it is also getting more advantageous in economic aspects as well. For example, by 2022, while the cost of fossil fuels was 0.2691 USD kWh^{-1}, solar photovoltaics got down to 0.0643 USD kWh^{-1}[10]. Although those numbers can be deceiving since the costs of fossil fuel sources increased immensely in the recent years due to various global crises, it remains clear that renewable energy is getting cheaper. But despite progress in the field of renewable energy production, the main source of energy is still non-renewable: by 2023, fossil fuels accounted for 76.84% of the primary energy consumption while renewable sources reached 19.44%; the part of nuclear energy, which is not a renewable source either, was 3.72%[11] (Figure I.1).

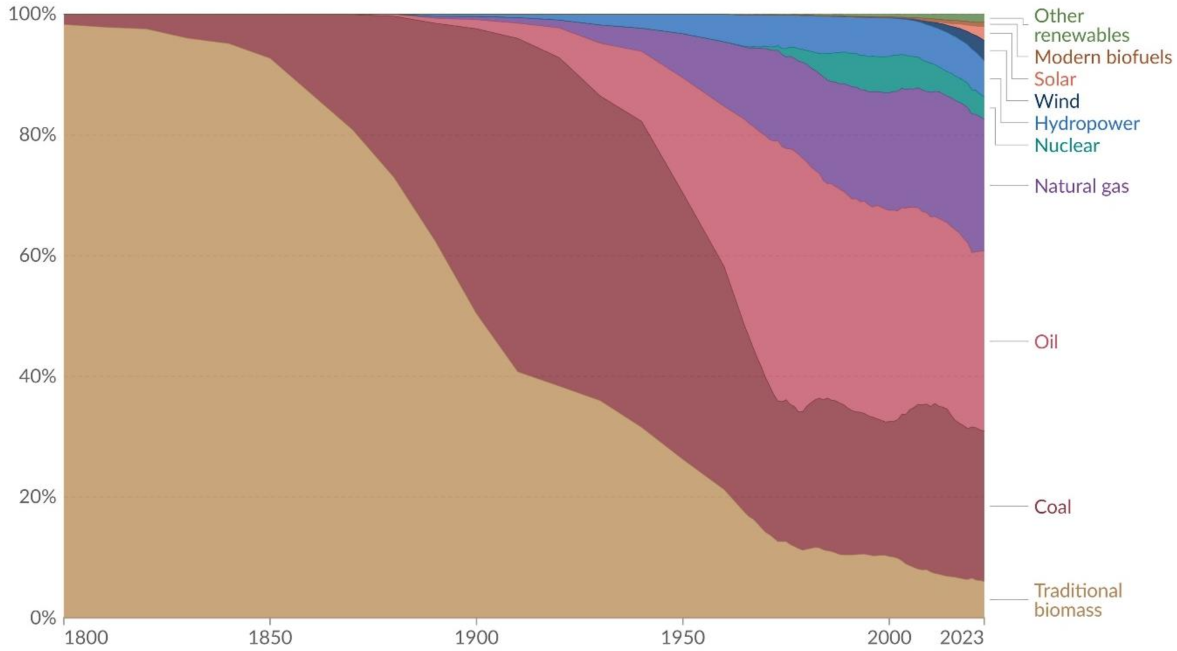

Figure I.1. Global primary energy consumption percentages by source per year [11] .

Although renewable energy sources seem to be an obvious way to reduce the greenhouse gasses emissions while bringing economic advantages, several hurdles still keep them from becoming the main source of energy. The biggest downside is that the development of these technologies still requires the use of immense amounts of energy. Another downside is that, except for biomass, renewable energy sources simply cannot be turned on and off whenever it is needed or not, which makes renewable energy difficult to manage. In that case, energy should be stored in large amounts when overproduction is possible, and used when needed. To do so, the massive development of energy storage devices is mandatory.

I.2. Energy storage devices

Energy can be stored thermally, mechanically, chemically or electrochemically. Thermal systems can store energy by heating and cooling. For example, seasonal thermal energy storage is a method that collects the energy (*i.e.* waste heat from air conditioning equipment during hot months) during the warm season and uses it in the cold season[12]. Energy can also be stored mechanically through hydroelectric dams[13]. Water is pumped to higher altitude during low electricity demand and released onto the lower reservoir through a turbine, producing electrical energy. Finally, electrochemical devices store electrical energy *via* redox reactions.

Many types of electrochemical energy storage systems exist, and can be chosen based on the requirements of the applications (Figure I.2). Although the ideal device would store a lot of energy quickly and discharge it quickly, current systems are basically far away from this ideal device. Therefore, a selection of materials and design is needed in order to supply the specific need of each application. For example, supercapacitors charge and discharge very quickly, which makes them suitable for fast-reaction systems such as acceleration and start-stop mechanisms of electric vehicles. However, their capacity is simply not enough to be considered as main energy storage devices in applications such as power reserves. On the contrary, batteries are the most popular energy storage devices since their capacity is much higher than supercapacitors and they can charge/discharge within a reasonable timeframe, even though much longer that supercapacitors. Batteries are nowadays used in almost all portable electronic devices, other small applications (such as watches, remotes, *etc.*), transportation and also for grid level storage.

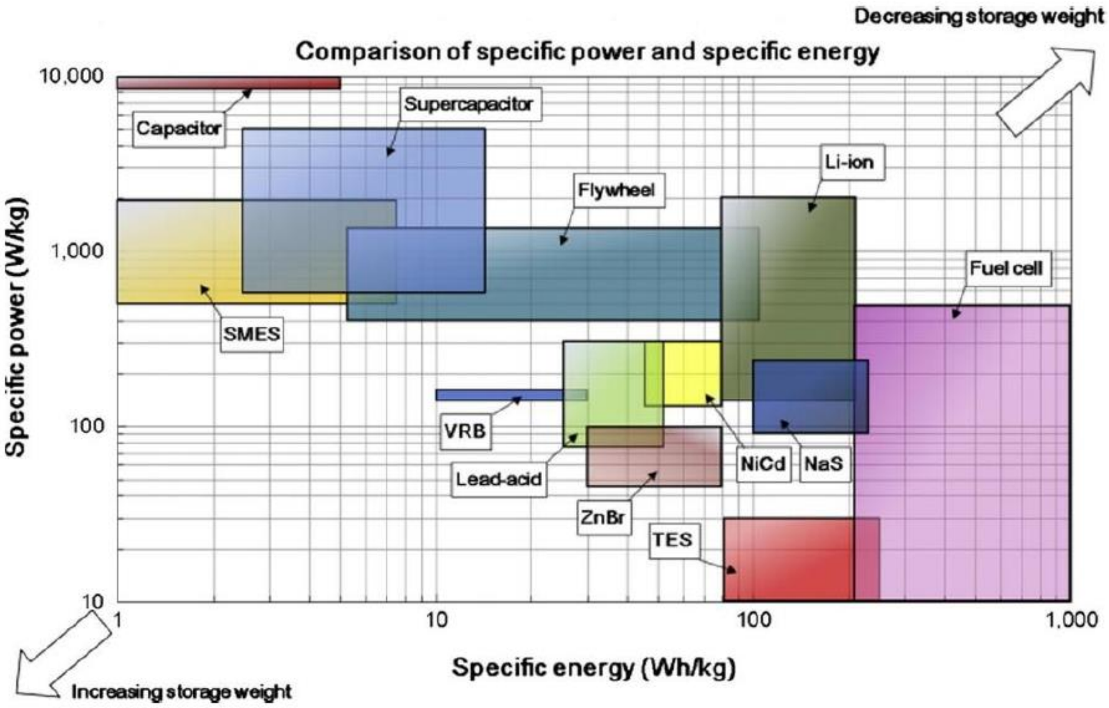

Figure I.2. Comparison of energy storage devices based on their specific power and specific energy[14] .

I.2.1. Batteries

The first electrochemical battery, the voltaic cell, was built by Alessandro Volta in 1800[15] (Figure I.3a). Although Volta did not completely understand the working mechanisms and claimed it to be an inexhaustible source of energy, he opened a door for people to follow on. Scientists who succeeded him pushed the battery technology further but their designs, similar to Volta's, were not rechargeable. Once their reactants were spent, they were simply dead. The second huge door was opened when the first rechargeable battery was invented by Gaston Planté as he built the lead-acid battery[15](Figure I.3b). He realized that those batteries could be reused simply by applying a reverse current through it, regenerating the pristine reactants. Following his path, both energy density, power density and safety of those primary and secondary batteries were progressively improved by other chemists, *via* the development of many designs using a wide variety of reactive materials. The latest determining door was unlocked by John B. Goodenough, S. Whittingham and A. Yoshino, who respectively discovered $LiCoO_2$ positive electrode[15], intercalation reactions and carbonaceous materials as negative electrodes. These discoveries brought them the Nobel Prize in Chemistry in 2019, and many others lead to the modern Li-ion technology we are using today. After that, as the need of energy storage increased even further, the development of battery technology advanced exponentially.

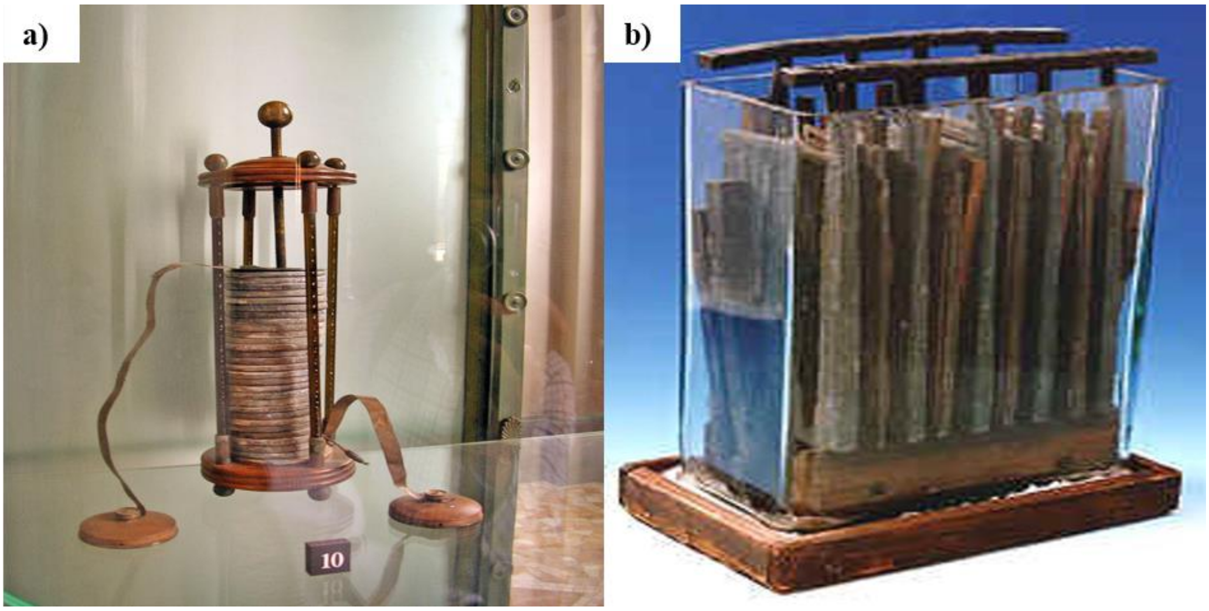

Figure I.3. (a) First voltaic cell made by Alessandro Volta and (b) first rechargeable battery built by Gaston Planté[16][17].

I.2.2. Working mechanism of rechargeable batteries

Batteries are electrochemical energy storage devices that produce or store electricity through electrochemical reactions. Namely, oxidation and reduction reactions happening in the cell respectively free and catch electrons. If connected to an external electrically conducting circuit, electrical current flows from one side to the other and can be used to supply electrical energy to a device. The reversible oxidation/reduction reactions take place at the electrodes and the ions are transferred by the electrolyte which is electronically insulating. The separator physically keeps the electrodes from each other in order to prevent any internal short-circuit. During the charging process, the two electrodes are connected externally to an electrical supply. This external supply forces electrons to be released at the positive and move to the negative electrode through the external circuit while the ions move internally in the same direction (Figure I.4). During the discharge process, electrons move from the negative electrode to the positive electrode *via* the external unit, which produces electrical work, while ions move from the negative electrode to the positive electrode in the electrolyte. The ions that are used in rechargeable batteries can vary. The most popular family used in rechargeable batteries is that of alkalis, which includes lithium, sodium and potassium. Li-ion batteries (LIBs) are nowadays the most widespread and advanced ones, with a wide variety of materials that can host and release Li^+ *via* different types of storage mechanisms. Those mechanisms include intercalation, alloying and conversion, the most conventional type of materials being the intercalation-type ones.

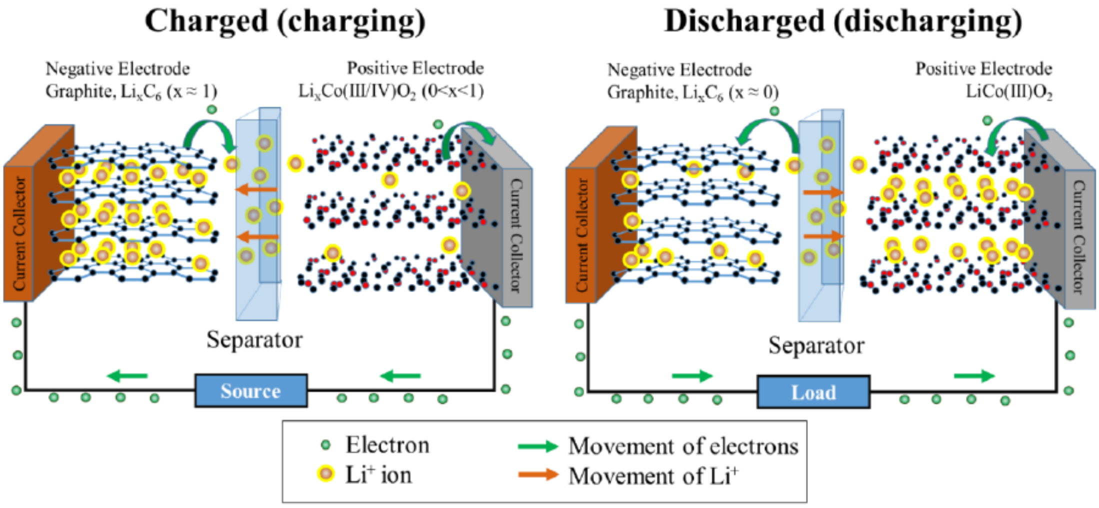

Figure I.4. Schematic visualization of charge and discharge mechanism of $LiCoO_2$/graphite Li-ion battery[18].

I.2.3. Configuration and manufacturing of batteries

The main goal of electrochemical energy storage is to use electroactive material to store and supply electricity. However, those materials must be assembled into a suitable configuration. All batteries are composed of four major components: (i) a positive electrode, (ii) a negative electrode, (iii) an electrolyte and (iv) a separator. Electrolyte is used as the medium of the ion transfer while a separator is used to prevent internal short-circuits; electrons are forced through the external circuit, the electrolyte being an electronic insulator. Additionally, electrodes also consist of active material, conductive additive, binder and current collector. Since the active materials are generally manufactured in powder form, they need to be physically stabilized on a conductive surface (current collector) in order to be able to connect them to a setup (Figure I.5). Therefore, binders are used to stick them onto the surface of current collector. Additionally, conductive additives can be included in the electrode formulation to boost their conductivity given that some electrode materials are intrinsically poorly conductive. In general, conducting carbons such as carbon black, carbon nanotubes or even graphene can be used in that ambit.

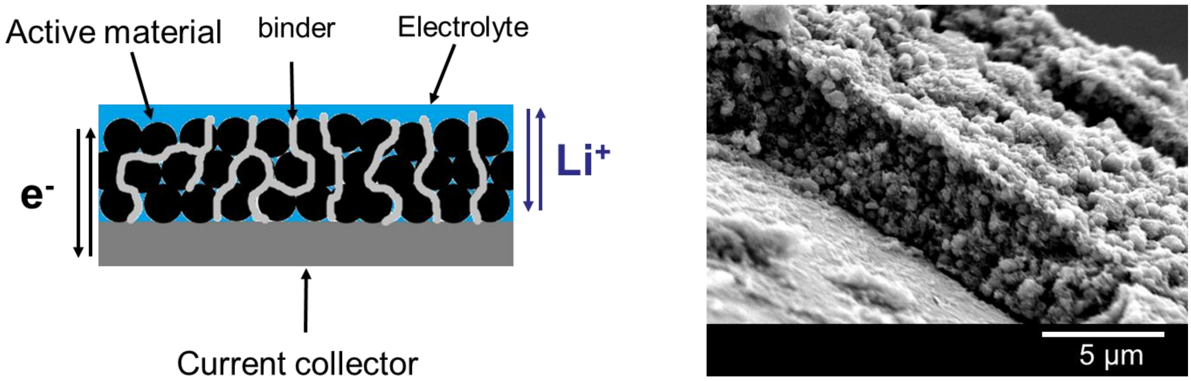

Figure I.5. (a) Scheme of a composite battery electrode and (b) scanning electron micrograph of an electrode coated on a current collector[19].

All the items listed above should be deposited onto a surface, *i.e.* the current collector, to be used in electrochemical systems. Usually, an ink containing all the components is prepared by mixing them in an appropriate solvent. This solvent should be able to dissolve the binder so that, when the solvent dries up, the binder can hold everything together, bonded to the surface of the current collector. The solvent should also be able to homogeneously disperse the powder materials (active material and conductive additive) to avoid any electrode composition or thickness heterogeneity. Several methods to deposit this ink onto surfaces exist[20]: doctor blade-coating and spray coating are the most popular. Doctor blade-coating consists in spreading a viscous ink onto the current collector surface using a moving blade; the blade height is adjusted to set the coating thickness[20]. This method is highly efficient and it is the main process used and developed in the industry as slot-die coating[21]. In slot-die coating, instead of putting the ink in front of the blade, the ink flows through a head that is moving on the substrate and coats the ink onto the surface. However, adjusting the amount of material coated onto the current collector is rather challenging and drying is relatively slow given that the whole electrode thickness is deposited in one step. Spray-coating uses pressurized gas to atomize a very fluid liquid ink and spray it onto the surface of the current collector. The ink is thus dropped in very small amounts and dries quickly, making it ready for the second layer. The thickness of the electrode, and thus the desired amount of active material, can be adjusted by increasing the number of passes onto the same electrode spot. However, this method can take longer to finalize since it requires spraying of several layers, compared to one single process of coating *via* doctor-blade coating.

Besides the selection of the deposition method, a selection of materials is needed for a battery design. The first and most important step is of course the selection of active materials. Two different kinds of materials (for positive and negative electrodes) need to be selected. The selection firstly can depend on safety. Indeed, some types of active material can be regarded as safer. For example, $LiFePO_4$ (LFP) has a lower risk of overheating and provoking fire compared to other LIB materials thanks to its thermal/structural stability. Following this, in principle, positive electrodes constitute the source of lithium within the battery cell and they would need to have a high insertion/deinsertion potential *vs.* Li^+/Li. Materials such as LFP, $LiCoO_2$ (LCO), $LiNi_xMn_yCo_{1-x-y}O_2$ (NMC), *etc.* can be used in this setup. The biggest issue in most of these materials is their mining procedure and their limited availability. Indeed, cobalt, manganese, nickel and lithium are costly, demanding to extract and purify, and their production environmental cost is immense. Also, deposits of these raw materials are concentrated on particular countries in the world (Figure I.6). Namely, 50% of the entire cobalt extraction is done in Democratic Republic of Congo while 41% and 34% of lithium originates from Australia and Chile, respectively[22]. For the negative electrodes, a material that can host Li^+ ions with a low potential *vs.* Li^+/Li should be selected. Graphite is widely used as negative electrode material. Although it does not seem to be as precious as Li or Co, global supply issues exist as well. Indeed, 65% of the natural graphite production is currently performed in China

[22]. The details of these materials and their working mechanism is explained in detail in the following section.

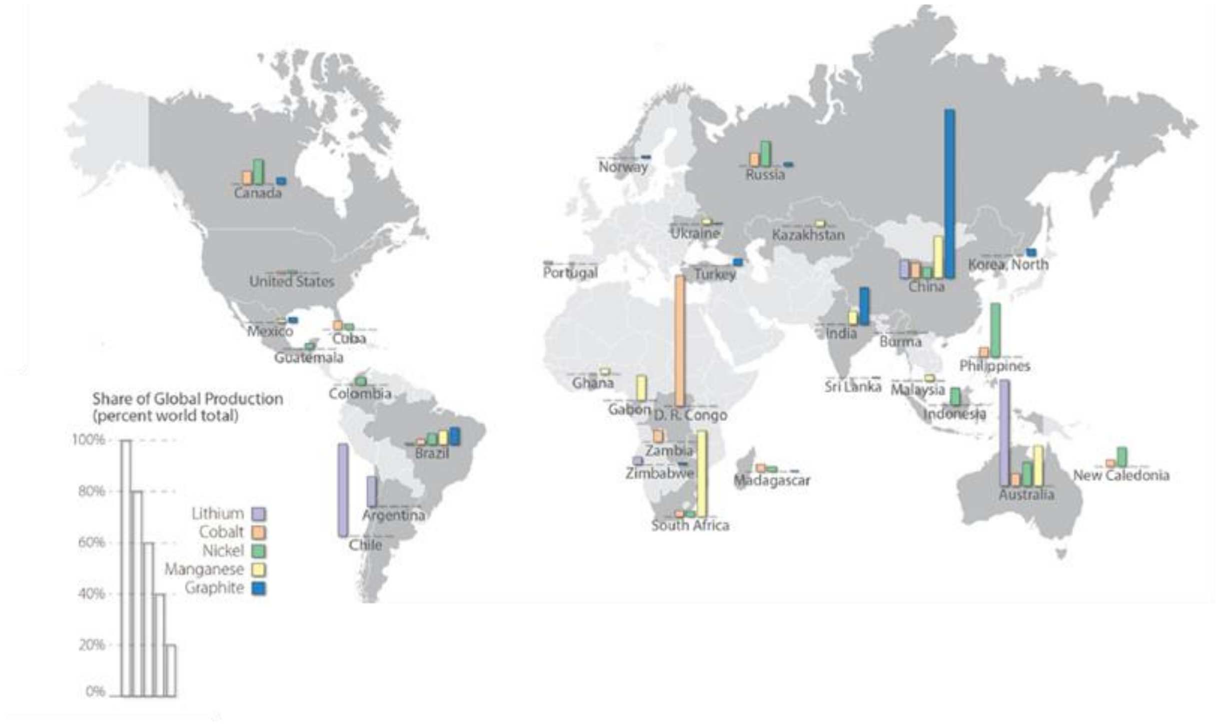

Figure I.6. The share of production of battery materials by countries [22].

Apart from active material choice, the selection of the binder is also crucial in terms of environmental impact. For example, polyvinylidene fluoride (PVDF) as a binder and N-methyl-2-pyrrolidone (NMP) as the solvent is one of the most popular combination used for ink preparation in industry. However, NMP is classified as toxic according to EU[23]. Therefore, the elimination of the NMP is one of the priorities in terms of moving to a greener battery design. In that ambit, water-soluble polymers such as styrene–butadiene rubber (SBR)/carboxymethyl cellulose (CMC)[24] and polyacrylic acid (PAA) can be used[25][26]. However, it should be noted that those water-compatible binders usually require one or more dispersants to obtain processable slurries, which adds additional mass that is not contributing to the electrochemical reactions. In the meantime, a previous study reported the use of xanthan gum (XG) as a water-compatible binder without any other additives[27]. This study, which developed $Li_4Ti_5O_{12}$ (LTO) and LFP electrodes by water-based processing, reached identical results compared to electrodes processed using the PVDF/NMP combination, both in half-cell and full cell (LFP/LTO) setup. Therefore, XG can be considered as a good candidate to replace the toxic PVDF/NMP combination.

I.2.4. Li-ion batteries

I.2.4.1. Intercalation-type active materials

Intercalation-type active materials are the most conventional, both in scientific literature and in practical applications, since it is the first type of LIB materials discovered. Indeed, $LiCoO_2$ (LCO) was first reported[28] to be able to host Li^+ within its structure, and was followed by many more, now used in LIBs. In that type of device, both electrodes are made of an intercalation-type active material. The mechanism basically consists of ions inserting/extracting in/from the interlayer spaces of layered structures. For the process to be reversible, this insertion/extraction must not result in any structural change other than disruption in the interlayer spacing[29]. The energy change for the intercalation, thus the disruption of interlayer spacing, is supplied by charge transfer occurring between the ion and the structure[30]. Most commonly, graphitic carbon is used as negative electrode material and the positive electrode is made of a lithiated oxide of transition metal. $LiCoO_2$ has long been preferred at the positive electrode because of its high insertion/deinsertion potential and high stability. However, one now observes an increase of popularity of LFP and NMC, which allows decreasing the amount of cobalt. For LCO, LFP and NMC (and other intercalation-type positive electrode materials), lithium is stored within their layered crystal structure. One notes that this type of storage mechanism can result in crystal structure changes. For example, for LCO, after 50% of lithium has been extracted from the parent structure, transformation from hexagonal to monoclinic phase can be observed. This transformation is difficult to reverse upon lithiation, and should be avoided. Therefore, only 50% of the 280 mAh g^{-1} theoretical capacity is usable[31]. At the negative electrode, graphite is the usual material: it stores the Li^+ ions by insertion in-between its graphitic sheets. The biggest advantages of graphite lie in (i) its moderated volume expansion and (ii) its very low overpotential, about 0.1 V *vs.* Li^+/Li; those features are due to the typical graphitic layer spacing, similar to the Li^+ ion radius[32]. Additionally, a passivation layer called Solid-Electrolyte Interface (SEI) is generated during the cycling of graphite. This layer is a product of interaction between the electrolyte and the negative electrode (graphite in this case) and the characteristics of this layer can vary depending on the content of the electrolyte or the type of electrode. Insertion/deinsertion potentials and capacities of other examples of intercalation-type materials can be found in Table I.1. Overall, $LiCoO_2$/graphite electrodes are used and energy is stored by following half-reactions:

Positive electrode: $LiCo(III)O_2 \rightleftharpoons Li_{1-x}Co(III/IV)O_2 + xLi^+ + e^- \quad 0 < x < 1$ (I.1)

Negative electrode: $C_6 + Li^+ + e^- \rightleftharpoons LiC_6$ (I.2)

Table I.1. Intercalation-type materials and their properties[33][34].

Material	**Potential** V *vs.* Li^+/Li	**Capacity** mAh g^{-1}	**Safety**
	Positive electrodes		
$LiFePO_4$	~3.5	120	Good
$LiNi_yMn_xCo_zO_2$	~4.2	160	Fair
$LiCoO_2$	~4.2	200	Fair
$LiMn_2O_4$	~4.2	150	Fair
	Negative electrodes		
$Li_4Ti_5O_{12}$	~1.5	160	Good
Graphite	~0.1	350	Good

I.2.4.2. Alloying-type active materials

Alloying-type materials generally refer to elements that can electrochemically alloy and form compound phases with Li at relatively low potential. Because of their low potential *vs.* Li^+/Li, they are generally used as negative electrode materials (Table I.2). Thus, instead of having a chemical species such as Li_aY, an alloy with lithium Li-Y is formed. Those materials generally display very high volumetric and gravimetric capacity but their volume change during charge and discharge limits their usage. Indeed, upon insertion, volume expansion can lead to fracturing the active material particles and to losing electrical contact with the current collector. The most well-known alloying-type material is silicon due to its extremely high capacity, low lithiation/delithiation potential and high chemical stability. A few examples of alloys are mentioned in Table I.2 along with their properties. The silicon/Li^+ alloying/dealloying in LIB electrode proceeds as follows[35]:

$Li_xSi \rightleftharpoons Si + xLi^+ + e^- \ (0 < x < 3.75)$ (I.3)

Table I.2. Alloying type negative electrode materials.

Material	**Potential** V *vs.* Li^+/Li	**Capacity** mAh g^{-1}	**Volume expansion** %
Li_xSi	0.4	4200	300
Li_xSn	0.5	993	240
Li_xSb	0.9	660	147

While silicon can display an extremely high capacity upon lithiation (4200 mAh g^{-1}), its volume expansion can reach up to 300%[36]. Also, continuous formation of SEI layer as the particles crack and expose new free surfaces to the electrolyte can be regarded as another drawback. Those alloying-type materials would need to be produced in small dimensions in order to support the mechanical integrity (*i.e.* below 150 nm for silicon[37]) and be deposited on a material with a sufficient void space to allow volume expansion. Therefore, those types of materials are generally used in composite structures to compensate the volume expansion[30]. More often, carbonaceous materials are the partner of alloying-type materials in a composite[28]. Conductive materials that can supply voids for expansion of alloying-type materials such as carbon nanotubes and disordered carbons are often targeted.

I.2.4.3. Conversion-type active materials

Conversion mechanisms involve the breakage and formation of chemical bonds, leading to the formation of new chemical species with different structures. A representation of conversion reaction can be seen as follows[30]:

$$TM_{\mathrm{a}}X_{\mathrm{b}} + (b.c)Li^{+} + (b.c)e^{-} \rightleftharpoons aTM^{0} + bLi_{\mathrm{c}}X \qquad \text{(I.4)}$$

where TM is a transition metal and X is an anionic species such as oxide, fluoride or sulphide. During the lithiation, TM is reduced to zero oxidation state, which usually involves more redox electrons compared to other storage mechanisms and therefore a higher theoretical capacity.

Firstly reported by Tarascon and co-workers in 2000[38], various transition metal oxide positive electrode materials were further discovered. Those materials are able to reach capacities up to 700 mAh g^{-1} over 100 reversible cycles. Chalcogens (S, Se and Te) and halogens undergo reaction presented in Equation I.4 and form Li_2X and LiX, respectively. Particularly, S and Se are regarded as attractive candidates as positive materials for LIBs. Especially, sulphur has a very high theoretical capacity (1672 mAh g^{-1})[39]. However, several drawbacks keep them from being commercially used. Namely, low conductivity of elemental sulphur and Li_2S results in low overall utilization of the electrode material. More importantly, polysulfides can diffuse back and forth between the negative and positive electrodes. They are reduced at the negative electrode and afterwards oxidized at the positive electrode. This phenomenon is called “polysulfide shuttle” and causes serious self-discharge[39].

I.2.4.4. Other alkali-metal batteries

Although LIBs are still the front runner of the battery family, shortcomings of critical materials such as Li and Co signal us that other options are needed in a very near future (Figure I.6). Also, LIBs have been studied through and through over the last 30 years, which means that we are reaching the limit of their potentiality and that it will be difficult to go beyond their current performance. Therefore, new concepts should be developed to overcome the energy storage need. Among other possibilities, changing the alkali metal from lithium to sodium or potassium could be a good route to follow in the view of decreasing the required amount of critical materials. Both sodium and potassium are quite abundant within the Earth’s crust, leaving the major problem of lithium extraction out. Apart from the higher abundancy of Na or K compared to Li, few things change. Indeed, the working mechanism of sodium-ion batteries (SIB) and potassium-ion batteries (PIB) is quite similar to LIBs since all are in the same alkali-metal group of the periodic table. However, both Na^+ (1.02 Å) and K^+ (1.38 Å) ions display higher sizes compared to Li^+ (0.76 Å), which requires hosting materials to undergo crystal-structure change during Na/K intercalation and de-intercalation[40]. Thus, although those battery types can show a high energy density (200-700 Wh kg^{-1})[41][42], their stability upon cycling can be quite low, especially for PIB given the biggest ion size of K^+. Additionally, several challenges of PIBs stand between their development and their commercialization. Indeed, PIBs suffer from low coulombic efficiency and lack of electrolyte options since potassium is highly reactive[43].

Na-ion batteries (NIBs) are the new hot topic for batteries since, economically, sodium is the fourth most abundant element on earth and very easy to extract. Additionally, unlike lithium, it does not form an alloy with aluminium, which enables using the latter as a current collector for negative electrodes instead of costly copper.

Several different materials have been suggested as positive electrode materials in NIBs, from TMOs to transition-metal sulphides, oxyanionic compounds, polymers, *etc* [44]. However, the main obstacle to overcome in order to obtain a functional NIB is the selection of an appropriate negative electrode material. In that regard, the first material that naturally comes to mind is graphite, the long-lasting friend of LIBs. However, graphite is not an appropriate material for NIB negative electrodes as Na^+ ions cannot properly intercalate between graphite layers [45]. However, carbonaceous materials offer more options than graphite. Disordered carbons that mix amorphous regions with small crystalline ones (hard carbons and soft carbons) are materials that allow insertion of sodium[44]. Therefore, the strategies of developments of sodium-ion battery negative electrodes focused mainly on disordered carbons during the last 20 years.

Soft carbons (SC) are made of a semi-graphitic structure with better oriented crystalline domains compared to hard carbon, meaning that they can connect upon heating to form larger graphitic domains (Figure I.7). SCs benefit from high electrical conductivity coming from their better oriented crystalline domains. Hard carbons (HC) are the other type of disordered carbons; they consist of randomly distributed, distorted graphene nanosheets. Generally, HCs can have different morphologies including nanowires, porous structures or spheres. HCs can be produced from various precursors (carbohydrates, biomass and polymers) by either direct pyrolysis (for synthetic precursors) or polycondensation and subsequent pyrolysis at various temperatures (800-2500°C)[46]. This variety of production pathways comes with easily modifiable end-products that display various physico-chemical and structural properties. However, the biggest obstacle to real use is their 1st cycle efficiency (*i.e.* the Initial Coulombic Efficiency, ICE) which is quite low due to the decomposition of the electrolyte onto their surface[45][47] resulting in an SEI layer. Carbon xerogels are one of the materials included in the family of hard carbons. Their morphology consists of interconnected nodules and their morphology (nodule size and pore texture) can be modified through the synthesis conditions. Although these materials are promising for further usage, they also display low ICE for the same reason as other hard carbons [45].

Figure I.7. Scheme of the structure of various carbonaceous materials[48] .

I.2.5. Battery design and dimensioning

Apart from material selection, design parameters such as the active material loading on the electrode, the dimensions of the electrode as well as the particle size of the materials are crucial to determine the performance of the batteries. To reach the best design, it is of course possible to perform exhaustive experimental work based on trial and error. This approach is however time-consuming. In order to rationalize the process, optimization studies based on theoretical work can be useful. In that regard, modelling of batteries can be used to determine optimized battery designs. Usually, some physical parameters are already known and need to be completed by theoretical electrochemical knowledge to develop the model and obtain results that would help driving the experimental work into the right direction.

Battery modelling is a wide subject that can rely on various approaches and frameworks depending on the aimed application. Based on their working principles, models can be classified as data-driven models[49], equivalent-circuit models[50] and physical models[51]. Due to their preciseness on capturing complex non-linear behaviours, data-driven models are quite popular. However, a huge amount of data is needed for the identification stage (*i.e.* teaching the parameters to the model) and they lack physical interpretability. In the meantime, equivalent-circuit models would interpret the battery as an electrical circuit with series resistance, capacitor and voltage generator[50]. Although this is an easier method computationally, those models are not useful to explain the correlation between the physical properties of the system and the performance of the battery. Finally, physical models do not require large amounts of data and they can be used to interpret the physical phenomena. Among all the electrochemical models, the Doyle-Fuller-Newman (DFN) model is the most popular[52]. This method uses charge and mass conservation in the solid phase and the electrolyte to get a better understanding on the interface of solid/electrolyte. However, the computational requirements of DFN-type models are quite high. Therefore, in an alternative way, reduced-order electrochemical models are developed. These models can be derived from the DFN model, which is simplified under suitable assumptions. For example, The Single-Particle Model (SPM) assumes that the active material consists of one big particle[53]. This model can be used to for an optimization study on battery design.

I.3. Main goals of thesis

The starting point of this PhD thesis is a collaborative research project between the Université Libre de Bruxelles (ULB) and the Université de Liège (ULiege), financed by the Fonds National de la Recherche Scientifique (FNRS – PDR project Convention T.0142.20). The global aim of the project was to develop a model that would help optimizing the design of a LIB. According to the repartition of the tasks, ULB took care of the model development while ULiege's mission was to produce experimental data and discuss the electrochemical phenomena. Indeed, the experimental data would be used for the identification and verification of the model. This called for defining (i) which model variables could be known or controlled and (ii) which ones had to be estimated from the model. First of all, a study was done to standardize the experimental conditions in order to obtain reproducible and reliable data. Later on, in that context, while producing the experimental data for the modelling, a systemic experimental plan has been implemented to investigate the effects of physical parameters of the electrode (such as active material powder particle size and active material loading on the electrode). To hit two birds with one stone, electrodes were meant to be produced *via* water-based processes. Selected active materials with different physical properties (*e.g.* particle size) and different electrode loadings were targeted to understand their impact on the electrode performance.

In parallel, various materials were tested to further increase the scope of water-based processes and to drive the research towards non-critical materials. In that regard, taking advantage of the lab group expertise on carbonaceous materials, carbon xerogels were used in two different circumstances. Carbon xerogels are hard carbons with interconnected spherical nodules which can be easily modified during their synthesis (Figure I.8). Those materials can be produced with high surface area, low surface area, large or smaller nodules, various surface chemistries, *etc*. Therefore, they can be considered either as support for conversion-type materials or as active material for Na-ion negative electrodes. In the first case, materials that suffer large volume changes during their charge/discharge can be deposited within the pore volume, at the surface of the carbon nodules. In that regard, silicon can be the first material that comes to mind as (i) it offers the highest capacity among LIB materials while (ii) its usage is limited by its extensive volume change. In the second case, carbon xerogels can be used as active materials in NIBs. Indeed, Na^+ intercalation is feasible in carbon xerogels (like in other hard carbons), which makes them a candidate for NIB negative electrodes. Even though a few studies using carbon gels as NIB electrode materials could be found[54][55] in the literature at the beginning of this thesis, understanding of the different design parameters of the CXs on the final electrode performance had not been studied in details yet. In particular, the impact of the nodule size as well as that of the surface area remained totally unclear. This called for a systematic study of those parameters in view of designing efficient hard carbons for NIB negative electrodes.

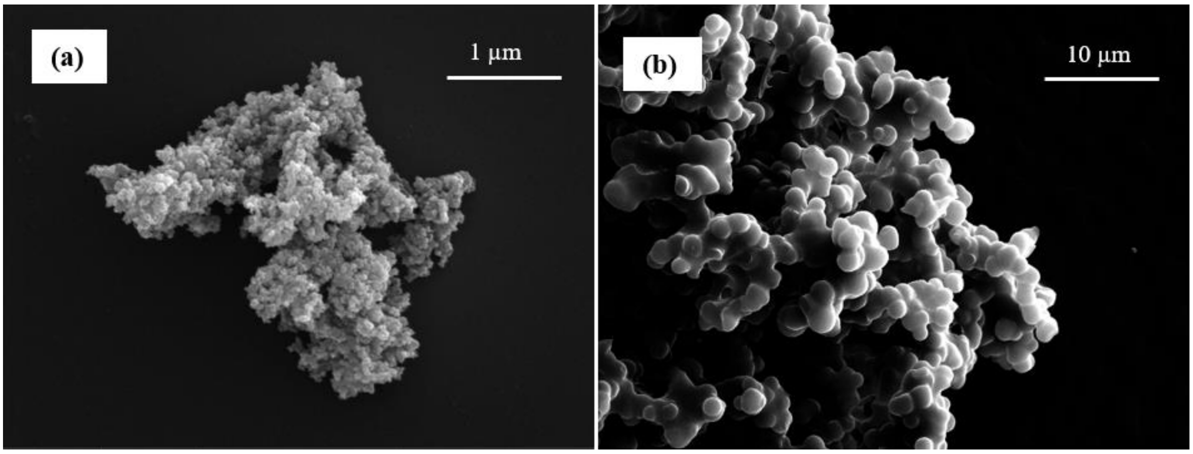

Figure I.8. SEM images of carbon xerogels with nodule size of (a) 50 nm and (b) 2 µm, prepared following previous studies[56].

To sum up, **the general aim of the thesis was to explore greener solutions for the batteries, both in their conception and final use**. In that ambit, three distinct strategies were pursued:

1- **Water-based processes were used for every single electrode produced**. Their usage, first developed for conventional materials (LFP and LTO) following previous studies [18], was expanded to new active materials to be used in both Li-ion batteries (Si/C composites) and Na-ion batteries (hard carbons).

2- Water-based processed **electrodes were designed using various LFP powders and electrode thicknesses to be used as systems for model identification and validation**.

The model, developed by ULB, should ultimately serve to better control charge and discharge processes in real full-cell batteries, hence expanding their efficiency and lifetime. This latter work is still going on between ULB and ULiège.

3- **Model hard carbons** were produced to study the impact of their physico-chemical features such as nodule size, pore texture micro- and meso/macropore surface area and composition, on their performance **as NIB negative electrode materials**. This study was performed in collaboration with the LRCS laboratory in Amiens and the ENSTIB/Institut Jean Lamour in Epinal. In parallel, those carbon scaffolds were used as supports for the deposition of Si nanoparticles by Physical Vapor Deposition process, performed with the help of the LARN laboratory in UNamur and Innovative Coating Solutions (ICS). Hopefully, those materials will (i) help the transition from LIBs to NIBs and (ii) enable the use of Si/C composites in order to decrease the needs of critical raw materials in rechargeable batteries. Overall, the approach developed in the present thesis work will serve as a basis to further design hard carbons with ideal structures from other raw materials sources (possibly bio-based). The subject remains in development at the NCE laboratory of ULiège.

I.4. Chapter overview

This thesis is structured as five chapters, each of them answering to some of the challenges raised in the previous sections, *via* the strategy explained in section 2 of the Introduction. Each chapter has the regular structure of a scientific publication. Strategy n°1 is adopted in all chapters, given that all electrodes were produced *via* a water-based manufacturing process. Strategy n°2 is covered in Chapters 1 and 2, while strategy n°3 concerns Chapters 3 to 5.

Chapter 1

In the first chapter, standardization of experimental conditions in order to obtain reproducible data to be used in electrochemical modelling was developed. In this chapter, a brief introduction to battery modelling is first presented. Then, all the standardization procedure of experimental procedures such as galvanostatic charge and discharge (GCPL), electrochemical impedance spectroscopy (EIS) and galvanostatic intermittent titration technique (GITT) were systematically done. For example, for EIS, the resting period before going on with the procedure, state of charge at the moment of EIS and how to calculate it were studied. The model was developed by ULB using the experimental data obtained. The dimensionless model consists in considering the electrode active material as a single particle, coupled with electrolyte presence. The model was developed in order to optimize the design of $LiFePO_4$ electrodes in terms of electrode thickness and particle size.

This chapter was published in a different format in:

L. D. Couto, M. Charkhgard, B. Karaman, N. Job, M. Kinnaert. Lithium-ion design optimization based on a dimensionless reduced-order electrochemical model. *Energy* 263 (2023) 125966.

The main contributions to that study were (i) the manufacturing of LFP electrodes, (ii) the design of the electrochemical characterization procedures and (iii) the electrochemical data production.

Chapter 2

In the second chapter, a systematic series of experiments were conducted in order to understand the effect of particle size and active material loading on the performance of $LiFePO_4$ (LFP) electrodes. In that ambit, two types of LFP powders were received from Prayon s.a.: one with an average particle size of 0.84 µm and a second with an average particle size of 0.24 µm. Both powders were coated on stainless-steel discs with various active material loadings starting from 1.6 to 6.4 mg cm^{-2}. The water-based manufacturing process using xanthan gum as binder, previously developed at the NCE laboratory of ULiège, was used to prepare the electrodes. The produced electrodes were used in galvanostatic charge and discharge tests in order to understand the impact of the powder morphology and electrode thickness on the capacity, rate capability and stability of the electrodes. Finally, electrochemical impedance spectroscopy was used to understand the impact of the active material loading (or electrode thickness) and LFP particle size on the electrochemical properties such as the internal resistance and charge transfer resistance of the electrodes.

This chapter is about to be submitted for publication in the Journal of Energy Storage:

B. Karaman, L. D. Couto, M. Charkhgard, M. Kinnaert, N. Job. Water-based processing of $LiFePO_4$ positive electrodes for Li-ion batteries: effect of particle size and active material loading on the performance of the electrodes. *In preparation*.

The contributions to the study were the electrode manufacturing, electrochemical characterization and full data treatment.

Chapter 3

In the third chapter, a series of carbon xerogels with various nodule sizes, from 50 nm to 2 µm, were synthesized by classical polycondensation of resorcinol with formaldehyde in water. Following drying and pyrolysis, the xerogels were used as negative electrode materials in Na-ion half-cells. Normally, the main issue with these materials is their high surface area (~600 m^2 g^{-1}, mainly due to micropores within the carbon nodules) leading to an extensive Solid Electrolyte Interface formation that traps Na^+ ions and to low Initial Coulombic Efficiencies. This typically hinders the usage of CX in Na-ion batteries. Thus, reducing the surface area accessible to the electrolyte should be a good method to overcome the issue. To do so, a secondary carbon layer was deposited at the surface of the microporous carbon nodules by Chemical Vapor Deposition (ethylene cracking). Additionally, the impact of the nodule sizes was studied. Materials were first characterized by physico-chemical techniques to get information on their crystal structure, pore structure and chemical composition. Then, water-base processed electrodes were characterized in Na-ion half-cells and compared on the basis of their capacity, galvanostatic profile, rate capability, initial coulombic efficiencies and stability.

This chapter, which is a collaboration between the NCE laboratory of ULiège, the LRCS laboratory of the Université Picardie Jules Verne of Amiens (France) and the ENSTIB/Institut Jean Lamour in Epinal (France), has been published in:

B. Karaman, H. Tonnoir, D. Huo, B. Carré, A. F. Léonard, J. Castro-Gutiérrez, M.-L. Piedboeuf, A. Celzard, V. Fierro, C. Davoisne, R. Janot, N. Job. CVD-coated carbon xerogels for negative electrodes of Na-ion batteries. *Carbon* 225 (2024) 119077.

The contribution to the study was the development of the (carbon-coated) carbon xerogels, their physico-chemical characterization (in collaboration with ENSTIB/IJL), the electrode manufacturing and the data treatment of the electrochemical characterization, performed in Amiens.

Chapter 4

For the 4th chapter, one carbon xerogel with 2 µm nodule size was synthesized by polycondensation of resorcinol with formaldehyde in water. In order to increase the amount of closed micropores, usually desired for applications in NIBs, the pristine carbon xerogel was activated *via* CO_2 treatment, then coated by Chemical Vapor Deposition to close the pores. The aim was to obtain increased area/volume to store Na^+ ions while keeping the contact surface area with the electrolyte as small as possible to avoid large SEI formation. The produced powders were first characterized by physico-chemical techniques to access properties such as pore texture, chemical composition and crystal structure. Then, the electrodes were manufactured using the usual water-based process and the materials were characterized by electrochemical methods in half-cell to obtain their capacity, galvanostatic profile, initial coulombic efficiency, rate capability and stability. This study aimed at understanding the impact of the carbon physico-chemical properties on the carbon/electrolyte interaction in terms of contact surface. Finally, this approach opens new strategies in the rational development and design of hard carbons for NIBs.

This study will shortly be submitted to *Carbon* as a continuation of the paper presented in Chapter 3:

B. Karaman, H. Tonnoir, D. Huo, J. Castro Gutiérrez, B. Carré, Z. Deckers, M. Bermont, A. F. Léonard, A. Celzard, V. Fierro, C. Davoisne, R. Janot, N. Job. Post-treatments on carbon xerogels for enhancing their performances as negative electrodes of Na-ion batteries. *To be submitted to Carbon*.

The contribution to the study was the development of the activated and carbon-coated carbon xerogels, their physico-chemical characterization (in collaboration with ENSTIB/IJL), the electrode manufacturing, the electrochemical characterization and the data treatment of the electrochemical characterization (in collaboration with the team of LRCS in Amiens).

Chapter 5

Chapter 5 explores the possibility of depositing Si nanoparticles on carbon xerogels *via* Physical Vapor Deposition (PVD). The study was performed in collaboration with Innovative

Coating Solutions and the University of Namur, the role of which was to perform PVD deposition of nanoparticles onto a carbon xerogel manufactured at the NCE laboratory. Although this has been practically done before on other carbon types, the impact of different procedures such as pre-treatment by Ar^+ etching and bias voltage during deposition was unknown. This chapter tries to shed some light on the impact of these parameters on the end product, Si/CX composite powders, and the performance of these different powders as negative electrode materials for Li-ion batteries. The composition of the powders, essentially the Si percentage deposited and the oxygen content, was determined. Electrochemical characterization was performed in half-cell configuration, leading to comparisons of reversible capacity, initial coulombic efficiency, rate capability and stability of various Si-C composites *vs.* the uncoated carbon xerogel. Again, the water-based process using xanthan gum as a binder was used to prepare the electrodes.

Although the chapter is presented as a regular scientific paper, the study should be pushed further before considering publication. Especially, the issue of Si stability remains to be tackled. The main contributions to the study were the synthesis and characterization of the carbon xerogel, the physico-chemical characterization of the Si/CX composites, the electrode manufacturing from the composites and their electrochemical characterization in half-cell, including full data treatment.

I.5. References

[1] J. Barzun, J.H. Salmon, N. P. Stearns, N. G. Parker, C. T. Champion, E. Peters, M. S. Sørensen, D. Weinstein, D. Herlihy, E. J. Herrin, R. J. Mayne, M. Frassetto, A. Hermann, *Encyclopedia Britannica*, **2024**, Available: https://www.britannica.com/topic/history-of-Europe. Accessed 28 August 2024.

[2] S. Arrhenius, *Philosophical Magazine and Journal of Science* **1896**, 41, 251.

[3] United Nations Environmental Programme, Report of the Intergovernmental Panel on Climate Change Mitigation of Climate Change, **2022**.

[4] United Nations, Climate action, Available: https://www.un.org/en/climatechange/net-zero-coalition Accessed on: Sep 26, **2024**.

[5] J. Barrett, S. Pye, S. Betts-Davies, O. Broad, J. Price, N. Eyre, J. Anable, C. Brand, G. Bennett, R. Carr-Whitworth, A. Garvey, J. Giesekam, G. Marsden, J. Norman, T. Oreszczyn, P. Ruyssevelt, K. Scott, Nat Energy **2022**, 7, 726.

[6] T. Gore, Confronting Carbon Inequality: Putting Climate Justice at the Heart of the COVID-19 Recovery, **2020**.

[7] H. Ritchie, Sector by sector: where do global greenhouse gas emissions come from? (**2020**) Available: https://ourworldindata.org/ghg-emissions-by-sector. Accessed on Sep 22, 2024.

[8] N.Y. Amponsah, M. Troldborg, B. Kington, I. Aalders, R.L. Hough, *Renewable and Sustainable Energy Reviews* **2014**, 39, 461.

[9] The Parliamentary Office of Science and Technology, Carbon footprint of electricity generation. Available: https://www.parliament.uk/globalassets/documents/post/postpn_383-carbon-footprint-electricity-generation.pdf. Accessed: August 28, 2024.

[10] International renewable Energy Agency, Renewable power generation costs in 2022, ISBN 978-92-9260-544-5

[11] International Renewable Energy Agency, Statistical Review of World Energy, 2024. ISSN 2976-7857.

[12] B. Wong, A. Snijders, L. Mcclung, *2006 IEEE EIC Climate Change Conference*, Ottawa, ON, Canada, **2006**, 1-7.

[13] Lobus, N.V.; Knyazeva, M.A.; Popova, A.F.; Kulikovskiy, *J. Carb Res.* **2023**, 9, 120.

[14] X. Luo, J. Wang, M. Dooner, J. Clarke, *Appl Energy* **2015**, 137, 511.

[15] B. Scrosati, *J Solid State Electr* **2011**, 15, 1623

[16] Wikipedia contributors. Voltaic pile. Wikipedia, The Free Encyclopedia; 2024 May 12, 17:04 UTC Accessed on Oct 8, 2024. Available: https://en.wikipedia.org/w/index.php?title=Voltaic_pile&oldid=1223512980.

[17] Corrosion doctors, Gaston Planté, Accessed on Oct 8, 2024. Available: https://en.wikipedia.org/w/index.php?title=Voltaic_pile&oldid=1223512980.

[18] J. Carabetta, *Carbon Xerogels Doped with Silicon or Tin Oxide for Lithium-Ion Battery Anodes*, **2021**, Doctoral dissertation.

[19] M.-L. Piedboeuf, Xérogels de carbone comme matériaux modèles pour l'étude du comportement électrochimique en tant qu'anodes de batteries Li-ion, Thesis defence presentation, October 20, **2016**.

[20] V. Singh, S. Kuthe, N. V. Skorodumova, *Batteries* **2023**, *9*, 184.

[21] X. Ding, J. Liu, T.A.L. Harris, *AIChE Journal* **2016**, *62*, 2508.

[22] A. Mayyas, D. Steward, M. Mann, *Sustainable Materials and Technologies* **2019**, *19*, e00087.

[23] European commission, SCCS (Scientific Committee on Consumer Safety), Opinion on Nmethyl-2-pyrrolidone (NMP), 22 March 2011

[24] H. Buqa, M. Holzapfel, F. Krumeich, C. Veit, P. Novák, *J Power Sources* **2006**, *161*, 617.

[25] S. Komaba, N. Yabuuchi, T. Ozeki, K. Okushi, H. Yui, K. Konno, Y. Katayama, T. Miura, *J Power Sources* **2010**, *195,* 6069.

[26] Z. Zhang, T. Zeng, C. Qu, H. Lu, M. Jia, Y. Lai, J. Li, *Electrochim Acta* **2012**, *80*, 440.

[27] A.F. Léonard, N. Job, *Mater Today Energy* **2019**, *12*, 168.

[28] N. Nitta, F. Wu, J.T. Lee, G. Yushin, *Mater Today* **2015**, *18*, 252.

[29] Y. Jung, Y. Zhou, J.J. Cha, *Inorg Chem Front* **2016**, *3*, 452.

[30] R. Borah, F.R. Hughson, J. Johnston, T. Nann, *Mater Today Adv* **2020**, *6*, 100046.

[31] C. Daniel, D. Mohanty, J. Li, D.L. Wood, in *AIP Conf Proc* **2014**, *1597*, 26.

[32] J. Asenbauer, T. Eisenmann, M. Kuenzel, A. Kazzazi, Z. Chen, D. Bresser, *Sustain Energy Fuels* **2020**, *4*, 5387.

[33] P. Thakkar, S. Khatri, D. Dobariya, D. Patel, B. Dey, A.K. Singh, *J Energy Storage* **2024**, *81*, 110452.

[34] A.K. Shukla, T. Prem Kumar, *Current Science*, **2008**, *94*, 3.

[35] D. Ma, Z. Cao, A. Hu, *Nanomicro Lett,* **2014**, *6*, 347.

[36] M.R. Kaiser, Z. Han, J. Liang, S.X. Dou, J. Wang, *Energy Storage Mater* **2019**, *19*, 1.

[37] X.H. Liu, L. Zhong, S. Huang, S.X. Mao, T. Zhu, J.Y. Huang, *ACS Nano* **2012**, *6*, 1522.

[38] P. Poizot, S. Laruelle, S. Grugeon, L. Dupont, J.-M. Tarascon, *Nature* **2000**, *407*, 496.

[39] S.H. Yu, X. Feng, N. Zhang, J. Seok, H.D. Abruña, *Acc Chem Res* **2018**, *51*, 273.

[40] J. Hu, Y. Hong, M. Guo, Y. Hu, W. Tang, S. Xu, S. Jia, B. Wei, S. Liu, C. Fan, Q. Zhang, *Energy Storage Mater* **2023**, *56*, 267.

[41] J.Y. Hwang, S.T. Myung, Y.K. Sun, *Chem Soc Rev* **2017**, *46*, 3529.

[42] X. Bie, K. Kubota, T. Hosaka, K. Chihara, S. Komaba, *J Mater Chem* A **2017**, *5*, 4325.

[43] S. Dhir, S. Wheeler, I. Capone, M. Pasta, *Chem* **2020**, *6*, 2442.

[44] E. Goikolea, V. Palomares, S. Wang, I.R. de Larramendi, X. Guo, G. Wang, T. Rojo, *Adv Energy Mater* **2020**, *10*, 44.

[45] N. Cuesta, I. Cameán, A. Arenillas, A.B. García, *MICROP M M* **2020**, *308*, 110542.

[46] C. Rios, A. Beda, L. Simonin, C. Ghimbeu. *Hard Carbon for Na-ion Batteries: From Synthesis to Performance and Storage Mechanism. Na-ion Batteries*, *1*, **2021**, 9781119818069

[47] L.F. Zhao, Z. Hu, W.H. Lai, Y. Tao, J. Peng, Z.C. Miao, Y.X. Wang, S.L. Chou, H.K. Liu, S.X. Dou, *Adv Energy Mater* **2021**, *11*, 2101650.

[48] D. Saurel, B. Orayech, B. Xiao, D. Carriazo, X. Li, T. Rojo, *Adv Energy Mater* **2018**, *8,* 1703268.

[49] S. Wang, P. Takyi-Aninakwa, S. Jin, C. Yu, C. Fernandez, D.I. Stroe, *Energy* **2022**, *254*, 124224.

[50] X. Hu, S. Li, H. Peng, *J Power Sources* **2012**, *198*, 359.

[51] D. Zhang, S. Dey, L.D. Couto, S.J. Moura, *IEEE Trans Control Syst Technol* **2020**, *28*, 1363.

[52] Fuller Thomas F., M. Doyle, J. Newman, *J Electrochem Soc* **1994,** *141*, 1.

[53] G. Ning, B.N. Popov, *J Electrochem Soc* **2004**, *151*, A1584.

[54] C. Deng, W. Lu, *J Electrochem Soc* **2021**, *168*, 080529.

[55] B. Lobato, N. Cuesta, I. Cameán, S.L. Flores-López, N. Rey-Raap, A. Arenillas, A.B. García, *Electrochim Acta* **2024**, *489*, 144234.

[56] N. Job, R. Pirard, J. Marien, J.P. Pirard, *Carbon* **2004**, *42*, 619.

Chapter 1

Standardization of experimental conditions for modelling of $LiFePO_4$ cells with dimensionless single particle model with electrolyte

Abstract

Model-based optimal cell design is an efficient approach to maximize the energy density of lithium-ion batteries. This maximization problem is solved in this work for a lithium iron phosphate (LFP) cell. We consider half- cells as opposed to full-cells typically considered, which are intermediate steps during battery manufacturing for electrode characterization and they are gaining popularity by themselves as lithium-metal batteries. Before moving to model, a systematic work in order to standardize experimental conditions to obtain reproducible results has been conducted. Those results are used to estimate the parameters and verify the model. Namely, methods such as galvanostatic cycling with potential limitations (GCPL), galvanostatic intermittent titration technique (GITT), and electrochemical impedance spectroscopy (EIS) have been used and experimental conditions are set. Following this, modelling process has been conducted in order to optimize the design of LFP cell. First, a dimensionless reduced-order electrochemical model is used instead of high-order models. Second, sensitivity equations are analysed to determine the ranking of the design parameters according to their impact on the energy density, which is often lacking in studies found in literature. Three parameters, namely electrode thickness, LFP particle radius and electrode cross sectional area, are shown to have the most influential effects on the energy density. Third, a novel adaptive particle swarm optimization with a specific stopping criterion is used for LIB design optimization. The proposed optimization framework is tested in simulation on an LFP half-cell battery. The results show that the design optimization yields 250 Wh kg^{-1} for an LFP electrode of 310 μm thickness, 10 nm particle radius and 2.10^{-4} m^{2} cross-sectional area, which is an increase of energy density of 61 Wh kg^{-1} with respect to an initial design proposed in the literature.

1.1. Introduction

The increase of demand in battery demand requires improved battery properties as well as improved usage of the technology we already have. Many parameters can affect the performance of batteries such as the nature of the electrode materials, the particle size of the active materials, the thickness of the electrode, the electrolyte composition, *etc.*[1] Therefore, a study of optimization of these many design parameters should be done to obtain a battery with ideal properties. Intensive experimental work is still going on to obtain batteries with improved capacity, power density, cost, *etc.* However, as one might guess, strategies of trial and error with endless number of parameters are highly time consuming. Therefore, a more systematic study including theoretical work can be useful. In that respect, modelling of batteries can be very beneficial in order to obtain an optimized battery design.

Battery modelling is a wide topic that includes many different approaches and different frameworks depending on the target application. Each model comes with a series of assumptions and simplifications. In order to check for the validity of these series of assumptions, a few parameters are needed to be determined experimentally and few others (*e.g.* C-rate, operating temperature) should be fixed beforehand. Some of these conditions and parameters should be taught to the model (identification) since the model does not have prior knowledge. The impact of those parameters, taken alone, would be rather limited, namely: diffusion coefficients, Li^+ concentrations, particle radiuses, resistances, *etc.* However, combination of these determines the performance of the cell. Thus, experimentally, one can build different cells with different design parameters and observe how those individual parameters change and identify/verify their model. Finally, the model can be used to obtain an optimized design of a Li-ion battery cell.

Battery models can be conceived as data-driven models[2][3], equivalent circuit model[4][5] and physical models[6][7]. Data-driven models are quite popular due to their preciseness on capturing complex non-linear behaviours by using machine learning techniques. However, they lack physical interpretability and also require a large amount of data for their identification while physical models require much less data and allow physical interpretability. Simpler models based on equivalent circuits have been used widely in battery management systems (BMS) which are used for control purposes, in order to operate large battery systems[4]. Those models would interpret the battery as an electrical circuit that consists of voltage generator, series resistance and capacitors. They are computationally cheap; however, they are not very useful to explain the relationships between the physical properties of the system and the battery behaviour. Therefore, those simple models are not adapted for experimental design studies.

Since it is ultimately intended to optimize the performance of the battery and analyse the associated electrochemical variables, work was focused on physical (electrochemical) models in the present study. Among all the physical electrochemical models, the most popular one is probably the Doyle-Fuller-Newman (DFN), also called pseudo-two-dimensional (P2D)[8][9] model (Figure 1.1). It consists in partial differential equations for charge and mass conservation in the solid and the electrolyte to understand the electrochemical reactions occurring on the interface of solid/electrolyte. This model has generally been used for physical understanding of electrochemical processes and validation of battery management systems[10]. In the meantime, it can be used for battery optimal design as well. For the battery optimal design, the DFN model has been extended with thermal[11] and mechanical[12] dynamics. Although these models are quite beneficial because of their high level of physical description, the computational requirements are quite high. In the meantime, a third modelling framework exists that is midway in terms of complexity: reduced-order electrochemical models. These models can be derived from the DFN model under suitable assumption of a given electrochemical process dominating over all others. Therefore, it is possible to reduce the computational complexity of numerical simulations. The Single-Particle Model (SPM, Figure 1.1) is one example of reduced-order model: it considers that the battery operation is limited by Li^+ diffusion in the active phase (*i.e.* within the active material composing the electrodes) while neglecting electrolyte dynamics[13][14]. In that model, the electrode is considered as a single particle in order to reduce further the complexity of the model. Other examples include the SPM model with thermal[15] and electrolyte dynamics[16][17], electrode-average model[18], kinetic battery model[19], reaction zone model[20] and so on. Although physically relevant and computationally efficient, these models have been scarcely used for battery design, highly descriptive DFN models being favoured.

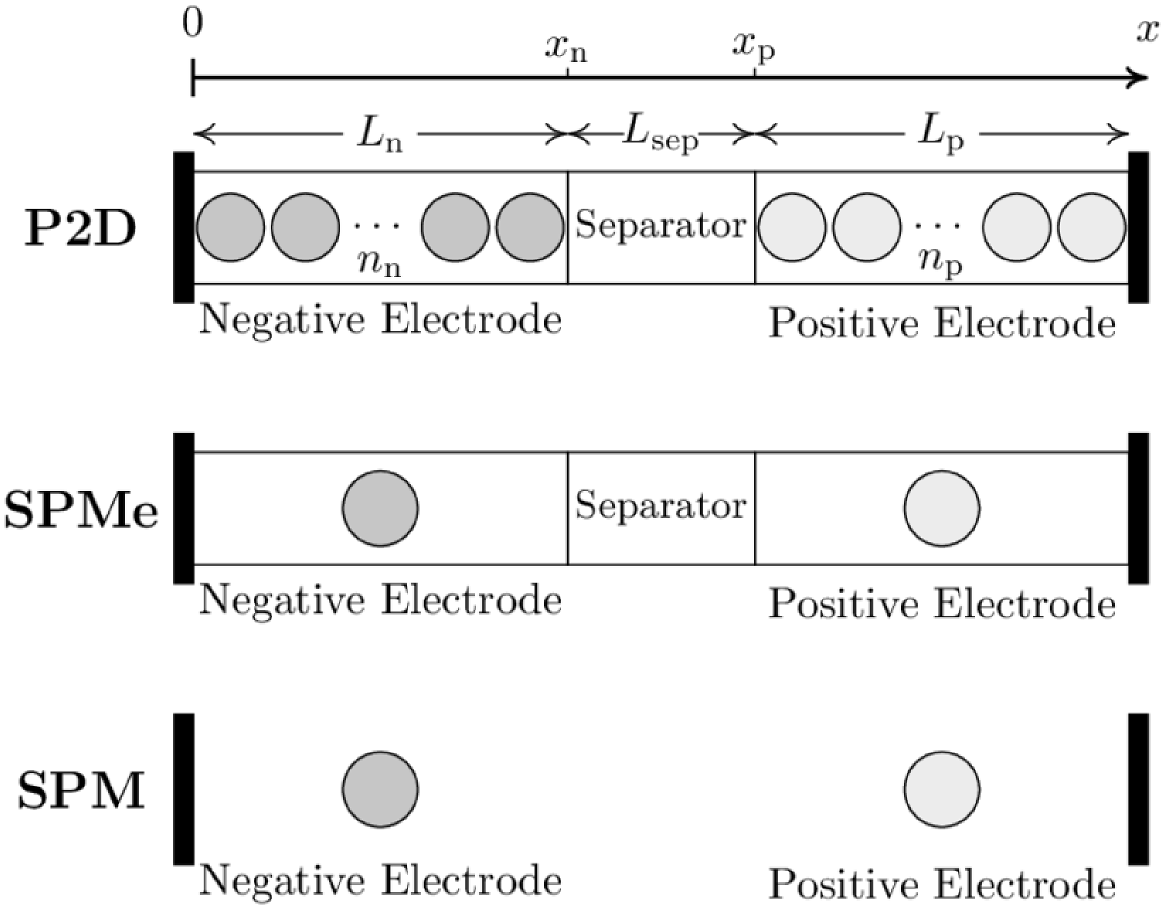

Figure 1.1. Illustration of differences between Pseudo-two-Dimensional (P2D), Single-Particle Model with electrolyte (SPMe) and Single-Particle Model (SPM) models[21].

In order to understand how wrong or how correct the model is, a cost function should be determined which shows how far a predicted value is from its actual value. Apart from underlying models, cost functions have been considered for battery design optimization. Generally, the objective of the design is to maximize the gravimetric/volumetric energy and/or the power density of the battery[11][12]. In some cases, other constraints such as power requirements[22][23] or electrode stresses[12] as well as minimizing degradation are aimed by the authors[24]. It should be noted that, for the case of minimizing the degradation, the optimization over thousands of cycles could preclude the use of full-order models. Standard design parameters usually involve active material volume fraction, electrode/separator thickness[25] and particle size[12][24]. Separator porosity[26][27], C-rate[11], conductivity[24] and diffusivity[23] were also included in previous works, even though less frequently. Some studies put more importance on a given subset of possible design parameters during optimization which were determined by sensitivity analyses such as analysis of variance[11][26], analysis of means[26] and adjoint sensitivity analysis[12]. After the objective function subject to given constraints and the design variable are specified, the battery design optimization problem is solved by different methods like building cost surfaces[11], sequential quadratic programming[23], nonlinear[12] and sequential approximate optimization[27], genetic algorithms[24][26] and direct search method[25]. Obviously, the battery chemistries such as graphite/lithium iron phosphate[11], graphite/lithium manganese oxide[22][25], etc. are highly determinant for the results obtained. It should be noted that the aims of these optimization efforts are generally placed on full-cells including both positive and negative electrode design parameters[22] while single electrode optimization in half-cell configuration[12] is more limited.

On the one hand, the intensive research on battery technology has been going on for a very long time in order to improve the capacity, stability and efficiency of the Li-on batteries. On the other hand, modelling has been used intensively to optimize the production and usage of the batteries that have been developed. However, those two communities communicate very little with each other even though they are working on the same subject. In this study, we tried to bridge the experimental and the modelling worlds of Li-ion batteries. To that aim, a collaboration with the Department of Control Engineering and System Analysis of the Université Libre de Bruxelles (ULB) has been established. The detailed modelling of the cells was performed by ULB. The experimental work, which aimed at linking design parameters to electrode performance, was done by the NCE laboratory of ULiège. Therefore, a wide library of different experimental results with different design parameters could be supplied for the battery modelling. Conversely, the modelling process involved discussions with experimenters in order to check what measurement was experimentally feasible or not.

The goal of this chapter is to link the activities performed both in ULiège and in ULB, *i.e.* explain what experimental information was needed for the model validation and how that information was obtained experimentally. This chapter thus first involves basics of battery modelling, then continues with experimental work that was conducted in order to validate the model. The reasoning for experimental work development and how outcoming results would be used in the modelling part is thus explained. Finally, the model that was developed by ULB for half-cell battery optimization based on a dimensionless reduced-order electrochemical model is presented in the final section.

1.2. Modelling of Batteries

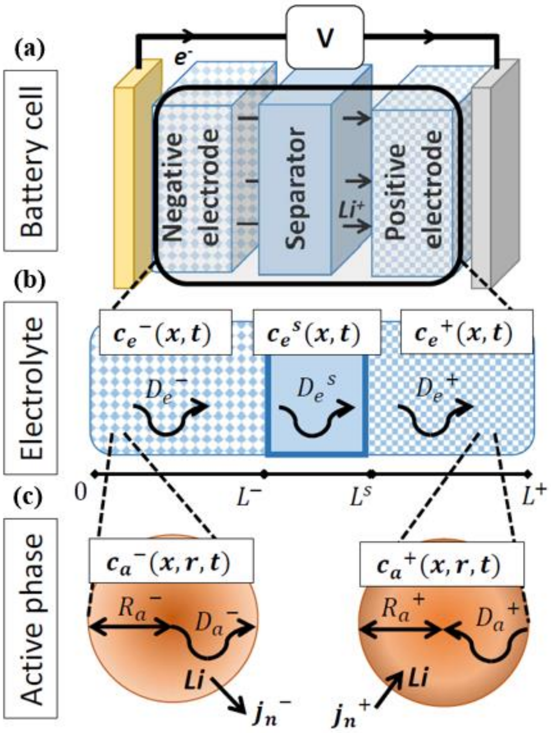

Figure 1.2. Discharging process of a full-cell LIB following the Doyle-Fuller-Newman (DFN) model. (a) Longitudinal view of the battery cell with three regions: negative electrode, separator and positive electrode, and two phases: active phase and electrolyte phase. (b) Representation of the electrolyte phase, and (c) representation of the active phases, considered as made of spherical particles.

One of the most accurate representations of the electrochemical phenomena occurring in a Li-ion battery (LIB) is the DFN model (Figure 1.2)[28]. The DFN model mathematically captures the electrochemical processes taking place in a battery (*i.e.* full-cell). Figure 1.2 shows a longitudinal view of these processes during battery discharge. When discharging (see Figure 1.2a), an electrostatic voltage difference appears between the electrodes; that difference drives the electrochemical phenomena. The lithium contained within spherical-like particles in the active-phase negative electrode diffuses from the bulk to the surface of the particles, where a de-insertion process occurs (see Figure 1.2c). The lithium, now in the form of ions in the electrolyte phase, moves from the negative electrode to the positive electrode by crossing the separator (see Figure 1.2b). Simultaneously, the electrons released in the negative electrode after the reaction are forced out of the battery due to the electronically insulating nature of the separator. After performing electrical work, the electrons come back to the battery through the positive electrode. In there, an insertion process happens at the surface of the active-phase spherical particles followed by a diffusion process of lithium from the surface to the bulk of the particle (see Figure 1.2c). All these phenomena are encoded in the DFN model, which is considered as a high-fidelity battery model and has been widely used by researchers.

The main equations of the DFN model are reported in Table S1.1., Supporting information 1.1. The interested reader is referred to[28] for more details. The DFN model is based on the porous electrode and concentrated solution theories[9][28], and it leads to Partial Differential Equations (PDEs) that are algebraically coupled. The main electrochemical equations and associated state variables are:

- conservation of mass (Equation (S1.4)) and charge (Equation (S1.5)) in the active phase, describing active-phase lithium concentration $c^{\pm}_{a}$ (x, r, t) and electric voltage $\varphi^{\pm}_{a}$ (x, t), respectively;
- conservation of mass (Equation (S1.6)) and charge (Equation (S1.7)) in the electrolyte phase, describing electrolyte-phase lithium concentration $c^{\pm s}_{e}$ (x, t) and electric voltage $\varphi^{\pm s}_{e}$ (x, t), respectively;
- Butler-Volmer kinetics for solid-electrolyte interphase (Equation (S1.8)), involving ionic currents $i^{\pm}_{e}$ (x, t) and pore-wall molar fluxes $j^{\pm}_{n}$ (x, t);
- material balance (Equation (A1.9)), since moles of lithium n_{Li} are preserved;

where subscripts a and e denote active and electrolyte phases, respectively, while +, s and − superscripts represent positive electrode, separator and negative electrode regions, respectively. x and r are the longitudinal (from one side to the other of the cell) and radial (within the particle) coordinates, respectively, and t is time.

This model can be reduced to simpler variations, such as the Single Particle Model (SPM), as discussed below.

1.3. Single particle model with electrolyte (SPMe)

As indicated in the Introduction, physical models such as the DFN model are usually too complex and computationally intensive for control purposes and design optimization; this issue has motivated the development of reduced-order electrochemical models derived from the more complex ones. A first attempt to do so is by considering the single spherical particle approximation of the electrode active-phase, leading to the so-called single-particle model

(SPM)[29]. This model is valid under low current loads[29], which limits its applicability. In an effort to alleviate this issue, electrolyte dynamics have been added to the SPM, giving rise to the SPMe[17][30].

The main assumption for deriving the SPMe from the DFN model is that the lithium concentration in the active phase, $c^{\pm}_{\mathrm{a}}\ (x, r, t)$, the exchange current density, $i^{\pm}_{0}(x, t)$, and the pore-wall molar flux, $j_{\mathrm{n}}(x, t)$, are independent of the spatial coordinate x, *i.e.*:

$$\begin{aligned} &c^{\pm}_{\mathrm{a}}(x,r,t) \approx c^{\pm}_{\mathrm{a}}(r,t),\\ &i^{\pm}_{0}(x,t) \approx i^{\pm}_{0}(t),\\ &j^{\pm}_{\mathrm{n}}(x,t) \approx j^{\pm}_{\mathrm{n}}(t) \end{aligned} \tag{1.1}$$

This assumption basically approximates the reaction throughout the cell thickness as uniform, under which the pore-wall molar flux $j^{\pm}_{\mathrm{n}}\ (t)$ can be expressed as proportional to the applied current $i(t)$, and is written as:

$$j^{\pm}_{\mathrm{n}}(t) = \frac{i(t)}{a^{\pm}_{\mathrm{a}} F L^{\pm} A} \tag{1.2}$$

where a_a is the specific interfacial area (m^2/m^3), F is Faraday’s constant (C mol^{-1}), L is the electrode thickness (m) and A is the electrode cross-sectional area (m^2). The resulting active-phase and electrolyte-phase diffusion PDEs along with the terminal voltage in the SPMe model are reported in Table 1.1. The details of nondimensionalization of the parameters can be found in the work published jointly by ULB and ULiège[31].

The DFN model has been compared with the SPM and the SPMe models in simulation for the same parameter set and it was shown that, while the SPM has a reasonable accuracy up to 1C charge-discharge rate, the SPMe can keep its validity up to *ca.* 5C[16]. The model to be developed will use the SPMe for optimal cell design, since it is considered as a physically-meaningful, yet relatively simple model that is able to capture a large part of important electrochemical dynamics in LIBs. This model, simpler than DFN, allows to perform fast simulation of the battery behaviour, which contributes to a short computational time during battery optimization and would also be beneficial in case of accounting for battery aging where thousands of cycles are expected.

Table 1.1. SPMe model equations for full-cell configuration.

Physical process	**Equation**
Active-phase diffusion	$\begin{cases} \frac{\partial c_{\mathrm{a}}^{\pm}}{\partial t} = \frac{1}{r^2}\frac{\partial}{\partial r}\left(D_{\mathrm{a}}^{\pm} r^2 \frac{\partial c_{\mathrm{a}}^{\pm}}{\partial r}\right) \\ \frac{\partial c_{\mathrm{a}}^{\pm}}{\partial r}(x,r,t)\big\vert_{r=0} = 0 \\ \frac{\partial c_{\mathrm{a}}^{\pm}}{\partial r}(x,r,t)\big\vert_{r=R_{\mathrm{a}}^{\pm}} = -\frac{1}{D_{\mathrm{a}}^{\pm}} j_{\mathrm{n}}^{\pm}(t) \end{cases}$ (1.3) with $c_{\mathrm{a},0}^{\pm}(r) = c_{\mathrm{a}}^{\pm}(r,0)$ and $c_{\mathrm{as}}^{\pm}(t) = c_{\mathrm{a}}^{\pm}\left(R_{\mathrm{a}}^{\pm},t\right)$
Electrolyte-phase diffusion	$\begin{gathered} \frac{\partial c_{\mathrm{e}}^{\pm\mathrm{s}}}{\partial t} = \frac{\partial}{\partial x}\frac{D_{\mathrm{e,eff}}^{\pm}}{\varepsilon_{\mathrm{e}}^{\pm}}\frac{\partial c_{\mathrm{e}}^{\pm\mathrm{s}}}{\partial x}\frac{a_{\mathrm{a}}^{\pm}(1-t_{\mathrm{c}}^{0})}{\varepsilon_{\mathrm{e}}^{\pm}} j_{\mathrm{n}}^{\pm} \\ \frac{\partial c_{\mathrm{e}}^{-}}{\partial x}(x,t)\big\vert_{x=0} = \frac{\partial c_{\mathrm{e}}^{+}}{\partial x}(x,t)\big\vert_{x=L} = 0 \\ D_{\mathrm{e,eff}}^{-}\frac{\partial c_{\mathrm{e}}^{-}}{\partial x}(x,t)\big\vert_{x=L^{-}} = D_{\mathrm{e,eff}}^{\mathrm{s}}\frac{\partial c_{\mathrm{e}}^{\mathrm{s}}}{\partial x}(x,t)\big\vert_{x=L^{-}} \qquad (1.4) \\ D_{\mathrm{e,eff}}^{\mathrm{s}}\frac{\partial c_{\mathrm{e}}^{\mathrm{s}}}{\partial x}(x,t)\big\vert_{x=L^{-s}} = D_{\mathrm{e,eff}}^{+}\frac{\partial c_{\mathrm{e}}^{+}}{\partial x}(x,t)\big\vert_{x=L^{-s}} \\ c_{\mathrm{e}}^{-}(x,t)\big\vert_{x=L^{-}} = c_{\mathrm{e}}^{\mathrm{s}}(x,t)\big\vert_{x=L^{-}} \\ c_{\mathrm{e}}^{\mathrm{s}}(x,t)\big\vert_{x=L^{-s}} = c_{\mathrm{e}}^{+}(x,t)\big\vert_{x=L^{-s}} \end{gathered}$
Voltage	$with\, c_{\mathrm{e},0}(x) = c_{\mathrm{e}}^{-}(x,0),\; c_{\mathrm{e}}^{0}(t) = c_{\mathrm{e}}^{-}(0,t)$ and $c_{\mathrm{e}}^{\mathrm{L}}(t) = c_{\mathrm{e}}^{+}(L,t)$ $\begin{gathered} \begin{aligned} v \quad = \quad & \eta^{+}(c_{\mathrm{as}}^{+}, c_{\mathrm{e}}^{\mathrm{L}}, j_{\mathrm{n}}^{\pm}) - \eta^{-}(c_{\mathrm{as}}^{-}, c_{\mathrm{e}}^{0}, j_{\mathrm{n}}^{\pm}) - F R_{\mathrm{f}}^{-} j_{\mathrm{n}}^{-} \\ & +U^{+}(c_{\mathrm{as}}^{+}) - U^{-}(c_{\mathrm{as}}^{-}) + \Delta\phi_{\mathrm{e}}(c_{\mathrm{e}}^{\{0,L\}}, j_{\mathrm{n}}^{\pm}) \end{aligned} \\ \eta_{s}^{\pm}(c_{\mathrm{as}}^{\pm}, c_{\mathrm{e}}^{\{0,L\}}, j_{\mathrm{n}}^{\pm}) = \frac{R_{\mathrm{g}} T_{\mathrm{ref}}}{\alpha_0 F}\sinh^{-1}\left(\frac{\mp F j_{\mathrm{n}}^{\pm}}{2 i_0^{\pm}(c_{\mathrm{as}}^{\pm}, c_{\mathrm{e}}^{\{0,L\}})}\right), \\ i_0^{\pm}(c_{\mathrm{as}}^{\pm}, c_{\mathrm{e}}^{\{0,L\}}) = k_{\mathrm{n}}^{\pm}\sqrt{c_{\mathrm{e}}^{\{0,L\}} c_{\mathrm{as}}^{\pm}(c_{s,\mathrm{max}}^{\pm} - c_{\mathrm{as}}^{\pm})} \qquad (1.5) \\ \Delta\phi_{\mathrm{e}}(c_{\mathrm{e}}^{\{0,L\}}, j_{\mathrm{n}}^{\pm}) = \frac{L^{+} + 2L^{\mathrm{s}} + L^{-}}{2\kappa_{\mathrm{e,eff}}} i(t) + k_{\mathrm{D}}(\ln(c_{\mathrm{e}}^{\mathrm{L}}) - \ln(c_{\mathrm{e}}^{0})) \\ k_{\mathrm{D}} = \frac{2R_{\mathrm{g}} T_{\mathrm{ref}}}{F}(1 - t_{\mathrm{c}}^{0})\left(1 + \frac{d\ln f_{\mathrm{c/a}}}{d\ln c_{\mathrm{e}}}\right) \end{gathered}$

1.3.1. SPMe impedance model

The model to be identified is the SPMe in frequency domain in order to obtain its parameters from electrochemical impedance spectroscopy data. Hence, the SPMe model in Table 1.1 needs to be converted from time-domain to frequency-domain. In order to achieve this, the next steps are followed: (1) take the Laplace transform of the diffusion PDE, (2) solve the resulting Ordinary Differential Equations (ODE) to get the general solution, (3) find the unknown constants by substituting the ODE solution in the boundary conditions and (4) evaluate the obtained transfer function at the desired spatial point.

Additionally, as expressed, the voltage equation assumes that the high-frequency dynamics associated to *e.g.* double-layer effects are much faster than diffusion dynamics in the active- and electrolyte phases, *i.e.* the kinetics are considered instantaneous and can be neglected. For electrochemical impedance spectroscopy, this is not a valid assumption since clear double-layer effects can be seen in the impedance response of batteries, which manifest as high-frequency semicircles[32][33]. To properly model the impedance of batteries, double-layer dynamics have to be accounted for. In this sense, two impedance double-layer models were derived, in order to be able to capture the two high-frequency semicircles in half-cells. These models are based on works reported in the literature[33][34]. The impedance model made of a set of transfer functions can be written as:

$$H_{\mathrm{v}}(s,\nu) = H_{\mathrm{as}}(s,\nu) + H_{\mathrm{e}}(s,\nu) + H_{\mathrm{dl}}(s,\nu) + H_{\mathrm{rc}}(s,\nu) + H_{\mathrm{i}}(s,\nu) \tag{1.6}$$

where s is the Laplace variable and ν is the vector of grouped parameters to be identified, $H_{\mathrm{as}}(s)$ corresponds to the voltage transfer function of the active-phase lithium surface concentration, $H_{\mathrm{e}}(s)$ emphasis the electrolyte-phase concentration, $H_{\mathrm{dl}}(s)$ is the first double-layer dynamics that are modelled using a physical model, $H_{\mathrm{rc}}(s)$ is the second double-layer dynamics that are modelled as an RC-pair, and $H_{\mathrm{i}}(s)$ models the ohmic drop. This frequency-domain SPMe model with two double layers (Equation 1.6) was used to estimate the grouped model parameters ν from electrochemical impedance spectroscopy data. Note that some of these parameters involve the active-phase diffusion time constant, τ_{d}, the kinetic reaction time constant, τ_{k} or the double-layer time constant, τ_{dl}, given by:

$$\tau_{\mathrm{d}} = \frac{R_{\mathrm{a}}^2}{D_{\mathrm{a}}}, \tag{1.7}$$

$$\tau_{\mathrm{k}} = \frac{R_{\mathrm{a}}}{k_{\mathrm{n}}\sqrt{c_{\mathrm{e,nom}}}}, \tag{1.8}$$

$$\tau_{\mathrm{dl}} = a_{\mathrm{a}} C\left(\frac{1}{\sigma_{\mathrm{eff}}} + \frac{1}{\kappa_{\mathrm{eff}}}\right)(L^{+})^{2} \tag{1.9}$$

where most physical parameters have been defined in the text except C, which corresponds to the double-layer capacitance.

1.3.2. Model identification for impedance

The measured impedance of a cell at a given frequency ω_{i} is given by the complex number $Z(\omega_{\mathrm{i}}) = Z'(\omega_{\mathrm{i}}) + iZ''(\omega_{\mathrm{i}})$, where Z' and Z'' denote the real and imaginary parts, respectively. The optimal parameter estimate can be obtained by solving the following optimization problem:

$$\underset{\nu}{min} J(\nu) = \underset{\nu}{min} \sum_{i=1}^{N_{\omega}} |Z(\omega_i) - H_{\nu}(\omega_i, \nu)|^2 \tag{1.10}$$

where N_{ω} is the number of evaluated frequencies. This optimization problem (Equation 1.10) is solved to find the best value of the parameter vector ν.

1.3.3. Optimal design of half-cell lithium-ion batteries

In this work, the aim is to optimize the design of a half-cell battery based on a dimensionless reduced-order electrochemical model. The optimization objective is to maximize the gravimetric energy density. The selected design parameters that could potentially be manipulated during battery manufacturing include active material volume fraction, electrode/separator thickness, particle radius of active material and cross-sectional area of the electrode. The algorithms were developed by ULB with the help of the group of ULiège for the electrochemical measurements. These algorithms were developed to formulate the optimization problem to be solved, *i.e.* the maximization of half-cell energy density by modification of the selected battery design parameters. The procedure is as follows. Firstly, the objective (or "cost function") to be optimized is defined. Then, sensitivity equations associated to the cost function with respect to the design parameters to be optimized are presented and used to determine the most influential parameters. Finally, the optimization problem is defined and the optimization algorithm is used to find the solution. The details of these equations and algorithms can be found in the joint publication by both groups[31].

1.3.4. Objective function formulation

In this work, it is intended to maximize the battery specific (gravimetric) energy density. The objective function then takes the following form:

$$E = \frac{1}{m_{\mathrm{cell}}} \int_0^{t_f} v\,(t) i(t) dt \tag{1.11}$$

where the mass of the cell is defined as $m_{\mathrm{cell}} = m^{\pm} + m^{\mathrm{s}} + m^{\mathrm{cc}}$ and accounts for the active materials of the electrodes ($m^{\pm}$), the separator (m^{s}) and the current collectors (m^{cc}). The electrodes, separator and current collectors' masses are respectively given by:

$$m^{\pm} \;=\; AL^{\pm}(\rho_{\mathrm{e}}^{\pm}\varepsilon^{\pm} \;+\; \rho_{\mathrm{a}}^{\pm}\,\varepsilon_{\mathrm{a}}^{\pm} + \rho_{\mathrm{b}}^{\pm}\,\varepsilon_{\mathrm{b}}^{\pm}\,) \tag{1.12}$$

$$m^{\mathrm{s}} \;=\; AL^{s}\rho_{\mathrm{e}}^{\mathrm{s}}\,\varepsilon_{\mathrm{e}}^{s} \tag{1.13}$$

$$m^{\mathrm{cc}} \;=\; ALc^{\mathrm{c}}\rho_{\mathrm{cc}} \tag{1.14}$$

where *ρ* denotes the density (with the same subscript conventions used before) together with *b* and *cc* standing for binder and current collector, respectively. The time t_{f} refers to the complete discharging time of the half-cell. The energy density *E* in Equation (1.11) is determined from the galvanostatic discharge of a fully charged cell down to a minimum cut-off voltage. As can be seen, this cost function shown in Equations (1.11-1.14) also depends on a set of design parameters that can be adjusted during LIB manufacturing. These physical parameters include: the electrode/separator thickness, $L^{\pm}{}_{\mathrm{s}}$, the radius of the active material particles, $R^{\pm}{}_{\mathrm{a}}$, the active material volume fraction, $\varepsilon^{\pm}{}_{\mathrm{a}}$, and the electrode cross-sectional area, *A*[11][12]. The parameter vector associated to such parameters in a half-cell model is thus defined as:

$$\theta = [L^{s}\; L^{\pm}\; R_{\mathrm{a}}^{\pm}\; \varepsilon_{\mathrm{a}}^{\pm}\; A]^{\top} \in \mathbb{R}^{n_{\theta}} \tag{1.15}$$

for $n_{\theta} = 5$ in this case.

Coming back to the energy density, Equation (1.11) is dimensional. The dimensionless form of this equation is given by:

$$\begin{aligned} E \quad &= \int_0^{t_{\mathrm{ref}}t_f^*} \frac{\beta_T v^*(t_{\mathrm{ref}}t^*) i_{\mathrm{typ}} i^*(t_{\mathrm{ref}}t^*) t_{\mathrm{ref}}}{\overline{m} m_{\mathrm{cell}}^*} dt^* \\ &= \frac{\beta_T i_{\mathrm{typ}} t_{\mathrm{ref}}}{\overline{m}} \int_0^{t_f^*} \frac{v^*(t^*) i^*(t^*)}{m_{\mathrm{cell}}^*} dt^* \end{aligned} \tag{1.16}$$

with $m^{*}_{\text{cell}} = m_{\text{cell}}/\overline{m}$ being the dimensionless mass of the cell while i_{typ} is an arbitrary current magnitude that can be set to equivalent to of 1C, t_{ref} is an arbitrary reference time, β_{T} is the so-called thermal voltage. Dimensionless quantities are denoted by superscript *. One can then write the dimensionless cost function from the dimensional one as:

$$E^{*} = E/\frac{\beta_{\text{T}} i_{\text{typ}} t_{\text{ref}}}{\overline{m}} \Rightarrow E^{*} = \int_{0}^{t_f^{*}} \frac{v^{*}(t^{*}) i^{*}(t^{*})}{m^{*}_{\text{cell}}} dt^{*} \qquad (1.17)$$

As can be seen, the dimensionless energy density E^{*} requires the appropriate scaling of Equation (1.11) with the variables defined in Table (1.2) and Table (1.3). Moreover, the coefficient $\beta_{\text{T}} i_{\text{typ}} t_{\text{ref}} / \overline{m}$ is a constant and, therefore, the dimensionless energy density is just a scaled version of the dimensional one.

Table 1.2. Dimensionless variables.

Definition	Symbol	Dimensionless variable
Solid-phase concentration	c^{*}_{a}	$c_{\text{a}}/c_{\text{a,max}}$
Current	i^{*}	i/i_{typ}
Time	t^{*}	t/t_{ref}
Electrolyte-phase concentration	C^{*}_{e}	$c_{\text{e}}/c_{\text{e,nom}}$
Voltage	$V*$	$v/ß_{\text{t}}$

Table 1.3. Scaling variables and time constants of the dimensionless SPMe model (dSPMe).

Definition	Symbol	Expression
Solid phase discharge	$\tau_{\text{c}}^{\mp}$	$F c_{\text{a,max}}^{\mp} L^{\mp} \varepsilon_{\text{a}}^{\mp} A / i_{\text{typ}}$
Solid phase diffusion	$\tau_{\text{d}}^{\mp}$	$(R_{\text{a}}^{\mp})^{2} / D_{\text{a}}^{\mp}$
Electrolyte phase discharge	$\tau_{\text{e,c}}^{\mp s}$	$F c_{\text{e,nom}}^{\mp} L^{\mp\text{s}} \varepsilon_{\text{e}}^{\mp\text{s}} A / ((1 - t_{\text{c}}^{0}) i_{\text{typ)}}$
Electrolyte phase diffusion	$\tau_{\text{e,d}}^{\mp\text{s}}$	$(L^{\mp\text{s}})^{2} / D_{\text{e}}^{\mp\text{s}}$
Reaction	$\tau_{\text{k}}^{\mp\text{s}}$	$R_{\text{a}}^{\mp} / (k_{\text{n}}^{\mp} \sqrt{c_{\text{e,nom}}})$
Thermal voltage	β_{t}	$R_{\text{g}} T_{\text{ref}} / (\alpha_{0} F)$
Ohmic drop in electrolyte	β_{Ki}	$(L^{+} + 2L^{s}) / (2K_{\text{e,eff}} A) i_{\text{typ}}$
Ohmic drop in electrode film	β_{Ri}	$R_{\text{f}}^{\mp} / (a_{\text{a}}^{\mp} L^{\mp} A) i_{\text{typ}}$

1.3.5. Optimization problem for half-cell battery design

The problem of maximizing the specific energy density by manipulating the battery design parameters can be formalized in the following way:

$$\max_{\theta} E^* = \frac{1}{m^*_{\text{cell}}} \int_0^{t_f} v^*(t^*) i^*(t^*) dt^* \tag{1.18}$$

$$i^*(t^*) = H(t^*) \tag{1.19}$$

$$v^*(0) = v^*_{\max} \tag{1.20}$$

$$v^*(t_f) = v^*_{\min} \tag{1.21}$$

$$\theta_{\min} \preceq \theta \preceq \theta_{\max}, \tag{1.22}$$

where $H(t^*)$ is the Heaviside step function and the operator $\preceq$ represents component-wise inequality between vector elements, meaning that the solution space is constrained with upper and lower bounds for the considered parameters.

The evaluation of the energy density is performed by imposing the equivalent of a normalized 1C discharge current (Equation 1.19) starting from a fully charged state (Equation 1.20) of the half-cell battery and finishing when it is empty (Equation 1.21). Note that, in this case, the battery power is intrinsically accounted for by imposing an applied current that is equivalent to 1C rate (*i.e.* the battery is discharged in 1 h); therefore, maximizing the power (P):

$$P = E/t_{\text{f}} \tag{1.23}$$

is equivalent to maximizing the energy E for the same discharging time, t_{f}.

The optimization problem defined by Equations 1.18 to 1.22 is solved by resorting to an adaptive particle swarm optimization with a specific stopping criterion, which is explained in the next section.

1.3.6. Particle swarm optimization algorithm

The particle swarm optimization (PSO) algorithm is based on social behaviour simulation. It was inspired by the behaviours of animals and insects that live in swarms. Each individual keeps a memory and experience as well as the information provided by his group in order to find the best food regions. In social behaviour simulations, each member of the group represents a so-called “problem solution”, *i.e.* a position, and it has an associated velocity. The members are known as particles that explore the search space.

First, a population of desired number of particles is generated, which does not change during exploration. Then, the position and velocity of each particle are adjusted based on its experience, *i.e.* track of its associated objective value and the best experiment (best objective value) of companion particles in the population. The goal is to let the particles go towards the best location of the search space. Each particle is associated with a value of objective function which should be devised based on problem targets. Here, the objective function is the dimensionless specific energy density $F(\bullet)=E^*$ as defined in (1.17) with "●" symbolizing the particle. At each iteration, the velocity and the new position of the particles are considered given the dimensionless model, design physical parameter vector θ and associated dimensionless energy density. Also, an adaptive form of particle swarm optimization algorithm (APSO) is used which adjusts some parameters at each step. Details of the algorithm are presented in the publication[31] and the obtained results are discussed in the next sections.

Now that the problem is formulated and the way of solving the problem is defined, the physical parameters that are needed to solve the problem have to be found. To that aim, a series of experiments were planned; this experimental work corresponds to the tasks performed by the PhD candidate in the framework of the PDR project.

1.4. Experimental studies

Models vary in terms of the different purposes such as thermal models, aging models, electric models. However, they also vary in the techniques adopted to estimate both parameters and states of the battery. Parameters can refer to the characteristic quantities of the system such as chemical (solid phase conductivity, diffusion coefficients) and electrical quantities (internal resistance, capacitance) while the state of the battery refers to its State of Charge (SoC) and State of Health (SoH). Estimating both parameters and states can be very challenging since it requires both mechanical efforts to set up and perform the tests and calculations including the hardware effort to implement the calculations. Therefore, there are different methods to optimize different aspects, with various advantages (simplicity, speed, accuracy, *etc.*). Apart from the usually known physical parameters such as the separator thickness or the active phase particle radius, electrochemical parameters can be obtained from electrochemical procedures.

Experimental methods such as cyclic voltammetry (CV), galvanostatic cycling with potential limitations (GCPL), Galvanostatic Intermittent Titration Technique (GITT) and Electrochemical Impedance spectroscopy (EIS) can be used to estimate some parameters.

Table 1.4. summarizes the electrochemical parameters needed for the SPMe model and the methods to obtain them.

Table 1.4. Electrochemical parameters for active phase material to be used in the model and how to find them.

Definition	**[units]**	**Symbol**	**Experimental method**	**Calculation/Observation**
Specific interfacial area	[m^2 m^{-3}]	a_a	CV	
Maximum lithium conc.	[mol m^{-3}]	$c_{a,max}$	Theoretical	-
Active-phase diffusion coefficient	[m^2 s^{-1}]	D_a	GITT, GCPL, EIS	Equation 1.24
Exchange current density	[A m^{-2}]	i^{Li}_0	EIS, GITT	Direct
Reaction kinetic constant	[$m^{2.5}$ $mol^{0.5} s^{-1}$]	k_n	GITT	Arrhenius equation
Film resistance	[Ω m^2]	R_f	EIS	Direct
Open circuit voltage (OCV) of LFP, Li	[V]	U^+, U_{Li}	GITT, GCPL	Direct
Charge transfer coefficient	[-]	$A0$	Theoretical	Direct
Electrical conductivity	[Ω^{-1} m^{-1}]	σ	4 probes	Direct

Experiments were planned in order to validate and estimate parameters for the electrochemical model developed by ULB. The planned experiments were the following: (i) GCPL experiments in order to estimate the parameters such as diffusion coefficients and OCV and verify the validity of the charge/discharge pattern obtained by the model, (ii) EIS in order to obtain electrochemical parameters such as resistances, exchange current density and diffusion coefficients and check the validity of the model by comparing the experimental data to those generated by the model in the frequency domain and (iii) GITT in order to obtain diffusion coefficient, exchange current density, reaction kinetic constant or OCV which can supply time constant values for the electrodes.

1.4.1. Electrode manufacturing

$LiFePO_4$ (LFP) electrodes were produced *via* the same robotic spray coating technique as used in Chapter 2. The mixture was prepared by using 12 wt% solids including LFP (provided by Prayon, commercial references P700 and P800) as active material, conducting carbon (Timcal C-nergy Super C65) and xanthan gum (Sigma-Aldrich) as binder in a weight ratio of 75 : 20 : 5 (active material : conducting carbon : binder) in MilliQ water. The mixture was stirred by using a magnetic stirrer for 3 h prior to spraying. The prepared ink was sprayed onto pre-weighted stainless-steel discs (Type 304, 15.5 mm, MTI corp.) used as current collectors and dried overnight at 60°C. The coated discs were weighted and dried again in an oven for 2 h under vacuum at 110°C before being introduced into the glovebox. The coin cell assembly was conducted by using the LFP electrode as positive electrode, metallic Li disc (PI-KEM) as counter and reference electrode, two Celgard® separators and 80 µL of electrolyte (1 M $LiPF_6$ in an ethylene carbonate:diethyl carbonate:dimethylcarbonate – 1 : 1 : 1 mixture, Sigma Aldrich). Prepared half-cells were then used for electrochemical characterization. Produced LFP half-cells were characterized using a BioLogic VMP3 multichannel potentiostat. Prior to electrochemical testing, all samples were submitted to formation cycles between 2.0 and 4.2 V *vs.* Li^+/Li by using galvanostatic charge and discharge mode. The sequence of formation cycles was designed as follows: 10 cycles at C/5 rate followed by 10 cycles at 1C rate.

1.4.2. Galvanostatic Cycling with Potential Limitations

GCPL experiments were performed to estimate the parameters and verify the model. Namely, parameters such as diffusion coefficient, OCV, *etc.* can be obtained from these experiments and the result of model can be visualized as charge-discharge graph and compared with the experimental result. Thus, GCPL experiments can be used to both identify and verify the model. GCPL experiments were conducted with half-cell setup between 2.0 and 4.2 V *vs.* Li^+/Li with various C-rates (C/100, C/50, C/20, C/5, C/2, C, 2C, and 5C). The applied current densities were calculated based on the theoretical capacity of LFP (mAh g^{-1})[35].

1.4.3. Electrochemical impedance spectroscopy

Electrochemical Impedance Spectroscopy (EIS) is a characterization method that is highly sensitive to the chosen experimental conditions. Therefore, an optimization of the procedure is needed to first obtain reproducible results, in order to further develop a reliable model. Parameters such as SoC, as well as voltages and relaxation time before the EIS play a crucial role on the reproducibility of the experiments. Even though information is available in the literature, no clear handbook of "how to characterize" exists for LFP electrodes. Therefore, a series of experiments were conducted in order to obtain reproducible EIS experiment datasets. EIS was conducted in the 10^{-2} - 10^{6} Hz frequency range with the same setup as the other electrochemical experiments.

Firstly, the investigation about SoC was conducted. The initial approach to the EIS experiments consisted in performing EIS at 0 and 100 SoC, two limit charge states of the electrodes. While this is considered valid in literature, running the EIS experiment at the limit voltages might affect the data. Namely, charge transfer resistance (R_{ct}) and Warburg resistance both increase significantly at 0 and 100 SoC in comparison to values obtained at other SoCs. These phenomena can be explained as follows: when the electrode is fully charged or discharged, it is harder for Li^+ ions to insert in or de-insert from the active material and, therefore, both resistances are higher[36]. To account for this information, the EIS measurements were performed at different SoC values: 0, 40, 60 and 100% SoC levels were chosen. However, this rises one question about the experiment conditions: how can the SoC be determined with accuracy? The initial experiments were designed so as to perform EIS measurements every 1 h for C/5 cycles, which would theoretically be correct to obtain values at every 20% of charge level. However, instead of theoretical values, division of obtained capacities by cycling and using those as charge limits would be more precise and it is also suggested in other studies[37].

After the first data of EIS were obtained, the results were analysed and some issues were raised. The above-described EIS experiments were initially designed to investigate the electrochemical property difference between electrodes with various thicknesses (see Chapter 2) in order to explain the capacity drop observed at high C-rates. However, no consistent conclusions could be drawn from these data: no clear trend can be observed when increasing/decreasing the electrode thickness. Especially, the importance of cells being at steady-state when performing EIS measurements was considered. This means that the battery needs to relax completely before EIS measurement. However again, a new question arises then:

how long should the relaxation step be to obtain steady state? Generally, in the literature dedicated to batteries, relaxation time before the EIS is not mentioned. Among the few studies that report such a step for Li-ion batteries, 40% indicate less than 1 h relaxation, 40% between 1 and 4 h and 20% longer than 4 h[38]. For the studies working on LFP, it has been suggested that 4 h or 150 min is suitable[39][40]. Given the lack of experiment standards, it was decided to first measure the relaxation time for this study specifically. However, the data obtained by long relaxation OCV show that it takes more than 90 h for the cell to be completely relaxed, which means that it would take more than 2 weeks to perform one full EIS characterization for one cell. So, instead of setting a fixed relaxation time, it was decided to consider relaxation to be finished when reaching a given change rate of voltage, which would guarantee that all the cells are in the same relaxation state. For instance, in the literature, steady-state is considered in the range of 5 mV h^{-1} change[38]. After checking the data obtained from modified GITT results, the cut-out rate was chosen equal to 0.5 mV h^{-1}, which is much lower (and thus safer) than values seen in the literature[38]. Finally, EIS was conducted between 10^{-2} Hz and 10^{6} Hz at 0, 40, 60 and 100% SoC, with 1C charging rate and limit relaxation rate equal to 0.5 mV h^{-1}.

The initial results of the GCPL experiments shows decrease of capacity with increasing electrode loading at high C-rates. Therefore, a reasoning should be done by EIS with the electrochemical parameters. EIS analyses are shown in Figure 1.3a. One can observe the increasing radius of semicircle (R_{ct}) with increasing electrode loading. Also, the place where the spectra cut the X-axis (R_{i}) is observed to be similar for all 3 electrode loadings. Although these results are in line with expected higher R_{ct}, it fails to explain the difference of capacities at high C-rates with increasing thickness. Meanwhile, R_{i} seems to be similar in all samples, which does not make sense since a thicker coating should have different diffusion and resistance properties with a thinner one. Thus, those results cannot explain the differences in performance and it shows the reverse of what was expected. In literature, it is quite often that both normalized and non-normalized EIS results can be observed. Although non-normalized usage is more common, numerous studies about the effect of material loading normalize the EIS results according to mass loading or thickness of the electrode[37][41]–[43]. Therefore, the results were normalized according to their active material masses, as shown in Figure 1.3b. Indeed, the normalized results fall in line with what was expected from literature. An increase of internal resistance can be observed with increasing thickness, which explains why the capacity decreases at higher C-rates.

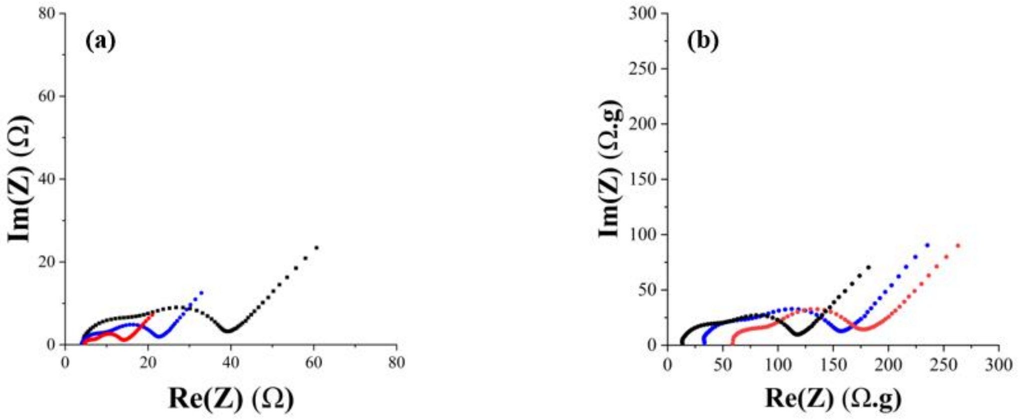

Figure 1.3. EIS spectra of LFP cells with (●) 3 mg, (●) 6 mg and (●) 12 mg LFP (a) prior and (b) after standardization per gram. The data are retrieved from Chapter 2.

As a conclusion, the EIS measurement procedure was optimized as follows: spectra were measured between 10^{-2} Hz and 10^{6} Hz, at 0, 40, 60 and 100% SoC after relaxation, using a cut-out rate of 0.5 mV h^{-1} to define the end of the relaxation step. The results obtained were used to validate the model as well as in Chapter 2.

1.4.4. Galvanostatic Intermittent Titration Technique (GITT)

GITT is an experimental procedure that consists of series of current pulses, each followed by a relaxation period (Figure 1.4). Figure 1.4a shows a half-cell upon charge. The current I is positive during charge while it is negative during discharge. The initial state can be described as equilibrium state where the concentration of mobile ions is homogenous throughout the electrode. A sudden voltage step can be observed, from E_1 to E_2, when a constant current pulse I_0 is applied at time t_0 due to current flux in the form of an IR drop. When a positive current pulse is applied at time t, Li^+ ions are deintercalated from the host and the voltage of the cell increases to a value E_3. After the pulse, during the relaxation time, the electrode evolves towards a more homogenous state by diffusion of Li^+ species. As a result, the voltage first suddenly decreases by a value proportional to the IR drop; second, the voltage decrease slowly continues until the electrode is in equilibrium and open circuit voltage is reached. Pulse-relaxation cycles continue until the cell is fully charged. This procedure can be used to obtain both thermodynamic and kinetic parameters but, most importantly, diffusion coefficients such as that of Li^+ in the active material.

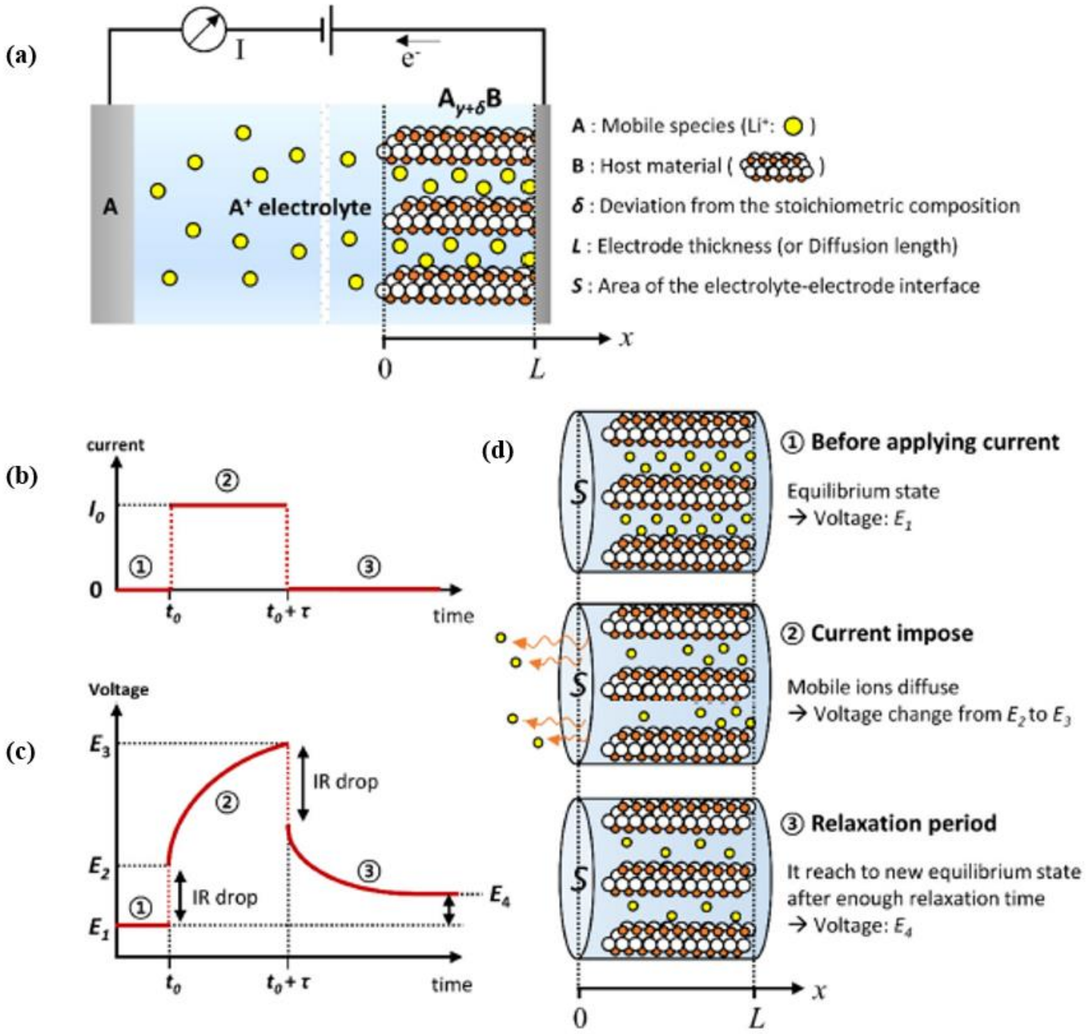

Figure 1.4. Visualization of GITT experiment and components. (a) A: mobile species, B: host material, y: arbitrary stoichiometric number, δ; deviation from the stoichiometric composition. The electrolyte-electrode interface is located at $x = 0$. S is the cross-sectional area of the electrode L is the electrode thickness. (b-d) Visualization of a single GITT step. (b) A constant current pulse (I_0) is applied for the duration (τ) at the time t_0 causing (c) voltage changes. (d) Illustration of the mobile ion motion during the galvanostatic titration steps (b) and (c)[44].

The GITT method can be used to calculate the Li$^+$ diffusion coefficient in the electrode at different SoC values simply from the voltage change. The basic idea is to calculate the number of ions passing through the electrolyte from the current measured. GITT method is derived from Fick's law by calculation of the number of mobile ions (Li$^+$) moving at the interface between the electrolyte and the electrode phase boundary and correlating these with the transient and steady-state voltage measurements. The Li$^+$ diffusion coefficient within the electrode material can be calculated at each step as[45]:

$$D = \frac{4}{\pi}\left(\frac{i\,V_\mathrm{m}}{z_\mathrm{A}FS}\right)^2 \left[\left(\frac{dE}{d\delta}\right) \Big/ \frac{dE}{d\sqrt{t}}\right]^2 \tag{1.24}$$

where i (A) is the current, V_m (m^3 mol^{-1}) is the molar volume of the active material, z_A is the charge number (of lithium in this case), F (96485 C mol^{-1}) is Faraday's constant and S (m^2) is the electrode surface area. Besides, d$E/d\delta$ is the slope of the coulometric titration curve, found by plotting the steady state voltages (Figure 1.5) E(V) measured after each titration step δ and d$E/d\sqrt{t}$ is the slope of the linearized plot of the potential E(V) during the current pulse of duration t(s).

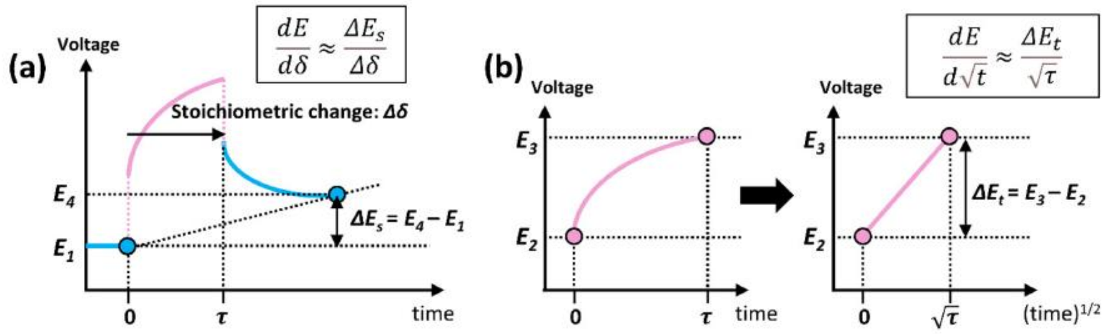

Figure 1.5. Schematic diagram of the two linear correlation assumptions in one galvanostatic titration step. (a) Steady-state voltage change is small by using a sufficiently small current for a short time. (b) Transient voltage change with time shows a straight-line behaviour in the E *vs.* $\sqrt{\tau}$ curve [44].

Firstly, GITT with C/100 current pulses and 16 h rest were attempted, as suggested in literature. However, those very low current pulses and very long relaxation periods resulted in month-long GITT experiments. Besides the inconvenience of such long experiment durations, any small issue in building the cell can cause severe experimental problems several weeks after starting the experiment, thus requiring to start over again. Therefore, with the joint decision of ULB, a new GITT method has been developed.

This method includes two GITT procedures at the same time: (i) one procedure with very long relaxation times but less data points in different parts of the charge/discharge curve and (ii) another procedure with very short relaxation times but allowing to get many data points. Therefore, the aim is to use the long relaxation time data points as a pattern to fit the data points obtained by the quick procedure. The first slow procedure consists of C/25 current pulses for given times followed by 48 h of resting period. Calculations were done to obtain at least 3 points between 2 V *vs.* Li^+/Li and the plateau, 3 points on the plateau and 3 points between the plateau and the cut-off voltage, set at 4.2 V *vs.* Li^+/Li. In theory, this should provide information about time constants at various SoC levels with very long resting periods. However, since this procedure would not cover the entire SoC levels, the second procedure includes 15 min of C/25 current pulses and 3 h of resting (Figure 1.6). From previous experiments, it was concluded that 3 h resting time is not enough to reach steady-state and calculate the time constants for the electrode. However, since the long rests in different parts of SoC are already obtained, it can be superimposed onto the short rest GITT and get a full GITT in much shorter time. The long GITT would be obtained from fewer SoC levels but higher amount of relaxation points. On the contrary, the short GITT would obtain many SoC levels but fewer relaxation points. Therefore, the idea is to use the low measurement but high data points that is obtained by long GITT, and superimpose it to the trends of the numerous measurement points obtained from short GITT.

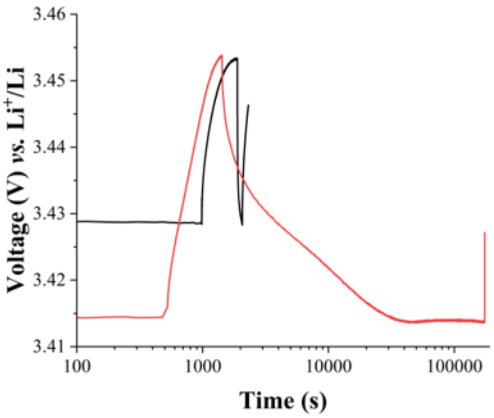

Figure 1.6. Experimental results of pulse and relaxation periods for (▬) long-rest GITT and (▬) short-rest GITT.

1.5. Result and discussion

Several experiments were initially planned for the modelling, namely GCPL, EIS and GITT. Results of EIS have been used in the optimization study in this chapter (Figure 1.3) while GCPL results are used in Chapter 1. In the supporting information, examples of results for GITT and GCPL of LFP half-cell can be found (Figure S1.2.1.), even though those have not been included in the modelling part yet. Although not used further in this chapter, both GITT (Figure S1.2.1a) and GCPL (Figure S1.2.1b) results are in good agreement with the literature[46][47]. The next paragraphs will deal with the cell optimization and impedance identification.

1.5.1. Optimization results

The proposed optimization framework has been tested in light of simulation studies where optimal design of a half-cell LIB is considered with LFP as positive electrode material. The dSPMe model with finite differences is used. The model parameters are obtained from the literature and validity of the model choice has been done by model identification using LFP half-cell impedance data. For this, the experimental data presented in Figure 1.3 is used to validate the model. The parameters are defined and reported in Table S1.3 in the supporting information. The results obtained from a sensitivity analysis of the voltage with respect to each design parameter are shown in Figure 1.7. It is interesting to see the dynamic behaviour of these sensitivities as they are the main contributor for the overall cost function sensitivity given in (25). The equivalent of a 1C input current profile used to discharge the considered LFP half-cell is depicted in Figure 1.4a.

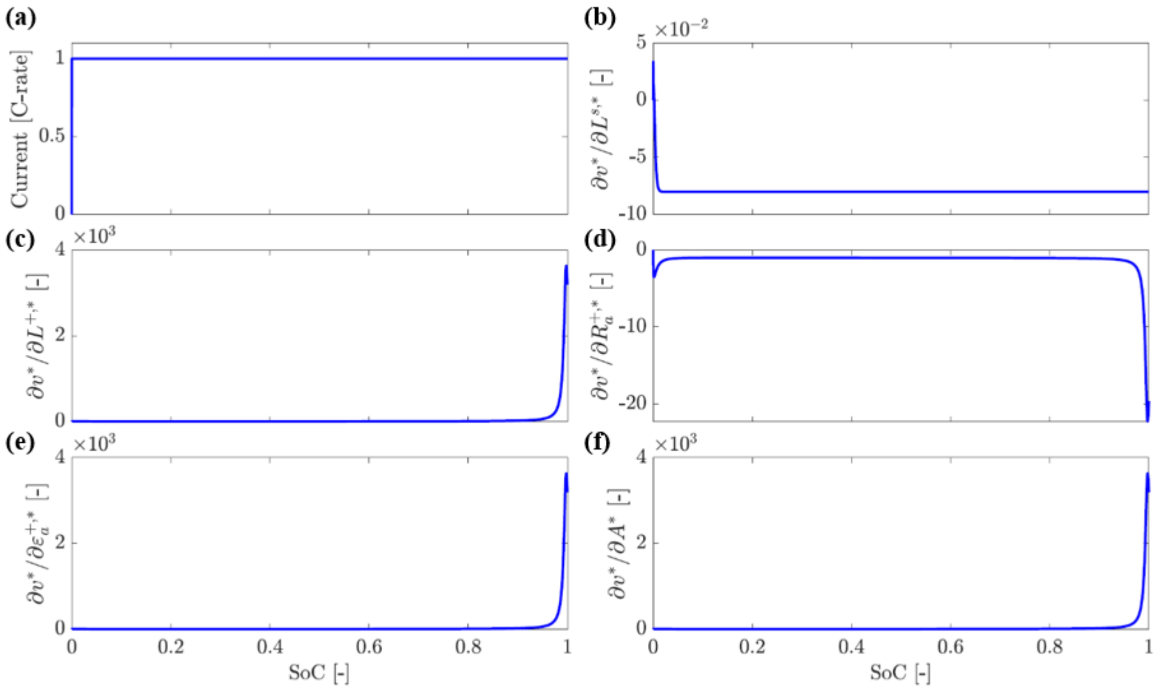

Figure 1.7. Sensitivity trajectories of the voltage with respect to the design parameters. Plot (a) shows the discharge current, whereas plots (b) to (f) portray the voltage sensitivity with respect to separator thickness (L^s), electrode thickness (L^+), particle radius (R_a^+) , volume fraction (ε_a) and electrode cross-sectional area (A), respectively.

The plots are being drawn with respect to SoC for convenience where the SoC is defined in terms of electrochemical variable for an SPM-type model as[16][48]:

$$\mathrm{SoC}(t) = \frac{3}{c_{\mathrm{a,max}} R_{\mathrm{a}}^3} \int_0^{R_{\mathrm{a}}} r^2 c_{\mathrm{a}}(r,t) dr. \qquad (25)$$

It should be noted that SoC goes from 0 to 1 for a charging LFP half-cell known that, the LFP electrode is actually being lithiated, which means that the concentration of lithium in the electrode increases upon discharge of the half-cell. The sensitivity of voltage to the design parameters are shown in Figure 1.7b to Figure 1.7f for separator/electrode thickness, particle radius, volume fraction and cross-sectional area, respectively. Most influential parameters exhibit a flat region in the mid-SoC range (from 10% to 90%) which follows from the typically flat charge/discharge curve characteristics of LFP electrodes. Moreover, the separator thickness has the lowest influence magnitude among the considered design parameters, whereas electrode thickness, particle radius and cross-sectional area are the most sensitive parameters. However, influence of the parameters change in different SoC ranges. For instance, separator thickness is important at low SoC whereas electrode thickness, particle radius and area are more relevant at high SoC. Therefore, when their voltage contribution is considered, electrode thickness, particle radius and the cross-sectional area of the electrode found as the most influential parameters.

Following this, full cost function is considered for the sensitivity analysis instead of only observing their contribution to voltage. The influence of the cost with respect to the different parameters can be ranked in accordance to the impact of each design parameter. This parameter ranking is shown in Figure 1.8. The most influential parameter is the particle radius followed by the separator thickness, electrode thickness and cross-sectional area, whereas the least influential parameter is the active material volume fraction. The reason why the latter parameter with relatively large voltage influence became the least influence parameter for the dimensional cost is because the nominal parameter $\varepsilon^{+}{}_{a}$ (volume fraction in active phase) is the largest among the others by at least three orders of magnitude. Since transforming the dimensionless cost into a dimensional one involves the division by the nominal parameter following from $\theta^{*} = \theta^{-}/\theta$ (where θ = physical parameter vector), smaller nominal parameters increase the value of the sensitivity cost.

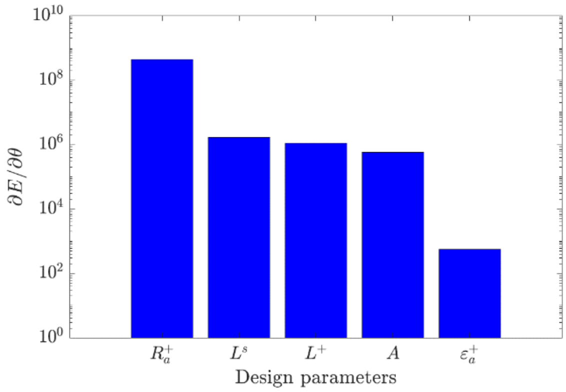

Figure 1.8. Ranking of the sensitivity of the cost function for each design parameter to separator (L^{s}) thickness, electrode thickness (L^{+}), particle radius (R_a^+), volume fraction (ε_a^+) and area (A).

From a sensitivity analysis, three design parameters were found to have the most influential effects on the energy density E, namely the electrode thickness L^+, the particle radius $R^+{}_a$ and the cell cross-sectional area A. The remaining possible design parameters include the active material volume fraction and the separator thickness. Effect of the former on energy density is smaller and it can be difficult to modify it during manufacturing; the latter cannot be arbitrarily reduced since too low thickness would lead to internal short-circuits during the experiments. Therefore, L^+, $R^+{}_a$ and A are taken as the design parameters for maximizing the cell specific (gravimetric) energy density. Let's first discuss the shape of the cost surface for two of the design parameters. Figure 1.9 shows the surface of the specific energy density over the space of L^+ and $R^+{}_a$ within the range of [10, 350] μm and [10, 300] nm, respectively, and for a cell cross-sectional area of $A = 2.43 \times 10^{-4}$ m^2. As can be seen, the calculated maximum energy density is around 249 Wh kg^{-1} and this maximum corresponds to design parameter values of $L^+ = 305$ μm and $R^+{}_a = 10$ nm approximately. The optimal solution indicating the minimum radius is expected, since smaller particle sizes imply shorter diffusion paths for the lithium in the active phase (less diffusion limitations) and therefore larger energy density. In order to validate the APSO algorithm, the attained maximum was compared to the one obtained from the exhaustive search method, in the case of two design parameters L^+ and $R^+{}_a$, of the cost surface in Figure 1.9. The optimization problem (1.18)–(1.22) was solved using the APSO algorithm in a 2.6 GHz 6-core laptop with 64 GB of RAM using Matlab R2021b®. The resulting optimal values are 250 Wh kg^{-1} for $L^+ = 307$ μm and $R^+{}_a = 10$ nm, which agrees with the depicted surface. The optimization time to solve this problem was *ca.* 137 s. The design parameter space was then enlarged to three parameters as stated above, namely L^+, $R^+{}_a$ and A, and the resulting optimal design was investigated. Now the maximum specific energy density is 250 Wh kg^{-1} with optimal parameters values as given in Table 1.5; the optimization time was *ca.* 133 s. It can be seen in Table 1.5 that, compared to the initial design, the optimal design features a thicker coating of electrode together with a smaller spherical particle of the active material in a smaller cross-sectional area. It is worth highlighting that, while both the particle size and the cell cross-sectional area hit their lower bounds, the electrode thickness does not go up to its upper bound. This is likely to be the result of the trade-off between having a thicker electrode that provides more half-cell capacity at the expense of increasing the associated weight as discussed next.

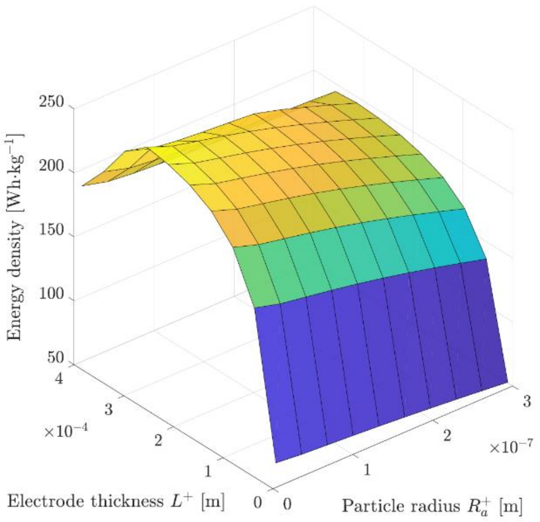

Figure 1.9. Surface of specific energy density over electrode thickness (L^+) and particle radius (R_a^+).

Figure 1.10 presents the discharge profile of current (Figure 1.10a) and voltage (Figure 1.10b) for the initial design (id) and optimal design (od) of the battery as reported in Table 1.5. The discharge current for both designs fixed was fixed to 1C, *i.e.* the current required for delithiation of the LFP half-cell battery from maximum to minimum cut-off voltage in one hour, as it can be confirmed by the voltage profile (Figure 1.7b). However, since the design parameters change, the current magnitude equivalent to the 1C current also changes. In the case that current changes, the optimal design corresponds to a smaller area and a thicker electrode compared to the initial design. Since the current corresponding to 1C is larger for the optimal design (see Figure 1.10a), this means that the half-cell is effectively bigger. So, although the optimal design has a reduced cross-sectional area compared to the initial design, it can be overshadowed by the increase of electrode thickness. In terms of voltage (Figure 1.10b), both designs depict a similar response. Regarding the mass of the electrode, it is heavier in the optimal design than in the initial one, as illustrated by Figure 1.10c. However, the overall computation of specific energy density involves the integral of the product between current and voltage, and the division by the cell mass (see Equations (1.18)–(1.22)). This results in the optimal design having 61 Wh kg^{-1} more specific energy than the initial one, *i.e.* an increase from 188 Wh kg^{-1} to 250 Wh kg^{-1}.

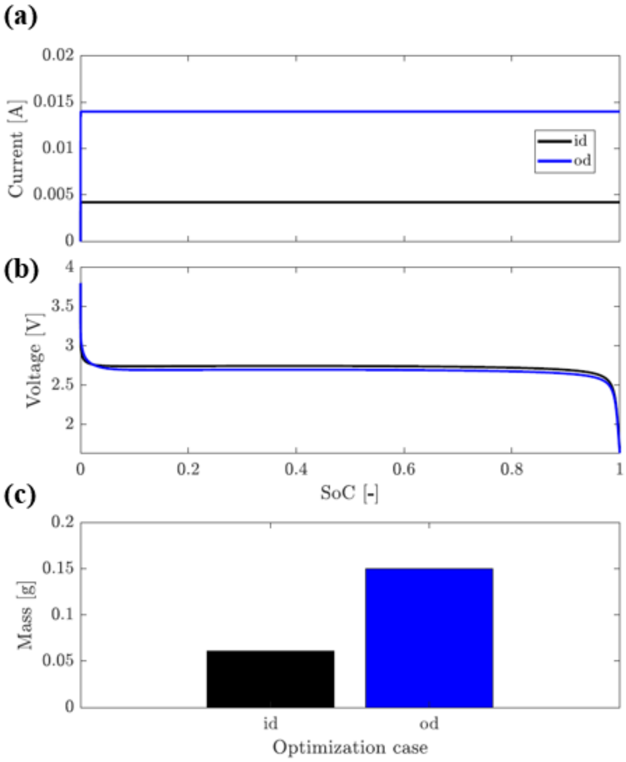

Figure 1.10. Discharge profile with respect to the SoC for the initial design (id) and optimal design (od) of LFP half-cell design presented in Table 1.5. The plots show (a) the discharge current, (b) the voltage response and (c) the resulting cell masses.

Just to get more physical insight into the optimal cell design, one can now look at the internal states (Li^+ concentrations) of the simulated LFP half-cell for both initial and optimal cases. Figure 1.11 shows the obtained results in terms of temporal evolution of normalized concentrations, with the active phase in Figure 1.11a, the electrolyte phase in the separator in Figure 1.11b and the electrolyte-phase in the positive electrode in Figure 1.11c. Instead of showing the entire concentration profile for a given spatial discretization, the figures show the upper (ub) and lower (lb) bounds for these concentrations. These bounds are obtained at given boundary positions within the half-cell (*e.g.* at the surface of the spherical particle or at the positive electrode/current collector interface), and enclose all the other internal concentration dynamics for a constant discharge profile as the one used here (rate of 1C). Note that, in the optimal design, the efficiency of the half-cell is higher since the dimensionless concentration values are closer to 1 (Figure 1.11a) compared to initial design. Moreover, since the current effectively applied to reach 1C equivalence is larger for the optimal design than for the initial one, the electrolyte concentrations in both the separator and the positive electrode regions exhibit a larger gradient, as reflected by the lower and upper bounds in Figures 1.11b and 1.11c. These aspects contribute to a larger overvoltage of the cell, which explains why the voltage plateau of the optimal design is slightly lower than that of the initial design (see Figure 1.10b).

Another way to look at these results is by inspecting the spatial distribution of the internal state of the half-cell at given time instants. Figure 1.12 shows the radial distribution $r^* = r/R_a$ of the normalized active-phase concentration c_a^* every 10 min (Figure 1.12a), followed by the electrolyte-phase profiles along the x dimension at the separator $c_\mathrm{e}^{s,*}$ (Figure 1.12b, where $x^{s,*}= x^s/L^s$) and the positive electrode region concentration $c_\mathrm{e}^{+,*}$every 10 s (Figure 1.12c, where $x^{+,*} = x^+/L^+$). For simplicity, x values located in the separator are defined as x^s and those located in the positive electrode regions are denoted as x^+. The time differences reflect the speed of each process, where electrolyte dynamics tend to be faster than active-phase dynamics [30]. In Figure 1.12a, one can see that the initial concentration is uniform and close to the minimum value. As time elapses, the concentration increases towards the maximum value of 1, and the curve of

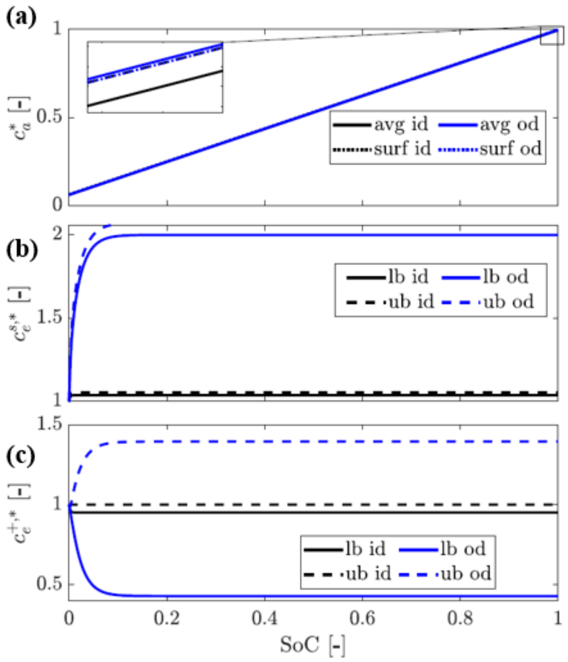

Figure 1.11. Temporal evolution of normalized concentrations for the simulated LFP half-cell with initial design (id) and optimal design (od). Plot (a) shows the average (avg) and surface (surf) active-phase concentration (c_a^*), whereas plots (b) and (c) show the upper bound (ub) and lower bound (lb) for the electrolyte-phase concentration in the separator ($c_e^{s,*}$) and the positive electrode regions ($c_e^{+,*}$), respectively.

the concentration bends with the maximum concentration at the r^* = 1 boundary and the minimum concentration at the r^* = 0 boundary (see Figure 1.12a), representing the surface and the centre of the spherical particle, respectively. Note that the optimal design incurs in a smaller concentration gradient compared to the initial design, which is due to the smaller particle sizes suggested by the optimization algorithm. A similar trend can be found when analysing the electrolyte profiles (see Figures 1.12b and 1.12c) as the discharge of the electrode proceeds: the concentration in the electrolyte starts from a uniform position around 1 and is displaced to higher values. Given that the effective current is larger for the optimal design, the resulting electrolyte concentration gradients are larger compared to the initial design. Moreover, a thicker electrode also contributes to obtain larger concentration gradients in the positive electrode region. The maximum electrolyte concentrations appear at the $x^{\mathrm{s},*}$= 0 boundary of the separator (see Figure 1.12b) corresponding to the lithium foil-separator interface, whereas the minimum electrolyte concentrations at the $x^{+,*}$ = 1 boundary of the positive electrode (see Figure 1.12c) are associated with the positive electrode/current collector interface.

The results of the APSO algorithm during the searching procedure of optimal solutions are shown in Figure 1.13. As can be seen, after 20 iterations the algorithm stops and reaches the best solution. Figure 1.13a depicts the best cost function at the end of each iteration, and it seems that it reaches the maximum point after 8 iterations. However, the value of the swarm norm (*i.e.* swarm radius $\|\Theta n\|$) indicates a non-homogeneous space distribution of the particle population (see Figure 1.13b), meaning that they have not concentrated around the optimal solution. By checking the normalized swarm radius $R^{\theta}{}_{\mathrm{norm}}(n)$ (see Figure 1.13c) and considering the stopping criteria, one can see that, at iteration 20, most of the particles have gathered around a specific solution. At that moment, the deviation of the swarm norm is the lowest, which led to accept the stopping condition of the search process.

.

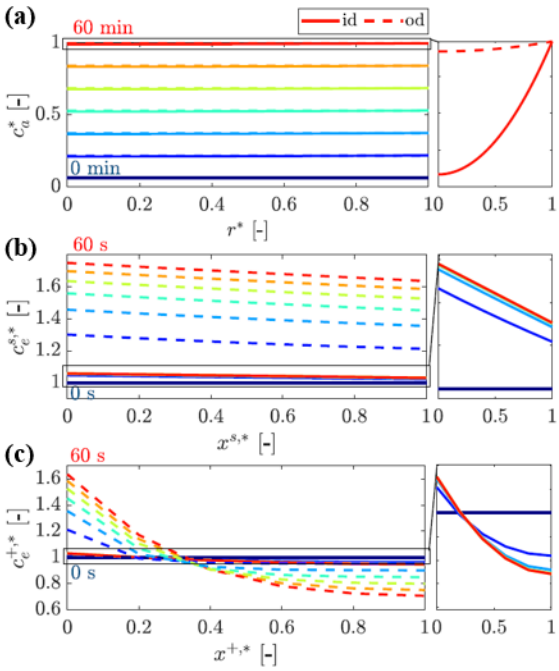

Figure 1.12. Temporal evolution of normalized concentrations with respect to the normalized space for the simulated LFP half-cell with initial design (id) and optimal design (od). Plot (a) shows the active-phase concentration (c_a^*) (with $r^*=r/R_\mathrm{a}$) whereas plots (b) and (c) show the electrolyte-phase concentration in the separator ($c_\mathrm{e}^{\mathrm{s},*}$) (with $x^{\mathrm{s},*} = x_\mathrm{s}/L_\mathrm{s}$) and the positive electrode regions ($c_\mathrm{e}^{+,*}$) (with $x^{+,*} = x^+/L^+$) respectively. The color gradient of the curves from blue to red corresponds to initial and final times, respectively. While the active-phase results are shown every 10 min up to 60 min, the electrolyte-phase ones are every 10 s up to 60 s.

Table 1.5. Results of the optimization based on the APSO algorithm

Design parameters	Units	Lower bound	Upper bound	Initial design	Optimal Design
L^+	[μm]	10	390	70	309
R_a^+	[nm]	10	300	36.5	10
A	[m^2]	1.8×10^{-4}	3.0×10^{-4}	2.4×10^{-4}	1.8×10^{-4}
E	[Wh kg^{-1}]	-[a]	-[a]	188	250

[a] Not pertinent because it is calculated and corresponds to the objective function

Additionally, one can also look at the different time constants that govern the electrochemical processes of the considered LFP half-cell battery. Table 1.6 shows the resulting time-constant values for both initial and optimal designs. Results indicate that the (dis)charge time scales in both active ($\tau_{c}^{\pm}$) and electrolyte ($\tau_{s}^{\pm}$) phases, as well as the diffusion time constant for the electrolyte-phase ($\tau_{\mathrm{e,d}}^{+}$) have increased for the optimal design with respect to the initial design. Larger time scales validate the notion of having a bigger half-cell in both phases requiring larger absolute currents for full discharge (see Figure 1.10a). Also, the larger electrolyte phase time constant can be verified in Figures 1.11b and c where the electrolyte subsystem for the optimal design is slower than for the initial design. Contrarily, the diffusion time constant for the active phase ($\tau_{\mathrm{d}}^{\pm}$) and the reaction kinetics time constants ($\tau_{\mathrm{k}}^{\pm \mathrm{s}}$) are lower for the optimal design with respect to the initial design. The shorter diffusion time is the result of having shorter diffusion paths due to particle size reduction. Also, decrease of particle size can result in increased surface area of the active material. Increased surface area can help to fasten kinetics by facilitating the transfer of charges from the electrolyte to the active phase. Finally, while the initial design was limited by the reaction kinetics given the large value of $\tau^{+}{}_{k}$, the optimal design shifted the limiting step to the electrode (dis)charge capacity due to the large value of $\tau^{+}{}_{c}$.

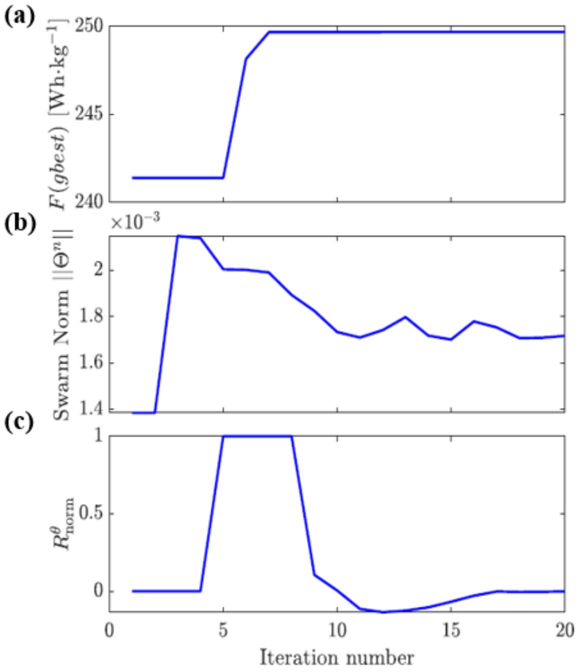

Figure 1.13. Results of the APSO algorithm optimal search in the design space. (a) Best cost function in each iteration, (b) swarm norm $\|\Theta^{n}\|$, and (c) normalized swarm radius $R^{\theta}{}_{\mathrm{norm}}(n)$.

Table 1.6. Values for the time constants of the considered LFP half-cell for the initial design and the optimized design.

Constants	Initial design [s]	Optimized design [s]
τ_{c}^{+}	4603	22827
τ_{d}^{+}	167	13
$\tau_{\mathrm{e,c}}^{+}$	233	1156
$\tau_{\mathrm{e,d}}^{+}$	18	432
τ_{k}^{+}	37757	10344

1.5.2. Impedance identification results

The optimal parameter estimation for the optimization problem (Equation 1.10) was done in order to complete the model verification. EIS experimental data obtained in Chapter 2 and represented in Figure 1.3b were used as reference and compared with the Nyquist plot obtained by the model. The results are shown in the Nyquist plot of Figure 1.14, where the impedance data is depicted as black dots, the model response with the parameter initialization is the solid blue curve and the model response with the optimal parameter set is the dashed red curve. From the figure, one can conclude that the proposed model is able to capture the typical response of LFP half-cells, including the two semi-circles at high frequency and the low-frequency content associated to diffusion in active and electrolyte phases. The presented curves show that the proposed electrochemical model can be adjusted to fit the measured impedance data coming from an LFP half-cell, which validates the model choice and can be considered as successful model identification. However, there are still some issues, notably when attempting to link the transfer function parameters to the physical half-cell parameters. Taking for instance the time constants in (A.2), it is still unclear how to optimize with respect to R_{a} if only τ_{d} and τ_{k} are known, or how to link the double-layer effects to the kinetic reaction, both of which being in the domain of fast dynamics. These are nontrivial issues that the ULB group is currently exploring, and which need to be solved before being able to make the link with the experimental validation. Once this is done, the next step would be to use the identified model to optimize the cell performance using the approach proposed in the present study, which will complete the experimental validation part of the work. Additionally, GITT results will be used in further study in order to understand the time constants of the LFP half-cells better and optimize it accordingly.

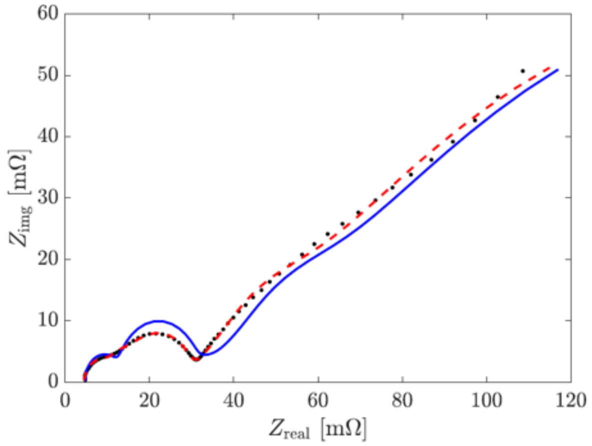

Figure 1.14. Nyquist plots of impedance response of an LFP half-cell battery for (●) experimental data, (--) initial result, (—) optimized result.

1.6. Conclusion

The maximization of the specific (gravimetric) energy density of a lithium-ion battery (LIB - LiFePO$_4$ half-cell configuration) was proposed based on a reduced-order model, *i.e.* derivation of Doyle-Fuller-Newman (DFN) model under suitable assumptions in order to simplify complexity of numerical simulations. In that ambit, the dSPMe (dimensionless single particle model with electrolyte) was considered, which approximates the DFN model by considering the electrode as a single particle. This simplified model allowed us to reduce significantly the computational complexity. The dimensionless form of the SPMe shed light on limiting processes, like the fact that the initial standard design was limited by reaction kinetics while the optimal design shifted the limitation to the (dis)charge time scale, thus the discharge capacity. On the basis of a sensitivity analysis, the most relevant design parameters affecting the energy density were found to be (i) the particle radius, (ii) the electrode thickness and (iii) the electrode cross-sectional area. An adaptive particle swarm optimization algorithm tuned for fast convergence was used to solve the LIB optimal design problem. The optimal design resulted in an energy density of 250 Wh kg^{-1} for an LFP electrode of 310 μm thickness, 10 nm particle radius and 2×10^{-4} m^{2} electrode cross-sectional area. This corresponds to an increase of energy density of 61 Wh kg^{-1} with respect to an initial standard design obtained from the literature. This highlights the importance of the proposed approach for optimizing battery performance. An evident limitation of the half-cell battery optimal design of this work is that it relies on a reduced-order electrochemical model, making it valid for low current rates typically found in standalone energy storage applications, for instance. Given the model simplicity, one could solve the optimization problem over multiple charge–discharge cycles of the battery in order to *e.g.* minimize the capacity loss. Another possible extension of this work is to consider a full-cell lithium-ion battery and properly dimension both positive and negative electrodes simultaneously. Finally, ongoing work concerns the experimental validation of the proposed approach which will involve using experimental data obtained with different masses of LFP at different C-rates.

1.7. References

[1] N.A. Chaturvedi, R. Klein, J. Christensen, J. Ahmed, A. Kojic, *IEEE Control Syst* **2010**, *30*, 49.

[2] S. Wang, S. Jin, D. Bai, Y. Fan, H. Shi, C. Fernandez, *Energy Reports* **2021**, *7*, 5562.

[3] S. Wang, P. Takyi-Aninakwa, S. Jin, C. Yu, C. Fernandez, D.I. Stroe, *Energy* **2022**, *254*.

[4] X. Hu, S. Li, H. Peng, *J Power Sources* **2012**, *198*, 359.

[5] Y. Wang, H. Fang, L. Zhou, T. Wada, *IEEE Control Syst* **2017**, *37*, 73.

[6] C. Zou, C. Manzie, D. Nešić, *IEEE Trans Control Syst Technol.* **2016**, *24*, 1594.

[7] D. Zhang, S. Dey, L.D. Couto, S.J. Moura, *IEEE Trans Control Syst. Technol* **2020**, *28*, 1363.

[8] Fuller Thomas F., M. Doyle, J. Newman, *J Electrochem Soc* **1994,** *141,* 1.

[9] Doyle Marc, T.P. Fuller, J. Newman, *J Electrochem Soc* **1992**, *140*, 1526.

[10] J. and D.R.M. Thomas Karen E. and Newman, in *Advances in Lithium-Ion Batteries* (Ed: B. van Schalkwijk Walter A. and Scrosati), Springer US, Boston, MA **2002**, 345.

[11] E. Hosseinzadeh, J. Marco, P. Jennings, *Energies* **2017**, *10*, 1278.

[12] S. Golmon, K. Maute, M.L. Dunn, *Int J Numer Methods Eng* **2012**, *92*, 475.

[13] G. Ning, B.N. Popov, *J Electrochem Soc* **2004**, *151*, A1584.

[14] S. Santhanagopalan, Q. Guo, P. Ramadass, R.E. White, *J Power Sources* **2006**, *156*, 620.

[15] M. Guo, G. Sikha, R.E. White, *J Electrochem Soc* **2011**, *158*, A122.

[16] S.J. Moura, F.B. Argomedo, R. Klein, A. Mirtabatabaei, M. Krstic, *IEEE Trans Control Syst Technol* **2017**, *25*, 453.

[17] T.R. Tanim, C.D. Rahn, C.Y. Wang, *Energy* **2015**, *80*, 731.

[18] D. Di Domenico, A. Stefanopoulou, G. Fiengo, *J Dyn Sys Meas Control* **2010**, *132,* 061302.

[19] J.F. Manwell, J.G. McGowan, *Solar Energy* **1993**, *50*, 399.

[20] J. Newman, *J Electrochem Soc* **1995**, *142*, 97.

[21] W. Ai, Y. Liu, *J Energy Storage* **2023**, *67*, 107512.

[22] J.S. Kim, D.C. Lee, J.J. Lee, C.W. Kim, *Sci Rep* **2020**, *10*, 829.

[23] N. Xue, W. Du, A. Gupta, W. Shyy, A. Marie Sastry, J.R.R.A. Martins, *J Electrochem Soc* **2013**, *160*, A1071.

[24] C. Liu, L. Liu, *J Electrochem Soc* **2017**, *164*, E3254.

[25] Y. Dai, V. Srinivasan, *J Electrochem Soc* **2016**, *163*, A406.

[26] D.C. Lee, K.J. Lee, C.W. Kim, *Int. J. of Precis. Eng. and Manuf.-Green Technol.* **2020**, *7*, 829.

[27] J.S. Kim, D.C. Lee, J.J. Lee, C.W. Kim, *Sci Rep* **2020**, *10*.

[28] Newman, John and Balsara, Nitash, *Electrochemical Systems*, John Wiley& Sons **2021** ISBN: 978-1-119-51460-2.

[29] S.J. Moura, N.A. Chaturvedi, M. Krstić, *J Dyn Sys Meas Control* **2014**, *136*, 011015.

[30] S.G. Marquis, V. Sulzer, R. Timms, C.P. Please, S.J. Chapman, *J Electrochem Soc* **2019**, *166*, A3693.

[31] L.D. Couto, M. Charkhgard, B. Karaman, N. Job, M. Kinnaert, *Energy* **2023**, *263*, 125966.

[32] U. Westerhoff, K. Kurbach, F. Lienesch, M. Kurrat, *Energy Technology* **2016**, *4*, 1620.

[33] R. Drummond, A.M. Bizeray, D.A. Howey, S.R. Duncan, *IEEE Trans Control Syst Technol* **2020**, *28*, 1284.

[34] R. Drummond, S.R. Duncan, in *IFAC-PapersOnLine* **2020**, *53(2)*, 12452.

[35] Q. Zhao, Y. Zhang, Y. Meng, Y. Wang, J. Ou, Y. Guo, D. Xiao, *Nano Energy* **2017**, *34*, 408.

[36] P. Liu, W. Zhang, Y. Zhang, X. Dai, F. Wu, in *IOP Conf Ser: Mater Sci Eng* **2018** *45*, 032089.

[37] J. Illig, J.P. Schmidt, M. Weiss, A. Weber, E. Ivers-Tiffée, *J Power Sources* **2013**, *239*, 670.

[38] N. Meddings, M. Heinrich, F. Overney, J.S. Lee, V. Ruiz, E. Napolitano, S. Seitz, G. Hinds, R. Raccichini, M. Gaberšček, J. Park, *J Power Sources* **2020**, *480*, 228742.

[39] F.M. Kindermann, A. Noel, S. V. Erhard, A. Jossen, *Electrochim Acta* **2015**, *185*, 107.

[40] Y. Fernández Pulido, C. Blanco, D. Anseán, V.M. García, F. Ferrero, M. Valledor, *Measurement* **2017**, *106*, 1.

[41] K.Y. Song, G.S. Jang, J. Tao, J.H. Lee, S.K. Joo, *J Nanosci Nanotechnol* **2017**, *18*, 992.

[42] D. Dees, E. Gunen, D. Abraham, A. Jansen, J. Prakash, *J Electrochem Soc* **2008**, *155*, A603.

[43] N. Ogihara, Y. Itou, T. Sasaki, Y. Takeuchi, *J Phys Chem C* **2015**, *119*, 4612.

[44] J. Kim, S. Park, S. Hwang, W.S. Yoon, *J Electrochem Sci Technol* **2022**, *13*, 19.

[45] Y.C. Chien, H. Liu, A.S. Menon, W.R. Brant, D. Brandell, M.J. Lacey, *Nat Commun* **2023**, *14*, 2289.

[46] Y. Chen, L. Wang, T. Anwar, Y. Zhao, N. Piao, X. He, Q. Zhu, *Electrochim Acta* **2017**, *241*, 132.

[47] K. Tang, X. Yu, J. Sun, H. Li, X. Huang, *Electrochim Acta* **2011**, *56*, 4869.

[48] R. Klein, N.A. Chaturvedi, J. Christensen, J. Ahmed, R. Findeisen, A. Kojic, *IEEE Transactions on Control Systems Technology* **2013**, *21*, 289.

[49] M. Safari, C. Delacourt, *J Electrochem Soc* **2011**, *158*, A562.

[50] S. Stewart, P. Albertus, V. Srinivasan, I. Plitz, N. Pereira, G. Amatucci, J. Newman, *J Electrochem Soc* **2008**, *155*, A253.

[51] P. Albertus, J. Couts, V. Srinivasan, J. Newman, *J Power Sources* **2008**, *183*, 771.

[52] J. Christensen, *J Electrochem Soc* **2010**, *157*, A366.

[53] L.O. Valoén, J.N. Reimers, *J Electrochem Soc* **2005**, *152*, A882.

1.8. Supporting information

Equations associated to the DFN model and electrochemical variables

This supporting information lists the main equations associated to the DFN model in Table S1.1. Then, the main electrochemical variables of the dSPMe are reported in Table S1.2., followed by the nomenclature and model parameters of the dSPMe model in Table S1.3.

Table S1.1. DFN model equation.

Physical Process	Equation
Active phase	
Conservation of Li	$\frac{\partial c_{\mathrm{a}}^{\pm}}{\partial t} = \frac{1}{r^2}\frac{\partial}{\partial r}(D_{\mathrm{a}}^{\pm} r^2 \frac{\partial c_{\mathrm{a}}^{\pm}}{\partial r})$
Conservation of charges	$\frac{\partial^2 \varphi_{\mathrm{a}}^{\pm}}{\partial x^2} = \frac{a_{\mathrm{a}}^{\pm} F}{\sigma_{\mathrm{a}}^{\pm}} j_{\mathrm{n}}^{\pm}$
Electrolyte phase	
Conservation of Li[b]	$\frac{\partial c_{\mathrm{e}}^{\pm s}}{\partial t} = \frac{\partial}{\partial x}\frac{D_{\mathrm{e,eff}}^{\pm s}}{\varepsilon_{\mathrm{e}}^{\pm s}}\frac{\partial c_{\mathrm{e}}^{\pm s}}{\partial x} + \frac{a_{\mathrm{a}}^{\pm}(1 - t_{\mathrm{c}}^{0})}{\varepsilon_{\mathrm{e}}^{\pm}} j_{\mathrm{n}}^{\pm}$
Conservation of charges[a,b]	$\frac{\partial^2 \varphi_{\mathrm{e}}^{\pm s}}{\partial x^2} = -\frac{a_{\mathrm{a}}^{\pm} F}{\kappa_{\mathrm{e,eff}}^{\pm}} j_{\mathrm{n}}^{\pm} + \kappa_{\mathrm{D}}^{\pm s}\frac{\partial^2 c_{\mathrm{e}}^{\pm s}}{\partial x^2}$
Electrode kinetics	
Intercalation reaction[c]	$j_{\mathrm{n}}^{\pm} = \frac{2}{F} i_{0}^{\pm} \sinh(\frac{\alpha_0 F}{RT}\eta_{s}^{\pm})$ where $\eta_{s}^{\pm} = \varphi_{\mathrm{a}}^{\pm} - \varphi_{\mathrm{e}} - U^{\pm} - R_{f}^{\pm} j_{\mathrm{n}}^{\pm}$
Moles of Li	$n_{Li} = \sum_{j \in \{\pm\}} \frac{3\varepsilon_{\mathrm{a}}^{j}}{(R_{\mathrm{a}}^{\mathrm{j}})^3} \int_0^{L^j} \int_0^{R_a^j} r^2 c_{\mathrm{a}}^{\mathrm{j}} dr dx$

[a] Linearized equation [45].

[b] For the separator region, $j_{\mathrm{n}} = 0$ (it is not defined).

[c] Assuming $\alpha_0 = 0.5$[9].

Table S1.2. Electrochemical parameters used in the dSPMe.

Variable	Units	Symbol
Li concentration in active phase	[mol m^{-3}]	$c^{\pm}_{a}$
Li concentration at active particle surface	[mol m^{-3}]	$c^{\pm}_{as}$
Li concentration in electrolyte phase	[mol m^{-3}]	$c^{\pm s}_{e}$
Li concentration in electrolyte phase boundaries	[mol m^{-3}]	$c^{\pm s}_{e,bc}$
Active-phase electric voltage	[V]	$\varphi^{\pm}_{s}$
Electrolyte electric voltage	[V]	$\varphi^{\pm s}_{e}$
Ionic current	[A m^{-2}]	$i^{\pm}_{e}$
Pore-wall molar flux	[mol m^{-2} s^{-1}]	$j^{\pm}_{n}$
Exchange current density	[A m^{-2}]	$i^{\pm}_{0}$
Surface/lithium over-voltage	[V]	$\eta^{\pm}_{s}$ / η_{Li}
Applied current	[A]	i
Terminal voltage	[V]	v

Table S1.3. Definition of dSPMe parameters and initial values used in the LFP half-cell simulation.

Definition	[units]	Symbol	Value	Reference
Active-phase parameters				
Specific interfacial area	$[\mathrm{m^2\ m^{-3}}]$	a_a	3.53×10^{7}	[49]
Maximum lithium conc.	$[\mathrm{mol.^{-3}}]$	$c_\mathrm{a,max}$	2.298×10^{4}	[50]
Active-phase diffusion coefficient	$[\mathrm{m^2\ s^{-1}}]$	D_a	8×10^{-18}	[50]
Exchange current density	$[\mathrm{A\ m^{-2}}]$	i_0^Li	19.0	[49]
Reaction rate	$[\mathrm{m^{2.5}\ mol^{0.5}\ s^{-1}}]$	k_n	3.05×10^{-14}	[49]
LFP electrode thickness	[μm]	L^+	70	[49]
Current collector thickness	[μm]	L^cc	25	[50]
Particle radius	[nm]	R_a	36.5	[49]
Film resistance	$[\Omega\ \mathrm{m^2}]$	R_f	0.001	[a]
Open circuit voltage (OCV) of LFP, Li	[V]	U^+, U_Li	Eq (A.1)[c],0	[49][51]
Charge transfer coefficient	[-]	a_0	0.5	[49]
Volume fraction in active-phase electrode	[-]	ε_a	0.43	[49]
Volume fraction of filler	[-]	ε_f	0.27	[a]
Mass density of active phase	$[\mathrm{kg\ m^{-3}}]$	ρ_a	3600	[50]
Mass density of filler	$[\mathrm{kg\ m^{-3}}]$	ρ_f	1800	[50]
Mass density of current collector	$[\mathrm{kg\ m^{-3}}]$	ρ_cc	2707	[50]
Electrical conductivity	$[\Omega^{-1}\ \mathrm{m^{-1}}]$	σ	7.4×10^{-3}	[50]
Electrolyte-related parameters				
Electrolyte-phase diffusion coefficient	$[\mathrm{m^2\ s^{-1}}]$	D_e	2.7877×10^{-10}	[52]
Activity coefficient	[-]	$\frac{d\ln f_{c/a}}{d\ln c_\mathrm{e}}$	Eq. (A.3)	[53]
Separator thickness	[μm]	L^s	25	[a]
Transference number	[-]	t_c^0	0.4	
Volume fraction in electrolyte-phase electrode	[-]	ε_e^+	0.3	[a]
Volume fraction in electrolyte-phase separator	[-]	ε_e^s	0.5	[a]
Ionic conductivity	$[\Omega^{-1}\ \mathrm{m^{-1}}]$	κ	Eq. (A.2)[c]	[50]
Mass density of electrolyte phase	$[\mathrm{kg\ m^{-3}}]$	ρ_e	1200	
Cell-level parameters				
Cross-sectional area	$[\mathrm{m^2}]$	A	2.43×10^{-4}	[a]
Bruggeman exponent	[-]	b	1.5	[14]
Electrolyte nominal conc.	$[\mathrm{mol\ m^{-3}}]$	$\bar{c}_\mathrm{e}$	1000	[49][50]
Faraday's constant	$[\mathrm{C\ mol^{-1}}]$	F	96487	[14]
Universal gas constant	$[\mathrm{J\ mol^{-1}\ K^{-1}}]$	R_g	8.31	[14]
Reference temperature	[K]		298.15	[a]

[a] Used in this work.

[b] For the separator region, $j_\mathrm{n} = 0$ (it is not defined).

[c] Calculated by using referred equation

Obtained GITT results

This supporting information includes the experimental results that are not yet used in the modelling study. Result of charging galvanostatic intermittent titration technique (GITT) represented in Figure S1.2.1a while the result of galvanostatic cycling with potential limitations experiment shown at Figure S1.2.1b. Both results are in line with what has been observed in literature and will be used in further modelling studies.

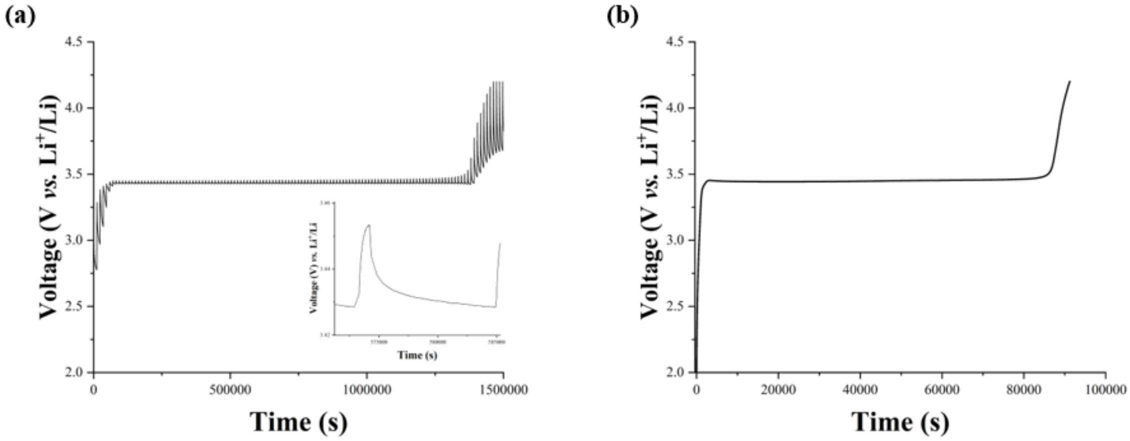

Figure S1.2.1. (a) Obtained GITT curve and (b) GCPL charging curve of LPF half-cells.

Chapter 2

Water-based processing of $LiFePO_4$ positive electrodes for Li-ion batteries: effect of particle size and active material loading on the performance of the electrodes

Abstract

$LiFePO_4$ (LFP) powders with 0.84 µm and 0.24 µm average particle sizes are studied as Li-ion battery materials using a water-based electrode manufacturing process. Along with the compatibility with aqueous processing, the impact of particle size and active material loading on the performance of the electrodes is studied, especially in terms of capacity, rate capability and stability. Decrease of rate capability and capacity with increasing electrode loading is observed for both cases due to increase of internal resistance with increasing electrode loading. However, the LFP with lower particle size is much less affected by the increase of electrode loading due to considerably lower charge transfer resistance at the material surface. Degradation upon cycling highly depends on the electrode loading, the phenomenon being more and more acute as the electrode loading goes from 1.6 to 6.4 mg cm^{-2}. Degradation is due to the increase of both internal resistance and charge transfer resistance; however, it is pointed out that degradation is lessened by decreasing the LFP particle size. In conclusion, both the material morphology and the electrode design have to be taken into account for electrode manufacturing.

2.1. Introduction

In the current evolution of the world, the energy demand increases year by year, which calls for better resource management. To change direction towards a more sustainable world, the electrical energy generated by solar, wind and other renewable sources needs to be stored and used more efficiently. Electrochemical storage devices are thus key technologies. For that purpose, along with other systems, Li-ion batteries are one of the most popular energy storage devices due to their high energy and power density [1]. However, since a battery is made of several components, various design selections should be considered in the production process of the batteries, depending among others on the final use. The main components of the battery cells are the electrolyte, the electrodes (including current collectors) and the separator. Among these, it must be pointed out that electrodes are usually composite media, including (i) the active material that stores Li^+ ions, (ii) binders, (ii) conductive additives, all having an impact on the cell properties; thus, the design of the electrode is highly important.

First, the selection of the electrode active material among various options is crucial. In the case of the positive electrode, Lithium Cobalt Oxide (LCO) remains very common due to its high insertion/deinsertion potential (~4 V *vs.* Li^+/Li), which results in high energy density cells when coupled to, *e.g.*, graphite as negative electrode material (insertion/deinsertion potential ~0.5 V *vs.* Li^+/Li). However, due to high cost, as well as availability and safety issues associated with cobalt, NMC (*i.e.* $LiNi_{1-y-z}Mn_yCo_zO_2$) are progressively taking the lead. To fully eliminate Co, other active materials are also currently considered [1,2]. Among those, $LiFePO_4$ (LFP) is one of the most popular positive electrode materials for Li-ion batteries due to its increased safety, abundancy of precursor materials and relatively high capacity [3]. However, LFP displays relatively low density, poor electronic conductivity and low ionic diffusivity [4].

Second, the design of the electrode from its components must be carefully considered. In particular, the active material must be blend with a binder in a solvent to finally be deposited (usually by blade casting) onto a metallic current collector, the final electrode being obtained after solvent elimination. Although current processes still use PolyVinyliDene Fluoride (PVDF) and N-methyl-pyrrolidone (NMP) as binder and solvent, respectively, it appears more and more necessary to move towards water-based suspensions for both economic and environmental reasons. In that field, Na-CMC-styrene-butadiene rubber combinations have been widely used for aqueous formulation of electrodes [5]. Alternatively, in previous works [6], our research group developed a water-based spray-coating process using xanthan gum, which proved efficient to manufacture both LFP and $Li_4Ti_5O_{12}$ (LTO) electrodes assembled as full cells.

Coming back to the active material, its chemical nature is not the only parameter to be considered. Given that electrodes are prepared from powders, the active material granulometry has an impact on both the manufacturing process and on the final electrode properties [7,8] given that the Li^+ ions have to diffuse within those particles during insertion/deinsertion. For example, Sinha *et al.* [9] explain in a review how the particle size of the widely used positive electrode materials powders (such as LCO, LFP, Lithium Manganese Oxide - LMO, *etc.*) affects the performance of the cells. The coating thickness also has an impact due to electron and ion conductivity limitations within the active material and the electrolyte. As an example, in a study that focuses on the impact of the electrode thickness on the electrochemical and thermal characteristics of Li-ion batteries, Zhao *et al.* [10] concluded that the thicker electrodes release more heat by ohmic effect at the same discharge rate compared to thinner ones. Additionally, those parameters affect diffusion distances and concentration polarization, both having high impacts on the performance of the cells. Therefore, such parameters must be controlled and chosen carefully to meet the expectations in terms of performance and stability of the battery.

More specifically, with regard to LFP electrodes, a detailed study by Logan *et al.* [12] focused on how the specific surface area and the particle size of the LFP powder affect the cell aging; it concluded that, after long-term cycling, LFP particles with large size display micro-fractures and lose their storage capacity. In another paper, the impact of the particle size distribution on the rate capability of the electrodes was studied by Zhang *et al.* [12]. The results show that broader particle size distribution of the LFP powders offers better pathways for electron transport and reduces the contact resistance, hence improving the rate capability of the cells. Although many studies focused on different design parameters, works considering the joint impact of both the powder particle size and the electrode loading are less common, especially when water-based formulations are considered.

The aim of the present study is to link the effects of the LFP particle size and electrode loading with the performance and stability of LFP electrodes manufactured using a water-based process. In particular, it aims at understanding how the impacts of those two design parameters can compensate each other. To that aim, electrodes with two different LFP particle sizes and various electrode loadings were prepared. The electrodes were assembled in half-cells and their performance and stability were studied by galvanostatic charge-discharge method. Electrochemical impedance spectroscopy was also performed to understand the origin of the performance and stability differences observed. The whole study was performed on electrodes prepared *via* the process previously developed at the laboratory, *i.e.* spray-coating of a water-based electrode formulation using xanthan gum as a binder. The obtained results show a clear impact of the particle size on the electrode performance, and allow to define electrode loading limits with regard to the expected performance at high cycling speed.

2.2. Experimental

2.2.1. Preparation of electrodes

Two different $LiFePO_4$ (LFP) powders were selected for this study: P700 and P800 from Prayon/PuLead and referred to as LFP-1 and LFP-2 hereafter. Following the manufacturer, the two materials are carbon-coated to enhance electron conductivity. The powders were characterized and used as received. Electrodes were produced *via* robotic spray coating of a water-based suspension by adapting a previously published method [6] where manual airbrush was used. The aqueous suspension, prepared in MilliQ water, contained 12 wt% solids including LFP, xanthan gum (Sigma-Aldrich) and conductive additive (carbon black Timcal C-nergy Super C65) in a weight ratio of 75:20:5 (active material:conducting carbon:binder). The mixture was stirred at room temperature with a magnetic stirrer for 3 h prior to electrode manufacturing. The prepared ink was sprayed onto pre-weighted stainless-steel discs current collectors (type 304, $\varnothing$ = 15.5 mm, MTI corp.) and dried overnight at 60°C under air in an oven. Different LFP loadings were prepared: 3 mg (1.59 mg cm^{-2}), 6 mg (3.17 mg cm^{-2}) and 12 mg (6.35 mg cm^{-2}). The coated discs were then weighted and dried again in an oven for 2 h under vacuum (2000 Pa) at 110°C before being introduced into the glovebox. The half-cells were assembled using LFP electrode as positive electrode, metallic Li disc (PI-KEM) as counter and reference electrode, two Celgard® separators and 80 µL of electrolyte (1 M $LiPF_6$ in an ethylene carbonate:diethyl carbonate:dimethylcarbonate – 1:1:1 mixture, Sigma Aldrich). Prepared half-cells were then used for electrochemical characterization.

2.2.2. Characterization

2.2.2.1. Physico-chemical characterization

The LFP powders were analysed by nitrogen adsorption-desorption. The isotherms were measured at -196°C using a Micromeritics ASAP 2420 automatic device (Micromeritics, Norcross, USA). The samples were degassed overnight at 270°C under vacuum (133 Pa) prior to the measurements. The specific surface area, A_{BET}, was calculated using the Brunauer-Emmett-Teller (BET) equation, the adsorption data being taken in the adequate range of relative pressure ($P\ P_0^{-1}$), accounting for the Rouquerol criterion. Scanning electron microscopy (SEM) images were obtained on a FEG-SEM Tescan CLARA at 15 kV under high vacuum conditions. The samples were coated with a 15-nm gold layer by sputtering and mounted with carbon adhesive prior to observation.

2.2.2.2. Electrochemical characterization

LFP half-cells were characterized using a BioLogic VMP3 multichannel potentiostat. Prior to any electrochemical test, cells were first submitted to formation cycles between 2.0 and 4.2 V *vs.* Li^+/Li by using galvanostatic charge and discharge cycling in the following sequence: 10 cycles at C/5 (*i.e.* 5 h of charge and 5 h of discharge) and 10 cycles at C (*i.e.* 1 h of charge and 1 h of discharge). Then, the overall cell performance was assessed by performing 10 cycles at C/5, C/2, C, 2C, 5C. Finally, to compare the stability of the cells, 100 cycles of galvanostatic charge-discharge cycles at C were added and the cycling finalized with a second performance assessment sequence including again 10 cycles at C/5, C/2, C, 2C, 5C. Cells were compared according to their capacities at given C-rates and capacity retention after long-term cycling. Note that all applied current densities were calculated considering a theoretical capacity of 170 mAh g^{-1} for LFP [13].

Electrochemical impedance spectroscopy (EIS) was conducted with the same device in the 10^{-2} - 10^6 Hz frequency range at 25°C. Apart from the frequency range, the State Of Charge (SOC) level of the cells greatly affects the results of EIS spectra; therefore, its value should be chosen beforehand. According to literature, SOC levels were selected separately for performance and stability investigations. Indeed, in earlier studies, it has been observed that EIS spectra differences are more apparent at 100% SOC for stability investigations [14]; the same SOC was thus chosen for stability studies. For performance investigations, SOC was fixed as 40% since it has been stated in literature that limit potentials, compared to mid potentials, leads to higher polarization, possibly due to side reactions [15]. EIS was performed after the formation cycles and at the end of the second performance cycling sequence to highlight the impact of aging on the electrode properties.

2.3. Results and discussion

2.3.1. Physico-chemical characterization of the LFP powders

LFP powders were first observed by SEM (Figure 2.1) to check their morphology and determine their particle size distribution. LFP-1 is constituted of particles of very variable size (Figure 2.1a) while LFP-2 displays a much more homogeneous structure (Figure 2.1b). A minimum of 90 particles were randomly selected and their diameter measured manually to calculate the mean particle size (along with its standard deviation, *σ*) of both samples (Figure 2.2). Values were calculated equal to 0.84 and 0.26 µm for LFP-1 and LFP-2 powders, respectively. The corresponding standard deviations, *σ*, equal 0.45 and 0.26 µm, meaning that LFP-2 presents smaller particles with much narrower size distribution than LFP-1.

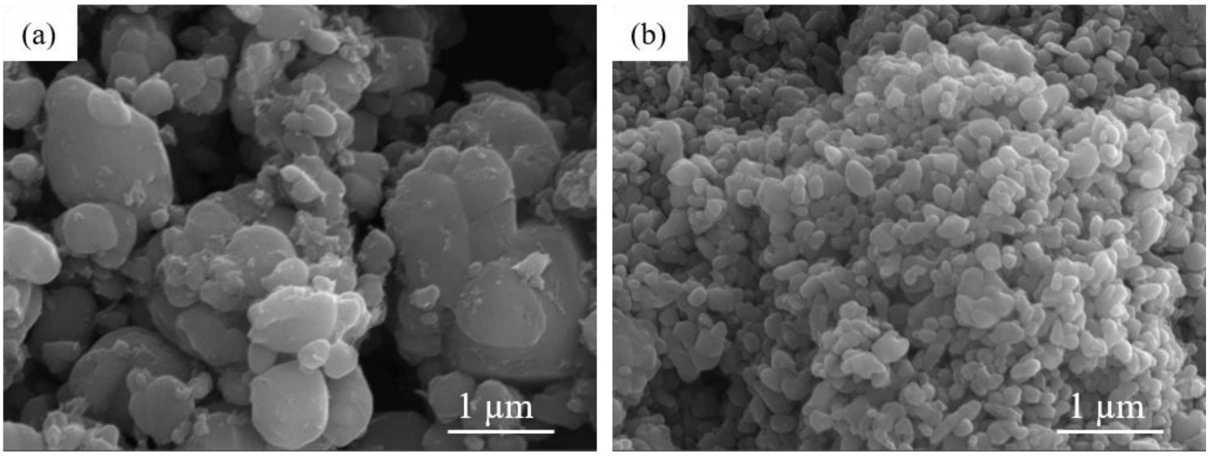

Figure 2.1. Representative examples of SEM images of (a) LFP-1 and (b) LFP-2 powders.

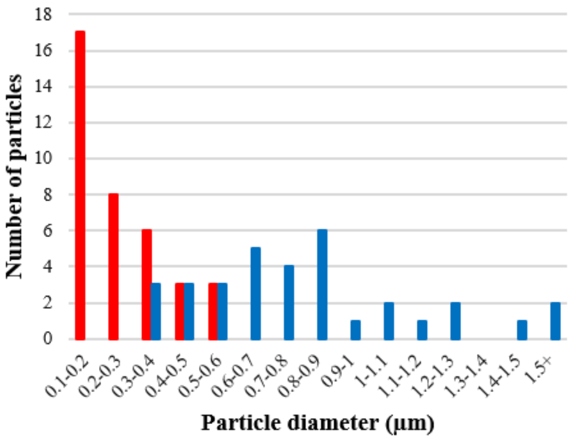

Figure 2.2. Particle size distribution of (▬) LFP-1 and (▬)LFP-2 powders observed *via* SEM.

The two powder samples were characterized by N_2 adsorption-desorption technique to determine their specific surface areas. Values calculated by the BET method, A_{BET}, were found to be 10.7 $m^2\ g^{-1}$ and 13.1 $m^2\ g^{-1}$ for LFP-1 and LFP-2, respectively. Those surfaces much certainly correspond to the external surface of LFP particles: indeed, the adsorption isotherms (Figure 2.3) correspond to a type II isotherm (non-porous or microporous material) following IUPAC's classification. Although those values do not seem to be very different, it has been noted in several studies that such a discrepancy is significant enough to impact the performances of Li-ion battery electrodes [11,16].

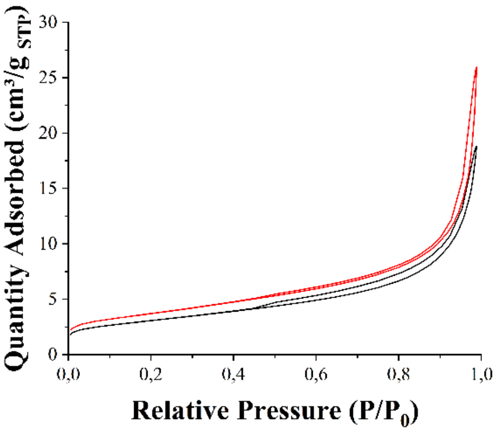

Figure 2.3. N_2 adsorption-desorption isotherms of the LFP-1 (▬) and LFP-2 (▬) powders.

2.3.2. Electrode performance

Galvanostatic charge and discharge was performed to determine the electrode capacity retention as a function of both the electrode thickness (*i.e.* the LFP loading) and cycling rate. The results are compared according to the LFP loading of the electrodes (Figure 2.4).

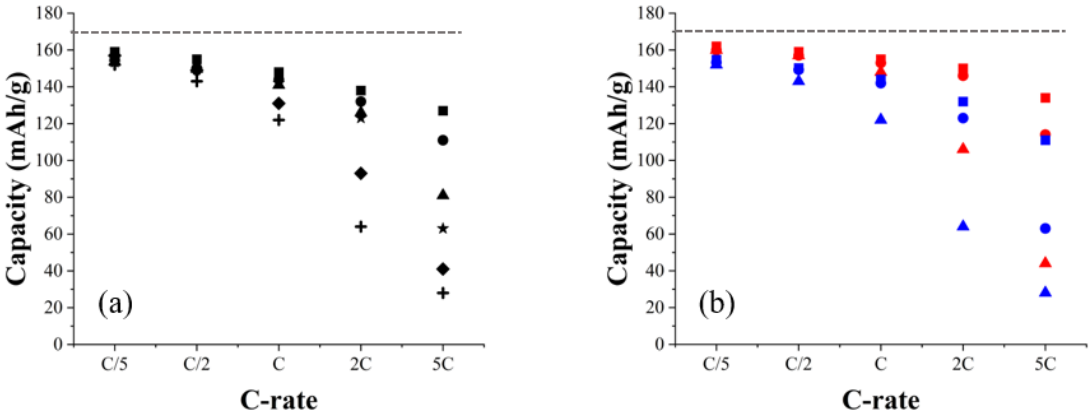

Figure 2.4. (a) Comparison of LFP-1 electrodes capacity *vs.* C-rate as a function of the LFP loading. (■) Below 2 mg, (●) 2-4 mg, (▲) 4-6 mg, (★) 6-8 mg, (♦) 8-10 mg, (+) 12 mg. (b) Comparison of (—) LFP-1 and (—) LFP-2e lectrode *vs.* C-rate as a function of the loading on the electrodes; (■) 3 mg, (●) 6 mg, (▲) 12 mg. The dashed line on both figures represents the theoretical capacity of LFP. Measurements performed at 25°C.

Table 2.1 shows all the data obtained from the experiments performed on electrodes of various loadings prepared with samples LFP-1~~.~~ Firstly, it was aimed at observing the direct effect of material loading on the capacity of the electrodes. In order to do that, a wide range of LFP-1 loadings starting from below 2 mg up to 12 mg has been selected and minimum of 2 cells used each time. Then, in order to observe how the particle size affects phenomena observed with LFP-1 electrodes of various loadings, a second set of charge-discharge tests was performed with LFP-2. For the sake of simplicity of comparison, electrodes prepared with loadings around 3 mg (±0.5 mg), 6 mg (±0.5 mg) and 12 mg (±0.5 mg) have been used. Those selected electrodes are noted as 3 mg, 6 mg and 12 mg LFP loading electrodes from now on for simpler notation. Results are gathered in Table 2.1. In that table, the values indicated are the average values obtained on at least 3 cells displaying LFP loadings within the mentioned range.

Table 2.1. Average capacities of the LFP-1 electrodes with various LFP loading at various cycling speed.

LFP loading[a] (mg)	**Capacity**[b] ($mAh\ g^{-1}$) **C/5**	**C/2**	**C**	**2C**	**5C**
< 2	159 (±2)	155 (±3)	148 (±2)	138 (±2)	127 (±5)
2-4	154 (±5)	150 (±2)	144 (±2)	132 (±1)	111 (±6)
4-6	154 (±2)	150 (±2)	141 (±2)	126 (±5)	81 (±8)
6-8	153 (±1)	149 (±4)	142 (±6)	123 (±10)	63 (±10)
8-10	158 (±2)	150 (±2)	134 (±3)	91 (±6)	41 (±9)
10-12	153 (±3)	144 (±1)	124 (±4)	71 (±7)	34 (±8)

[a] Range of loading for the LFP-1 electrodes considered. [b] Average capacity on at least 3 cells.

In the case of LFP-1 (Table 2.1.), for all electrodes, the capacity observed at a low C-rate (C/5) is very similar (153 – 159 mAh g^{-1}), even though it slightly decreases with increasing loading. At low loading (below 2 mg), the capacity also decreases from 159 to 127 mAh/g when increasing the C-rate from C/5 to 5C. Capacity decrease is observed for all electrode loadings. As expected, it gets more pronounced as the LFP loading increases and is especially dramatic for the high C-rates: at 5C and for the highest LFP loading, the difference is about 100 mAh/g compared to the lowest loading. The reasons of the decrease in capacity at high C rates can be explained by charge transport limitation within the electrode: as the electrode gets thicker, charge transport across the electrode gets more difficult, which explains the change in observed electrochemical properties.

As indicated above, LFP-2 half-cells were characterized in the same way to highlight the effect of the material particle size on the performance of the battery (Figure 2.4b). The obtained capacities are reported in Table 2.2, along with those of LFP-1 with similar LFP loadings. Firstly, one observes that the rate capability (*i.e.* electrode ability to accommodate different C-rates) of LFP-2 is significantly different from that of LFP-1. When comparing the 3 mg LFP coatings, the capacity at 5C drops to 67% of that observed at C/5 in the case of LFP-1. By comparison, LFP-2 can sustain up to 85% of its capacity when the cycling rate increases from

C/5 to 5C. Secondly, the drastic capacity difference at high C-rates observed between 12 mg LFP coatings from LFP-1 and LFP-2 shows that LFP-2 electrodes are much less affected by the increase of coating thickness. For LFP-1, the capacity retentions compared to C/5 (considered as 100%) are 94%, 80%, 42% and 18% for C rates of C/2, C, 2C, 5C, respectively. For LFP-2, those values increase to 98%, 92%, 66%, 27% for the same C rates.

The reason for these discrepancies between electrodes prepared either using LFP-1 or LFP-2 was further investigated by Electrochemical Impedance Spectroscopy (EIS). The high frequency region (10 kHz to 1 kHz) and mid frequency region (1 kHz to 1 Hz) of the Nyquist plot is used to quantify both the internal resistance (R_i) and the charge transfer resistance (R_{ct}). On the one hand, R_i corresponds to the internal resistance value of the bulk of the electrode, including current collector, active material, electrolyte and separator [17,18]. On the other hand, R_{ct} represents the charge transfer resistance at the electrode/electrolyte interface [17–19]. While the intersection between the EIS spectra and the X-axis corresponds to R_i, R_{ct} is obtained from the radius of the semi-circle in mid-frequency range [21,22].

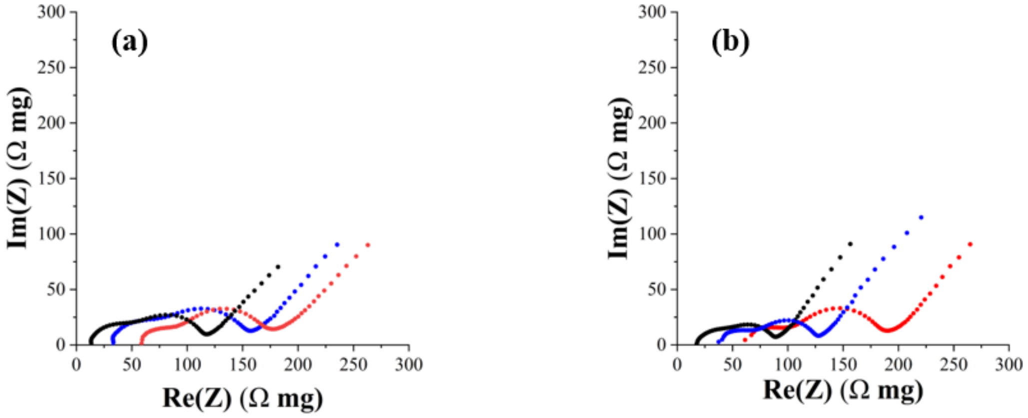

Figure 2.5. Electrochemical impedance spectra of (a) LFP-1 and (b) LFP-2 cells with LFP loading of (●) 3 mg, (●) 6 mg, (●) 12 mg. Measurements performed at 25°C.

Table 2.2. Average capacities of the LFP-1 and LFP-2 electrodes with various LFP loading at various cycling speed.

		Capacity[b] (mAh g^{-1})					Resistance	
	LFP loading[a] (mg)	**C/5**	**C/2**	**C**	**2C**	**5C**	R_i (Ω mg)	R_{ct} (Ω mg)
LFP-1	**3**	155 (±3)	150 (±2)	144 (±1)	131 (±1)	109 (±5)	15	93
	6	153 (±1)	151 (±2)	144 (±2)	127 (±6)	75 (±3)	32	96
	12	155 (±3)	143 (±6)	125 (±3)	77 (±10)	32 (±7)	56	98
LFP-2	**3**	162 (±2)	159 (±1)	158 (±2)	150(±2)	134 (±3)	17	53
	6	160 (±2)	156 (±2)	150 (±3)	138 (±9)	96 (±12)	40	70
	12	158 (±3)	153 (±6)	148 (±8)	106 (±2)	39 (±5)	61	88

[a] Range ± 0.5 mg

. [b] Average capacity on at least 2 cells

In the case of the LFP-1 electrodes, R_i is observed equal to 15 Ω mg, 32 Ω mg and 56 Ω mg for 3 mg, 6 mg and 12 mg electrodes, respectively (Figure 2.5a). In other words, an increase in the internal resistance of the electrode with increasing LFP loading is observed, as expected. When the electrode loading increases, charge transport within the coating becomes more difficult, which is reflected in the EIS spectra as a shift of the semi-circle intersection with the X-axis towards higher values. This phenomenon is also seen in other studies and explains the differences in the electrochemical performance such as capacity, rate capability, *etc.* (Figure 2.4a) [19,22]. Meanwhile, LFP-2 cells were also characterized using the same procedure. The same phenomenon is observed: with increasing LFP loading, R_i increases as well. R_i for 3 mg LFP coating is measured equal to 17 Ω mg while it increases to 40 Ω mg and 61 Ω mg for 6 mg and 12 mg LFP coating, respectively (Figure 2.5b). Therefore, an increase of the internal resistance can be the cause of capacity drop at high C-rates. However, R_ct does not change as drastically as R_i: values are determined as 93, 96 and 98 Ω mg for 3 mg, 6 mg and 12 mg LFP-1 loadings respectively. This observation was expected since the charge transfer resistance depends mainly on the active material particle size [23]. However, more apparent changes can be observed for LFP-2 since the charge transfer resistances are equal to 53, 77 and 88 Ω mg for 3 mg, 6 mg and 12 mg LFP-2 loadings, respectively. Therefore, one can argue that the advantage of having more surface area with lower particle size fades away with increased electrode loading. The increase of loading, and therefore the increase of coating thickness, possibly leads to a decrease of electrolyte accessibility to the LFP surface.

Following this, LFP-1 and LFP-2 cells are compared (Table 2.2); for both 3 mg and 12 mg LFP cells, one realizes that the R_i values do not differ much from each other. However, huge differences between R_ct values measured on 3 mg LFP electrodes can be observed: indeed, one obtains R_ct values of 93 Ω mg and 53 Ω mg for LFP-1 and LFP-2, respectively (Figure 2.6). This is expected as higher surface area offers more area for electrons to transfer, which reduces the charge transfer resistance [20,23]. Therefore, the better rate capability of the LFP-2 can be explained by reduced charge transfer resistance (Figure 2.5b). However, when observing the 12 mg LFP electrodes, the difference between charge transfer resistances of LFP-1 and LFP-2 electrodes is much less pronounced: indeed, one obtains 98 and 88 Ω mg for LFP-1 and LFP-

2, respectively. Although a difference is observed between the two different LFP powders, the impact of the particle size gets lower with increasing electrode loading.

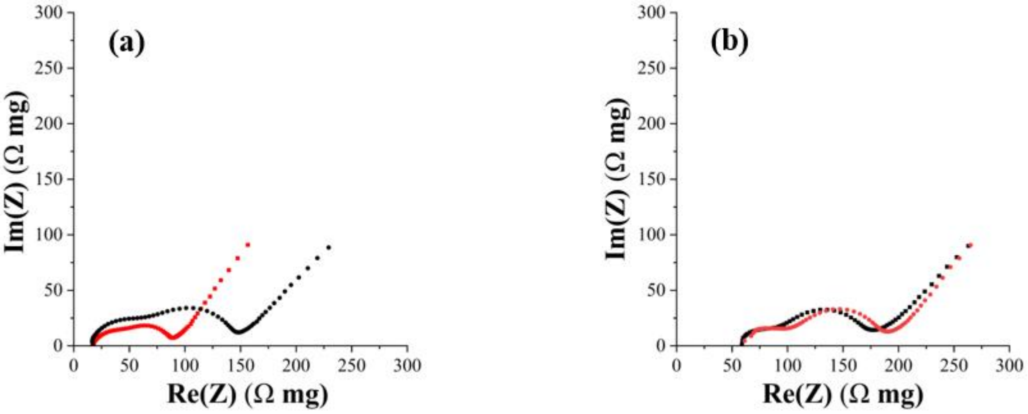

Figure 2.6. Electrochemical impedance spectra of (●) LFP-1 and (●)LFP-2 for (a) 3 mg LFP and (b) 12 mg LFP. Measurements performed at 25°C.

2.3.3. Stability

The electrode stability was studied by galvanostatic charge and discharge method. Electrodes were first submitted to 5 different C-rates (C/5, C/2, C, 2C, 5C) to obtain the results shown previously in Figure 2.4; then, they underwent 100 cycles at C and, finally, were tested again at the same 5 different C-rates. Results are now compared on the basis of capacity retention at the same C-rates before and after the series of 100 cycles at C. Also, the first 5 cycles of the 100-cycle sequence were compared with the last 5 cycles to quantify the impact of long-term cycling at stable C-rate on the electrode capacity. The stability study was conducted for both LFP-1 and LFP-2 samples and for different LFP loadings (3, 6 and 12 mg). Table 2.3. gathers the results obtained; those results are presented as the percentage of capacity retention between the two sequences. As an example, the column “C/5” displays the percentage of capacity remaining at C/5 between the two sequences at variable rate, before and after the series of 100 cycles at C. The last column, labelled as “C × 100”, corresponds to the capacity retention between the beginning (first 5 cycles) and end (last 5 cycles) of the sequence of 100 cycles at C.

The stability of the electrodes greatly depends on their loading. Whatever the LFP sample chosen, the electrodes with 3 mg of LFP seem to be the most stable at any C-rate while 12 mg LFP electrodes are observed to be the least stable ones. The deviation from that trend, observed at 2C and 5C for 6 mg and 12 mg electrodes, probably comes from the already low capacity values measured at high C-rates.

Table 2.3. Capacity retention values of LFP-1 and LFP-2 electrodes with various LFP loadings at different C-rates.

		Capacity retention (%)					
	LFP loading (mg)	**C/5**	**C/2**	**C**	**2C**	**5C**	**C × 100[b]**
LFP-1	**3**	95	95	94	92	73	96
	6	92	74	52	36	49	68
	12	84	48	28	42	67	32
LFP-2	**3**	95	94	94	90	81	97
	6	94	89	82	69	53	88
	12	87	56	33	37	68	36

[a] Range ± 0.5 mg.

[b] Comparison between the 5 first cycles and the last 5 cycles of the 100-cycle series at C.

Those results show that, although the stability is similar for LFP-1 and LFP-2 with thin electrode coatings, the difference gets quite significant in the case of thicker coatings, *i.e.* with 6 mg and 12 mg loadings. When results obtained with 6 mg LFP coatings are thoroughly examined, significant differences between LFP-1 and LFP-2 can be observed. At 2C especially, the capacity of LFP-1 after the series of 100 cycles at C falls to 36% of the value measured before. By contrast, after long-term cycling, sample LFP-2 can hold 69% of its initial capacity at the same cycling speed. For the 12 mg LFP coatings, a difference between LFP-1 and LFP-2 electrodes is still observed; however, that difference is not as significant as in the case of 6 mg LFP coatings as LFP-1 can hold 66% of its initial capacity while LFP-2 can hold 88%. Therefore, 12 mg LFP coatings in general are not so appropriate regarding stability aspect.

EIS was conducted at the end of the 100-cycle series, using the same procedure as earlier. Both R_i and R_{ct} generally increase with electrode aging (Table 2.4.) [24–26]. The R_i increase might be ascribed to phenomena such as microcracks appearance, gas evolution, corrosion of current collector, *etc.* and it is usually difficult to distinguish which one is the main reason without intensive *post mortem* analysis. Regarding R_{ct}, one can argue that the decrease of total electrode surface due to the decrease of loading results in decreasing the contact surface between the active material and the electrolyte. Therefore, more limited area for charge transfer would result as charge transfer resistance increase[19] . Although increase of resistances by aging of the electrodes has been reported many times in literature, the impact of particle size and electrode loading on this phenomenon is not inspected thoroughly. However, measurements could not be performed properly for 6 mg and 12 mg electrode groups as the cells were severely damaged by cycling and were not able to provide meaningful EIS signals. Therefore, the comparisons are made between 3 mg electrodes only, for both LFP-1 and LFP-2 samples. In the case of LFP-1, the EIS spectra before and after long-term cycling (Figure 2.7a) shows obvious differences. The intersection between the EIS curve and the X-axis shifts towards higher values; therefore, R_i increases. In the meantime, the radius of the semi-circle at medium frequencies, which corresponds to R_{ct}, gets bigger. Before long-term cycling, R_i is equal to 16 Ω mg while, after the 100-cycle sequence, it doubles to 32 Ω mg (Table 2.4). Increase of R_i by aging is observed in many studies and can be ascribed to losses of active materials by dissolution of active substances, lithium plating, *etc.* [14,25–27]. A significant increase of R_{ct} is also observed: from 42 to 65 Ω mg. Therefore, the decrease in capacity and rate capability from the beginning to the end of the testing sequence can be explained by the increase of both resistances.

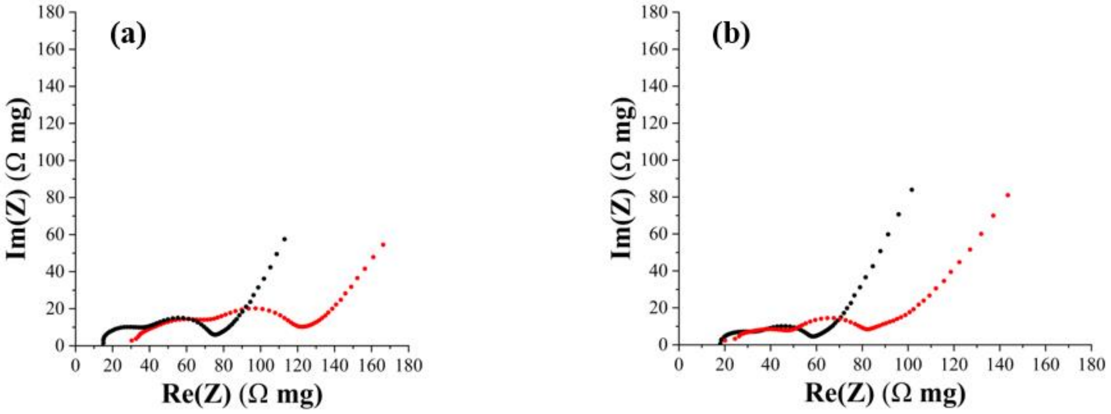

Figure 2.7. Electrochemical impedance spectra of (a) 3 mg LFP-1 electrodes and (b) 3 mg LFP-2 electrodes (●) before and (●) after cycling. Measurements performed at 25°C.

In the case of LFP-2, EIS measurements conducted on the 3 mg coating (Figure 2.7b) also show a shift of spectra to X-axis increasing values and an increase of the radius of the semi-circle in the mid-frequency range, but not to the same extent as LFP-1. The value of R_i slightly increases, from 18 to 20 Ω mg; however, the charge transfer resistance, R_{ct}, displays the highest increase by going up from 28 to 43 Ω mg. An increase in charge transfer resistance upon ageing was observed in other studies [24,28]. However, those works do not highlight the impact of the particle size effect aging phenomena while it is obvious in the present study. Although both 3 mg LFP-

1 and 3 mg LFP-2 electrodes show R_i and R_{ct} increases upon aging, the impact is much less pronounced for LFP-2. Small particles are thus much less prone to aging than large ones.

Table 2.4. Internal resistance and charge transfer resistance of LFP-1 and LFP-2 electrodes with 3 mg LFP loading before and after cycling.

	LFP-1		**LFP-2**	
	Before	**After**	**Before**	**After**
R_i (Ω mg)	16	32	18	20
R_{ct} (Ω mg)	42	65	28	43

2.4. Conclusion

$LiFePO_4$ (LFP) electrodes with two different LFP particle sizes were manufactured using a water-based process and xanthan gum as binder. The impact of both the particle size of the LFP and the electrode loading on the performance and stability of the electrodes was studied. Dramatic differences were observed between two different electrode groups made of LFP powders with different particle size distribution. Increased active material loading affects both electrode groups, especially at high C-rates, but differences are striking when the particle size distribution changes. While both electrode groups can hold their initial capacity at low C-rates (*e.g.* C/5), the results diverge for cycling rates of C and above. On the one hand, multiplying by 4 the LFP loading (from 3 to 12 mg on 1.88 cm^2 disc electrodes) has a significant impact on cells made of LFP with larger particles (0.84 µm); the capacity of those electrodes decreases almost by half at 2C. On the other hand, the capacity of the cells only decreases by about 30% at 2C when the particle size is decreased to 0.24 µm. The better rate capability of smaller LFP particles can be explained by the differences in charge transfer resistance, which is significantly lower when the particle size decrease. The difference of resistances results in performance modification, as observed in other works with classical electrodes manufactured using PVDF and NMP.

For the stability study, both groups were subjected to long-term cycling (100 cycles at C rate) and electrodes made of both LFP materials were affected by degradation. However, within the same group (*i.e.* same particle size), the capacity of cells with low loading (3 mg) was much less impacted than that of the cells with high loading (12 mg). While capacity retention was kept around 73% of its initial value for low loading, it can drop as low as 28% for high loading. In the meantime, cells prepared with smaller LFP particles gets much less degraded by long-term cycling. This phenomenon can be explained by Electrochemical Impedance Spectroscopy measurements. Indeed, one observes that both the interfacial and the charge transfer resistances, R_i and R_{ct}, increase for both LFP materials. However, the increase of R_i and R_{ct} upon cycling is less pronounced in the case of small LFP particles.

This work shows that, when considering manufacturing, one must take into account both the raw materials properties and the electrode design parameters such as its maximum thickness. Indeed, both are interrelated when considering the final electrode response to cycling. Depending on material and assembly costs and on the final battery use, one might adjust the electrode design to best fit the target. Finally, performance and phenomena observed were quite similar to those of Polyvinylidene fluoride (PVDF)/ N-Methyl-2-pyrrolidone (NMP)-based electrodes and xanthan gum is thus confirmed to be a viable alternative to this classical toxic binder/solvent duo for LFP electrodes.

2.5. REFERENCES

[1] N. Nitta, F. Wu, J.T. Lee, G. Yushin, Mater Today, **2015**, *18*, 252–264.

[2] J.R. Dahn, E.W. Fuller, M. Obrovac, U. von Sacken, Solid State Ion, **1994,** *69*, 265–270.

[3] A.K. Padhi, K.S. Nanjundaswamy, J.B. Goodenough, J Electrochem Soc, **1997**, *144*, 1188–1194.

[4] W.J. Zhang, , J Power Sources, **2011**, 196, 2962–2970.

[5] H. Buqa, M. Holzapfel, F. Krumeich, C. Veit, P. Novák, J Power Sources, **2006**, *161* 617–622.

[6] A.F. Léonard, N. Job, Mater Today Energy, **2019**, *12*, 168–178.

[7] L. Bläubaum, F. Röder, C. Nowak, H.S. Chan, A. Kwade, U. Krewer, ChemElectroChem, **2020**, *7* 4755–4766.

[8] A. Soloy, D. Flahaut, J. Allouche, D. Foix, G. Salvato Vallverdu, E. Suard, E. Dumont, L. Gal, F. Weill, L. Croguennec, *ACS Appl Energy Mater*, **2022**, *5*, 5617-5632.

[9] N. Sinha, M. Nookala, *J Indian Inst Sci*, **2009**, *89*, 381–392.

[10] R. Zhao, J. Liu, J. Gu, *Appl Energy*, **2015**, *139*, 220–229.

[11] E.R. Logan, A. Eldesoky, Y. Liu, M. Lei, X. Yang, H. Hebecker, A. Luscombe, M.B. Johnson, J.R. Dahn, *J Electrochem Soc*, **2022**, *169*, 050524.

[12] Y. Zhang, J.A. Alarco, J.Y. Nerkar, A.S. Best, G.A. Snook, P.C. Talbot, *J Electrochem Soc,* **2019**, *166*, A4128–A4135.

[13] Q. Zhao, Y. Zhang, Y. Meng, Y. Wang, J. Ou, Y. Guo, D. Xiao, *Nano Energy*, **2017**, *34*, 34408–420.

[14] Y.F. Pulido, C. Blanco, D. Anseán, M. González, J.C. Viera, V.M. García, in: 2017 IEEE International Conference on Environment and Electrical Engineering and 2017 IEEE Industrial and Commercial Power Systems Europe (EEEIC / I&CPS Europe), **2017**: pp. 1–5.

[15] J. Jiang, W. Shi, J. Zheng, P. Zuo, J. Xiao, X. Chen, W. Xu, J.-G., *J Electrochem Soc*, **2014**, *161*, A336–A341.

[16] W. Duan, M. Husain, Y. Li, N. ur R. Lashari, Y. Yang, C. Ma, Y. Zhao, X. Li, *RSC Adv* **2023**, *13*, 25327–25333.

[17] W. Choi, H.C. Shin, J.M. Kim, J.Y. Choi, W.S. Yoon, *J Electrochem Sci Technol*, **2020**, *11*, 1–13.

[18] L. Wen, L. Wang, Z. Guan, X. Liu, M. Wei, D. Jiang, S. Zhang, *Ionics*, **2022**, *28*, 3145–3153.

[19] K.Y. Song, G.S. Jang, J. Tao, J.H. Lee, S.K. Joo, *J Nanosci Nanotechnol*, **2017**, *18* 992–998.

[20] M.D. Murbach, V.W. Hu, D.T. Schwartz, *J Electrochem Soc*, **2018**, *165*, A2758.

[21] J. Chidiac, L. Timperman, M. Anouti, *J Taiwan Inst Chem Eng*, **2021**, *126*, 88–101.

[22] H. Zheng, J. Li, X. Song, G. Liu, V.S. Battaglia, *Electrochim Acta*, **2012**, *71*, 258–265.

[23] K. Ariyoshi, M. Tanimoto, Y. Yamada, *Electrochim Acta*, **2020**, *364*, 137292.

[24] E. Teliz, C.F. Zinola, V. Díaz, *Electrochim Acta*, **2022**, 426, 140801.

[25] J.M. Reniers, G. Mulder, D.A. Howey, *J Electrochem Soc*, **2019**, *166*, A3189–A3200.

[26] Z. Zhou, Y. Liu, M. You, R. Xiong, X. Zhou, *Green Energy Intell. Transp.*, **2022**, *1*, 100008.

[27] M. Ceraolo, G. Lutzemberger, D. Poli, C. Scarpelli, *Energies*, **2021**, 14, 4813.

[28] R. Scipioni, P.S. Jørgensen, D.I. Stroe, R. Younesi, S.B. Simonsen, P. Norby, J. Hjelm, S.H. Jensen, *Electrochim Acta*, **2018**, *284* 454–468.

Chapter 3

CVD-coated carbon xerogels for negative electrodes of Na-ion batteries

Abstract

Carbon xerogels (CX) with varying nodule sizes, from 50 nm to 2 µm, are synthesized via polycondensation of resorcinol with formaldehyde in water, followed by pyrolysis at 800 ℃ to investigate their electrochemical properties as negative electrode material in Na-ion batteries. All samples exhibit high specific surface areas (~600 m² g^{-1} by N_2 physisorption) due to the presence of a large volume of micropores. Chemical Vapor Deposition (CVD) is used to fill or mask the micropores to mitigate the typical detrimental effects of high surface areas on the Initial Coulombic Efficiency (ICE). Larger nodules correlate with increased Na^+ storage capacity and ICE (up to 80 %), independently of the measured specific surface area. Notably, the sample displaying 2 µm nodule size reach a reversible capacity of 248 mAh g^{-1} and 80 % ICE at C/20 cycling rate. CVD-deposited carbon layers show a graphitic-like structure and completely block the micropores, reducing the specific surface area and improving both reversible capacity and ICE up to 298 mAh g^{-1} and 84 %, respectively. Such materials composed of two different carbons show great promise in the advancement of carbon-based materials for Na-ion batteries.

3.1. Introduction

The rechargeable battery market is expected to grow dramatically over the next few years, given the demand for electrical energy storage in vehicles, stationary applications and small electronics [1]. This huge deployment, mostly driven by lithium-ion batteries (LIBs), requires the development of new solutions, both in terms of concepts, materials and manufacturing processes, to avoid shortages of key components and ensure that batteries do not become yet another environmental issue [2][3]. In particular, the electrodes must be designed so as to limit the amount of critical materials (i.e., Li, metals such as Cu or Co, and even graphite according to some reports) [4] and non-recyclable compounds such as fluorinated binders (e.g. PolyVinyliDene Fluoride, PVDF) [5]. Finally, the electrode components should ideally be compatible with water-based manufacturing processes, in order to replacing methods using organic solvents (e.g., N-methyl-pyrrolidone, NMP) [5].

Switching from Li-ion batteries (LIBs) to Na-ion batteries (NIBs) would make it possible to get rid not only of Li, which is becoming more and more controversial in terms of availability and extraction impact, but also of Co and Cu and, if properly manufactured, of PVDF and NMP. Indeed, Na is much more abundant in the earth’s crust and can be more easily extracted than Li. In addition, since Na does not alloy with Al at low voltage, Cu used for the negative electrodes in LIBs can be replaced by Al and, thus, Al can be used as a current collector for both electrodes. This contributes to a reduction in the price of the final battery [6]. All these reasons make NIBs very good alternative candidates to LIBs from an environmental and cost point of view. However, the energy density of NIBs remains low compared with LIBs (i.e., around 140 Wh kg^{-1} for NIBs against up to 250 Wh kg^{-1} for LIBs) [7]; further research into battery components is thus required to improve energy density.

Carbonaceous materials, mainly graphite, are widely used as negative electrode components in LIBs. However, graphite is unsuitable for NIBs due to poor Na^+ intercalation. Indeed, the electrochemical capacity is limited to ~35 mAh g^{-1}, corresponding to an NaC_{64} stoichiometry, i.e., a stage-8 graphite intercalation compound only [8][9]. For comparison, 370 mAh g^{-1} is reached in the case of Li^+ insertion into graphite (LiC_6). [10] Conversely, non-graphitizable carbons (i.e., hard carbons) are good candidates due to their amorphous structure and large interlayer spacing. Such materials feature randomly oriented turbostratic domains, leading to a large volume of open and closed micropores (i.e., < 2 nm in size) [11][12], suitable for Na storage. Hard carbons can be obtained by pyrolysis of various precursors, mainly oxygen-rich molecules and polymers, which can be bio-based or not [13]–[15]. When used as materials for NIB negative electrodes, such materials can show reversible capacities of up to 320 mAh g^{-1}. [16] However, their coulombic efficiency at 1st cycle (i.e., the Initial Coulombic Efficiency, ICE) is low due to electrolyte decomposition on their usually highly developed surface area [17][18]. ICE is indeed often directly linked to the carbon specific surface area in the literature: for example, Bommier et al. [19] used hard carbons with total specific surface areas ranging from 25 m^2 g^{-1} to 266 m^2 g^{-1} and observed 80 % and 65 % ICE, respectively. In addition, these materials suffer from poor insertion kinetics: high capacities, up to 300 mAh g^{-1}, have been obtained from pyrolyzed glucose [8][20][21], but only at very low cycling rate (C/80, meaning 80 h to charge or discharge the cell). Finally, their insertion potential is a bit too close to that of Na metal, which might raise safety issues.

Although discussions are still ongoing about Na storage mechanisms in hard carbons, most studies highlight the importance of the pore-filling mechanism by Na^+ ions. In the early 2000s, while studying the galvanostatic profiles of hard carbons (i.e., voltage vs. capacity curves), Stevens and Dahn associated for the first time the low-voltage plateau region (i.e., potential lower than 0.1 V vs. Na^+/Na) with the mechanism of carbon micropore filling by Na^+ ions [8][20][21]. Subsequently, numerous studies have reported similar conclusions that micropore filling is an important storage mechanism in hard carbons. For example, Komaba et al. [22], Stratford et al. [23] or Titirici et al. [24] have all associated the low-voltage plateau with micropore filling. It therefore seems that controlling the microporosity of hard carbons suitable for Na^+ ion storage could be a way of tailoring their electrochemical response. However, it must be noted that increasing capacity and increasing ICE seem to evolve in opposite directions when dealing with microporosity modification. Indeed, as mentioned above, while increasing microporosity can improve capacity, the ICE can in turn drop if the electrolyte can access these micropores. Thus, ideally, and to tackle both issues, the targeted hard carbon should combine (i) a low specific surface area, (ii) a large volume of micropores that the electrolyte itself cannot access, and (iii) a primary particle size compatible with electrode manufacturing and sufficient contact with the electrolyte. In that respect, several methods such as heteroatom doping, surface engineering, pore engineering and so forth have been envisaged in the literature [25].

For specific surface area and pore engineering, coating techniques have been used to tune the carbon surface properties. For example, Lu et al. [26] coated hard carbons with Al_2O_3 films by atomic layer deposition to develop an artificial SEI layer, leading to both lower BET surface area and pore volume; this strategy improved both the capacity, from 260 mAh g^{-1} to 355 mAh

g^{-1}, and the ICE from 67% to 75% (at 20 mA g^{-1}). Additionally, Li et al. [27] used a Chemical Vapor Deposition (CVD) method to modify the surface of sieving carbons; this led to high capacities (up to 390 mAh g^{-1}) with around 80% ICE (at 50 mA g^{-1}); it was claimed that CVD was able to regulate the pore entrance diameter, improving the screening out of solvated sodium ions and enabling the formation of sodium clusters. Therefore, surface and pore engineering of carbons via coatings seems to be an interesting way to improve the capacity and ICE of hard carbons.

Carbon xerogels (CXs) are hard carbons obtained by evaporative drying and pyrolysis of organic gels, e.g., resorcinol-formaldehyde aqueous gels [28]. They are composed of sphere-like microporous nodules, the size of which can be tailored from a few nm to a few µm by modifying the gel composition [29]. Consequently, the meso/macropore texture can also be tailored from a few nm to a few µm. Such carbons have previously been used as negative electrode materials for NIBs [18], but the measured ICE was unsurprisingly low (15 %) given their high specific surface area (~600 m² g^{-1}), mainly related to open micropores, while the obtained reversible capacity was reasonably high (~200 mAh g^{-1}). Regarding capacity, it must be noted that the CXs studied so far were mostly made of mesoporous samples, i.e., materials composed of fairly small carbon nodules (~50 nm); to our knowledge, materials made of large carbon nodules (i.e., µm-sized) have not yet been used. It thus seems interesting to investigate the impact of nodule size on electrode performance, especially if large nodules (in the µm range) are used. However, to avoid low ICE, it is also necessary to decrease the surface area accessible to the electrolyte while preserving or even developing closed micropores.

One possible way to reach that goal is to deposit a secondary carbon layer on the surface of CXs nodules by Chemical Vapor Deposition (CVD). In a previous work, Piedboeuf et al. [30] used both physical activation (with CO_2) and CVD (by ethylene cracking) to either increase or decrease the specific surface area of CXs. The initial objective was to analyze the impact of the micropore texture of CXs on their behavior as LIB negative electrode, especially the accessibility of the electrolyte to the carbon surface. Firstly, it was shown that the pore texture of the carbon remained intact in the electrode when using a water-based electrode processing, while the microporosity of the materials was partially blocked when applying a conventional PVDF/NMP processing. As a result, the water-based process developed, using xanthan gum as a binder, is perfectly suitable for studies dealing with the impact of the active material surface area on electrochemical properties. Secondly, it was found that activation indeed increased the accessibility of carbon to the electrolyte, but also that Li^+ ions remained trapped in the microporosity unless delithiation was performed up to 3 V vs. Li^+/Li, which is totally impractical for real-world applications. Conversely, CVD led to the complete blocking of the micropores, leaving a surface area of about 100 $m^2 g^{-1}$ corresponding roughly to the external nodule surface. This technique could thus be used to cover the surface of CX nodules in order to decrease the electrolyte/carbon surface contact, and thus increase the ICE for NIBs.

The objectives of this study are therefore (i) to determine the impact of the nodule size of carbon xerogels on their behavior as negative electrodes for NIBs, and (ii) to determine whether the ICE of such materials can be improved by blocking their micropore surface from the electrolyte. To this end, several CXs with various nodule sizes (and thus various meso/macropore textures) were synthesized over a very wide range, especially targeting large nodule sizes (up to a few µm). The same materials were then CVD-coated with carbon to mask the micropores. All the samples were finally processed as electrodes using a water-based technique and xanthan gum as a binder, a method that preserves the pore texture of the powder when processed as an electrode. [31] The obtained electrodes were assembled in half-cell configuration and characterized by electrochemical techniques. The impacts of the nodule size and carbon coating on (i) galvanostatic profile, (ii) ICE, and (iii) rate capability were then determined.

3.2. Experimental

3.2.1. Carbon xerogel synthesis

Carbon xerogels (CXs) were prepared following a procedure described in a previous study [28]. First, a 35 wt.% aqueous solution of resorcinol (R) (Merck) was prepared in a sealable glass flask. Then, sodium carbonate (C) (Merck) was added. The *R/C* ratio was used to regulate the nodule size (and thus the meso/macropore size) of the final carbon materials. For this study, four different *R/C* ratios were used: 450 (CX-450), 1500 (CX-1500), 2500 (CX-2500) and infinite (i.e., without sodium carbonate). The latter sample is named low-pH CX (CX-LPH) hereafter. A 37 wt.% solution of formaldehyde was then added to the mixture with a resorcinol/formaldehyde molar ratio of 0.5. The dilution ratio *D*, i.e., the water/reactants molar ratio, was equal to 5.7. The obtained mixture was then magnetically stirred for 1 h. After mixing, the sealed glass flask was put in an oven, at 85 °C and for 72 h, for gelation and aging. Finally, to dry the gel, the container was opened and put in a vacuum oven at 60 ºC. The pressure was progressively decreased down to 12 Pa, and the samples were left to dry overnight.

At the end of drying, organic xerogel monoliths were retrieved. To obtain a narrow final particle size distribution, the materials were ground prior to pyrolysis, following a procedure from a previous work [31]. After coarse milling by hand in a mortar, the materials were ground to powders using a Fritsch planetary mill (Mono Mill P6). Samples were ground at 400 rpm for 24 cycles of 1 min each, followed by 15 s of rest. Finally, to obtain carbon xerogels, the powders underwent pyrolysis at 800 ºC under N_2 with the following procedure. The temperature was increased to (1) 150 ºC at 1.7 ºC min^{-1} and held for 15 min; (2) from 150 ºC to 400 ºC at 5 ºC min^{-1} and held for 60 min; and (3) from 400 ºC to 800 ºC at 5 ºC min^{-1} and held for 120 min. Finally, the oven was let to cool down to room temperature overnight.

3.2.2. Carbon coating by CVD

Chemical Vapor Deposition (CVD) was performed in a stainless-steel tubular oven, following the process described in a previous study [30]. First, the temperature of the oven was set at 685 ºC under inert atmosphere (N_2, flow rate: 0.025 mol min^{-1}). Once the oven had reached 685 ºC, the CX powders were introduced into the oven in a quartz boat while using a reverse flow system to maintain the protective inert atmosphere inside the oven. The reactive mixture was then introduced into the system (total flow rate: 0.082 mol min^{-1}), consisting of 80 % ethylene (Air Liquide N25, 0.066 mol min^{-1}) and 20 % nitrogen (Air Liquide Alphagaz 1, 0.016 mol min^{-1}). The CVD treatment time was set at 30 min, and the temperature was maintained at 685 °C. The atmosphere was then changed to 100 % nitrogen (flow rate: 0.025 mol min^{-1}). Finally, after complete purging, the oven temperature was increased to 900 ºC and held for 2 h. Then, the oven was cooled down under nitrogen atmosphere, and the resulting powders were collected. To distinguish uncoated from coated materials, the samples are named as follows: "CX-R/C" for non-coated samples and "CX-R/C-C" for CVD-coated samples.

3.2.3. Physicochemical characterization of the carbon materials

The pore texture of CX powders was assessed by nitrogen adsorption-desorption measurements. The isotherms were collected at -196 °C using a Micromeritics ASAP 2420 analyzer. Prior to the measurements, the samples were degassed under high vacuum (2×10^{-4} Pa) at room temperature for 5 h and at 270 °C for 2 h. The specific area, A_{BET}, was calculated using the Brunauer-Emmett-Teller (BET) equation, with adsorption data taken over the relative pressure range of 0.05 to 0.25 for CVD-coated samples and 0.01 to 0.1 for non-coated samples, in order to fulfill the Rouquerol criterion. The micropore volume, V_{μ}, was calculated using the Dubinin-Radushkevich equation. For samples CX-450 and CX-450-C, the external surface area, S_{ext}, corresponding to the nodule surface area (internal micropores excluded), was calculated using the t-plot method. However, this method is unsuitable for the other samples, given their very low nodule external area.

To assess in more detail the microporosity of the materials, hydrogen adsorption-desorption measurements were also carried out. The samples were degassed under high vacuum at 180 °C for 24 h before acquisition of the isotherms at -196 °C using a Micromeritics 3Flex analyzer. The 2D non-local density functional theory for heterogeneous surface (2D-NLDFT-HS) was applied simultaneously to the nitrogen and hydrogen adsorption isotherms using the SAIEUS software from Micromeritics to obtain the pore size distributions (PSDs). Textural properties such as the specific surface area (S_{DFT}), the total pore volume ($V_{\mathrm{T,DFT}}$), and the ultramicro-, supermicro- and mesopore volume ($V_{\mathrm{u\mu,DFT}}$, $V_{\mathrm{s\mu,DFT}}$, and $V_{\mathrm{meso,DFT}}$, respectively) were calculated from the obtained PSDs.

Although it provides information about pore texture, the nitrogen adsorption technique is not suitable for its exhaustive determination, since carbon xerogels are simultaneously micro- and meso/macroporous materials. To assess their meso/macropore texture, mercury porosimetry was performed with a Quantachrome Poremaster 60 in a pressure range from 0.01 to 400 MPa. The analysis was carried out for coated and uncoated carbon xerogels in powder form. Analysis of the mercury intrusion data obtained enables pore volume, V_{Hg}, and PSD to be determined for pores with diameters larger than 3.8 nm. The PSD was calculated using the Washburn equation, valid for mercury intrusion without crushing; the values considered for the equation parameters were (i) an average value of liquid/solid contact angle of 140° and (ii) a mercury surface tension of 0.485 N m^{-1}.

The skeletal density of the samples, ρ_{s}, was measured by He pycnometry using a Quantachrome Ultrapycnometer 1000e, set at a temperature of 20 °C.

SEM was used to observe the carbon morphology and determine the size of the carbon nodules, D_n. Images were obtained using a Tescan CLARA FEG-SEM at 15 kV under high-vacuum conditions. The samples were sputter-coated with gold and mounted with carbon adhesive prior to observation. Average nodule sizes were calculated based on a minimum of 30 measurements per sample. To visualize the microstructure of the CVD-deposited carbon layer, the CX-LPH and CX-LPH-C samples were observed by transmission electron microscopy (TEM) using a FEI Tecnai F20-S-TWIN microscope and a JEOL JEM-ARM 200F Cold FEG equipped with a spherical aberration probe corrector, both equipment were operated with an acceleration voltage of 200 kV. Samples were prepared by suspending the powder in ethanol. Then, one or two drops of the suspension were deposited on a copper grid with a holey carbon film. High-resolution imaging was performed by controlling the electron dose in order to avoid electron beam-induced artefacts. The d-spacing between graphene layers in the different samples was obtained by Fast Fourier Transform on the HR-TEM images.

X-ray diffraction was used to assess the crystallinity of the materials before and after CVD coating. Measurements were performed in Bragg-Brentano configuration for diffraction angles 2θ between 10° and 80° and a step size of 0.021° with a Bruker AXS D8 Advance diffractometer using a copper X-ray source ($\lambda_{K\alpha}$ = 0.15418 nm). A shallow sample holder with a zero-background single-crystal Si plate was used to minimize sample transparency. The XRD patterns were analyzed using the model developed by Mallet-Ladeira [43]. The average lateral size of the graphene domains (L_a) and the average stacking thickness of the graphene layers (L_c) were determined using Scherrer's equation from reflections (10l) and (002), respectively.

Elemental analysis (EA) was performed in a Vario EL Cube analyzer (Elementar) to measure the bulk C, H, N, S and O contents. Prior to measurements, the samples were dried overnight at 105 °C to remove moisture, and then a small amount of material (~2 mg) was placed in the equipment to be burned in a furnace from which the gas is separated using trapping and chromatographic columns. A thermal conductivity detector quantifies the gases, from which carbon, hydrogen and nitrogen contents can be calculated, with the exception of sulphur being measured with a specific infrared detector. The oxygen content was measured separately in another column using a similar procedure.

3.2.4. Electrode manufacturing

The electrode manufacturing procedure chosen [30] is known to preserve the pore texture of the carbon material in the electrode configuration, meaning that the carbon specific surface areas measured on both the powder and the final electrode are the same. Additionally, this method avoids the use of toxic solvents and fluorinated polymers as binders. The ink for spray coating was prepared in MilliQ water with 12 wt.% solids, including carbon xerogels and xanthan gum (Sigma-Aldrich) as a binder, in a weight ratio of 92:8. The mixture was stirred with a magnetic stirrer at room temperature for 3 h. The prepared ink was sprayed onto pre-weighed stainless-steel discs current collectors (Type 304, 15.5 mm, MTI corp.) and dried overnight at 60 °C. The obtained electrodes were then stored in a glove box under Ar. The mass loading of active material ranged from 1.5 mg cm^{-2} to 2 mg cm^{-2} for all samples. It should be noted that the electrodes had to be transferred from one laboratory to another for electrochemical characterization: the electrodes manufactured in the NCE laboratory were thus put back into air, and sent in sealed flasks to the LRCS laboratory. Therefore, before half-cell assembly, and to ensure that all adsorbed water was removed, the electrodes were placed between two glass slides and dried at 110 °C under vacuum in a Büchi glass oven for 12 h.

3.2.5. Electrochemical characterization

Electrochemical studies were carried out in two-electrode coin-cells (CR2032) using the chosen carbon xerogel as the working electrode, sodium metal (Sigma-Aldrich) as counter and reference electrode, a glass fiber separator (Whatman, 1 mm-thick), and a 1 M solution of sodium hexafluorophosphate ($NaPF_6$, Stella Chemifa) in a mixture of ethylene carbonate and dimethyl carbonate (EC/DMC, Solvionic, 1:1 mass ratio) as the electrolyte (referred to as NP30). The coin cells were assembled in a glovebox under Ar atmosphere (O_2 and H_2O concentration < 1 ppm).

Two series of tests were performed in order to characterize the electrochemical properties of the materials. The first was aimed at evaluating the materials' performance at low C-rates. Therefore, the cells were cycled between 0 V and 2.5 V (vs. Na^+/Na) for 5 cycles at C/20 (which corresponds to 18.6 mA g_{carbon}^{-1}, calculated considering the hypothetical formation of a NaC_6 phase during sodiation with a theoretical specific capacity of 372 mAh g^{-1}), 5 cycles at C/10, 5 cycles at C/5 and then for a further 100 cycles at C/20. A rate of C/n thus corresponds to the insertion of one Na^+ ion for every 6 carbon atoms, in n hours. The second series of tests was designed to evaluate the response of the carbon materials to high C-rates. The first charge/discharge cycles were carried out at a low C-rate (i.e., C/20) to enable the formation of SEI, and then the C-rate was gradually increased to 5C. Thus, the cells were cycled between 0 V and 2.5 V (vs. Na^+/Na) for 5 cycles at C/20, C/10, C/5, C/2, C, 2C and 5C, and then for a further 100 cycles at C/20.

3.3. Results and discussion

3.3.1. Physicochemical properties of carbon xerogels

Samples were weighed before and after the CVD procedure to determine the mass increase, which corresponded to 30 %, 19 %, 15 % and 4 % for the samples CX-450, CX-1500, CX-2500 and CX-LPH, respectively. The powders were observed by Scanning Electron Microscopy (SEM) to determine their morphology and nodule size. Figures 3.1a to 3.1h show representative SEM images of the four carbon xerogels before and after CVD coating. In all samples, a network of well-connected nodules can be observed, and the size of the nodules, D_n, increases as the *R/C* ratio increases, as expected from data published in the literature [28]. D_n rises from about 50 nm for CX-450 to approximately 1.0 µm, 1.3 µm and 2.0 µm for CX-1500, CX-2500 and CX-LPH, respectively (Table 3.1). After CVD coating, no significant difference in nodule size is observed. However, some carbon deposits can be seen on samples CX-450-C, CX-1500-C and CX-2500-C (Figure 3.2a, Figures 3.1d and 3.1f), i.e., the three samples with the highest mass uptake during CVD coating. These deposits seem to consist of small carbon aggregates of various shapes.

Table 3.1. Pore texture and morphological parameters determined for the four pristine carbon xerogels and their CVD-coated counterparts.

Morphological parameters					**Textural parameters**						
					Determined by N_2 adsorption at 77 K			Determined by N_2 and H_2 adsorption at 77 K			
Sample	D_n[a] (μm)	ρ_s[b] (g cm^{-3})	d_p[c] (μm)	$S_\mathrm{n,ext}$[d] (m^2 g^{-1})	A_BET[e] (m^2 g^{-1})	S_ext[e] (m^2 g^{-1})	V_μ[e] (cm^3 g^{-1})	S_DFT[f] (m^2 g^{-1})	$V_\mathrm{u\mu,DFT}$[f] (cm^3 g^{-1})	$V_\mathrm{s\mu,DFT}$[f] (cm^3 g^{-1})	$V_\mathrm{T,DFT}$[f] (cm^3 g^{-1})
CX-450	0.05	1.93	0.053[f]	91[g]	670	181	0.24	1061	0.16	0.10	0.77
CX-450-C	0.05	1.63			135	118	0.05	145	0.02	0.01	0.44
CX-1500	1.0	1.85	1.4[g]	5[g]	651	-[h]	0.25	1117	0.18	0.10	0.28
CX-1500-C	1.0	1.98			36	-[h]	0.01	191	0.04	0.02	0.09
CX-2500	1.3	1.95	2.6[g]	3[g]	646	-[h]	0.25	1126	0.18	0.11	0.28
CX-2500-C	1.3	2.04			3	-[h]	<0.01	66	0.00	0.02	0.05
CX-LPH	2.0	2.08	3.9[g]	2[g]	643	-[h]	0.25	1113	0.16	0.12	0.28
CX-LPH-C	2.0	1.88			2	-[h]	<0.01	69	0.00	0.02	0.05

[a] D_n: average nodule size calculated from SEM images.

[b] ρ_S: skeletal density measured by He pycnometry.

[c] d_p: pore diameters measured by Hg porosimetry.

[d] $S_\mathrm{n,ext}$: external surface area calculated from geometric considerations.

[e] A_BET and S_ext: BET and external surface areas, respectively, and V_μ: micropore volume, calculated from nitrogen adsorption-desorption isotherms at 77 K.

[f] S_DFT, $V_\mathrm{u\mu,DFT}$, $V_\mathrm{s\mu,DFT}$, and $V_\mathrm{T,DFT}$: specific surface area, ultramicropore, supermicropore, and total pore volume calculated from the PSD obtained from nitrogen and hydrogen adsorption isotherms at 77 K.

[g] No significant difference between pristine and CVD-coated materials.

[h] Not measurable.

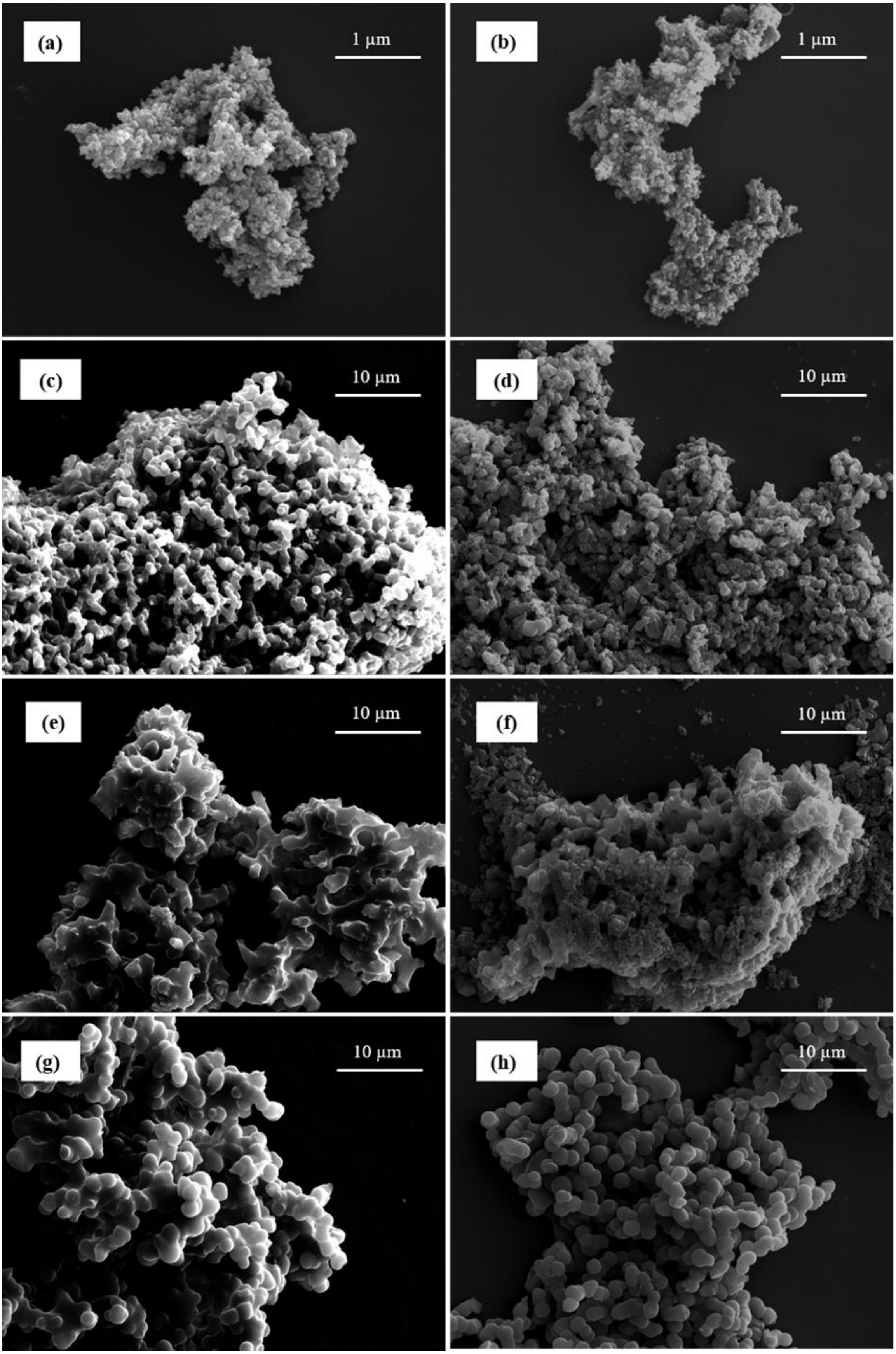

Figure 3.5. SEM images of (a) CX-450, (b) CX-450-C, (c) CX-1500, (d) CX-1500-C, (e) CX-2500, (f) CX-2500-C (g) CX-LPH, (h) CX-LPH-C.

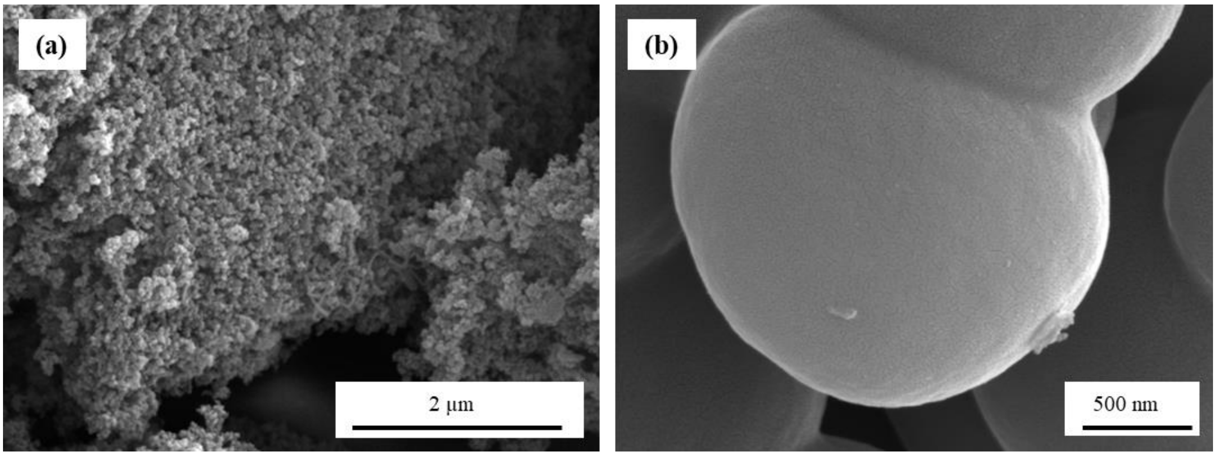

Figure 3.6. SEM images of (a) CX-450-C and (b) CX-LPH-C at higher magnification.

The XRD patterns of the samples are shown in Figure 3.3. Note that, given the very small differences observed between CX-450 and CX-LPH or between CX-450-C and CX-LPH-C, the curves obtained with the samples in the middle of the series (CX-1500, CX-2500, CX-1500-C and CX-1500-C), which are quite similar to their pristine or coated counterparts, have been omitted for clarity. Diffractograms of CX-450, CX-450-C, CX-LPH and CX-LPH-C (Figure 3.3) display a first broad band at around $2\theta = 23°$ (002) and a second broad band around $2\theta = 43°$ (10l), both typical of highly disordered carbon. The (002) band is more intense for CX-450-C and CX-LPH-C than for their uncoated counterparts, which could be due to some coating contribution. The complete structural parameters of coated and uncoated samples are shown in Table 3.2. Small differences are observed between samples. Indeed, a slightly larger coherence length L_a is observed for CX-LPH-C (3.82 nm vs. 3.38 nm for CX-LPH) and CX-450-C (4.54 nm vs. 3.89 nm for CX-450). One might think that these differences are due to the processing temperature of 900 °C used for the CVD samples. To check this hypothesis, the organic gel prepared at low pH was also pyrolyzed at 900 °C. Figure S3.1. shows the XRD patterns of CX-LPH pyrolyzed at either 800 °C or 900 °C, as well as that of CX-LPH-C (treated at 900 °C). The patterns of carbon gels pyrolyzed at either 800 °C or 900 °C are very similar. The structural parameters obtained from these three XRD patterns are presented in Table S3.1. The coherence length L_a obtained for CX-LPH pyrolyzed at 800 °C and 900 °C is very close (3.38 nm and 3.34 nm, respectively), while it is higher for CX-LPH-C (3.82 nm). The increase of L_a value is therefore probably due to pyrolytic carbon deposition. With regard to L_c, the values are very similar for all samples: around 1.0 nm (Tables 3.2 and S3.1.). A slight decrease in the graphene interlayer distance, $d_{(002)}$, is observed for CX-LPH-C (0.392 nm vs. 0.405 nm for CX-LPH) and CX-450-C (0.393 nm vs. 0.407 nm for CX-450) (Table 3.2).

Table 3.2. Structural parameters of CX-450, CX-450-C, CX-LPH and CX-LPH-C samples.

			CX-450	**CX-450-C**	**CX-LPH**	**CX-LPH-C**
XRD	L_a	(nm)	3.89 ± 0.04	4.54 ± 0.02	3.38 ± 0.01	3.82 ± 0.01
	L_c	(nm)	1.25 ± 0.30	1.12 ± 0.16	1.09 ± 0.19	0.99 ± 0.11
	$d_{(002)}$	(nm)	0.407 ± 0.001	0.393 ± 0.001	0.405 ± 0.001	0.392 ± 0.001
TEM	$d_{(002)}$	(nm)			0.409 ± 0.040	0.392 ± 0.037

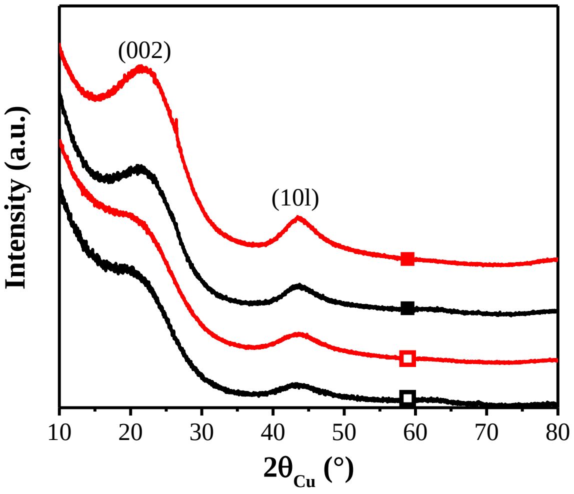

Figure 3.3. X-ray diffractograms of CX-450 (□), CX-450-C (■) CX-LPH (□) and CX-LPH-C (■).

To understand better the organization of the carbon layers, CX-LPH and CX-LPH-C were observed by HR-TEM (Figure 3.4). CX-LPH exhibits a highly disordered structure (Figures 3.4a and 3.4b) while its coated counterpart shows a much more ordered and graphitic structure at some places (Figures 4c and 4d), identified as being close to the nodule surface (Figures 3.4e and 3.4f). Numerous alignments of graphene-like sheets a few nm long can be observed after CVD (Figure 4d, orange boxes). The distances between graphene layers determined by TEM are consistent with the results obtained by XRD: the uncoated sample has a higher $d_{(002)}$ value than the coated sample (0.409 nm vs. 0.392 nm, respectively, Table 3.2). This can be explained by the presence of the carbon layer, which seems to be more ordered according to TEM observations.

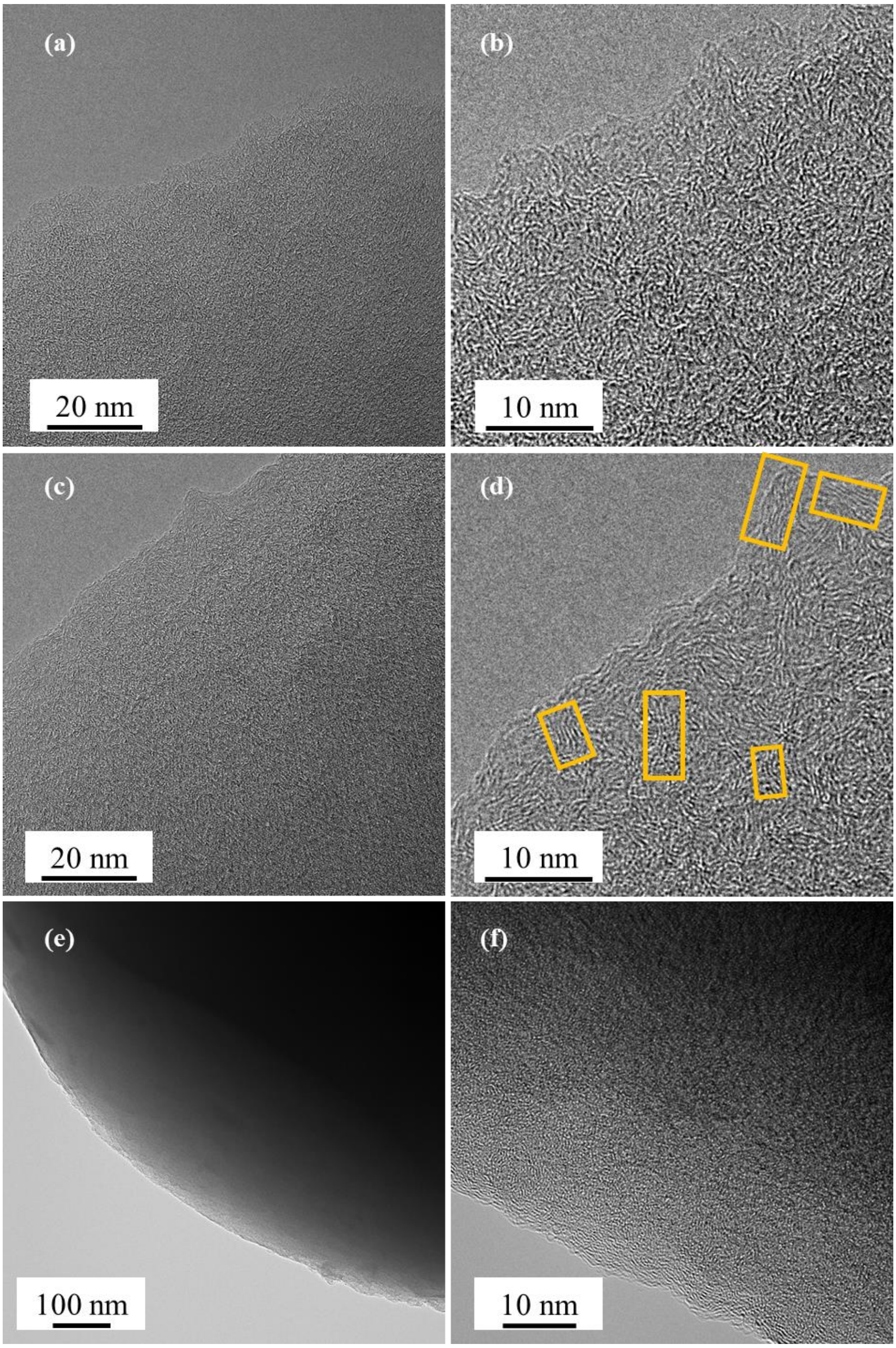

Figure 3.4. TEM images of (a) and (b) CX-LPH, and (c) and (d) CX-LPH-C. In orange: turbostratic domains. Micrographs (e) and (f) show more precisely the edge of a xerogel particle for sample CX-LPH-C at different magnifications.

As expected, the Hg porosimetry curves performed on the powders show two stages for all samples (Figure S3.2a): (i) progressive powder compaction at low pressure followed by (ii) a steep intrusion step at higher pressure (marked by arrows in Figure S3.2a). Pore sizes were calculated from the intrusion step and led to average pore diameters, d_p, of 53 nm, 1400 nm, 2600 nm and 3900 nm for samples CX-450, CX-1500, CX-2500 and CX-LPH respectively (Table 3.1). No significant modification was observed after CVD treatment (Figure S3.2b).

N_2 and H_2 adsorption-desorption were used to determine the specific surface area of the samples and gain insight into the micro-mesoporous texture. Results are gathered in Figure 3.5 and Table 3.1. Nitrogen adsorption-desorption isotherms are shown in Figure 3.5a. While the CX-1500, CX-2500 and CX-LPH samples are strictly microporous (type I isotherms), CX-450 also exhibits meso/macroporosity (type I + II isotherm), as suggested by the corresponding SEM micrograph (Figure 3.1a). The isotherms of the CVD-coated samples show a drastic modification in the low-pressure region corresponding to micropores, in accordance with previous results [30]; this indicates that carbon coating by CVD can be used to block the micropores and reduce the surface area of carbon xerogels, whatever the nodule size. Indeed, A_{BET} calculated from the N_2 adsorption isotherms of the uncoated samples are close (Table 3.1): 670, 651, 646 and 643 $m^2\ g^{-1}$ for samples CX-450, CX-1500, CX-2500 and CX-LPH, respectively. Calculated values for CVD-coated samples decrease sharply: from 640-650 $m^2\ g^{-1}$ to 36, 3 and 2 $m^2\ g^{-1}$ for samples CX-1500, CX-2500 and CX-LPH, respectively. However, the decrease for the sample CX-450-C is less pronounced (from 670 to 135 $m^2\ g^{-1}$). Accordingly, the micropore volume obtained by the Dubinin-Radushkevich method, V_μ, is almost constant for the pristine carbon xerogels (0.24 – 0.25 $cm^3\ g^{-1}$); it drops to 0.05 $cm^3\ g^{-1}$ for CX-450-C and is below the measurement limit for the other coated samples. Note that V_μ is in fact closely related to A_{BET}: both methods are indeed sensitive to adsorption on the external surface [32] and it is thus normal that they evolve in the same way.

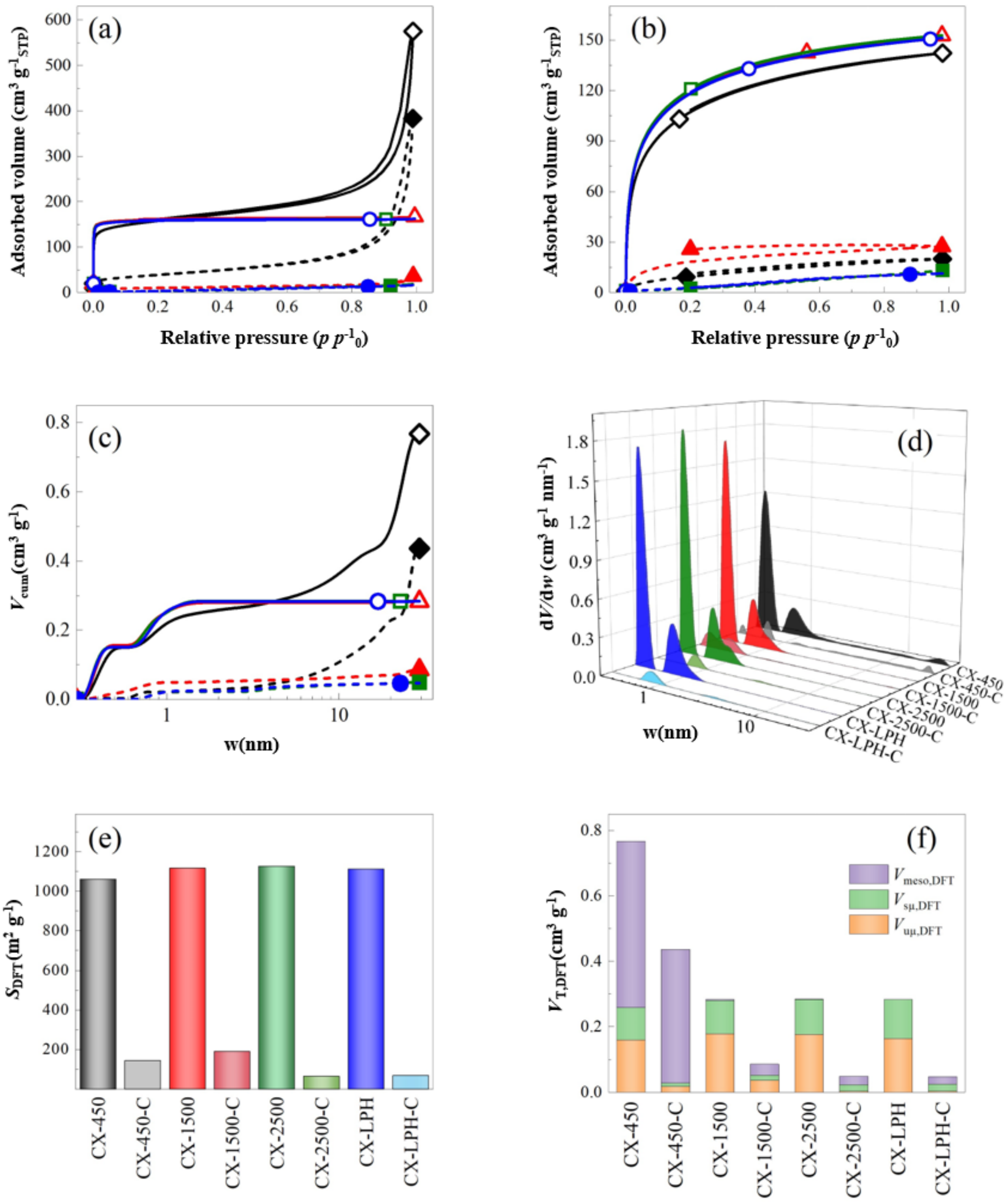

Figure 3.5. Pore texture analysis from gas sorption. (a) N_2 and (b) H_2 adsorption-desorption isotherms of the pristine and coated xerogels. (c) Cumulative and (d) differential pore volume distributions. (e) Total surface calculated by the non-local DFT theory using both N_2 and H_2 adsorption isotherms. (f) Pore volume distribution as a function of their classification. For figures (a), (b) and (c): (◇) CX-450, (◆) CX-450-C, (△) CX-1500, (▲) CX-1500-C, (□) CX-2500, (■) CX-2500-C, (○) CX-LPH and (●) CX-LPH-C.

Figure 3.5b displays the H_2 adsorption-desorption isotherms of the eight samples. The cumulative pore volume as a function of the pore width, w, and the derivative pore size distribution (PSD), calculated by combination of N_2 and H_2 adsorption isotherms, are shown in Figures 3.5c and 3.5d, respectively. The evolution of the total specific surface area, S_{DFT}, and the pore volume distribution among the mesopores, supermicropores and ultramicropores ($V_{\mathrm{meso,DFT}}$, $V_{\mathrm{s\mu,DFT}}$ and $V_{\mathrm{u\mu,DFT}}$, respectively) upon coating are displayed in Figures 3.5e and 3.5f. The H_2 isotherms of the uncoated samples are close again, leading to similar S_{DFT} values: from 1061 to 1126 m² g^{-1} (Table 3.1). However, the behavior of the coated samples upon H_2 adsorption is quite peculiar. As the nodule size increases, the amount of adsorbed H_2 first increases for samples CX-450-C and CX-1500-C (145 and 191 m² g^{-1}, respectively), then drops to 66 and 69 m² g^{-1} in the case of samples CX-2500-C and CX-LPH-C. When detailing the pore volume distribution, one can observe that the CVD coating leads to (i) a loss of 78 – 88 % of $V_{\mathrm{u\mu,DFT}}$ for samples CX-450-C and CX-1500-C, (ii) a complete loss of $\mathrm{V}_{\mathrm{u\mu}}$ for CX-2500-C and CX-LPH-C, and (iii) a decrease between 80 – 90 % of $V_{\mathrm{s\mu,DFT}}$ for all samples.

Skeletal density values, ρ_{s}, measured by He pycnometry, are equal to 1.93, 1.85, 1.95 and 2.08 g cm^{-3} for samples CX-450, CX-1500, CX-2500 and CX-LPH, respectively (Table 3.1). These values are more or less constant and indicate that the structure of the carbon nodules is rather similar, whatever their size. Interestingly, CVD affects the values of ρ_{s} differently for CX-450 and CX-LPH samples than for CX-1500 and CX-2500 samples. While a decrease in ρ_{s} is observed after CVD for CX-450 and CX-LPH, a slight increase can be observed for CX-1500 and CX-2500. A possible explanation could be a different pore filling upon CVD for the various materials, depending on both meso/macropore size and nodule size. It is possible that in the case of sample CX-450, which is made of small nodules separated by meso-macropores, some of the spaces between the nodules are blocked by carbon deposits. This would lead to the closure of existing mesopores and a decrease of the skeletal density (Figure 3.6a). In addition, Figures 3.2a-b show an irregularly compacted carbon deposit on the surface of the carbon xerogel, with possible gaps beneath the structure. This could also contribute to changes in the material’s skeletal density, especially given the high carbon intake upon CVD (30 %). In the case of samples CX-1500 and CX-2500, which have much larger pore sizes and intermediate nodule sizes, carbon deposition by CVD could fill the micropores without clogging the macropores. This filling might not be complete, but given that the carbon deposit is a more ordered structure suggesting a graphitic-like character, and thus denser than the original carbon xerogels, the incomplete filling of the micropores might be compensated, resulting in an overall increase in skeletal density (Figure 3.6b). Finally, in the case of the CX-LPH sample, the microporous nodules might be too large to allow the deposition of pyrolytic carbon deep inside the nodules, leading to the formation of closed micropores and a decrease in nodule density (Figure 3.6c).

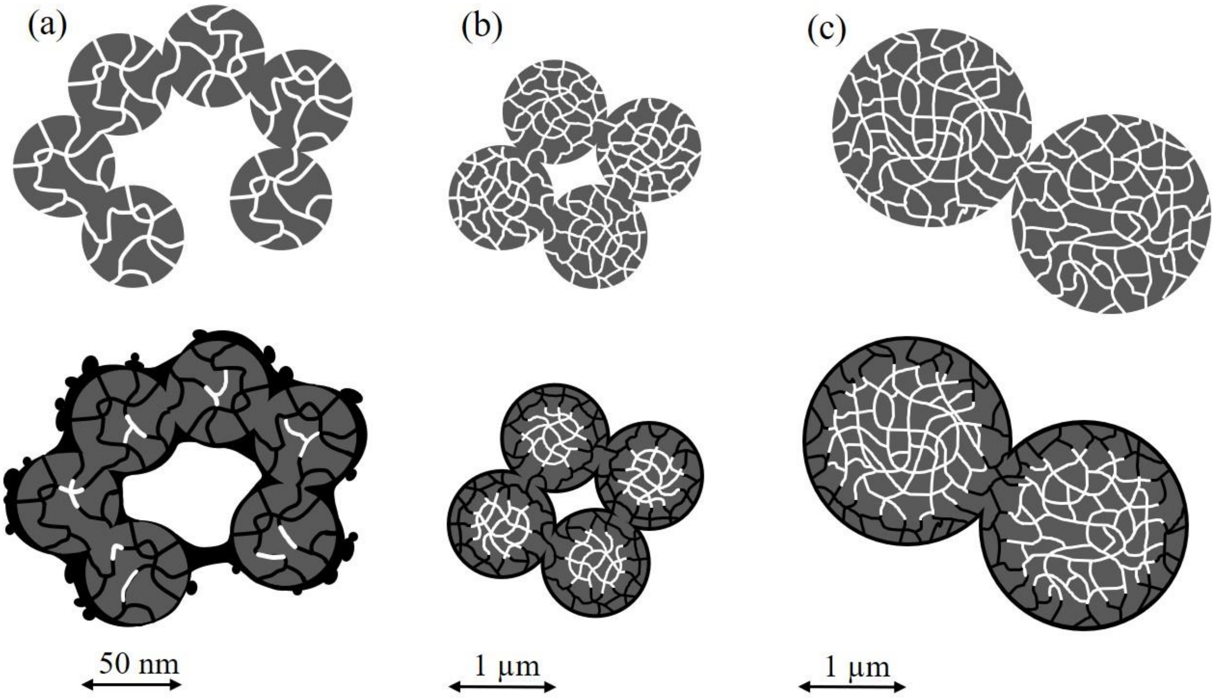

Figure 3.6. Effect of CVD procedure on the pore texture of carbon xerogels (a) CX-450, (b) CX-1500 and CX-2500 and (c) CX-LPH.

All these results show that the CVD coating procedure effectively masks the micropores and certainly fills them, at least in part, with a more ordered carbon, HR-TEM analysis suggesting a graphitic-like character. The latter is further supported by electrochemical measurements, as will be shown in section 2.2.3. Depending on the mass uptake, deposits of irregular shape may also be present, as in sample CX-450-C (Figure 3.2a). Calculation of remaining surface areas, by distinguishing between the internal and external area of the carbon nodules, might help understanding what surface remains available for the electrolyte in the final electrode. To this end, the external nodule surface area can be determined either by experimental procedures or by geometric calculation. In the case of CX-450 and CX-450-C samples, the external surface area, S_{ext}, was calculated from the N_2 adsorption isotherms using the t-plot method. S_{ext}, which excludes micropores, amounts to 181 m² g^{-1} and 118 m² g^{-1} for CX-450 and CX-450-C, respectively. This seems to show that the CVD coating has little impact on the external surface of the nodules, while all pristine micropores are completely inaccessible. This could correspond to a homogeneous coating of the nodule surface, which is somewhat contradictory to the SEM micrographs where irregular carbon deposits are also seen, and to the hypothesis of mesopore clogging. It is likely that the measured S_{ext} actually corresponds to two contributions: (i) the remaining external nodule surface after clogging and (ii) the additional surface corresponding to irregular carbon deposits (which would compensate for the loss of surface area due to mesopore clogging). In the case of the other samples, the external surface areas of the nodules are too small to be determined accurately by the t-plot method, given the large size of the nodules. However, their values can be estimated by a geometric calculation, considering the micropore volume, V_{μ}, the nodule size, D_{n}, and the skeletal density of the carbon material, ρ_{s}. Indeed, the bulk density of the carbon nodules can be calculated as follows:

$$\rho_{n,bulk} = \frac{1}{V_{\mu} + \frac{1}{\rho_s}} \tag{3.1}$$

Then, considering that the nodules are spheres of diameter D_{n}, the total area corresponding to the outer surface of the nodules can be calculated as follows:

$$S_{n,ext} = n.S_n = nV_n\frac{S_n}{V_n} = \frac{1}{\rho_{n,bulk}}\frac{6}{D_n} \tag{3.2}$$

where V_{n} and S_{n} are the volume and surface area of one nodule, respectively, and n is the number of nodules in 1 g of carbon material. The calculated surface areas (Table 3.1) are equal to 91, 5, 3 and 2 m² g^{-1} for samples CX-450, CX-1500, CX-2500 and CX-LPH, respectively. $S_{\mathrm{n,ext}}$ correspond very well to A_{BET} of the CVD-coated samples in the case of CX-2500 and CX-LPH, which indicates that the carbon layer homogeneously covers the surface of the large nodules, as confirmed by the N_2 adsorption data and Figure 3.2b. $S_{\mathrm{n,ext}}$ values are, however, lower than the A_{BET} of CVD-coated samples in the case of CX-1500 and CX-450, which amount to 36 and 135 m² g^{-1}, respectively. These two samples present the highest mass intake (19 % and 30 %, respectively), which can be explained by the fact that a greater area is available outside the nodules for carbon deposition. This also led to rougher nodule surfaces after CVD treatment, resulting in larger areas measured by N_2 adsorption. The SEM micrographs in Figures 3.1 and 3.2 confirm this assumption. It should be kept in mind that the carbon deposition by CVD has not been optimized in terms of mass intake: in the procedure, the deposition time was kept constant. Obtaining a homogeneous coating around the nodules without additional carbon deposits certainly requires precise optimization of the process, which will be the subject of further research.

H_2 adsorption can also help distinguishing between pore filling and pore masking. For CX-450-C and CX-1500-C samples, Figure 3.5f shows that the CVD treatment leads to the near complete disappearance of the supermicropores, while part of the ultramicroporosity remains present. This corresponds well to a micropore filling mechanism where ethylene fragments cannot access the smallest pores when the nodule size increases, leaving a larger part of the ultramicropores untouched. However, the behavior of samples CX-2500-C and CX-LPH-C remains unexplained. Especially in the case of CX-LPH-C, it seems that coating the nodules with carbon by CVD leaves a significant amount of porosity within the nodules, as deduced from the decrease of the skeletal density (from 2.08 to 1.88 g cm^{-3}, Table 3.1), but that the carbon layer is not permeable to H_2. In addition, one notes that the mass intake is the lowest of all for that sample (4 %), and that the coating seems very smooth (Figure 3.2b). This means that the layer deposited is quite thin. Indeed, one can consider that the nodules of sample CX-450 have a bulk density, ρ_{bulk}, of:

$$\rho_{bulk} = \frac{1}{V_{T,DFT} + \frac{1}{\rho_S}} \tag{3.3}$$

which amounts to 1.3 g cm^{-3} for CX-LPH. If one considers that the nodules are spheres with diameter of 2 µm, and that the mass uptake (4 %) is due to the deposition of a regular carbon layer with a density close to that of graphite (2.2 g cm^{-3}) around the nodule, one can estimate that the maximum layer thickness (i.e., without micropore filling) would be close to 8 nm. Given that the micropores are probably partially filled, the layer is much certainly even thinner, but, to a large extent, impermeable to H_2 and thus without defects or cracks. This astonishing result calls for further investigation to understand properly the exact structure of the CX-LPH composite. Note that in the case of CX-2500-C, the same conclusions may apply; however, the skeletal density increases a little, from 1.95 to 2.04 g cm^{-3}. One must however keep in mind that the mass intake was in that case much higher (15 %), meaning that the micropore masking might be counterbalanced by the addition of carbon with higher skeletal density.

Regarding elemental analysis (Table 3.3), no significant difference can be observed with the change of nodule size, except in the case of CX-LPH, which has a lower oxygen content: 2.4 wt.% vs. 3.5-3.9 wt.% for the other pristine CXs. For the CVD-coated samples, a clear impact can be observed as all samples display a higher carbon content than their uncoated counterparts

(97-98 wt.% vs. 94-96 wt.%); CVD-coated samples contain less oxygen and less hydrogen. Note that Table 3.3 shows discrepancies between the sum of all element contents and 100 %, typically around 1%. These discrepancies are likely attributable to experimental errors in determining individual element values. Given the sample preparation procedure, the mineral content (unknown) should be extremely low.

Table 3.3. Elemental analysis of carbon xerogels before and after CVD treatment.

Sample	**N** (wt.%)	**C** (wt.%)	**H** (wt.%)	**S** (wt.%)	**O** (wt.%)
CX-450	0.1	94.1	0.8	0.0	3.5
CX-450-C	0.2	97.3	0.3	0.0	2.2
CX-1500	0.1	94.3	0.7	0.0	3.7
CX-1500-C	0.4	97.5	0.4	0.0	3.3
CX-2500	0.1	94.1	0.8	0.0	3.9
CX-2500-C	0.2	97.5	0.3	0.0	2.1
CX-LPH	0.1	96.2	0.9	0.0	2.4
CX-LPH-C	0.2	98.0	0.3	0.0	2.8

3.3.2. Electrochemical properties

Following structural and morphological characterization, uncoated and coated samples were electrochemically tested in half-cell configuration to determine their performance as negative electrode materials for Na-ion battery. Figures 3.7a and 3.7b show the first galvanostatic charge-discharge curves for pristine and CVD-coated samples, respectively. The same curves comparing directly the same material before and after CVD treatment are displayed in Figures 3.7c to 3.7f for better comparison. The corresponding data are summarized in Table S3.2. The total capacity value at first discharge (e.g., first sodiation) is reported as $C_{\mathrm{tot,disch}}$. The reversible capacity (C_{rev}) is the capacity delivered by the first charge (e.g., first desodiation), while the irreversible capacity (C_{irrev}) is the difference between these two values. The ICE was calculated from these values as the ratio between C_{rev} and $C_{tot,disch}$. Finally, the capacities corresponding to the sloping part and to the low-voltage plateau of the first-discharge curve are reported as C_{slope} and $C_{plateau}$, respectively, along with their contribution (in %) to the total first-discharge capacity.

The results of cycling at various C-rates are grouped together in Figure 3.8, for both uncoated (Figures 3.8a, c, e and g) and CVD-coated (Figures 3.8b, d, f, and h) materials. Data are reported in terms of capacities upon sodiation (black) and desodiation (red); the coulombic efficiency at each cycle is also plotted (blue).

3.3.2.1 Impact of carbon nodule size

The impact of nodule size on the first galvanostatic charge-discharge of uncoated carbon xerogels can be seen in Figure 3.7a. The first observation concerns the total discharge capacity, which decreases as nodule size increases: from 563 to 312 mAh g^{-1} for samples CX-450 and CX-LPH, respectively. However, the most striking result concerns the ICE (Table 3.4). As the nodule size increases, the ICE increases significantly: from 29 to 80 % for samples CX-450 and CX-LPH, respectively. In the literature, the ICE is generally directly related to the material's specific surface area measured by gas sorption [33]–[35]. However, all the pristine carbon xerogels display similar A_{BET} and S_{DFT} values (Table 3.1), which precludes any direct impact of total specific surface area on electrolyte decomposition in this case. Nor are the ICE values proportional to the external nodule area; in fact, the ICE seems to correspond to an intermediate area between the external area of the nodule and the total specific surface area determined from gas adsorption. Given that any influence of the binder can be ruled out [31], the only possible explanation is that the electrolyte only partially enters the micropore volume of all materials, and that the volume into which the electrolyte can enter depends on the size of the nodule. For large nodules, the electrolyte would only penetrate the outer fraction of the nodules, while a larger fraction, possibly corresponding to a similar penetration depth, would be accessible in the case of small nodules. Conversely, the entire open micropore volume is accessible to H_2, regardless of nodule size. Therefore, both N_2 and H_2 adsorption fail to predict the solid-electrolyte interphase (SEI) formation area and ICE values, since the calculated surface areas probably do not correspond to the total surface area accessible to the electrolyte. Such a phenomenon was indeed already observed in Li-ion systems, where electrode capacitance was measured using cyclic voltammetry on a symmetric cell made of two identical carbon xerogel-based electrodes [30]: the capacitance was measured proportional to the external surface area of the nodules, and not to the total surface, because the electrolyte could not access the micropores. Determination of the surface area accessible to the electrolyte could be done in the same way in a further study. Another factor that can have an impact on the ICE is the amount of oxygen and heteroatoms in the structure. Indeed, with a higher electronic density, heteroatoms contribute to sodium ad/chemisorption, thus enhancing sodium storage in hard carbons, as described in more detail in the literature, but their amount must be optimized so as not to decrease the ICE too much [36][37]. For the carbon xerogels described in this study, the total amount of heteroatoms, decreases slightly. Especially, the oxygen content drops from 3.5 wt.% for CX-450 to 2.4 wt.% for CX-LPH as the nodule size increases (Table 3.3). Although the difference is small between the four samples, this may contribute somewhat to the better ICE observed for CX-LPH.

Galvanostatic profiles of uncoated samples display further differences as nodule size increases (Figure 3.7a). Importantly, CX-450 shows no low-voltage plateau, while the plateau starts to appear in the CX-1500 sample (i.e., 19 mAh g^{-1}, around 6 % of the 1st discharge capacity $C_{tot,disch}$, Table S3.2.) and continues to increase as nodule size increases, the highest value being obtained for CX-LPH (i.e., 99 mAh g^{-1}, around 32 % of $C_{tot,disch}$). As previously discussed in the introduction, although the mechanism is the subject of much debate, the low-voltage plateau region is widely attributed to the filling of micropores by Na^+ ions. However, these micropores can only be accessed to by Na^+ ions if the electrolyte does not decompose on their surface, thus filling their volume with SEI. As a result, for carbon xerogels, the appearance and increase of the plateau could correspond to the filling of micropores that remain in the material after their entrance has been filled by SEI, leaving part of the micropore volume untouched. This would explain why no plateau is observed for CX-450, while the plateau lengthens with increasing nodule size. The increase in total reversible capacity can be attributed to the appearance and lengthening of the plateau; indeed, C_{slope} remains similar for all samples while $C_{plateau}$ increases with nodule size.

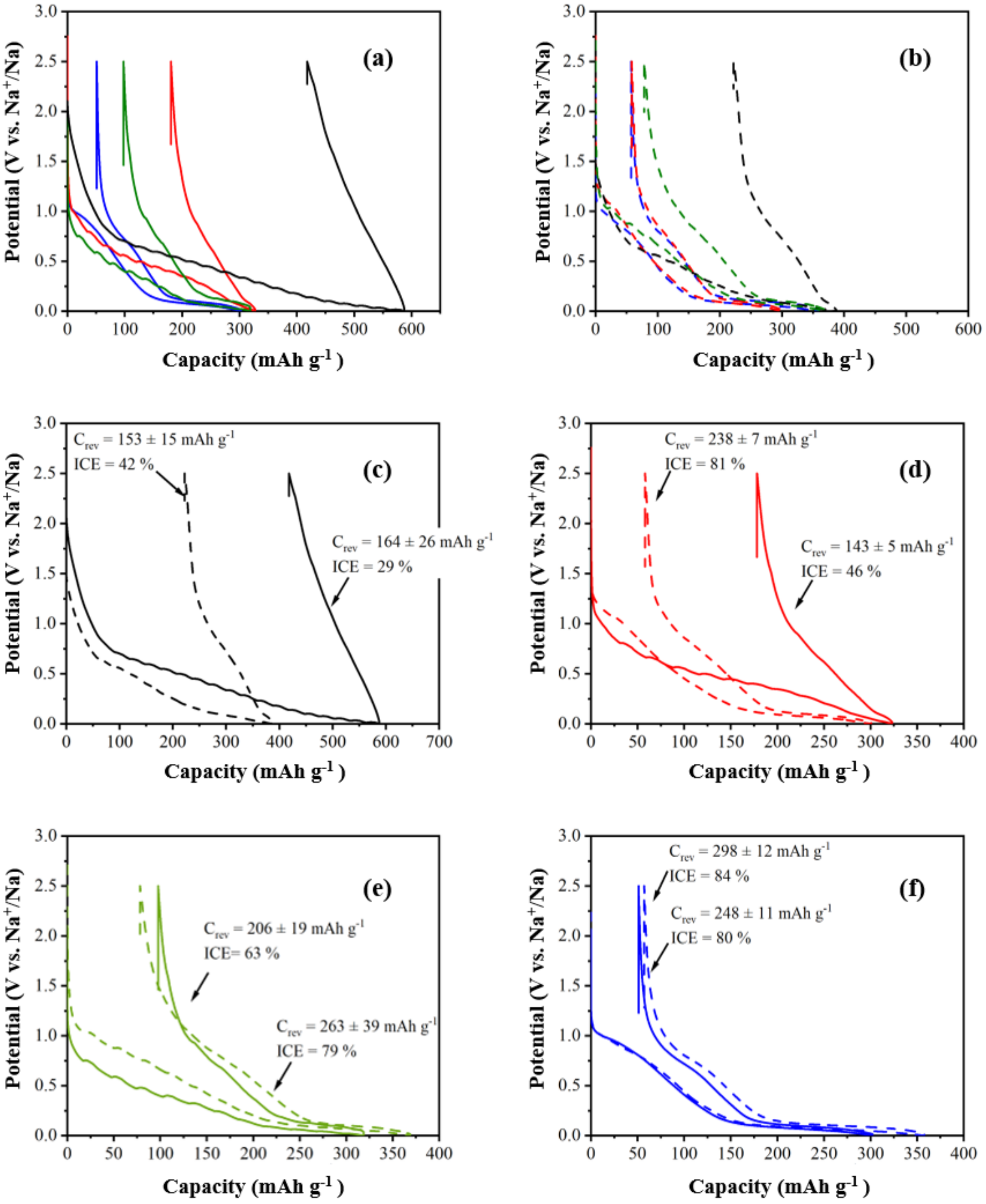

Figure 3.7. (a) Galvanostatic charge-discharge profiles of the uncoated samples: (▬) CX-450, (▬) CX-1500, (▬) CX-2500, (▬) CX-LPH. (b) Galvanostatic charge-discharge profiles of the CVD-coated samples: (---) CX-450-CVD, (---) CX-1500-CVD, (---) CX-2500-CVD, (---) CX-LPH-CVD. (c-f) First cycle galvanostatic profiles for non-coated (solid) and CVD-coated (dashed) carbon xerogels for the different *R/C* ratio: (c) CX-450, (d) CX-1500, (e) CX-2500 and (f) CX-LPH. Half-cells with NP30 electrolyte, cycling at C/20 (corresponding to 18.6 mA g_{carbon}^{-1}).

It must be highlighted that one of the variables that most affects the performance of hard carbons as Na-ion electrode materials is their pyrolysis temperature [36][38]. According to the literature, it may range from 500 °C up to 2500 °C. The performance observed as a function of pyrolysis conditions is difficult to generalize. Tonnoir et al. [10] found that the reversible capacity of non-graphitizing carbons decreases with increasing pyrolysis temperature from 1000 °C up to 2500 °C while Rios et al. [39] suggested that hard carbons produced at low pyrolysis temperatures (below 1000 °C) exhibit both lower reversible capacity (< 200 mAh g^{-1}) and lower ICE (< 50 %). The results seem to be very precursor-dependent, as the final structure of the hard carbons strongly depends on the initial structure of the precursor [36][38]. Here, it is worth mentioning that the pyrolysis temperature was kept low (800 °C), but a reversible capacity as high as 248 mAh g^{-1} with 80 % ICE was obtained. To the best of our knowledge, the values achieved in the present work are the best result ever obtained with such low pyrolysis temperature for hard carbons. It is clear, however, that the key variable for high reversible capacity is nodule size in the case of carbon xerogels. Indeed, for comparison, total capacities of ~400 – 550 mAh g^{-1}, but with only 15 – 30 % ICE, were obtained for carbon xerogels made of nodules around 20-50 nm in size [18]. No plateau was observed in this case, although a higher pyrolysis temperature (1000 °C) was used.

Cycling at different C-rates was performed to understand the relationship between nodule size and rate capability (Figures 3.8a, c, e and g). First, it must be pointed out that the coulombic efficiency quickly stabilizes at 100 %, except for CX-450 and just after the change in C-rate for the other samples. The capacities reported hereafter are thus considered reversible. When cycling at low C-rates, such as C/20, C/10 and C/5, the capacity trends observed in the first cycle remain the same: the larger the nodule size, the higher the capacity. However, the situation changes when the C-rate is higher than C/2: the capacity of samples CX-1500, CX-2500 and CX-LPH drops drastically, while that of CX-450 remains fairly stable. CX-450 is the only sample to show a capacity of around 100 mAh g^{-1} at a C-rate of 5C, while the other samples show capacities close to 0 mAh g^{-1}. The reason for this behavior probably lies in the smaller nodule size of CX-450, which provides shorter diffusion paths for Na^+, and is therefore less affected by an increase in C-rate. [40] Additionally, since a larger carbon surface area is accessible to the electrolyte for the CX-450 than for the other samples, electron transfer is facilitated, which limits capacity drops at high C-rate values. After cycling at high C-rates, all samples recover much of their initial capacity: around 83 % for CX-450 after 5 cycles back to C/20, 97 % for CX-1500, 95 % for CX-2500 and 96 % for CX-LPH, showing that the electrode is not degraded at high C-rates. It is also worth mentioning that, for CX-1500, CX-2500 and CX-LPH, the plateau is no longer visible at C-rate values higher than C (Figure S3.3.a, c, e and g). This is probably due to a difference in kinetics: as the C-rate increases, it becomes more difficult for Na^+ ions to be stored in the inner porosity of the carbon xerogel, far from the nodule surface.

To sum up, both reversible capacity and ICE increase with nodule size, which is most probably related to the fact that the electrolyte does not access the whole volume and surface of the micropores as the nodule size increases. However, smaller carbon nodules perform better at higher C-rates due to shorter pathways and larger exchange areas. Finally, a very high reversible capacity (248 mAh g^{-1}) and a high ICE (80 %) were both achieved in the case of sample CX-LPH, i.e., a carbon material composed exclusively of microporous hard-carbon spheres with a diameter of around 2 µm. To our knowledge, a reversible capacity of 248 mAh g^{-1} and a first-cycle efficiency of 80 % are among the highest values achieved, especially at such a low pyrolysis temperature (800 ºC).

3.3.2.2. Impact of CVD coating

Figure 3.7b shows the first galvanostatic charge-discharge curve for all CVD-coated carbon xerogels. This figure, along with the corresponding data reported in Table 3.4, shows that the total capacity decreases sharply for CX-450-C, does not change much for samples CX-1500-C and CX-2500-C, and increases slightly for CX-LPH-C. The reversible capacity increases after CVD for all samples, except for CX-450 (slight decrease, from 164 to 153 mAh g^{-1}). For CX-1500, CX-2500 and CX-LPH, the increase in reversible capacity is mostly because the low-voltage plateau lengthens; this could correspond to a significant increase of the volume of closed micropores, inaccessible to the electrolyte but still available for Na^+ storage. For samples CX-450-C, CX-1500-C and CX-2500-C, this goes in line with the evolution of $V_{\mathrm{T,DFT}}$ measured by N_2 and H_2 adsorption (Figure 3.5f, Table 3.1), which shows that micropores are still present after coating. However, given that the reversible capacity also increases after coating for CX-LPH-C, one can conclude that despite its impermeability to H_2, the coating does not hamper Na^+ insertion. In parallel, all irreversible capacities decrease, and the drop is very pronounced for small nodules (from 398 to 211 mAh g^{-1} for CX-450) while it is quite moderate for large nodules (from 64 to 56 mAh g^{-1} for CX-LPH). This is clearly related to the masking of micropores after CVD, leading to a decrease of both A_{BET} and S_{DFT} (Table 3.1), and to the fact that the initial micropores are not equally accessible in all uncoated samples. In CX-450, which has small nodules and, presumably, easier access to micropores by the electrolyte, the area on which the SEI may form is greatly decreased after coating. Conversely, in the case of CX-LPH, the micropores are only partially accessible to the electrolyte, and the impact of the carbon coating on the irreversible capacity is lower overall.

In terms of ICE, the increase after coating is especially spectacular for samples CX-1500-C and CX-2500-C, rising from 45 and 63 % to 81 and 79 %, respectively. The ICE of sample CX-450 increases only from 29 to 42 % (with, in reality, a sharp decrease both in total and irreversible discharge capacities). Although the other samples show an increase too, it is not as drastic as for CX-1500 and CX-2500 samples. In the case of CX-LPH, the change is less significant (80 to 84 %) given the already very high ICE for the non-coated material, but most of the increase in total capacity is due to the lengthening of the plateau.

As already pointed out, the carbon coating deposited by CVD has a tremendous impact on the low-voltage plateau region of the galvanostatic profiles for all samples. Indeed, after CVD treatment, the plateau capacity increases from 19 to 88 mAh g^{-1} for CX-1500, from 56 to 75 mAh g^{-1} for CX-2500, and from 99 to 129 mAh g^{-1} for CX-LPH. A short plateau becomes even visible for CX-450. Conversely, the impact observed on the sloping capacity is low for all samples, even though the slope seems more defined for all samples after CVD. It has been reported in the literature that the plateau region capacity seems to correlate with the volume of suitable (micro)pores for sodium storage. [41] Therefore, it can be concluded that CVD leads to the formation of closed pores suitable for Na^+ storage. In the literature, a pore diameter of 1 nm is reported to be the optimum value for promoting the pore-filling mechanism [42].

Cycling at different C-rates was also performed for the CVD-coated samples (Figure 3.8b, d, f and h). Although the CVD-coated materials display a much higher capacity at slower C-rates (except for CX-450-C), the drop with increasing rate is sometimes more severe compared to non-coated samples. This is the case, for instance, with CX-1500: the coated sample has a higher capacity at C/5 (around 190 mAh g^{-1} for the coated sample vs. around 115 mAh g^{-1} for the uncoated one), but the values almost catch up with those of the uncoated sample at rate C and above. A similar observation can be made for larger nodules. In the case of CX-LPH, the capacity of the coated material may even drop below that of the uncoated one at high C-rate. Moreover, as previously observed for the uncoated sample, the low-voltage plateau disappears for C-rate values above C (Figures S3.3.b, d, f and h). Capacities are also less stable with the number of cycles (Figures 3.8b, d, f and h), especially for CX-LPH-C. The reason for this phenomenon has yet to be elucidated, along with the exact nature of the carbon layer given the peculiar H_2 adsorption results obtained for this sample. It most probably depends on the structure of the carbon layer, which in turn needs to be optimized in terms of thickness and structure. Although coated samples seem to be more affected by cycling at high C-rate values than their uncoated counterparts, all samples recover much of their initial capacity after cycling at high C-rate values: around 96 % for CX-450-C after 5 cycles back to C/20, 95 % for CX-1500-C, and 92 % for CX-2500-C. For CX-LPH-C, cycling back to C/20 enables recovery of about 91 % of its initial capacity after 5 cycles, but the capacity drops rapidly to 82 % of its initial value after 60 cycles (i.e., 15 cycles after cycling back to C/20).

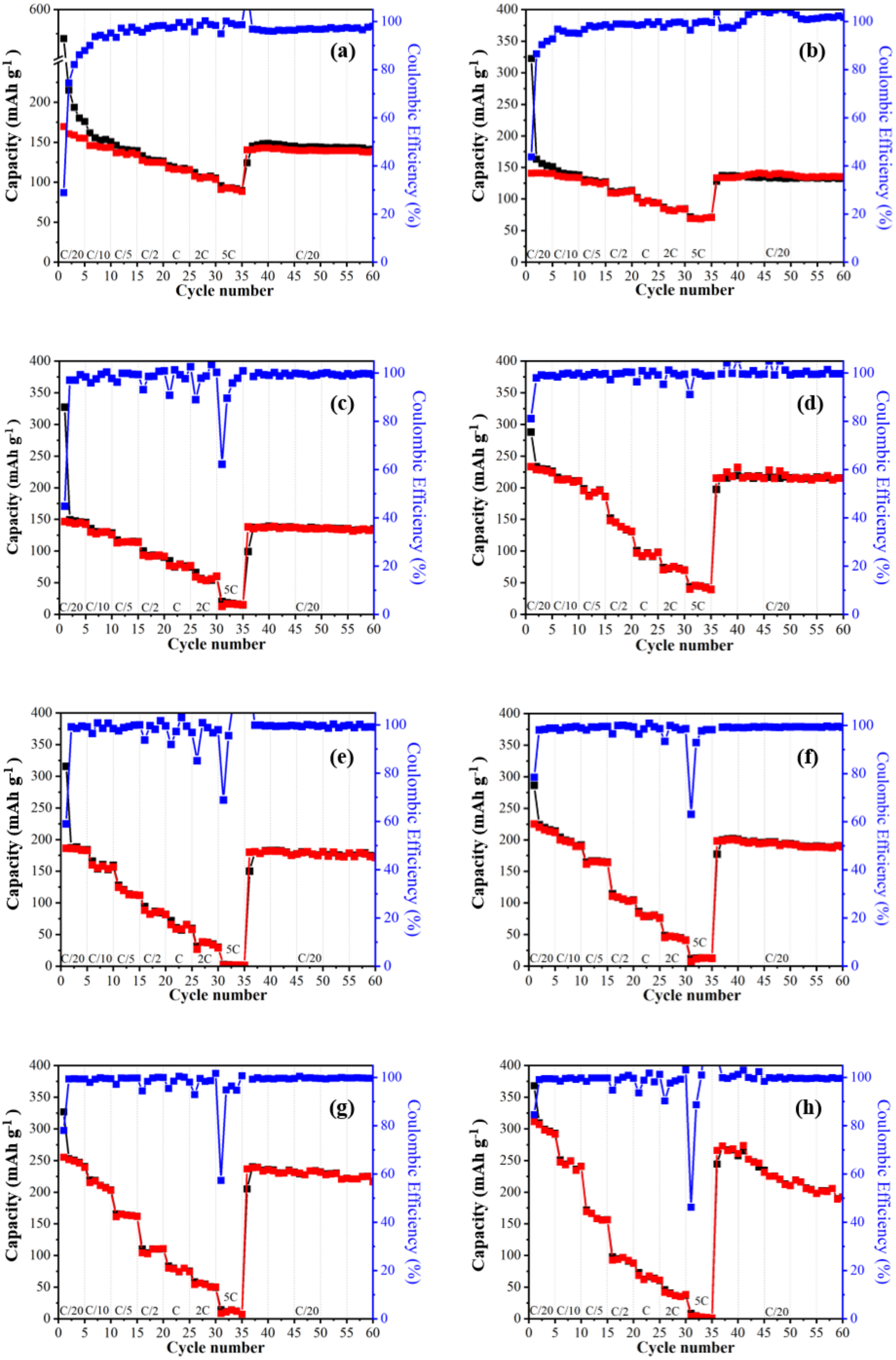
(a)
(b)
(c)
(d)
(e)
(f)
(g)
(h)
Capacity (mAh g^{-1})
Coulombic Efficiency (%)
Cycle number
C/20 C/10 C/5 C/2 C 2C 5C C/20
5C
0 50 100 150 200 600
0 50 100 150 200 250 300 350 400
0 20 40 60 80 100
0 5 10 15 20 25 30 35 40 45 50 55 60

Figure 3.8. Galvanostatic charge-discharge performances according to desodiation capacities (■) sodiation capacity (🟥) and coulombic efficiency (🟦). (a) C-450, (b) CX-450-CVD, (c) CX-1500, (d) CX-1500-C, (e) CX-2500, (f) CX-2500-C, (g) CX-LPH, (h) CX-LPH-C at various cycling rates *vs*. coulombic efficiency in each step.

3.3.3. Insight into the structure of the carbon layer

Electrochemical characterization in LIB half-cell can also provide some information about the structure of the carbon layer. Indeed, Li^+ ions do insert into graphite below 0.5 V vs. Li^+/Li, while uncoated carbon xerogels show no specific peak, insertion indeed taking place over a very wide voltage range [30]. As mentioned previously, uncoated and CVD-coated CXs have been used in the past as electrode materials for LIBs, in half-cell configuration, in order to understand the role of the micropores on Li^+ storage [31]. On this occasion, cyclic voltammetry was performed but the results on the CVD-coated material were not published at that time. However, these results might prove relevant to the present study.

The samples examined in reference [31], referred to as CX-Ref and CX-CVD for pristine and CVD-coated materials, respectively, are close to CX-450 and CX-450-C (macropore size of 80 nm, CVD treatment of 30 min under the same conditions, leading to a mass increase of 25 %). The electrode preparation was identical to that reported in reference [31] and in the present study. Experimental details are also given in the S3. Figures S3.4a and b present the stabilized cyclic voltammetry curves (cycle #10) for the two CX samples, along with the curve shown in reference [31] for graphite. While the uncoated material displays the usual carbon xerogel profile, without clear insertion potential, the coated material exhibits a small peak around 0.25 V vs. Li^+/Li (Figure S3.4b), exactly where the insertion peak is observed in graphite (Figure S3.4a). Although this peak is not as sharp as in graphite, its presence in the voltammogram indicates the existence of a graphitic-like structure in the coated CX, which obviously corresponds to the layer deposited by CVD. The layer probably contains many defects, but its position matches that of graphite crystals. Along with the HR-TEM micrographs, this observation suggests that the CVD coating is at least partially graphitized.

3.4. Conclusions

Carbon xerogels (CXs) with different nodule sizes were synthesized by polycondensation of resorcinol with formaldehyde in water, followed by drying and pyrolysis at 800 °C. The size of the carbon nodules was tailored between 50 nm and 2 µm, while ensuring similar high-specific surface areas, in order to determine its impact on the electrochemical properties of these carbons as Na-ion battery negative electrode materials. The CX nodules were coated with a secondary carbon layer by Chemical Vapor Deposition (CVD) to mask or fill their micropores and improve their Initial Coulombic Efficiency (ICE).

Increasing the nodule size leads to an increase in both total Na^+ insertion capacity and ICE: in particular, ICE values change drastically from 29 % to 80 % as the nodule size increases from 50 nm to 2 µm. In contrast to commonly drawn conclusions in existing literature, ICE appears to be independent of the specific surface area of the sample. This suggests that the surface probed by gas adsorption does not correspond to the surface area accessible to the electrolyte, especially if the nodule size is large. Remarkably, reversible capacity and ICE values of up to 248 mAh g^{-1} and 80 %, respectively, were observed at a cycling rate of C/20 for the sample with the largest nodule size, 2 µm, which is, to the best of our knowledge, unmatched in literature, especially for such a low pyrolysis temperature. Notably, the response of samples at higher C-rates is in the opposite direction, with smaller nodules leading to lower capacity loss, due to the shorter diffusion path length of Na^+ ions inside carbon nodules.

The CVD layer exhibits relatively large graphitic domains on the outer surface of the nodules, and completely masks the microporosity. Indeed, the specific surface area measured by nitrogen adsorption drops from about 600 to 135 m^2 g^{-1} for the sample with 50 nm nodules, and as low as 2 m^2 g^{-1} when the nodule size is 2 µm. ICE increases significantly for all samples, reaching 84 % for the largest nodule size, because the surface area accessible to the electrolyte decreases. The total capacity increases too (up to 298 mAh g^{-1}), and is mainly related to the lengthening of the plateau at low voltage (< 0.1 V vs. Na^+/Na) usually ascribed to the filling of small micropores by Na^+. Thus, the secondary carbon layer deposited by CVD leads to the masking of micropores, consequently expanding the volume of closed micropores suitable for Na^+ storage.

Optimizing CVD coating thickness and carbon xerogel nodule size, while comprehending Na^+ insertion-deinsertion processes through the graphitic-like carbon layer, is expected to pave the way for substantial progress in the engineering of hard carbons for negative electrodes of sodium-ion batteries.

3.5. References

[1] H. Zhang, Y. Huang, H. Ming, G. Cao, W. Zhang, J. Ming, R. Chen, *J Mater Chem A Mater* **2020**, *8*, 1604.

[2] J.F. Peters, M. Baumann, B. Zimmermann, J. Braun, M. Weil, *Renew Sustain Energy Rev* **2017**, *67*, 491.

[3] B.C. Gibb, *Nat Chem* **2021**, *13*, 107.

[4] B.E. Lebrouhi, S. Baghi, B. Lamrani, E. Schall, T. Kousksou, *J Energy Storage* **2022**, *55*, 105471.

[5] D.L. Thompson, J.M. Hartley, S.M. Lambert, M. Shiref, G.D.J. Harper, E. Kendrick, P. Anderson, K.S. Ryder, L. Gaines, A.P. Abbott, *Green Chemistry* **2020**, *22*, 7585.

[6] T. Perveen, M. Siddiq, N. Shahzad, R. Ihsan, A. Ahmad, M.I. Shahzad, *Renew Sustain Energy Rev* **2020**, *119*, 109549.

[7] K. Chayambuka, G. Mulder, D.L. Danilov, P.H.L. Notten, *Adv Energy Mater* **2020**, *10*, 2001310.

[8] D.A. Stevens, J.R. Dahn, *J Electrochem Soc* **2001**, 148, A803.

[9] P. Ge, M. Fouletier, *Solid State Ion* **1988**, *28–30*, 1172.

[10] H. Tonnoir, D. Huo, C. Davoisne, A. Celzard, V. Fierro, D. Saurel, M. El Marssi, M. Benyoussef, P. Meunier, R. Janot, *Carbon* **2023**, *208*, 216.

[11] C. Bommier, T.W. Surta, M. Dolgos, X. Ji, *Nano Lett* **2015**, *15*, 5888.

[12] D. Saurel, B. Orayech, B. Xiao, D. Carriazo, X. Li, T. Rojo, *Adv Energy Mater* **2018**, *8*, 1703268.

[13] A. Gomez-Martin, J. Martinez-Fernandez, M. Ruttert, M. Winter, T. Placke, J. Ramirez-Rico, *Chem Mater* **2019**, *31*, 7288.

[14] N. Daher, D. Huo, C. Davoisne, P. Meunier, R. Janot, *ACS Appl Energy Mater* **2020**, *3*, 6501.

[15] H. Tonnoir, D. Huo, R.L.S. Canevesi, V. Fierro, A. Celzard, R. Janot, *Mater Today Chem* **2022**, *23*, 100614.

[16] E.M. Lotfabad, J. Ding, K. Cui, A. Kohandehghan, W.P. Kalisvaart, M. Hazelton, D. Mitlin, *ACS Nano* **2014**, 8, 7115.

[17] L.F. Zhao, Z. Hu, W.H. Lai, Y. Tao, J. Peng, Z.C. Miao, Y.X. Wang, S.L. Chou, H.K. Liu, S.X. Dou, *Adv Energy Mater* **2021**, *11*, 2002704.

[18] N. Cuesta, I. Cameán, A. Arenillas, A.B. García, *Microp M M. Micropor* **2020**, *308,* 110542.

[19] C. Bommier, W. Luo, W.Y. Gao, A. Greaney, S. Ma, X. Ji, *Carbon* **2014**, *76*, 165.

[20] D.A. Stevens, J.R. Dahn, *J Electrochem Soc* **2000**, *147*, 1271.

[21] D.A. Stevens, J.R. Dahn, *J Electrochem Soc* **2000**, *147*, 4428.

[22] S. Komaba, W. Murata, T. Ishikawa, N. Yabuuchi, T. Ozeki, T. Nakayama, A. Ogata, K. Gotoh, K. Fujiwara, *Adv Funct Mater* **2011**, *21*, 3859.

[23] J.M. Stratford, P.K. Allan, O. Pecher, P.A. Chater, C.P. Grey, *Chemical Communications* **2016**, 52, 12430.

[24] M.M. Titirici, H. Alptekin, H. Au, A.C.S. Jensen, E. Olsson, M. Goktas, T.F. Headen, P. Adelhelm, Q. Cai, A.J. Drew, *ACS Appl Energy Mater* **2020**, *3*, 9918.

[25] Y. Yang, C. Wu, X.X. He, J. Zhao, Z. Yang, L. Li, X. Wu, L. Li, S.L. Chou, *Adv Funct Mater* **2024**, 34, 2302277.

[26] H. Lu, X. Chen, Y. Jia, H. Chen, Y. Wang, X. Ai, H. Yang, Y. Cao, *Nano Energy* **2019**, *64*, nwac084.

[27] Q. Li, X. Liu, Y. Tao, J. Huang, J. Zhang, C. Yang, Y. Zhang, S. Zhang, Y. Jia, Q. Lin, Y. Xiang, J. Cheng, W. Lv, F. Kang, Y. Yang, Q.H. Yang, N*atl Sci Rev* **2022**, *9*, 103903.

[28] N. Job, R. Pirard, J. Marien, J.P. Pirard, *Carbon* **2004**, *42*, 619.

[29] A. Arenillas, J. Angel Menéndez, G. Reichenauer, A. Celzard, V. Fierro, F. José, M. Hodar, E. Bailón-Garcia, N. Job, In: Organic and Carbon Gels, Advances in Sol-Gel Derived Materials and Technologies Series (Eds: M. A. Aegerter, M. Prassas), Springer, ISBN 978-3-030-13896-7, **2019**.

[30] M.L.C. Piedboeuf, A.F. Léonard, F.L. Deschamps, N. Job, *J Mater Sci* **2016**, *51*, 4358.

[31] M.L.C. Piedboeuf, A.F. Léonard, G. Reichenauer, C. Balzer, N. Job, *Microp M M. Micropor* **2019**, *275*, 278.

[32] C. Scherdel, G. Reichenauer, M. Wiener, *Microp M M. Micropor* **2010**, 132, 572.

[33] R. Alcántara, J.M. Jiménez-Mateos, P. Lavela, J.L. Tirado, *Electrochem Commun* **2001**, *3*, 639.

[34] E.M. Lotfabad, J. Ding, K. Cui, A. Kohandehghan, W.P. Kalisvaart, M. Hazelton, D. Mitlin, *ACS Nano* **2014**, *8*, 7115.

[35] H. Wang, W. Yu, N. Mao, J. Shi, W. Liu, *Microp M M. Micropor* **2016**, *227*, 1.

[36] X. Dou, I. Hasa, D. Saurel, C. Vaalma, L. Wu, D. Buchholz, D. Bresser, S. Komaba, S. Passerini, *Materials Today* **2019**, *23*, 87.

[37] C. Matei Ghimbeu, J. Górka, V. Simone, L. Simonin, S. Martinet, C. Vix-Guterl, *Nano Energy* **2018**, *44*, 327.

[38] A. Gomez-Martin, J. Martinez-Fernandez, M. Ruttert, M. Winter, T. Placke, J. Ramirez-Rico, *Chemistry of Materials* **2019**, *3*, 7288.

[39] C. del Mar Saavedra Rios, A. Beda, L. Simonin, C.M. Ghimbeu, In: Na-Ion Batteries (Eds. L. Monconduit and L. Croguennec), Wiley, **2021**, ISBN 978-1-789-45013-2, Ch. 3, p.101.

[40] H. Hamed, L. Henderick, B.G. Choobar, J. D’Haen, C. Detavernier, A. Hardy, M. Safari, IScience **2021**, 24, 103496.

[41] X. Chen, C. Liu, Y. Fang, X. Ai, F. Zhong, H. Yang, Y. Cao, Carbon Energy **2022**, 4, 1133.

[42] X. Dou, I. Hasa, D. Saurel, C. Vaalma, L. Wu, D. Buchholz, D. Bresser, S. Komaba, S. Passerini, *Materials Today* **2019**, *23*, 87.

[43] P. Mallet-Ladeira, PhD thesis, Université Toulouse 3 Paul Sabatier, France, **2014**.

3.6. Supplementary Information

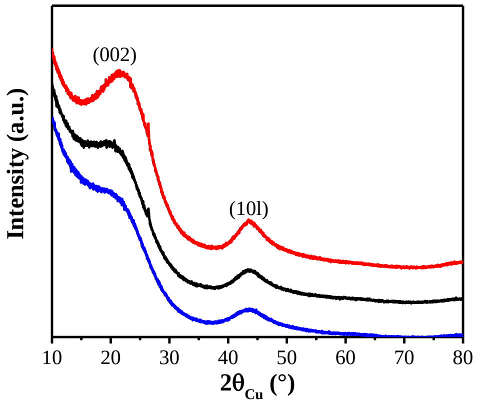

Figure S3.1. X-ray diffractograms of CX-LPH pyrolyzed at (▬) 800°C and at (▬) 900°C, and (▬) CX-LPH-C.

Table S3.1. Structural parameters of CX-LPH pyrolyzed at 800°C and 900°C, and CX-LPH-C samples.

			CX-LPH	**CX-LPH**	**CX-LPH-C**
Pyrolysis/processing temperature (°C)			800	900	900
XRD	**L_a**	(nm)	3.38 ± 0.01	3.34 ± 0.01	3.82 ± 0.01
	L_c	(nm)	1.09 ± 0.19	1.04 ± 0.16	0.99 ± 0.11
	$d_{(002)}$	(nm)	0.405 ± 0.001	0.409 ± 0.001	0.392 ± 0.001

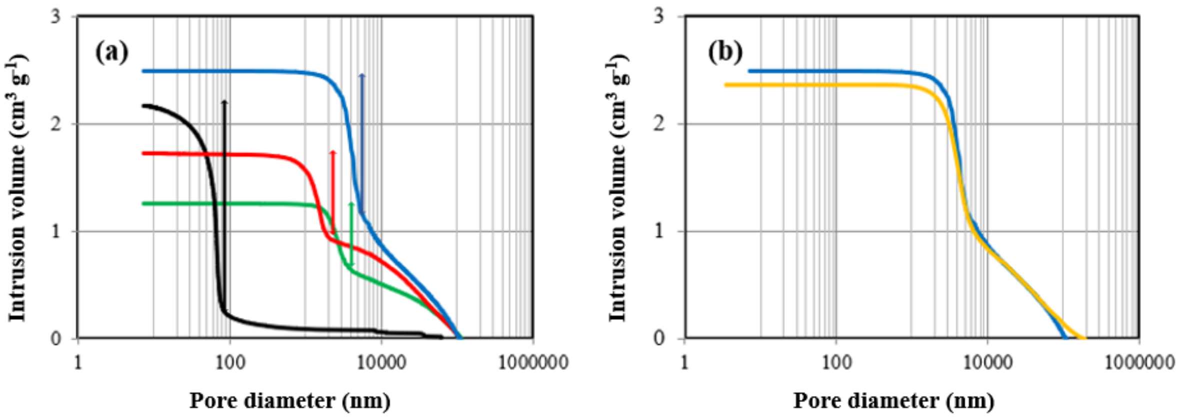

Figure S3.2. Hg porosimetry of (a) (▬) CX-450, (▬) CX-1500, (▬) CX-2500, (▬) CX-LPH (b) (▬) CX-LPH and (▬) CX-LPH-C. The intrusion volume corresponding to the meso/macropore volume of the material (excluding intrusion between particles) is indicated by vertical arrows.

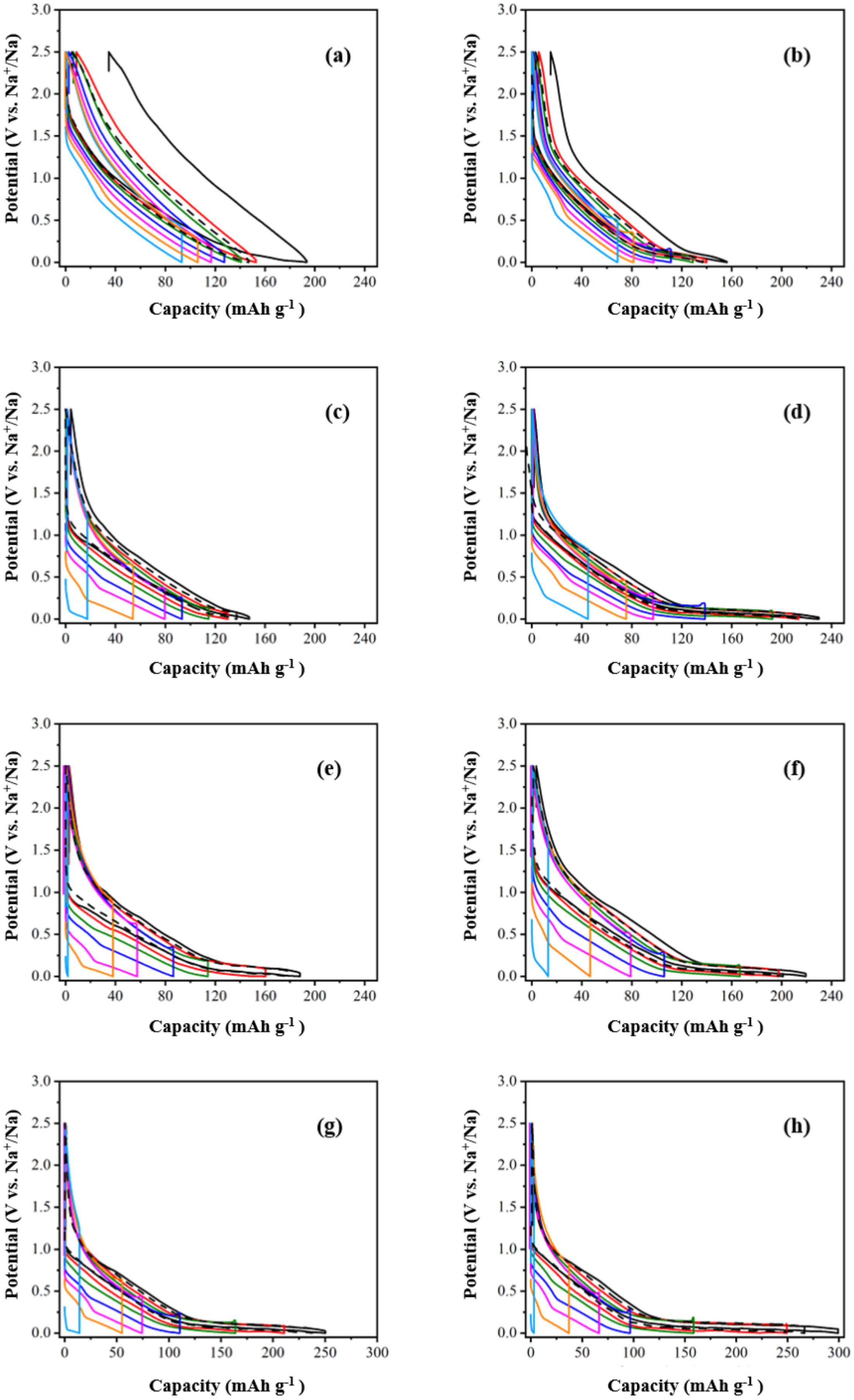
(a)
(b)
(c)
(d)
(e)
(f)
(g)
(h)
Potential (V vs. Na$^+$/Na)
Capacity (mAh g^{-1})
0.0
0.5
1.0
1.5
2.0
2.5
3.0
0
40
80
120
160
200
240
0
50
100
150
200
250
300

Figure S3.3. 3rd cycle in half-cell configuration of (a) CX-450, (b) CX-450-C, (c) CX-1500, (d) CX-1500-C, (e) CX-2500, (f) CX-2500-C, (g) CX-LPH et (h) CX-LPH-C at (▬) C/20, (▬)C/10, (▬)C/5, (▬) C/2, (▬) C, (▬) 2C, (▬) 5C and (– –) C/20.

Li$^+$ insertion-deinsertion in pristine CX and CVD-coated CX

The two materials selected correspond to samples CX-Ref (uncoated) and CX-CVD (CVD-coated) of reference [28]. The electrodes were prepared as detailed in reference [28] and in the present paper.

Half-cells were assembled in CR2032 coin cells [28], where the tested material acted as positive electrode and a Li-metal disk (MTI corp.) as the negative, reference and counter electrode. A Celgard® separator soaked with 80 µL of LP71 (1 M $LiPF_6$ in EC:DEC:DMC 1:1:1) electrolyte was placed in-between. The cell assembly was performed in an Ar-filled glove-box (MBraun). Cyclic voltammetry was performed at a scan rate of 0.05 mV/s between 0.005 and 1.5 V *vs.* Li$^+$/Li with a Biologic VMP3 multichannel potentiostat at a controlled temperature of 25°C.

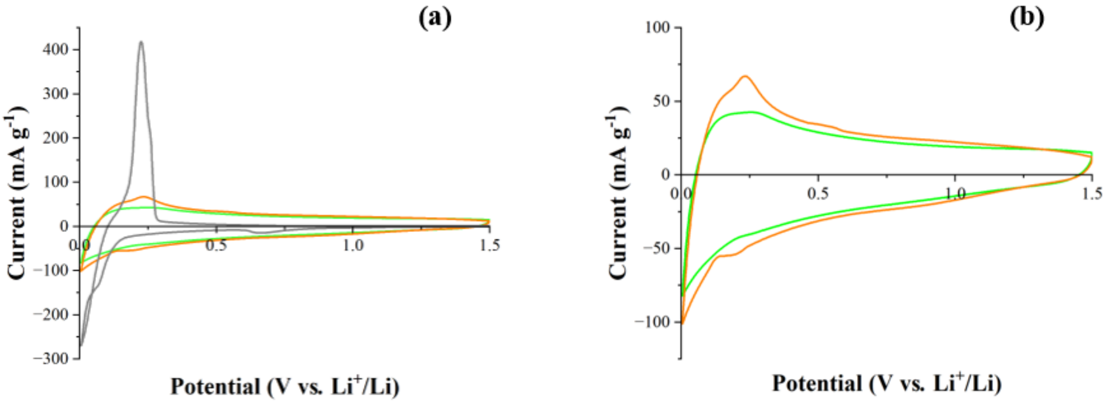

Figure S3.4. Cyclic voltammetries in LIB half-cell configuration for (▬) graphite, (▬) uncoated CX (CX-Ref [28]) and (▬) CVD-covered CX (CX-CVD [28]). (a) All three samples, (b) CX-Ref and CX-CVD alone, to better distinguish the insertion/deinsertion peak at ~0.25 V *vs.* Li$^+$/Li.

ANNEX 1

As discussed in Chapter 3, literature usually reports that the Initial Coulombic Efficiency (ICE) is related with the specific surface area of the carbon material, generally measured by adsorption techniques (*e.g.* the surface area determined by the Brunauer-Emmet-Teller equation, A_{BET}). However, our experimental results show that it is not correct given that samples with similar A_{BET} can have drastically different ICEs. In Chapter 3, it is hypothesized that the ICE should better be related with the carbon surface area accessible to the electrolyte, because that surface corresponds to the place where the Solid Electrolyte Interface (SEI) forms during the first lithiation. At the time of the article publication in Carbon[1], no experimental proof was available. However, when moving on to the experiments related to activated and/or coated samples presented in Chapter 4, it was decided to perform further electrochemical analyses to understand better what surface of the carbon material is in direct contact with the electrolyte, leading to the development of the SEI.

In that ambit, a different experimental setup was used: that setup corresponds to a supercapacitor-like device with two carbon electrodes instead of one carbon electrode and one sodium disc. In that setup, double-layer capacitance only is active as energy-storage mechanism. Data analysis can provide information about the extent of the interface between the electrolyte and the electrode which later will be related with the SEI, and thus the ICE.

Carbon xerogels prepared in Chapter 3 (CX-450, CX-1500, CX-2500 and CX-LPH, *i.e.* samples without secondary carbon layer coating) were used under the electrode form as described: all the manufacturing and assembly procedures were identical to those described in Chapter 3, apart from the fact that the two electrodes were carbon xerogel electrodes. Electrodes of similar masses were used in order to balance the surfaces. The separator (GF/D) and the electrolyte (NP30, *i.e.* 1 mol L^{-1} solution of sodium hexafluorophosphate in a mixture of ethylene carbonate and dimethyl carbonate (EC/DMC, 1:1 mass ratio)) remained the same.

Cyclic voltammetry (CV) was performed between cell voltages of -0.3 V and 0.3 V at 20 mV s^{-1} for all samples. The capacitance (in F g^{-1}) of the cell was calculated as[2]:

$$C = \frac{\int i(V)dv}{2\mu m \Delta V} \qquad \text{(A.1)}$$

where the integral, which corresponds to the area within the CV curve, is the total charge (A.V), μ is the scan rate (V/s), m is the total mass of active material in both electrodes (g) and ΔV is the potential window of cycling (V). The calculated capacitance was divided by the total active material mass (carbon xerogel in both electrodes in this case) to obtain the specific capacitance, C_{spec} (F g^{-1}). It should be noted that absolute capacitance values are quite dependent on the set-up (*e.g.* electrolyte nature and concentration) and conditions (*e.g.* potential window). Here, the experiments were designed to compare the samples with each other under conditions as close as possible to the half-cell setup, meaning that these capacitance values are not comparable with the those in literature dedicated to supercapacitors.

As a reminder, samples CX-450, CX-1500, CX-2500 and CX-LPH correspond to carbon xerogels with 50 nm, 1 µm, 1.3 µm and 2 µm nodule sizes, respectively. They all show similar surface areas measured *via* gas physisorption (A_{BET} ~650 m^2 g^{-1} by N_2 physisorption; S_{DFT} ~ 1100 m^2 g^{-1} by H_2 physisorption. However, upon cycling, ICE values were 29%, 46%, 63% and 80% for CX-450, CX-1500, CX-2500 and CX-LPH, respectively.

Figure A1 shows the cyclic voltammograms of supercapacitors built with the same materials. Sample CX-450 shows a tremendously higher capacitance than the other three carbon xerogels, given that the voltammogram surface is way larger (Figure A1a). The close-up (Figure A1b) indicates that the capacitance decreases as the nodule size increases.

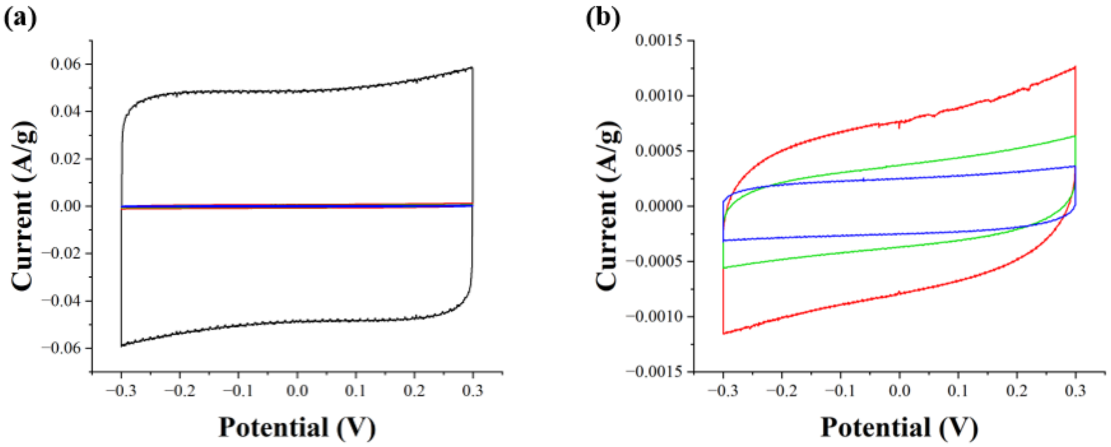

Figure A7. Cyclic voltammogram of (a) (▬) CX-450, (▬) CX-1500, (▬) CX-2500, (▬) CX-LPH in supercapacitor setup at 20 mV s^{-1}, (b) close-up without (▬) CX-450.

The specific capacitances (C_{spec}) calculated using Equation A.1 are reported in Table A.1, along with the values of reversible capacity (C_{rev}) and ICE measured in Chapter 3. C_{spec} equals 2.5 F g^{-1}, 0.037 F g^{-1}, 0.017 F g^{-1} and 0.012 F g^{-1} for the samples with 50 nm, 1 µm, 1.3 µm and 2 µm nodule sizes, respectively. The sample showing the highest C_{spec} (CX-450, 2.5 F g^{-1}) shows the lowest ICE value (29%); the ICE increases as C_{spec} decreases, and reaches up to 80% for CX-LPH. There is however no proportional relationship between C_{spec} and the total specific surface area of the materials, which remains almost constant. These results show that, even though the micropores within the nodules are accessible to N_2 or H_2, they are not accessible to the electrolyte. However, they are still being used by Na^+ ions since high reversible capacities (C_{rev}) were measured. It can be concluded that neither A_{BET} nor S_{DFT} can be related with the ICE because the electrolyte-carbon interaction surface is drastically different from that accessible to gases. These results confirm the hypothesis made in Chapter 3. More probably, the carbon-electrolyte contact surface would correspond to (i) the external nodule surface and (ii) a contribution from the micropores, assuming that their entrance remains accessible down to a limited penetration depth. Overall, the micropore volume would be more accessible to the electrolyte in the case of small nodules, if the penetration depth is considered constant. This seems to go in line with the results. Indeed, the capacitance is almost proportional to the external nodule surface, $S_{\mathrm{n,ext}}$, calculated considering spherical nodules, for samples CX-1500, CX-2500 and CX-LPH, indicating a low contribution of the micropores. However, the specific capacitance of CX-450 is around 250 times higher than CX-LPH while $S_{\mathrm{n,ext}}$ is only 50 times higher. This shows that the micropores of CX-450 are more accessible to the electrolyte than in the case of CX-LPH, and significantly contribute to both the capacitance and the SEI formation in half-cell setup. Those results also may explain why no plateau region can be seen for CX-450: micropores are probably significantly filled by SEI layer, making them inaccessible.

Table A3. Electrochemical performance of carbon xerogels.

Sample	C_{rev}[a] (mAh g^{-1})	ICE[a] (%)	C_{spec}[b] (F g^{-1})	$S_{n,ext}$[c] (m^2 g^{-1})
CX-450	164	29	2.500	91
CX-1500	143	46	0.037	5
CX-2500	206	63	0.017	3
CX-LPH	248	80	0.012	2

[a] Obtained by cycling in half-cell setup.

[b] Obtained by cycling in supercapacitor-like setup.

[c] External surface area calculated from geometric considerations.

References

[1] B. Karaman, H. Tonnoir, D. Huo, B. Carré, A.F. Léonard, J.C. Gutiérrez, M.L. Piedboeuf, A. Celzard, V. Fierro, C. Davoisne, R. Janot, N. Job, *Carbon* **2024**, *225, 119077*.

[2] B. Ranjan, D. Kaur, *Small* **2024**, *20*.

Chapter 4

Post-treatments on carbon xerogels for enhancing their performances as negative electrodes of Na-ion batteries

Abstract

Carbon xerogel (CX) with nodules size of ~2 µm was synthesized *via* polycondensation of resorcinol with formaldehyde in water, followed by pyrolysis at 800 °C. The obtained sample was subjected to surface treatments by Chemical Vapor Deposition (CVD) and/or CO_2 activation in order to fill/mask the pores with a secondary carbon layer or develop new micropores, respectively. This strategy aimed at understanding the impact of surface modification upon the performance of carbon xerogels as Na-ion battery negative electrode materials. The coating deposited by CVD was observed to display a more ordered structure with extended graphitic-like domains. However, due to its very high surface area, the activated sample displayed very low Initial Coulombic Efficiency (18%) and reversible capacity (62 mAh g^{-1}). Once the activated sample was covered with a thick carbon layer by CVD, the capacity reached up to 294 mAh g^{-1} with a high ICE, around 88%, and an enhanced insertion plateau at low voltage. Additionally, this activated-coated sample showed a high rate capability and much higher stability compared to the other samples. Such surface treatments can be used to optimize the performance of carbon materials used as negative electrodes of Na-ion batteries.

4.1. Introduction

Batteries play a crucial role for further electrification of the daily life, industry and transportation. Although Li-ion batteries (LIBs) are still the main player of the battery team, the limit of critical materials (Li and Co, but also Cu and graphite) shows that other options are needed[1][2]. In that context, Na-ion batteries (NIBs) can be seen as a promising candidate to help or maybe even overtake LIBs spot. Since sodium is much more abundant in the Earth's crust, the major problem of lithium extraction would not be so pronounced[3]. In addition to those environmental aspect, since Na does not alloy with Al at low voltages, Al can be used as current collector for both electrodes, eliminating the need of Cu, and therefore reducing the cost of the final product. Additionally, NIBs do not require Co; thus, limitations on critical materials would be much lower than in the case of LIBs[4]. However, even with all these advantages of NIBs compared to LIBs, the former is not very popular yet due to their lower power and energy density[5]. Therefore, current research focuses on increasing the total amount of energy supplied by NIBs per weight/volume.

Among the many strategies that can be followed to increase the energy density of NIBs, improving the negative electrode materials can be seen as the pivotal move. For this, carbonaceous materials are the first candidates that can be thought of. Graphite, which is widely used in LIBs, is however not suitable for Na-ion battery electrodes as its ability to intercalate Na^+ is very poor[6][7]. That issue can be avoided by using disordered carbon materials, a feature that can be found in hard carbons (HC). Hard carbons can be produced by pyrolysis of various precursors, generally oxygen-rich molecules or polymers. Those materials can be used as negative electrode of NIBs, can show capacities up to 320 mAh g^{-1} and possess different Na storage mechanisms which is quite interesting for practical applications[8][9]. However, electrolyte decomposition onto their surface leads to low initial coulombic efficiency (ICE) since hard carbons commonly display high specific surface areas[10][11]. Therefore, the main challenge with those materials is to improve their ICE, including strategies such as surface modifications to reduce the SEI formation area. In that ambit, it is important to notice that a better understanding of the actual electrode surface is needed. Indeed, in the literature[12], the ICE observed in half-cell is quite often linked to the specific surface area measured by gas sorption (*i.e.* the BET surface area), which at first sight makes sense since more surface area results in more SEI. However, recent work showed that materials with similar BET surface areas can display drastic differences in ICE[13]. One possible explanation could be that, although the carbon surface is reachable by gasses such as N_2, H_2 or CO_2 in adsorption experiments, it might not be the case for the liquid electrolyte in the final cell. This would result in the observation that adsorption data are not correlated to the final electrochemical performances. Additionally, the storage mechanism of Na^+ in hard carbons remains unclear, even though the slope region is ascribed to ion adsorption on carbons defects, and Na^+ intercalation between graphene layers while low-voltage plateau region is associated with cluster storage in micropores[14]–[17]. In turn, open micropores are generally the main contributors to the specific surface area measured by adsorption. Given the above-mentioned information, the ideal carbon material would display a large surface area accessible to Na^+ ions but not accessible to the electrolyte. This calls for a systematic study of the impact of the specific surface area on both the ICE and the capacity of hard carbon electrodes using model carbon materials such as carbon xerogels.

Carbon xerogels (CXs) are carbons that can be synthesized by evaporative drying and pyrolysis of organic gels (*e.g.* resorcinol-formaldehyde aqueous gels)[18]–[20]. Their structure consists of linked sphere-like microporous nodules which can be tailored in size, from a few nm to a few μm depending on the composition of the gel precursors' solution. As a result, their meso/macropore texture, which corresponds to the voids between the microporous nodules, can be tailored from a few nm to a few µm. Mesoporous CXs have been used in a previous work[11] as anode materials for NIBs, but their ICE was low due their high accessible specific surface area (~600 m^2 g^{-1}). However, their reversible capacity could reach relatively high values, around 200 mAh g^{-1} (at 37.2 mA g^{-1}). In order to improve the CX performances, the impact of the nodule size has also been investigated in the past: it has been reported that carbon xerogels with large nodule size (1-2 µm) that are produced at low pyrolysis temperature (800 °C) can lead to a quite good reversible capacity (248 mAh g^{-1}) and very high ICE (80%)[13]. This high ICE value was ascribed to the non-accessibility of the electrolyte to the micropores within the nodule, while the Na^+ ions can be stored within these micropores. Masking the micropores via the deposition of a secondary carbon layer by Chemical Vapor Deposition (CVD), led to even higher reversible capacity (298 mAh g^{-1}) and ICE (84%). Therefore, surface accessibility of the electrolyte seems to be the key to high performances of CXs as NIB electrode materials.

In order to get a deeper understanding of the CX surface impact on the electrochemical properties, the microporosity of CXs can be tuned in various ways. First, as mentioned above, CVD is an efficient method to close the open micropores by depositing a secondary carbon layer onto the outer nodule surface, thus limiting the accessibility of the electrolyte to the carbon nodules inner surface. Second, CO_2 activation can be used to increase the total surface area by formation of new micropores[21]. Indeed, CO_2 activation can be viewed as the exact opposite of what is typically required for an ideal electrode material. However, combination of these two procedures (i.e. CO_2 activation followed by CVD coating) can be beneficial given that it could lead to a large closed micropores volume, which is desired to obtain a large volume accessible to Na^+ but not to the electrolyte. Therefore, CO_2 activation would enhance microporosity and carbon coating by CVD would limit their accessibility to the electrolyte. In that manner, it could be possible to obtain a carbon xerogel with enhanced capacity and high ICE.

In this study, a carbon xerogel with large nodule size (~2.0 µm) and standard specific surface area (643 $m^2\ g^{-1}$) was activated *via* CO_2 in order to obtain increased microporosity, thus increased total specific surface area. Following this, the pores were closed with a secondary carbon layer *via* CVD in order to reduce the accessibility of the electrolyte to the nodule inner surface. The materials obtained after activation and after CVD-coating were characterized using various physico-chemical methods, and their electrochemical performance in NIB half-cells were determined. The results were compared to those obtained previously with the pristine CX and the same material after CVD treatment without any activation. The results highlight the impact of both post-treatments on the electrochemical performance of those hard carbons as NIB negative electrode materials.

4.2. Experimental

4.2.1. Carbon xerogel synthesis

Carbon xerogels (CXs) were prepared following a procedure described in a previous study[13]. First, a 35 wt.% aqueous solution of resorcinol (R, Merck) was prepared in a sealable glass flask. A 37 wt.% solution of formaldehyde (F) in water was then added to the mixture with a resorcinol/formaldehyde molar ratio of 0.5. The dilution ratio *D*, *i.e.* the water (including the water in F)/reactants molar ratio, was equal to 5.7. Note that, normally, sodium carbonate is added as basification agent to regulate the nodule size. However, for this study, no sodium carbonate was added in order to produce carbon xerogels under low pH conditions, so as to obtain materials with large nodule size[13]. The obtained mixture was stirred *via* magnetic stirrer for 1 h. Following the mixing, the sealed glass flask was put in an oven, at 85 °C for 72 h, for gelation and aging. Finally, the container was opened and put in a vacuum oven at 60 ºC to dry the gel. The pressure was progressively decreased down to 12 Pa, and the samples were left to dry overnight.

Following drying, organic xerogel monoliths were retrieved and ground to obtain a narrow particle size distribution. First, a coarse milling by hand using an agate mortar was performed; then, the organic gel particles were ground to fine powder using a Fritsch planetary mill (Mono Mill P6). The sample was ground at 400 rpm for 24 cycles of 1 min each, followed by 15 s of rest. Finally, the powder underwent pyrolysis at 800 ºC under N_2 with the following procedure in order to obtain the pristine carbon xerogel. The temperature was increased to (1) 150 ºC at 1.7 ºC min^{-1} and held for 15 min; (2) from 150 ºC to 400 ºC at 5 ºC min^{-1} and held for 60 min; and (3) from 400 ºC to 800 ºC at 5 ºC min^{-1} and held for 120 min. Finally, the oven was let to cool down to room temperature overnight.

The initial sample obtained after pyrolysis is denoted as LPH (low-pH carbon xerogel).

4.2.2. Physical activation with CO_2

The physical activation of the pristine carbon xerogel took place in the same tubular oven used for pyrolysis, switching N_2 to CO_2. The oven was supplied with nitrogen and carbon dioxide by a three-way valve in order to be able to switch between procedures. Once the pyrolysis process was done, the oven temperature was increased from 800℃ to 900℃ and the atmosphere was then switched from N_2 to CO_2. The procedure duration was 5 h and the gas flow rate was chosen equal to 0.004 mol min^{-1}. Finally, the atmosphere was switched back to N_2 for cooling and the sample was collected from the oven.

The activated sample is named LPH-A hereafter.

4.2.3. Carbon coating by chemical vapor deposition

Chemical Vapor Deposition (CVD) was performed in a stainless-steel tubular oven, following the process described in a previous study[13] and involving ethylene cracking at moderate temperature. The oven was first heated at 685 ºC under inert atmosphere (N_2, flow rate: 0.025 mol min^{-1}). The quartz boat holding the CX powder was introduced inside the oven once the target temperature was reached. The introduction of the quartz boat was done using a reverse flow system to maintain the protective inert atmosphere inside the oven. The reactive mixture was then introduced into the system (total flow rate: 0.082 mol min^{-1}), consisting of 80 % ethylene (Air Liquide N25, 0.066 mol min^{-1}) and 20 % N_2 (Air Liquide Alphagaz 1, 0.016 mol min^{-1}). The CVD treatment duration was set at either 30 or 60 min while the temperature was maintained at 685 °C. The atmosphere was then switched back to 100 % N_2 (flow rate: 0.025 mol min^{-1}) for purging after the coating process was completed. Finally, after complete elimination of ethylene, the oven temperature was increased to 900 ºC and held for 2 h. Then, the oven was cooled down under N_2 atmosphere, and the resulting powders were collected.

In total, three coated samples were produced: (i) non-activated LPH coated for 30 min (LPH-C30), (ii) activated LPH coated for 30 min (LPH-A-C30) and (iii) activated LPH coated for 60 min (LPH-A-C60). Table 4.1 summarizes the post-treatment conditions applied to the five carbons investigated in this study.

Table 4.4. Description of samples based on the surface modifications.

Sample	CO_2 activation	CVD coating
LPH	No	None
LPH-C30	No	30 min
LPH-A	Yes	None
LPH-A-C30	Yes	30 min
LPH-A-C60	Yes	60 min

4.2.4. Physicochemical characterization of carbon materials

The pore texture of the five CX powders was analyzed by N_2 adsorption-desorption measurements. Prior to the measurements, the samples were degassed under high vacuum (2 × 10^{-4} Pa) at room temperature for 5 h and at 270 °C for 2 h. The isotherms were collected at -196 °C using a Micromeritics ASAP 2420 analyzer. The specific surface area, A_{BET}, was calculated using the Brunauer-Emmett-Teller (BET) equation; in order to fulfill the Rouquerol criterion, adsorption data were taken over the relative pressure range of 0.01 to 0.1 for non-coated samples and 0.05 to 0.25 for CVD-coated samples. The Dubinin-Radushkevich equation was used to calculate the micropore volume, V_{μ}.

Hydrogen adsorption-desorption measurements were also carried out in order to assess in more detail the microporosity of the materials. The samples were degassed under high vacuum at 180 °C for 24 h before acquisition of the isotherms at -196 °C using a Micromeritics 3Flex analyzer. The 2D non-local density functional theory for heterogeneous surface (2D-NLDFT-HS) was applied simultaneously to the N_2 and H_2 adsorption isotherms using the SAIEUS software from Micromeritics to obtain the pore size distributions (PSDs). Textural properties such as the specific surface area (S_{DFT}), the total pore volume ($V_{\mathrm{T,DFT}}$), and the ultramicro-, supermicro- and mesopore volume ($V_{\mathrm{u\mu,DFT}}$, $V_{\mathrm{s\mu,DFT}}$, and $V_{\mathrm{meso,DFT}}$, respectively) were calculated from the obtained PSDs.

Mercury porosimetry was performed in order to obtain information about the CX meso-macroporosity as the N_2 adsorption technique is not suitable for the analysis of the largest pores of the materials. Measurements were performed with a Quantachrome Poremaster 60 in a pressure range of 0.01 to 400 MPa. The analysis was carried out for all samples in powder form. Analysis of the mercury intrusion data enabled determining the cumulated pore volume, V_{Hg}, and the PSD for pores with diameters larger than 3.8 nm. The PSD was calculated using the Washburn equation, valid for mercury intrusion without sample crushing; the values considered for the equation parameters were (i) an average value of liquid/solid contact angle of 140° and (ii) a mercury surface tension of 0.485 N m^{-1}.

SEM was used to observe the carbon morphology and determine the size of the carbon nodules, D_{n}. Images were obtained using a Tescan CLARA FEG-SEM at 15 kV under high-vacuum conditions. The samples were gold-coated in a sputtering device (Balzers, SCD004 sputter coater, Vaduz, Liechtenstein) and mounted with carbon adhesive prior to observation. Average nodule sizes were calculated based on a minimum of 30 measurements per sample.

To observe the effect of activation, the samples were observed by transmission electron microscopy (TEM) using a FEI Tecnai F20-S-TWIN microscope and a JEOL JEM-ARM 200F Cold FEG equipped with a spherical aberration probe corrector; both operations went through an acceleration voltage of 200 kV. Samples were prepared by suspending the powder in ethanol. Then, one or two drops of the suspension were deposited on a copper grid with a holey carbon film. High-resolution imaging was performed by controlling the electron dose in order to avoid electron beam-induced artefacts. Fast Fourier Transform on the HR-TEM images was used to obtain the d-spacing (d_{002}) between graphene layers.

X-ray diffraction was used to assess the crystallinity of the materials before and after CVD coating. Measurements were performed in Bragg-Brentano configuration for diffraction angles 2θ between 10° and 80° and a step size of 0.021° with a Bruker AXS D8 Advance diffractometer using a copper X-ray source ($\lambda_{\mathrm{K\alpha}}$ = 0.15418 nm). A shallow sample holder with a zero-background single-crystal Si plate was used to minimize sample transparency. The XRD patterns were analyzed using the model developed by Mallet-Ladeira[22]. The average lateral size of the graphene domains (L_{a}) and the average stacking thickness of the graphene layers (L_{c}) were determined using Scherrer's equation from reflections (10l) and (002), respectively.

Elemental analysis (EA) was performed in a Vario EL Cube analyzer (Elementar) to measure the bulk C, H, N, S and O contents. The samples were dried overnight at 105 °C to remove moisture, and then a small amount of material (~2 mg) was placed in the equipment to be burned in a furnace from which the gas was separated using trapping and chromatographic columns prior to measurements. A thermal conductivity detector quantified the gases, from which carbon, hydrogen and nitrogen contents can be calculated, with the exception of sulfur; the latter was measured with a specific infrared detector. The oxygen content was measured separately in another column using a similar procedure.

4.2.5. Electrode manufacturing

Xanthan gum (Sigma-Aldrich) was used as binder for the electrode manufacturing knowing that it preserves the pore texture (even micropores) of the carbon material in the electrode configuration, which means that the carbon specific surface areas measured on both the powder and the final electrode are the same[13]. Additionally, this procedure helps avoiding the use of toxic solvents and fluorinated polymers as binders. Prior to spraying, the ink was prepared in MilliQ water with 12 wt.% solids, including carbon xerogels and xanthan gum (Sigma-Aldrich) as a binder, in a weight ratio of 92:8. The mixture was magnetically stirred at room temperature for 3 h. The prepared ink was sprayed onto pre-weighed stainless-steel discs (Type 304, 15.5x0.55 mm, MTI corp.), used as current collectors, *via* airbrush (Harder & Steenbeck) and dried overnight at 60 °C. The obtained electrodes were then stored in a glove box under Ar. The mass loading of active material ranged from 1.5 mg cm^{-2} to 2 mg cm^{-2} for all samples.

4.2.6. Electrochemical characterization

Cyclic voltammetry (CV) was used to analyse the accessibility of the electrolyte to the electrode material surface. In that ambit, a supercapacitor-like setup with two carbon xerogel electrodes was built; electrodes of similar masses were used in order to balance the surfaces. CV experiments were conducted between cell voltage of -0.3 V and 0.3 V at 20 mV s^{-1} for all samples with commercial NP30 (1 mol L-1 solution of sodium hexafluorophosphate in a mixture of ethylene carbonate and dimethyl carbonate (EC/DMC, 1:1 mass ratio)) as electrolyte. However, for LPH-A, due to its high surface area, the sweeping rate was later decreased to 0.1 mV s^{-1}. The capacitance (in F g^{-1}) of the cell was calculated as[23]:

$$C = \frac{\int i(V)dv}{2\mu m\Delta V} \tag{4.1}$$

where the integral, which corresponds to the area within the CV curve, is the total charge (A.V), μ is the scan rate (V/s), m is the mass of the active material (g) and ΔV is the potential window of cycling (V). The calculated capacitance was divided by the total active material mass (carbon xerogel in both electrodes in this case) to obtain specific capacitance.

Electrochemical characterizations in half-cell configuration were done by using two-electrode coin-cell (CR2032) setup with carbon xerogel as the working electrode, sodium metal (Sigma-Aldrich) as counter and reference electrode, a glass fiber separator (Whatman, 1 mm-thick), and commercial NP30 (1 mol L^{-1} solution of sodium hexafluorophosphate in a mixture of ethylene carbonate and dimethyl carbonate (EC/DMC, 1:1 mass ratio)) as electrolyte. The coin cells were assembled in a glovebox under Ar atmosphere (O_2 and H_2O concentration < 1 ppm).

In order to evaluate the materials' performance at both low and high C-rates, two different series of tests were performed. For the first sequence, the cells were cycled between 0 V and 2.5 V *vs.* Na^+/Na for 5 cycles at C/20 (which corresponds to 18.6 mA g_{carbon}^{-1}, calculated considering the hypothetical formation of a NaC_6 phase during sodiation with a theoretical specific capacity of 372 mAh g^{-1}), 5 cycles at C/10, 5 cycles at C/5 and then for a further 100 cycles at C/20. A rate of C/n thus corresponds to the insertion of one Na^+ ion for 6 carbon atoms, in n hours. For the second series of tests, the first insertion/deinsertion cycles were carried out at a low C-rate (*i.e.* C/20) to enable the formation of SEI, and then the C-rate was gradually increased to 5C. Thus, the cells were cycled between 0 V and 2.5 V *vs.* Na^+/Na for 5 cycles at C/20, C/10, C/5, C/2, C, 2C and 5C, and then for a further 100 cycles at C/20.

4.3. Results and discussion

Powders were characterized with respect to their physicochemical properties as well as their electrochemical properties. The results for the pristine carbon xerogel (LPH) and the coated carbon xerogel (LPH-C30) were reused from an earlier study[13] as comparison baseline for the activated samples (without or with CVD coating).

4.3.1. Physicochemical properties of carbon xerogels

Mass changes of samples were calculated by weighing the powders before and after CVD and/or activation procedures. For the LPH sample, 4% increase in mass was observed after 30 min of CVD treatment. When LPH was treated under CO_2, the activated sample, LPH-A, displayed a mass loss around 50%. The mass uptake of LPH-A upon CVD treatment is much higher than in the case of LPH: 9% for 30 min and 19% for 60 min of CVD treatment. However, SEM images (Figure S4.1) do not show any significant difference on the nodule size, D_n, or on any feature of the material morphology, either after activation (Figure S4.1b) or after coating (Figures S4.1c to S4.1e) compared to the pristine carbon xerogel sample LPH (Figure S4.1a).

All samples were observed by Transmission Electron Microscopy (TEM) to distinguish the carbon layers organization (Figure 4.1). As observed before[13], coating by CVD seems to introduce a more ordered structure. Indeed, one can observe more organized carbon layers near the outer surface of the nodule. Especially for LPH-A-C60 sample, very long graphene-like sheets, about 10 nm long and a few nm thick, can be observed. The sheet pilings appear shorter and thinner in the case of sample LPH-C30. Meanwhile, activated samples seem to display onion-like structures. These onion-like structures have been observed before in literature[24][25]

N_2 and H_2 adsorption were used to understand the micro-mesoporous texture as well as to determine the specific surface area of the samples (Figure 4.2). The reference sample (LPH) is strictly microporous, with a specific surface area A_{BET} equal to 643 m² g^{-1} and a micropore volume V_μ of 0.25 cm³ g^{-1} (Table 4.2). CO_2 activation does not modify the pore texture of the carbon xerogel in terms of pore type as LPH-A sample remains strictly microporous (type I isotherm). However, as expected, one observes an increase of specific surface area, up to 853 m^2 g^{-1}. The micropore volume increases as well, up to 0.32 cm³ g^{-1}. CVD coating induces significant changes in the low-pressure region corresponding to micropores, especially for the LPH-C30 sample. As observed in a previous study[13], the carbon coating produced *via* CVD blocks the micropores and reduces the total specific surface area. The A_{BET} value decreases down to 2 m^2 g^{-1} after 30 min of CVD treatment on sample LPH. However, when the same duration of CVD treatment is applied to the LPH-A sample, A_{BET} only decreases from 853 to 504 m^2 g^{-1} (sample LPH-A-C30), while V_μ is still equal to 0.20 cm³ g^{-1}. This shows that the micropore surface is not entirely covered by the carbon coating. Therefore, in the case of the activated sample, a longer CVD duration is needed to fully mask the micropores. Indeed, 60 min of coating process decreases the specific surface area and the microporous volume down to 30 m^2 g^{-1} and 0.03 cm³ g^{-1}, respectively (sample LPH-A-C60). Given the higher mass uptake, it is possible that all the micropores are blocked, the remaining surface corresponding to the coating roughness, even though no significant morphological difference can be seen on the SEM images (Figure S4.1). Another important difference for LPH-A-C60 is reflected on the N_2 adsorption isotherm shape as it exhibits a small volume of meso/macropores (type I + type II isotherm). Since both uncoated materials (LPH and LPH-A) show no mesoporosity at all, the newly introduced mesoporous structure could again come from the thicker coating of LPH-A-C60 (Figure 4.2a).

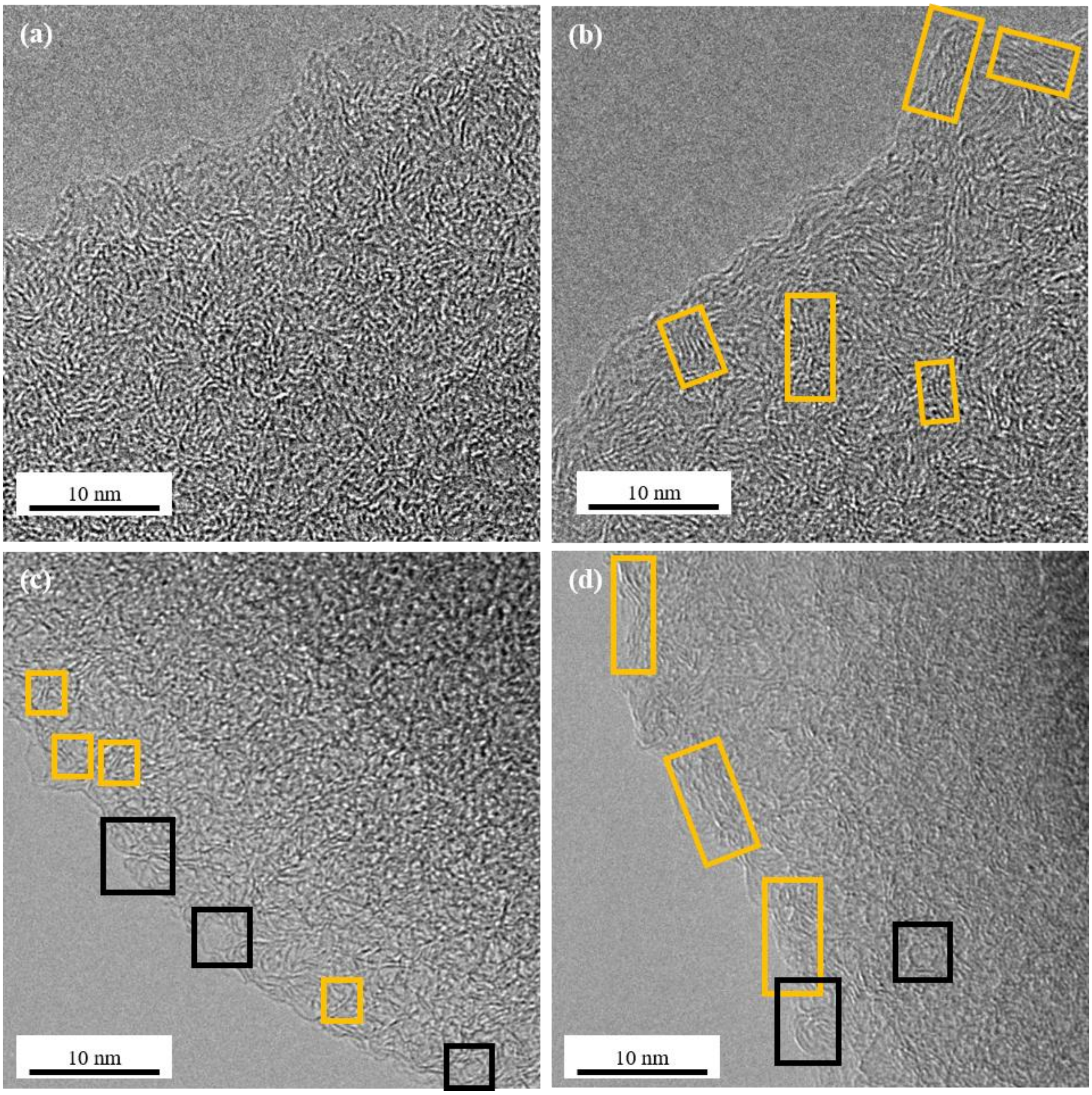

Figure 4.1. TEM images of (a) LPH, (b) LPH-C30, (c) LPH-A, (d) LPH-A-C30. In orange: turbostratic domains. In black: onion-like structures.

H_2 adsorption isotherms are displayed on Figure 4.2b while the cumulative pore volume as a function of pore width, *w*, as well as the derivative pore size distribution, calculated by combination of N_2 and H_2 adsorption isotherms, are shown in Figures 4.2c and 4.2d, respectively. The total specific surface area of the samples, S_{DFT} and the pore volume distribution among the mesopores, supermicropores and ultramicropores ($V_{meso,DFT}$, $V_{s\mu,DFT}$ and

$V_{\mathrm{u\mu,DFT}}$, respectively) are displayed in Table 4.3. Similar to the N_2 adsorption isotherms, an increase of S_{DFT} can be observed after CO_2 activation, from 1113 m^2 g^{-1} for sample LPH to 1535 m^2 g^{-1} for LPH-A sample. This modification mainly corresponds to an increase of the ultramicroporous volume (size < 0.7 nm). As expected, CVD treatment is observed to be an effective way to mask/fill micropores. Indeed, the S_{DFT} value of LPH-C30 decreases down to 69 m^2 g^{-1}. LPH-A-C30 and LPH-A-C60 display values of S_{DFT} equal to 1149 m^2 g^{-1} and 238 m^2 g^{-1}, respectively. Note finally that an increase of $V_{\mathrm{meso,DFT}}$ can be observed for LPH-A-C30 and LPH-A-C60, which confirms the observations on the N_2 isotherms.

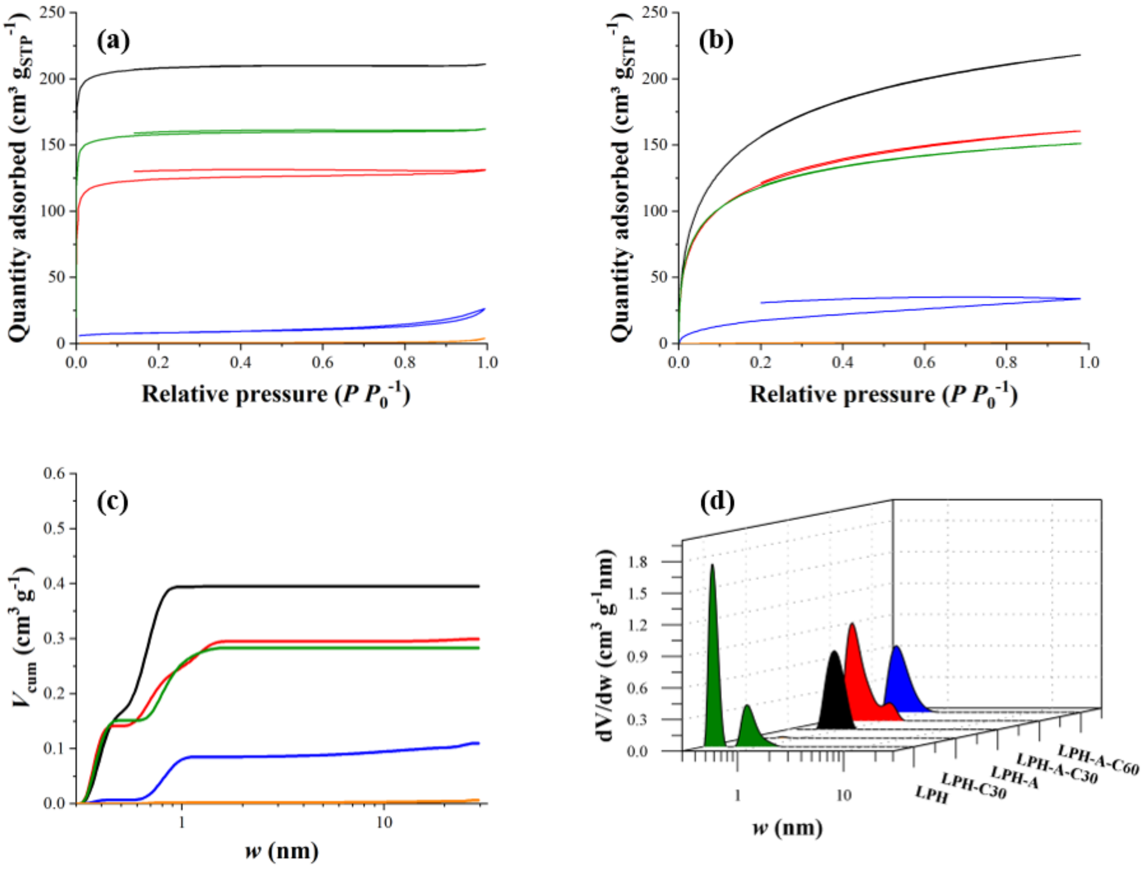

Figure 4.2. Pore texture analysis from gas sorption. (a) N_2 and (b) H_2 adsorption-desorption isotherms. (c) Cumulative and (d) differential pore volume distributions of (🟩) LPH, (🟧) LPH-C30, (⬛) LPH-A, (🟥) LPH-A-C30 and (🟦) LPH-A-C60.

Additionally, He pycnometry was thought to be used as another characterization method. However, and as observed previously[13], the reliability of the method in order to understand volume of closed pores may be questioned given the instability and non-reproducibility of the measurements. Such measurements issue could be related to the slow kinetics of He penetration in very small pores (ultramicropores) and to the impossibility to perform a thorough degassing of our samples prior analysis. Other techniques should be envisaged to determine the volume of closed pores (SAXS for example).

Hg porosimetry curves of the powder samples are shown in Figure 4.3; they are presented as cumulative pore volume as a function of the pressure. Average pore sizes were calculated using Washburn's law from the intrusion step visible between 2 and 5 µm, the volume change occurring at lower pressure being attributed to powder compaction. Average pore diameters (d_P) were calculated equal to 3.9 µm for all samples (Table 4.2). These pores correspond to the voids between the carbon nodules observed in Figure S4.1., and no significant change is noticed after both activation and CVD coating.

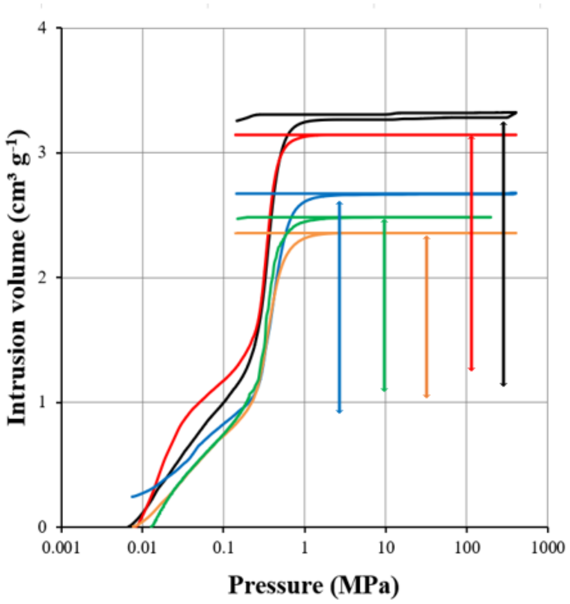

Figure 4.3. Mercury porosimetry curves of samples (🟩) LPH, (🟧) LPH-C30, (⬛) LPH-A, (🟥) LPH-A-C30 and (🟦) LPH-A-C60. The vertical arrows represent the mercury intrusion step. Volume increase at lower pressure is due to powder compaction.

Table 4.2. Morphological parameters and pore texture data determined of the samples.

Morphological parameters			**Textural parameters**						
			Determined by N_2 adsorption at -196 °C		Determined by combination of N_2 and H_2 adsorption at -196 °C				
Sample	D_n[a] (μm)	d_p[b] (μm)	A_{BET}[c] (m² g⁻¹)	V_μ[c] (cm³ g⁻¹)	S_{DFT}[d] (m² g⁻¹)	$V_{u\mu,DFT}$[d] (cm³ g⁻¹)	$V_{s\mu,DFT}$[d] (cm³ g⁻¹)	$V_{meso,DFT}$[d] (cm³ g⁻¹)	$V_{T,DFT}$[d] (cm³ g⁻¹)
LPH	2.0	3.9	643	0.25	1113	0.16	0.12	0	0.28
LPH-C30	2.0	3.9	2	<0.01	69	0.00	0.02	0	0.05
LPH-A	2.0	3.9	853	0.32	1535	0.31	0.09	0	0.40
LPH-A-C30	2.0	3.9	504	0.20	1149	0.19	0.10	0.004	0.30
LPH-A-C60	2.0	3.9	30	0.03	238	0.019	0.07	0.024	0.11

[a] D_n: average nodule size calculated from SEM images.

[b] d_p: pore diameters measured by Hg porosimetry.

[c] A_{BET}: BET and V_μ: micropore volume, calculated from nitrogen adsorption-desorption isotherms at -196 °C.

[d] S_{DFT}, $V_{u\mu,DFT}$, $V_{s\mu,DFT}$, and $V_{T,DFT}$: specific surface area, ultramicropore, supermicropore, and total pore volume calculated from the PSD obtained from nitrogen and hydrogen adsorption isotherms at -196 °C.

The XRD patterns of the samples are shown in Figure 4.4. Note that the curves were shifted upwards for better legibility. Overall, all the samples display the same peaks at the same diffraction angles. Namely, one observes a first broad band at around $2\theta = 23°$ (002) and a second broad band around $2\theta = 43°$ (10l); both of these wide peaks are quite common for highly disordered carbons. Another peak around $2\theta = 26°$ can be observed for samples LPH-C30 and LPH-A-C60. This peak, which is not always observed for CVD-coated samples, is in fact ascribed to carbon deposits formed outside of the carbon xerogel during the CVD procedure (*e.g.* formed onto the quartz boat or on the oven walls); it is considered as an impurity. Meanwhile, the intensity of the (002) band is higher for all CVD-coated samples, probably due to the contribution of the coating. However, CO_2 activation leads to the opposite effect as the intensity of (002) band is much lower for the LPH-A sample than for pristine LPH. The complete list of structural parameters values is shown in Table 4.3. The coherence length, L_a, is observed to increase after CO_2 activation, from 3.38 nm (LPH) to 3.71 nm (LPH-A). Upon CVD treatment, L_a increases after 30 min (LPH-C30: 3.82 nm; LPH-A-C30: 4.22 nm), and remains unchanged when the CVD time is prolonged to 60 min (LPH-A-C60: 4.22 nm). Regarding L_c, one can notice an increase for sample LPH-A compared to sample LPH, which shows that CO_2 activation might be increasing the average stacking thickness of the graphene layers. On the contrary, L_c decreases for the coated samples. Finally, a slight decrease in the graphene interlayer distance, $d_{(002)}$, can be observed for carbon coated samples compared with their uncoated counterparts. Overall, the structural changes observed via both XRD and TEM does not point to a significant change.

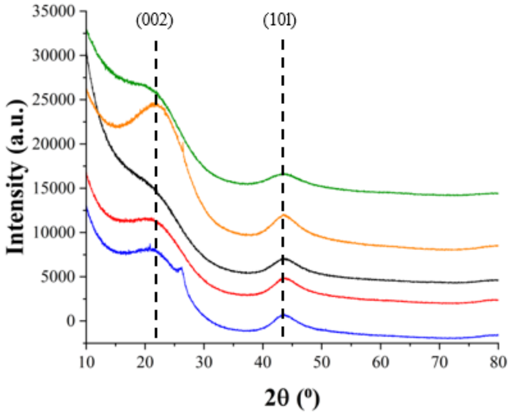

Figure 4.4. X-ray diffractograms of (🟩) LPH, (🟧) LPH-C30, (⬛) LPH-A, (🟥) LPH-A-C30 and (🟦) LPH-A-C60.

Table 4.3. Structural parameters of the samples.

			LPH	**LPH-C30**	**LPH-A**	**LPH-A-C30**	**LPH-A-C60**
XRD	d_{002}	(nm)	0.405 ± 0.001	0.392 ± 0.001	0.400 ± 0.001	0.398 ± 0.001	0.401 ± 0.001
	L_c	(nm)	1.09 ± 0.19	0.99 ± 0.11	1.32 ± 0.16	1.10 ± 0.09	1.15 ± 0.05
	L_a	(nm)	3.38 ± 0.01	3.82 ± 0.001	3.71 ± 0.06	4.22 ± 0.03	4.22 ± 0.02
TEM	d_{002}	(nm)	0.409 ± 0.040	0.392 ± 0.037	4.07±0.090	-[a]	3.97±0.070

[a] Not determined since LPH-A-C30 and LPH-A-C60 has same surfaces but LPH-A-C60 has thicker coating.

The elemental analysis (Table 4.4) shows a significant difference in terms of oxygen content. The low oxygen content (2.4 wt.%) of LPH increases by 50% upon CO_2 activation as LPH-A sample contains 3.6 wt.% of oxygen. However, although CVD coating slightly increases the oxygen content of LPH sample, from 2.4 to 2.8 wt.% for LPH-C30, it reduces the oxygen content of LPH-A sample to 3.2 wt% and 2.3 wt.% after 30 min and 60 min of CVD treatment, respectively. In the meantime, a general trend can be observed regarding hydrogen content: overall, the CVD-coated samples contain less hydrogen and more carbon than their uncoated counterparts. This trend agrees well with the observations made by TEM of longer graphitic-like domains after CVD coating.

Table 4.4. Elemental analysis of carbon xerogels before and after CO_2 activation and CVD treatment.

Sample	**N** (wt.%)	**C** (wt.%)	**H** (wt.%)	**S** (wt.%)	**O** (wt.%)
LPH	0.1	96.2	0.9	0.0	2.4
LPH-C30	0.2	98.0	0.3	0.0	2.8
LPH-A	0.1	93.6	0.6	0.0	3.6
LPH-A-C30	0.1	95.2	0.5	0.0	3.2
LPH-A-C60	0.4	97.2	0.4	0.0	2.3

4.3.2. Electrochemical properties of the carbon xerogels

Following the morphological and structural characterization, the electrochemical performance of the samples was assessed as negative electrode materials for Na-ion battery in a half-cell setup. Data are gathered in Table 4.5. $C_{\text{tot, disch}}$ represents the total capacity at first discharge (*i.e.* first sodiation) while C_{rev} is the capacity delivered by the first charge (*i.e.* first desodiation). The irreversible capacity, C_{irrev}, is calculated as the difference between $C_{\text{tot, disch}}$ and C_{rev}. Meanwhile, the Initial Coulombic Efficiency, ICE, is calculated as the ratio between C_{rev} and $C_{\text{tot, disch}}$. Finally, capacities in both the sloping region (above 0.1 V vs. Na^+/Na) and low-voltage plateau (below 0.1 V) of the first discharge (*i.e.* first sodiation) curve are reported as C_{slope} and C_{plateau}, respectively. Note that, in some cases, two distinct sloping regions were detected. C_{slope} is thus divided into C_{slope1} and C_{slope2} in Table 4.5. Curves corresponding to the first cycle are shown in Figure 4.5. Additionally, cyclic voltammetry was performed in a symmetrical supercapacitor setup in order to understand the electrolyte accessibility to the electrode material surface; in that ambit, the specific capacitance, C_{spec} is calculated by using Equation 4.1. Cyclic voltammograms are shown in Figure 4.6. Finally, the capacity retention of electrodes after various C-rate cycling is reported as C_{ret}; this parameter compares the first 5 cycles at C/20, at the start of cycling, and the last 5 cycles at C/20 after the various C-rate cycling sequence in order to measure stability of the electrodes. The overall results (capacity and faradaic yield *vs.* cycle number and C-rate) are shown in Figure 4.7.

The total discharge capacities, $C_{\text{tot, disch}}$, are close to each other for all samples: values are around 300-357 mAh g^{-1} (Table 4.5, Figure 4.5). However, the reversible capacities at first cycle, C_{rev}, and therefore the ICEs are strikingly different. The LPH sample shows C_{rev} equal to 248 mAh g^{-1}, which corresponds to 80% ICE. After 30 min of CVD treatment, the reversible capacity of LPH-C30 is measured as 298 mAh g^{-1} (84% ICE). As indicated previously[13], the difference in reversible capacity (248 *vs.* 298 mAh g^{-1}) is probably due to micropore closing by CVD and thus to a larger volume of closed micropores in LPH-C30[13] Since N_2 adsorption shows tremendous A_{BET} difference between these two samples (643 *vs.* 2 m^2 g^{-1} for LPH and LPH-C30, respectively), one could have expected a huge modification of ICE as well, which is not the case; this indicates that A_{BET} is not directly related to ICE values. It must be pointed out that our earlier study also showed that nodules with different sizes could reach different ICEs (29% for 50 nm nodule size *vs.* 80% for 2 µm nodule size) even though these CX carbons display very similar specific surface areas, as measured by N_2 gas adsorption (A_{BET} ~600 m^2 g^{-1}), with a majority of micropores. Therefore, it was proven that the ICE cannot be directly correlated with A_{BET}. The hypothesis behind that peculiar result was that the electrolyte does not always access the micropores, although the latter are open and reachable by N_2 or H_2 gases; this hypothesis will be discussed below. In contrast, LPH-A sample shows very low reversible capacity, 62 mAh g^{-1}, which corresponds to 18% ICE. This is not surprising at first sight given the surface increase. However, upon activation, A_{BET} increased by 30% only (from 643 to 853 $m^2\ g^{-1}$), and S_{DFT} by 38% (from 1113 to 1535 $m^2\ g^{-1}$); this shows again that specific surface area measured by gas adsorption is not a good indicator of the ICE obtained in half-cell. This calls for the determination of the surface to be considered for the development of the Solid Electrolyte Interphase (SEI). Much probably, CO_2 activation does not only develop micropores (essentially ultra-micropores, see Table 4.2), but also makes some of them more accessible to the electrolyte, either by enlargement of the openings or by modification of the carbon surface properties. Finally, like in the case of the LPH sample, the impact of the secondary carbon layer on the reversible capacity and ICE of the activated sample is striking. Indeed, LPH-A-C30 sample displays 66% ICE, which is a good improvement compared to LPH-A (18%). However, as observed from the adsorption data, LPH-A-C30 sample still displays a large surface area that remains uncovered by the CVD-deposited carbon layer, as A_{BET} remains high (504 $m^2\ g^{-1}$). The relatively low ICE value points at an easier access to the carbon surface compared to the pristine carbon xerogel, LPH. Finally, a longer CVD treatment duration (60 min) leads to decreasing further the specific surface area (LPH-C-60: A_{BET} = 30 $m^2\ g^{-1}$; S_{DFT} = 238 $m^2\ g^{-1}$). Obviously, covering the micropores helps improving the ICE and leads to very high reversible capacities given that LPH-A-C60 reaches a C_{rev} of 294 mAh g^{-1} with 88% ICE, the highest values for all samples although very close to those observed for LPH-C30 (C_{rev} of 298 $m^2\ g^{-1}$ and ICE equal to 84%). As a general conclusion, the development of open micropores by CO_2 activation obviously deteriorates the electrochemical properties of the carbon xerogels, even though the ICE and C_{rev} modification cannot be directly related to the increase of specific surface area. However, covering the micropores, either of the pristine sample or of the activated counterpart, by a secondary carbon layer using CVD is beneficial to both ICE and C_{rev}. Note also that the C_{rev} and ICE values obtained are quite remarkable for samples heat treated below 1000°C. Indeed, hard carbons are generally processed at 1200-1800°C and their ICE and capacity usually increase when treated at higher temperatures [27]. Additionally, the oxygen content and other heteroatoms are known to affect the ICE of the electrodes. In that respect, a lower oxygen content can be seen for samples LPH-A-C60, LPH and LPH-C30 compared to the others. These three samples are also showing very high ICE compared to LPH-A and LPH-A-C30, which could reveal that the CO_2 activation process leads to the formation of O-rich surface groups, the latter being responsible for irreversible reaction with sodium. XPS experiments are under progress to further investigate the surface chemistries of the post-treated carbon samples.

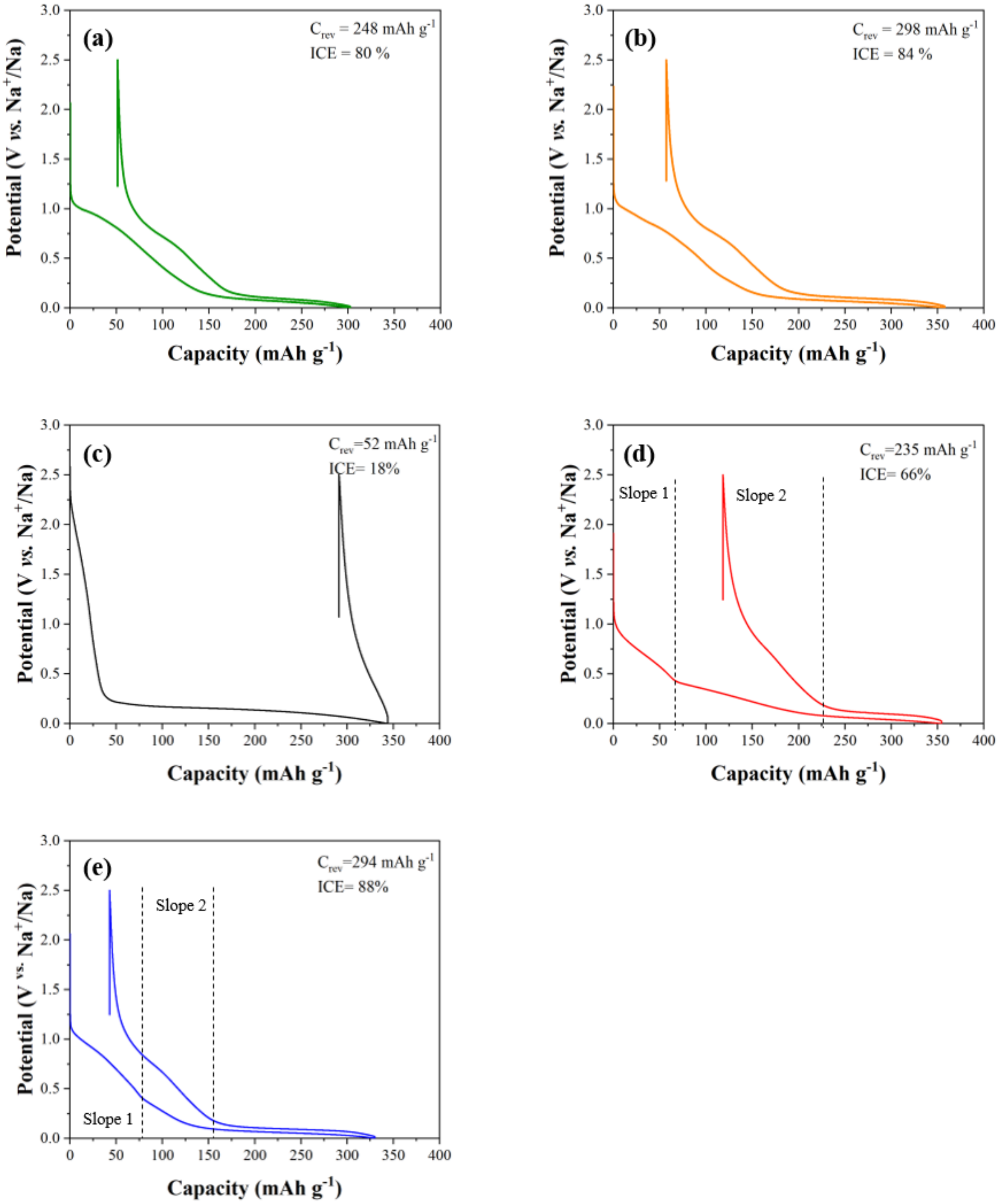

Figure 4.5. Galvanostatic charge-discharge profiles of the samples: (a) (▬) LPH, (b) (▬) LPH-C30, (c) (▬) LPH-A, (d) (▬) LPH-A-C30, (e) (▬) LPH-A-C60. Half-cells with NP30 electrolyte, cycling at C/20 (corresponding to 18.6 mA g$_{carbon}^{-1}$).

In order to better understand the discrepancy between surfaces measured by gas sorption and ICE, the electrolyte accessibility to the electrode surface was studied by cyclic voltammetry (CV) using symmetrical supercapacitor-like setup (Figure 4.6). Note that the absolute capacitance values are very dependent on the set-up and conditions, including the nature of the electrolyte. Here, the purpose of the CV experiments was to compare the samples to each other in a configuration that remains close to that of the half-cell, meaning that capacitance values are not comparable with those found in literature for carbon xerogels-based supercapacitors[28]. The LPH sample shows 0.012 F g^{-1} specific capacitance compared to 0.017 F g^{-1} for LPH-C30; those values are very close. The capacitance should be directly proportional to the electrolyte/carbon surface. Given the huge difference of measured specific surface areas (A_{BET} equal to 653 and 2 m² g^{-1} for LPH and LPH-C30, respectively), it is quite clear that the electrolyte/carbon surface does not corresponds to A_{BET}. In the case of the LPH-C30 sample, there is not much ambiguity: given that the micropores are not even accessible to N_2, the surface that can be in contact with the liquid electrolyte corresponds only to the external nodule surface, $S_{\mathrm{n,ext}}$, which was geometrically calculated as equal to 2 m² g^{-1}[13]. In the case of the LPH sample, and given the value of capacitance similar to that of LPH-C30, the electrode/electrolyte interface area should be of the same order of magnitude. This clearly indicates that the electrolyte does not enter the micropores in sample LPH, and that the electrode/electrolyte interface probably corresponds to the carbon nodule external surface as well. For LPH-A sample, a significant increase of specific capacitance is observed, up to 0.27 F g^{-1}. This can be explained by the increase of micropores volume and surface with CO_2 activation. However, the increase of capacitance between LPH-C30 and LPH-A (~ 15 times) is not proportional to the increase of specific surface area (multiplied by 426). Like in the case of sample LPH, it is quite clear that all the micropores of sample LPH-A are not filled with the electrolyte, even though a much larger surface is available compared to sample LPH. After CVD coating, the specific capacitances of the activated samples drop back to 0.035 F g^{-1} for LPH-AC30 and 0.036 F g^{-1} for LPH-A-C60. Interestingly, it seems that the contact area between the electrolyte and the electrode material slightly increases from LPH to LPH-C30 and from LPH-A-C30 to LPH-A-C60. In parallel, some mesoporosity was detected in the case of LPH-A-C60. This could mean that the structure of the carbon coating presents some roughness that would increase the electrolyte/electrode interface. However, an increase of electrolyte/carbon contact area is expected to lead to lower ICE, due to SEI formation, which is not the case here. On the contrary, ICE slightly increases with coating (from 80 to 84% for LPH and LPH-C30, and from 66 to 88% from LPH-A-C30 to LPH-A-C60). The SEI layer formation is actually highly dependent on the reactivity of the electrolyte over the electrode material. It has been mentioned in literature that more ordered carbon structures show improved ICE performances as Na-ion battery anodes[10], pointing towards a lower reactivity of ordered carbon surfaces with regard to SEI formation. Therefore, the surface of the CVD carbon layer is probably less reactive than that of the (activated) carbon xerogel.

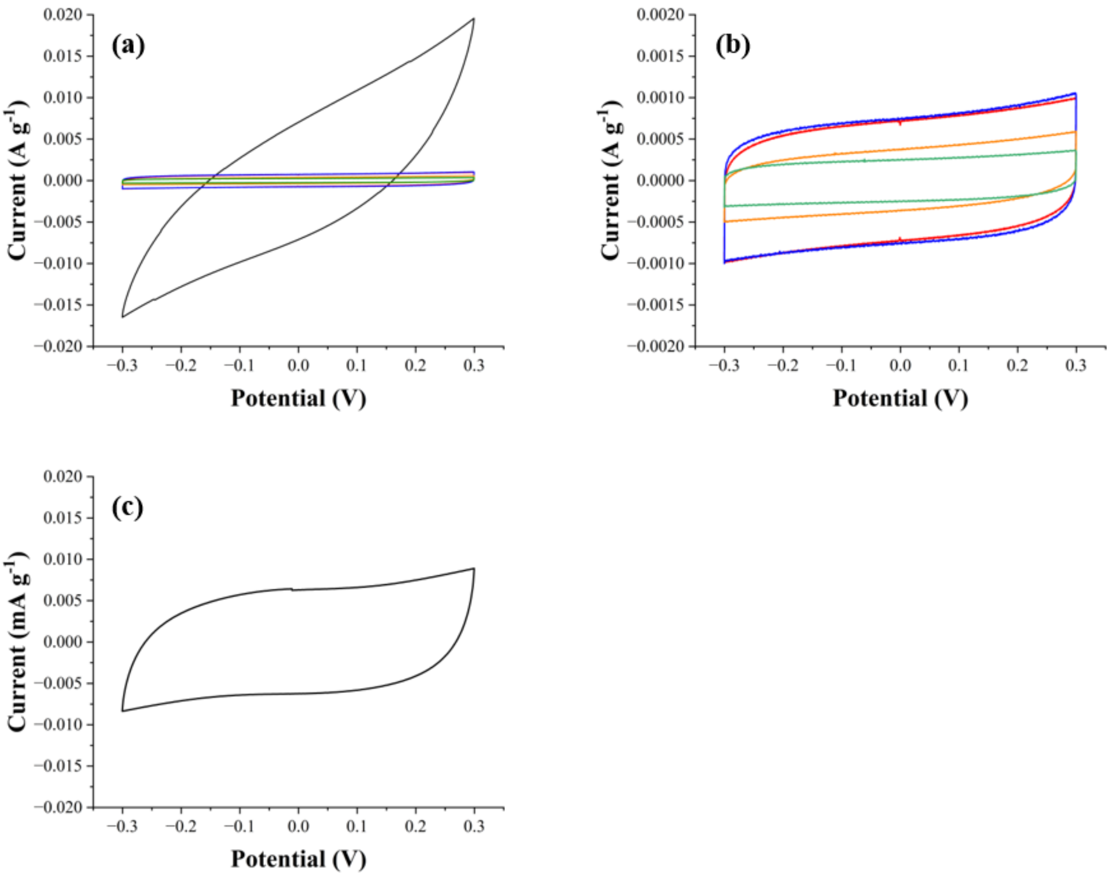

Figure 4.6. Cyclic voltammograms in supercapacitor setup. (a) (🟩) LPH, (🟧) LPH-C30, (⬛) LPH-A, (🟥) LPH-A-C30, (🟦) LPH-A-C60 at 20 mV s^{-1}. (b) Close-up of samples without LPH-A-C60 at 20 mV s^{-1} scan rate. (c) LPH-A at 0.1 mV s^{-1} scan rate.

Coming back to the galvanostatic profiles (Figure 4.5), some differences are also observed in the curve shape of the various samples. Firstly, LPH and LPH-C30 profiles looks very similar to each other as both show a slope region and a plateau region (Figures 4.5a and 4.5b). However, one can detect an increase of the length of the plateau region after CVD treatment, reflecting the impact of micropores closing. The activated sample, LPH-A, displays a very different profile (Figure 4.5c) with almost no plateau but a very long slope region for the first sodiation. As discussed before, the capacity of LPH-A is highly irreversible due to its very high surface area, partly accessible to the electrolyte. Similar to what has been observed before on the non-activated xerogel, the effect of coating is visible again on the galvanostatic profiles as both LPH-A-C30 and LPH-A-C60 show a plateau and two clearly distinct slope regions around 0.8 V and 0.3 V (Figures 4.3d and 4.3e) that are named “slope region 1” and “slope region 2” hereafter. Although the dominant storage mechanisms on these regions are still under debate, LPH-A-C30 shows a longer “slope 2” region compared to LPH-A-C60 (140 mAh g^{-1} *vs.* 77 mAh g^{-1}) while “slope 1” region is similar for both samples (68 mAh g^{-1} *vs.* 66 mAh g^{-1}). This 2-slope profile however disappears after the first sodiation: the slope change is barely visible upon first desodiation, and totally disappears on the second sodiation (Figure S4.2). Therefore, it is much probable that the presence of two distinct slope regions at first cycle is related with the SEI layer formation. In the meantime, LPH-A-C60 sample shows a very high plateau capacity (159 mAh g^{-1}). This is considerably higher than LPH (99 mAh g^{-1}), LPH-C30 (129 mAh g^{-1}) and LPH-A-C30 (108 mAh g^{-1}).

Compared to their full reversible capacities, plateau capacities correspond to 39%, 43%, 36% and 54% for electrodes LPH, LPH-C30, LPH-A-C30 and LPH-A-C60, respectively (Table 4.5). LPH-A-C30 displays the lowest plateau ratio (36%) probably due to micropores still not being masked completely. These results show indeed that forming new micropores by CO_2 activation and closing them with a carbon layer *via* CVD increase the closed micropores volume and leads to better electrochemical performances of the carbon xerogels.

Finally, the electrodes were cycled at different C-rates in order to understand the effect of activation and coating thickness on the rate capability (Figure 4.7). First of all, the coulombic efficiency quickly stabilizes around 100% for all samples, except LPH-A and LPH-C30, both after the first cycles and after any C-rate change. Electrodes show similar behavior at low C-rates such as C/20, C/10 and C/5 as well as a dramatic capacity drop after C/2. Although the LPH-C30 sample shows higher capacity than LPH at low cycling rate, it becomes equal around C/2 and lower after 1C. Also, the plateau region disappears at higher C-rates (Figure S4.3), which can be interpreted as Na^+ ions not having enough time to fill the inner pores of the carbon nodules. Similar to the other samples, LPH-A can keep some capacity up to C/2, but values drop to 0 at higher C-rates. However, the coating improves the performances of the activated sample as the capacity remains relatively high for both LPH-A-C30 and LPH-A-C60. The capacities obtained for LPH-A-C60 at each C-rate are quite similar to those of the LPH sample, indicating a recovery from activation and an improvement compared to LPH-C30. Increased electrode/electrolyte contact area is known to be helpful for rate capability since it can provide more surface for the charge transfer[29][30]. Thus, increased electrode-electrolyte interface of LPH-A-C60 compared to LPH-C30 might be the reason for better rate capability of the former carbon. Additionally, although it remains speculative, onion-like structures observed within the activated sample have been reported to increase the rate capability as they would be able to reduce the diffusion paths of Na^+[26]. The exact impact of those structures needs however to be studied further.

After cycling at various C-rate, the procedure was prolonged with 15 additional cycles at C/20 in order to determine the stability of the electrodes. Most samples recover 91% to 95% of their initial capacity; LPH-A almost reaches 100%, but its initial capacity was already quite low (62 mAh g^{-1}). Interestingly, LPH-A-C60 also keeps 95% of its initial capacity after 15 cycles at C/20, while it decreases to 88% for LPH, 65% for LPH-C30 and 89% for LPH-A-C30. The capacity retention after the 15 additional cycles remains close to 100% for LPH-A but, as mentioned previously, with low initial capacity. The CVD-coated carbon xerogel prepared without activation shows both high ICE and capacity, but its rate capability and stability are low. In contrast, LPH-A-C60 shows both high ICE and capacity without losing rate capability and stability. Developing the micropores volume as well as introducing onion-like structures might be essential to charge transfer. Combining this with a carbon coating to limit the contact between the carbon xerogel and liquid electrolyte seems a good way to improve the electrochemical performance of hard carbons in NIB negative electrodes.

Table 4.5. Electrochemical performance of the samples.

Sample	$C_{tot,disch}$[a]	C_{rev}[b]	C_{slope1}[a]	C_{slope2}[a]	$C_{plateau}$[b]	$C_{plateau}/C_{rev}$[b]	**ICE**	C_{ret}	C_{spec}
	(mAh g^{-1})	(mAh g^{-1})	(mAh g^{-1})	(mAh g^{-1})	(mAh g^{-1})	(%)	%	(%)	(F g^{-1})
LPH	300	248	170	-[c]	99	39	80	88	0.012
LPH-C30	357	298	184	-[c]	129	43	84	65	0.017
LPH-A	343	62	62	-[c]	-[d]	-[d]	18	100	0.270
LPH-A-C30	354	235	68	140	108	36	66	89	0.035
LPH-A-C60	329	294	66	77	159	54	88	95	0.036

[a] Calculated from the first discharge (*i.e.* first sodiation).
[b] Calculated from the first charge (*i.e.* first desodiation).
[c] Second slope region not observed.
[d] No plateau observed.

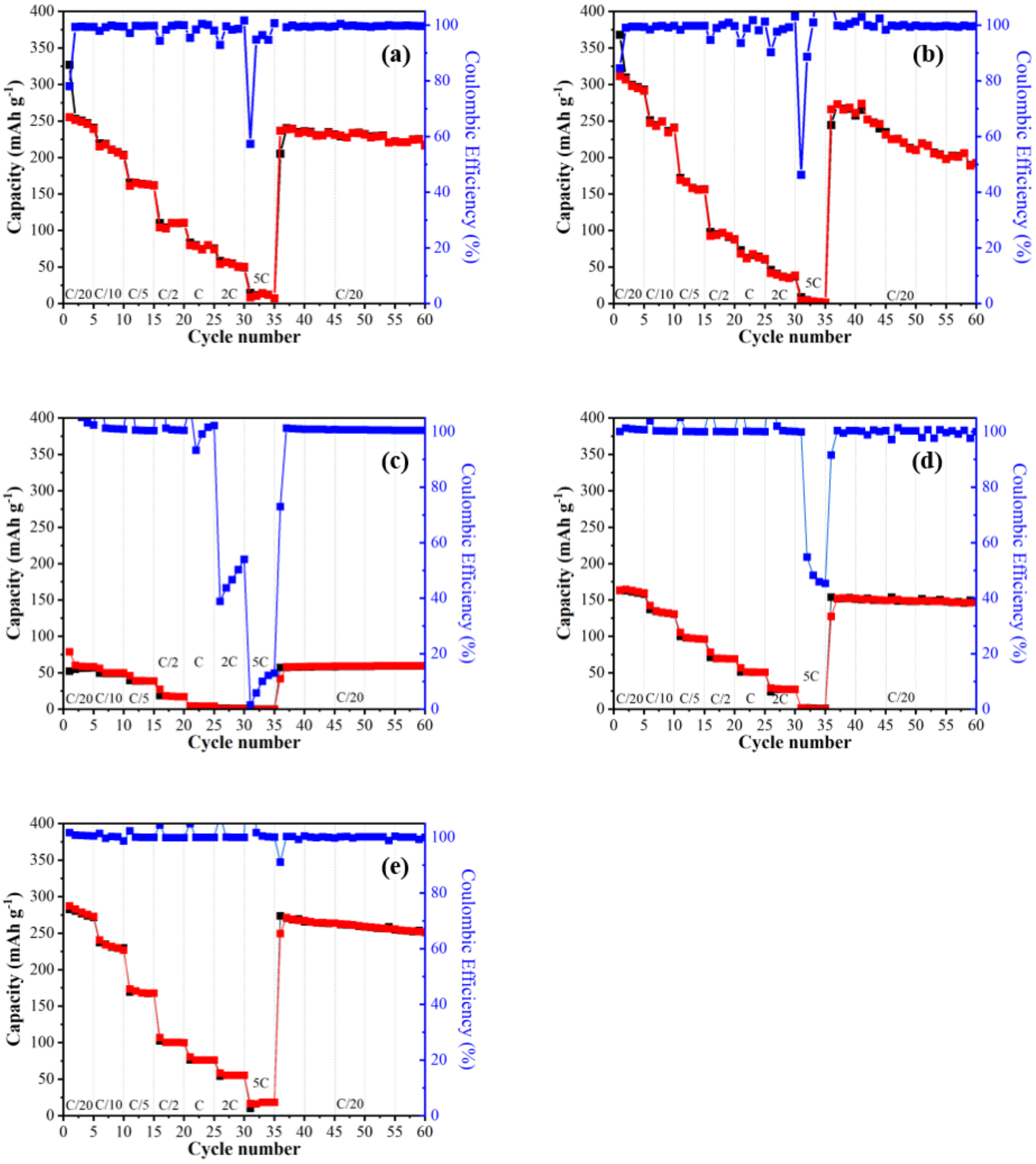

Figure 4.7. Galvanostatic charge-discharge performances at various cycling rates. (■) Desodiation capacity, (🟥) sodiation capacity and (🟦) coulombic efficiency for sample (a) LPH, (b) LPH-C30, (c) LPH-A, (d) LPH-A-C30, (e) LPH-A-C60.

4.4. Conclusions

The present paper aimed at understanding the impacts of both CO_2 activation and carbon coating by Chemical Vapor Deposition (CVD) on carbon xerogels, starting from the general agreement that a large volume of closed micropores and very low specific surface areas (S_{BET}

< 10 m² g^{-1}) should be targeted for applications as negative electrode in Na-ion batteries (NIBs). To do so, a carbon xerogel (CX) with large nodules size (~2 µm) was synthesized by drying and pyrolysis of a resorcinol-formaldehyde gel; this pristine CX displayed a specific surface area A_{BET} of 643 m² g^{-1}. Its surface was then modified either by CO_2 activation (to develop the microporosity up to 853 m² g^{-1}), or by deposition of a secondary carbon layer using CVD (to mask the micropores), or a combination of both. Direct CVD coating of the pristine CX led to decreasing A_{BET} down to 2 m² g^{-1}. In the case of the activated sample, the CVD coating duration had to be twice longer to completely mask the microporosity, leading to a rougher carbon coating with some mesoporosity (A_{BET} = 30 m² g^{-1}).

From electrochemical characterizations, it is clear that the specific surface areas measured by N_2/H_2 gas adsorption cannot be directly related to the carbon performances. In particular, both the pristine CX and its CVD-coated counterpart present high Initial Coulombic Efficiencies (ICE = 80 and 84%) and reversible capacities at first cycle (C_{rev} = 248 and 298 mAh g^{-1}), which is remarkable for carbons treated at temperatures below 1000°C. The insertion plateau at low voltage is longer after CVD coating, due to the closing of micropores. CO_2 activation increases the overall specific surface area, but this modification does not explain alone the harsh drop in electrochemical performances (down to 16% ICE and C_{rev} = 62 mAh g^{-1}) compared to the pristine and CVD-coated carbons. Finally, coating the activated carbon by a sufficiently thick CVD carbon layer restores the reversible capacity (C_{rev} = 294 mAh g^{-1}), increases the ICE (88%) and significantly improves the rate capability of the carbon.

Cyclic voltammetry using a supercapacitor-like setup was performed to understand which surface should be considered when analyzing hard carbons for NIB applications. From results in half-cells, it is indeed clear that the specific surface area measured by gas adsorption does not correspond to the electrode/electrolyte interface where the Solid Electrolyte Interphase forms upon the first carbon sodiation. Capacitance measurements in supercapacitor set-up show that the electrolyte does not enter the micropores of the pristine CX, while the micropore surface is only partly accessible in the case of the activated material. This highlights the fact that carbon wettability by the electrolyte and electrolyte reactivity at the carbon surface play a key role in the carbon performances, and that its properties as electrode material cannot be easily linked to *ex situ* physico-chemical characterizations.

Finally, this study shows that the combination of micropore development and surface masking by a secondary carbon layer could lead to low-temperature processed carbons with interesting properties as NIB negative electrodes. Given that they can be tuned in various ways, carbon xerogels also seem a good choice for further fundamental studies aiming at unveiling the various Na storage mechanisms at play in hard carbons. The next step would consist in *in situ* studies to understand how activation and CVD treatment modify the Na storage mechanisms. This strategy could then provide valuable information for the rational development of hard carbons for NIB applications.

4.5. References

[1] B.E. Lebrouhi, S. Baghi, B. Lamrani, E. Schall, T. Kousksou, *J Energy Storage* **2022**, *55*, 105471.

[2] J.F. Peters, M. Baumann, B. Zimmermann, J. Braun, M. Weil, *Renew. Sustain. Energy Rev.* **2017**, *67*, 491.

[3] H. Zhang, Y. Huang, H. Ming, G. Cao, W. Zhang, J. Ming, R. Chen, *J Mater Chem A Mater* **2020**, *8*, 1604.

[4] T. Perveen, M. Siddiq, N. Shahzad, R. Ihsan, A. Ahmad, M.I. Shahzad, *Renew. Sustain. Energy Rev.* **2020**, *119*.

[5] K. Chayambuka, G. Mulder, D.L. Danilov, P.H.L. Notten, *Adv Energy Mater* **2020**, *10,* 38.

[6] P. Ge, M. Fouletier, *Solid State Ion* **1988**, *28–30*, 1172.

[7] D.A. Stevens, J.R. Dahn, *J Electrochem Soc* **2001**, *148*, A803.

[8] C. Bommier, T.W. Surta, M. Dolgos, X. Ji, *Nano Lett* **2015**, *15*, 5888.

[9] D. Saurel, B. Orayech, B. Xiao, D. Carriazo, X. Li, T. Rojo, *Adv Energy Mater* **2018**, *8,* 1703268.

[10] L.F. Zhao, Z. Hu, W.H. Lai, Y. Tao, J. Peng, Z.C. Miao, Y.X. Wang, S.L. Chou, H.K. Liu, S.X. Dou, *Adv Energy Mater* **2021**, *11*, 2101650,.

[11] N. Cuesta, I. Cameán, A. Arenillas, A.B. García, *Microp M M. Micropor* **2020**, *308,* 110542.

[12] C. Bommier, W. Luo, W.Y. Gao, A. Greaney, S. Ma, X. Ji, *Carbon* **2014**, *76*, 165.

[13] B. Karaman, H. Tonnoir, D. Huo, B. Carré, A.F. Léonard, J.C. Gutiérrez, M.L. Piedboeuf, A. Celzard, V. Fierro, C. Davoisne, R. Janot, N. Job, *Carbon* **2024**, *225, 119077.*

[14] M.M. Titirici, H. Alptekin, H. Au, A.C.S. Jensen, E. Olsson, M. Goktas, T.F. Headen, P. Adelhelm, Q. Cai, A.J. Drew, *ACS Appl Energy Mater* **2020**, *3*, 9918.

[15] J.M. Stratford, P.K. Allan, O. Pecher, P.A. Chater, C.P. Grey, *Chem Comm* **2016**, *52*, 12430.

[16] D.A. Stevens, J.R. Dahn, *J Electrochem Soc* **2000**, *147*, 1271.

[17] D.A. Stevens, J.R. Dahn, *J Electrochem Soc* **2000**, *147*, 4428.

[18] A. Gomez-Martin, J. Martinez-Fernandez, M. Ruttert, M. Winter, T. Placke, J. Ramirez-Rico, *Chem. Mater.* **2019**, *31*, 7288.

[19] N. Daher, D. Huo, C. Davoisne, P. Meunier, R. Janot, *ACS Appl Energy Mater* **2020**, *3*, 6501.

[20] H. Tonnoir, D. Huo, R.L.S. Canevesi, V. Fierro, A. Celzard, R. Janot, *Mater Today Chem* **2022**, *23,* 100614.

[21] C.A. Páez, M.S. Contreras, A. Léonard, S. Blacher, C.G. Olivera-Fuentes, J.P. Pirard, N. Job, *Adsorption* **2012**, *18*, 199.

[22] P. Mallet-Ladeira, PhD Thesis, Universit´e Toulouse 3 Paul Sabatier, 2014. France.

[23] B. Ranjan, D. Kaur, *Small* **2024**, *20*, 2307723.

[24] P.J.F. Harris, *Crit. Rev. Solid State Mater. Sci.* **2005**, *30*, 235.

[25] P.J.F. Harris, A. Burian, S. Duber, *Philos Mag Lett* **2000**, *80*, 381.

[26] B. Yang, S. Liu, H. Song, J. Zhou, *Carbon* **2019**, *153*, 298.

[27] C. del Mar Saavedra Rios, A. Beda, L. Simonin, C.M. Ghimbeu, In: Na-Ion Batteries (Eds. L. Monconduit and L. Croguennec), Wiley, 2021, ISBN 978-1-789-45013-2, Ch. 3, p.101.

[28] J.A. and R.G. and C.A. and F.V. and M.H.F.J. and B.-G.E. and J.N. Arenillas Ana and Menéndez, in Organic and Carbon Gels: From Laboratory Synthesis to Applications, Springer International Publishing, Cham **2019**, 149-189.

[29] H. Zheng, J. Li, X. Song, G. Liu, V.S. Battaglia, *Electrochim Acta*, **2012**, *71*, 258.

[30] R. Zhao, J. Liu, J. Gu, *Appl Energy*, **2015**, *139*, 220.

4.6. Supplementary information

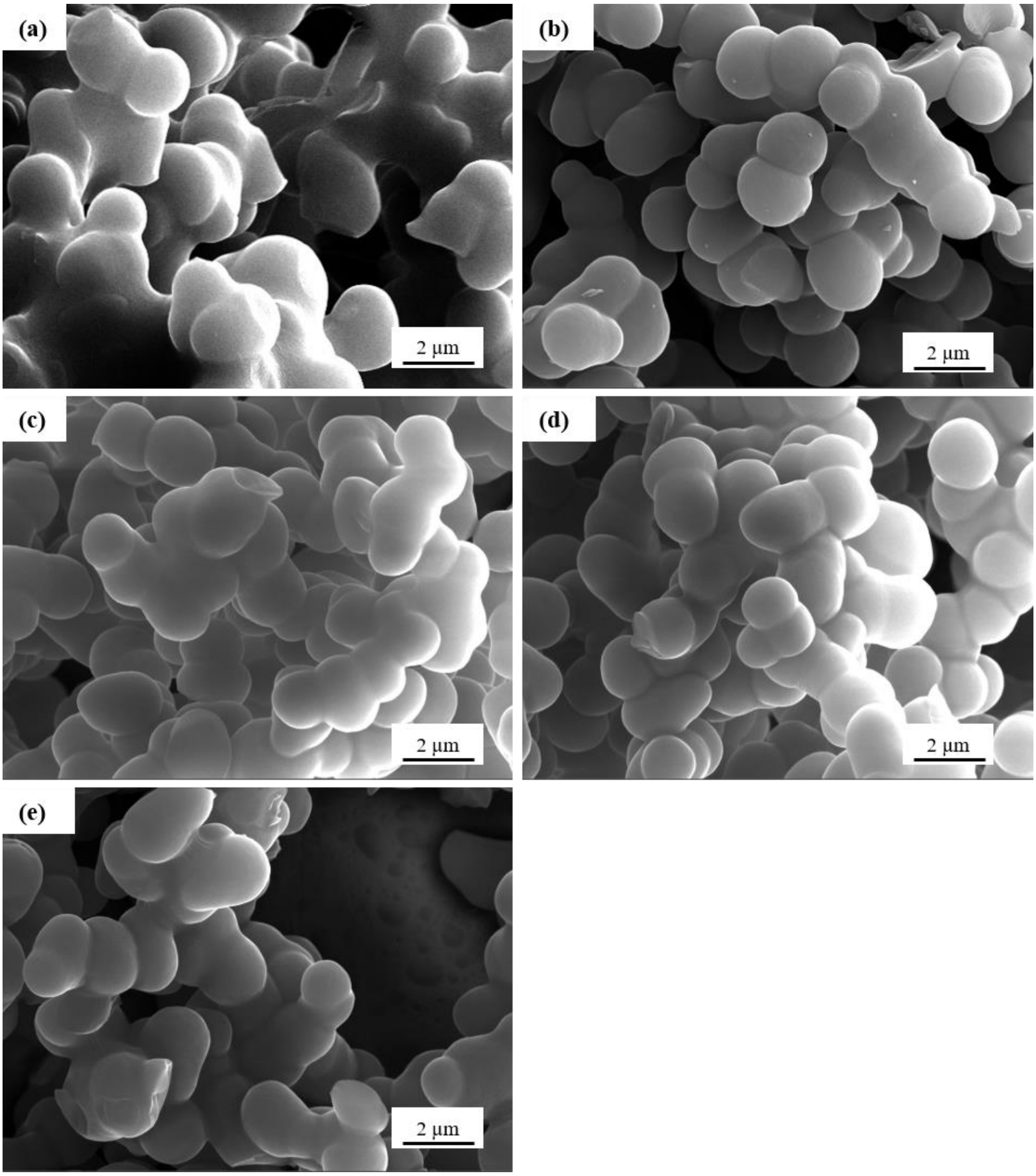

Figure S4.8. SEM images of (a) LPH, (b) LPH-C30, (c) LPH-A, (d) LPH-A-C30, (e) LPH-A-C60.

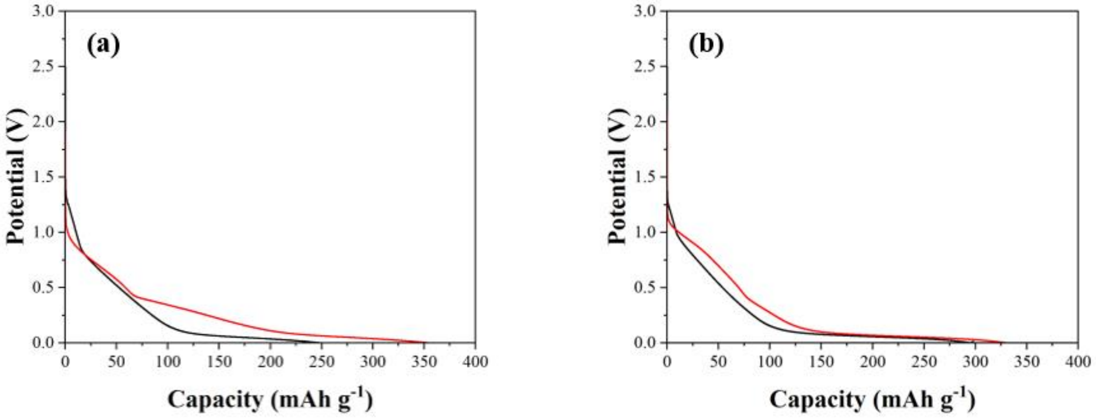

Figure S4.2. (▬) First and (▬) second sodiation cycles of a) LPH-A-C30 b) LPH-A-C60 samples

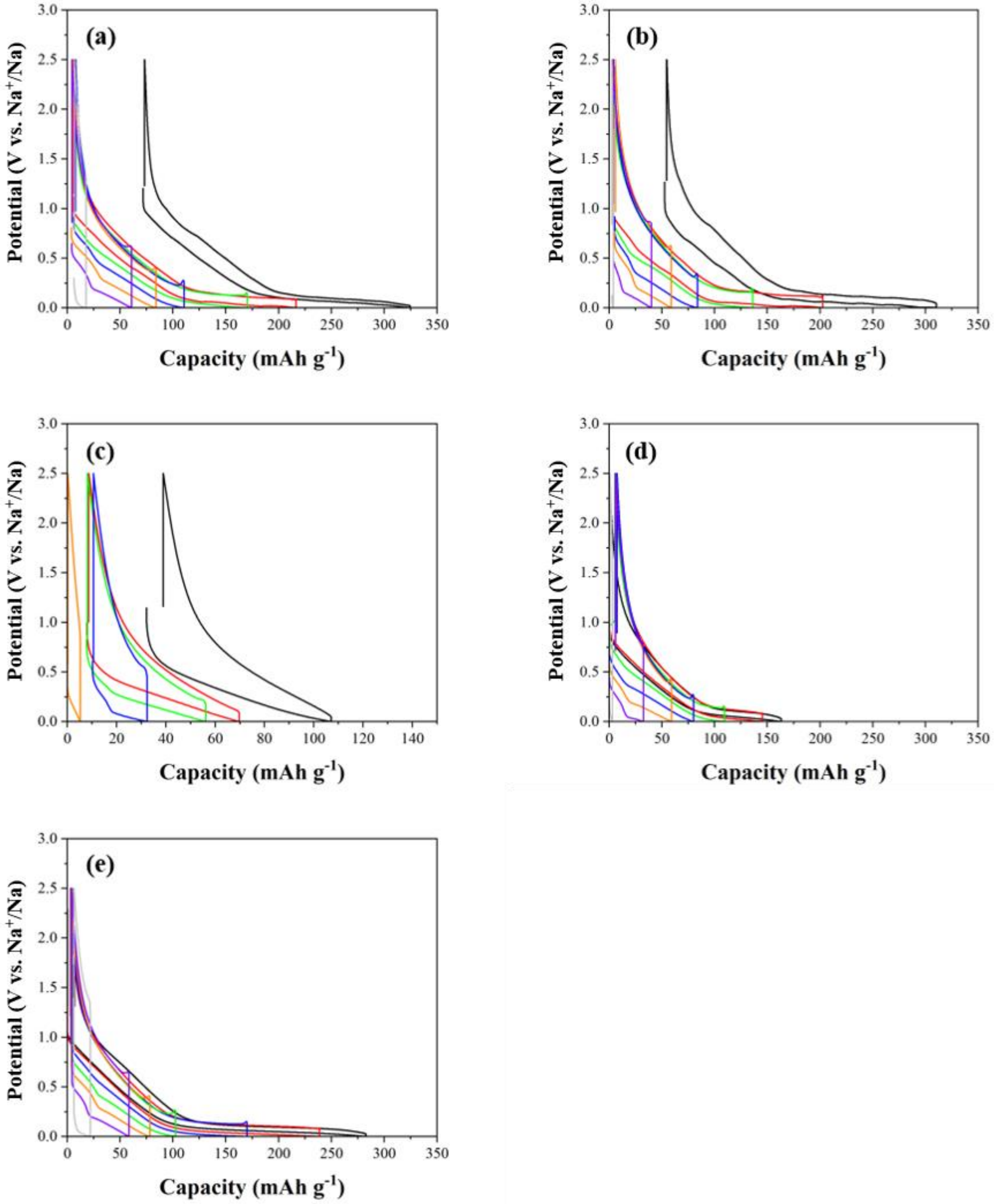

*=LPH-A samples charge-discharge profile is highly distrupted and not visible after C.

Figure S4.3 Galvanostatic charge-discharge profiles of the samples: (a) LPH, (b) LPH-C30, (c) LPH-A* , (d) LPH-A-C30, (e) LPH-A-C60 half-cells with NP30 electrolyte at (▬) C/20, (▬) C/10, (▬) C/5, (▬) C/2, (▬) C, (▬) 2C, (▬) 5C.

Chapter 5

Si nanoparticles supported on carbon xerogel prepared by Physical Vapor Deposition for applications in Li-ion battery negative electrodes

Abstract

Silicon nanoparticles (~15 nm) were deposited on a carbon xerogel with controlled primary nodule size (50 nm) *via* Physical Vapor Deposition (PVD). The aim was to produce sufficiently small nanoparticles to avoid Si pulverization upon cycling. During the PVD procedure, two different treatments were used to improve the nanoparticle deposition: Ar^+ etching prior to deposition and application of a bias voltage during the deposition. Both strategies led to a significant increase of deposited Si amount, even though the application of bias voltage during Si deposition proved more effective to increase the Si nanoparticle content in the final composite. Additionally, Si/C powders produced with either etching or bias displayed lower oxygen amount than the sample prepared without. The Si/C composites were then used to prepare negative electrodes of Li-ion batteries and characterized in half-cell configuration. A high initial capacity, around 1250 mAh g^{-1}, was observed for the sample with highest amount of Si (9.3 wt.%). However, it dropped to 560 mAh g^{-1} at second cycle and degradation continued at lower pace with cycling, reaching 40% of the initial capacity after 30 cycles. All samples displayed the same behaviour, which shows that decreasing the Si particle size is not sufficient to avoid degradation upon cycling. Most probably, degradation comes from the exposure of Si to the electrolyte and its continuous reaction to produce an unstable Solid-Electrolyte Interface.

5.1. Introduction

Li-ion batteries are the most used energy storage systems in portable devices and are now envisaged in stationary and transport applications. Although they are popular, they still require improvement of their energy density, power density and lifespan in order to match the demand. Their performance is highly related with the chosen electrode materials at both the negative and positive electrodes. Among possible electrode materials, alloying-type ones are an interesting group as they can be used instead of conventional graphite or other carbon materials as negative electrode material[1]. Their ability to form an alloy with lithium instead of intercalating Li^+ between graphitic layers offers improved energy density resulting from increased number of Li^+ ions stored[2][3]. Among those alloying-type materials, silicon is one of the most popular due to its low electrochemical lithiation/delithiation potential and very high theoretical capacity which can reach 4200 mAh g^{-1}. However, the use of silicon as electrode material for Li-ion batteries remains limited for two main reasons. First, its electrical conductivity is not sufficient. Second, and more significantly, bulk silicon inflates by 300% in volume upon alloying with Li^+, which leads to unstable Solid Electrolyte Interface (SEI), pulverization of silicon and loss of connection with the current collector [4][5]. As a result, electrodes made of silicon or containing silicon usually exhibit low stability over long-term cycling [3][4].

In the literature, several strategies have been developed to overcome these problems. The morphology of silicon has been observed to be critical: indeed, particles smaller than 150 nm in size do not pulverize[6]. Reducing the silicon particle size leads to decreasing the stress induced by large volume expansion, which limits pulverization and results in improved cycling performance. However, the issues of SEI instability and poor electrical conductivity both remain. Another technique consists in mixing silicon with another material in order to improve the charge transfer, mitigate the stress induced by volume expansion and limit the contact between the silicon surface and the electrolyte. Among the materials envisaged to prepare the silicon composites, carbonaceous materials stand out because of their high conductivity and wide range of various properties. Graphite is the first material that comes to mind when thinking about carbonaceous materials in Li-ion batteries as they became the standard material for the negative electrodes. Many works incorporate silicon/graphite compounds to Li-ion batteries[7]–[9], as negative active material. In the meantime, carbon materials offer a wide range of properties in terms of morphology, pore texture, surface structure and chemistry, composition, crystallinity, electrical conductivity, and so on. It is therefore quite possible to adapt the carbon support properties to the final application, especially in the present case regarding the pore texture. Indeed, choosing a carbon material with an appropriate pore texture could solve the issue of Si nanoparticles size change if those are embedded within a tailored scaffold.

Among the many porous carbons referenced in the literature, carbon xerogels (CXs) could be an interesting candidate. Those materials are made of interconnected microporous carbon nodules, the size of which can be modified (from ~10 nm to ~5 µm) through the synthesis variables[10]; in turn, the voids between those nodules are tailorable as well, leading to carbon structures with adjustable meso/macropore sizes. Moreover, their micropore content and/or surface chemistries can be modified as well[10]. CXs were previously used as negative electrode materials for Li-ion batteries because of their high stability as well as their good electron conductivity[11], but their limited reversible capacity (275 mAh g^{-1}) and lack of insertion-deinsertion plateau prevents them to be a good candidate for negative electrode material alone. Indeed, during insertion, Li^+ can massively penetrate within the CX; however, de-insertion of Li^+ from CX is only partial. The potential needs to reach 3 V *vs.* Li^+/Li in order to have a pronounced de-insertion which hampers the use in real applications[12]. However, Si/CX composites could be a good choice for Li-ion battery applications if the pore texture is appropriate.

Several methods have been envisaged in the past to prepare composites made of Si (under various forms) and CXs. Yuan *et al.*[13] were able to combine CXs with commercial amorphous SiO by ball-milling both powders at room temperature and atmosphere. The synthesized SiO/carbon xerogel material was able to reach around 850 mAh g^{-1} at 100 mA g^{-1} with 48% initial coulombic efficiency (ICE); however, capacity dropped to 547 mAh g^{-1} after 20 cycles. Gomez *et al.*[14] prepared a graphitized CX with the addition of graphene oxide and Si was incorporated by vigorous mechanical stirring in 2-propanol. Several powders were obtained and displayed homogenous Si particles with 50 nm diameter; the particles were well-distributed over the graphitized xerogel/graphene oxide matrix. The resulting powders had silicon content within the range of 20 to 50 wt.%. The best electrochemical performance was obtained with 30 wt.% Si: 1190 mAh g^{-1} initial capacity at 1000 mA g^{-1} and stabilization around 917 mAh g^{-1} up to 200 cycles. Higher amounts of Si brought higher capacities; however, the composite capacity quickly faded after a few cycles. Previous work by Li *et al.* [15] showed that the porous carbon network is able to accommodate the huge volume changes of silicon during lithiation/de-lithiation. Indeed, they produced SiOx/C composite by carbothermal reduction of silica-carbon binary xerogel. Resulting powders displayed a homogenous dispersion with low O/Si ratio of SiOx. The electrodes prepared with this composite material reached an initial capacity of 1400 mAh g^{-1} with 72% ICE; upon cycling, the capacity dropped and stabilized around 830 mAh g^{-1} after 100 cycles at 0.1 A g^{-1}.

Another technique, physical vapor deposition (PVD), has also been used to produce silicon/carbon composite electrodes. PVD relies on the use of ionized inert gasses to sputter a chosen material from a target and deposit it onto a substrate. The coating can be under the form of particles or continuous layer, depending on the sputtering conditions. Additional steps can be performed to modify and improve the coating properties, such as substrate pretreatment and application of a bias voltage. On the one hand, pretreatment by etching with Ar^+ ions can be used to remove contaminants from the surface and promote a better adhesion of the deposited material[16]. On the other hand, bias voltage can be used to attract positive ions during deposition to bring more energy to the surface of the powders. This usually leads to better adhesion and denser coating[17][18]. This method can lead to the obtaining of nanosized particles on a carbonaceous support, therefore achieving small particle size aimed for Si-based anodes while preserving the electrode conductivity. In literature, one can find a few studies focusing on the use of PVD methods to manufacture Si/C composites. Bensalah *et al.*[19] used radio frequency (RF) magnetron sputtering to coat Si thin film onto multiwalled carbon nanotubes. Although the material showed very high capacity (around 2000 mAh g^{-1} at 420 mA g^{-1}) and capacity retention (1250 mAh g^{-1} after 100 cycles), the ICE remained drastically low, down to 18%, due to side reactions of the electrolyte de-composition and the formation of the SEI film on the composite surface. Another study[20] focused on the effect of carbon content of Si/C composites produced by RF magnetron co-sputtering. The obtained electrodes showed capacities around 1510 mAh g^{-1} at 40 µA cm^{-2}. This study indicated that increased carbon content can improve the capacity retention: 63 at.% carbon-containing electrode showed 88% capacity retention after 100 cycles while it was only 73% for electrodes containing 49 at.% of carbon. All these studies indicate that PVD is a good candidate to provide Si/carbon composites with adapted structure. However, no previous studies focused on the understanding of the coating procedure on the performance of the electrodes and, to the best of our knowledge, such a deposition has not been attempted using CXs as supports yet.

This study aims to demonstrate the possibility of manufacturing a homogenously dispersed Si/CX material by PVD and analyze the effects of modifications of PVD process to the performance of Si/CX electrode. Carbon xerogels were picked as a supports because (i) their relatively large (mesoporous) surface area could help obtaining a homogenous dispersion of Si and (ii) their porous structure should be able to accommodate the volume change of Si during lithation and de-lithation. Si/CX samples were thus manufactured using different PVD conditions: (i) with or without Ar^+ etching (pretreatment) and (ii) with or without the application of a bias voltage during Si deposition. The resulting powders were thoroughly characterized by physico-chemical methods in order to understand the impact of the PVD deposition procedure on the powder properties. The obtained samples were then used as Li-ion electrode materials and were compared based on their electrochemical performance in half-cell.

5.2. Experimental

5.2.1. Carbon xerogel preparation

Carbon xerogels (CXs) were prepared following a procedure described in a previous study[10]. First, a 35 wt.% aqueous solution of resorcinol (R) (Merck) was prepared in a sealable glass flask. Then, sodium carbonate (C) (Merck) was added as basification agent. The *R/C* ratio was used as synthesis variable to regulate the pH of the solution (and thus the nodule size and meso/macropore size of the final carbon material) and set at 450 for this study. This *R/C* value was selected to obtain ~50 nm pore size[10]. A 37 wt.% solution of formaldehyde was then added to the mixture with a resorcinol/formaldehyde molar ratio of 0.5. The dilution ratio *D*, *i.e.* the water/reactants molar ratio, was chosen equal to 5.7. The obtained mixture was then magnetically stirred for 1 h. After mixing, the sealed glass flask was put in an oven, at 85 °C and for 72 h, for gelation and aging. Finally, to dry the gel, the container was opened and put in a vacuum oven at 60 ºC. The pressure was progressively decreased down to 12 Pa, and the samples were left to dry overnight. The obtained sample is identical the one used in Chapter 3 and analyzed thoroughly by its pore structure and morphology. A carbon xerogel with 2 µm nodule size, 643 $m^2 g^{-1}$ BET specific surface area and 3.9 µm pore size was obtained. The details of the characterization can be found in Chapter 3.

At the end of drying, organic xerogel monoliths were retrieved. To obtain a narrow final particle size distribution, the material was ground prior to pyrolysis, following a procedure from a previous work[12]. After coarse milling by hand in a mortar, the material was ground to powder using a Fritsch planetary mill (Mono Mill P6). The sample was ground at 400 rpm for 24 cycles of 1 min each, followed by 15 s of rest. Finally, to obtain a carbon xerogel, the powder underwent pyrolysis at 800 ºC under N_2 with the following procedure. The temperature was increased (1) to 150 ºC at 1.7 ºC min^{-1} and held for 15 min; (2) from 150 ºC to 400 ºC at 5 ºC min^{-1} and held for 60 min; and (3) from 400 ºC to 800 ºC at 5 ºC min^{-1} and held for 120 min. Finally, the oven was let to cool down to room temperature overnight.

5.2.2. Silicon deposition on carbon xerogels

Silicon depositions were produced by magnetron sputtering from 99.99% pure Si targets. In each trial, the carbon powder was continuously stirred in a dedicated reactor during the deposition process. Prior to deposition, the vacuum chamber was pumped down to reach a residual pressure lower than 6 $\times 10^{-3}$ Pa. Ar^+ etching pretreatment and substrate bias were performed by applying the voltage on the reactor. Si deposition was performed with Ar as processing gas during 1 h in all cases. The details of deposition as well as pretreatment procedures cannot be disclosed due to confidentiality issues. The Si/CX synthesis was performed with a different procedure for each sample. The bare CX that is used for coating is named CX hereafter; the sample without any pretreatment or bias is named CXSi; CXSi-E corresponds to a sample with surface pretreatment (etching) but no bias; CXSi-B was obtained without pretreatment but with voltage bias; finally, the sample with both pretreatment and bias is named CXSi-EB throughout the paper (Table 5.1).

Table 5.5. Description of samples based on their Si deposition procedure.

Sample	Ar^+ etching	Bias voltage
CXSi	No	No
CXSi-E	Yes	No
CXSi-B	No	Yes
CXSi-EB	Yes	Yes

5.2.3. Physicochemical characterization of Si/CX composites

Samples were first examined by thermogravimetric analysis (TGA) using a Mettler Toledo TGA/DSC 3+ STARe System device. The procedure took place under air, from room temperature to 800°C with a ramp of 10°C min^{-1}; then, the samples were held at 800°C for 90 min in order to ensure complete carbon elimination and silicon oxidation. During the course of

TGA, the combustion of carbon (mass decrease) is observed and followed by the oxidation of silicon (mass uptake). The remaining mass at the end of the procedure, which corresponds to SiO_2, can be used to calculate the Si weight percentage at the start, %Si, estimated as:

$$\%Si = \frac{m_{si}}{m_{CXSi}} \tag{5.1}$$

with:

$$m_{si} = m_{SiO_2}\left(\frac{M_{Si}}{M_{SiO_2}}\right) \tag{5.2}$$

where m_{Si} is the initial weight of silicon in the composite, M_{SiO_2} is the molecular weight of silica measured at the end of the TGA procedure, M_{Si} is the molecular weight of silicon and m_{CXSi} is the initial mass of the composite used for TGA experiment. Note that the silicon present in the Si/CX at the end of the manufacturing procedure probably gets oxidized when the sample is removed from the PVD reactor and put in contact with air. Therefore, although the exact amount of Si within the powders can be calculated *via* TGA (from the final mass, assumed to be SiO_2), the amount of Si/SiO_x in the initial sample is unknown. It cannot be derived from TGA experiments given that it is difficult to know when Si oxidation starts; the latter probably overlaps with carbon combustion.

SEM was used to observe the morphology and the size of the silicon particles. Images were obtained using a Tescan CLARA FEG-SEM at 15 kV under high-vacuum conditions. The samples were gold-coated in a sputtering device (Balzers, SCD004 sputter coater, Vaduz, Liechtenstein) and mounted on a holder with carbon adhesive prior to observation.

The powders were characterized by X-ray diffraction (XRD) using a Bruker D8 Twin-Twin diffractometer (Billerica, MA, USA) with a Cu Kα radiation source in the 2θ range from 10º to 80º with a step of 0.02º. The data analysis was performed by using the software Diffract.

X-ray photoelectron spectroscopy (XPS) analysis was performed using a ThermoFisher K-Alpha photoelectron spectrometer. The sample powders were deposited onto double-sided copper tape. A monochromatized Al Kα line (1486.6 eV) served as the photon source. Survey spectra and high-resolution spectra were recorded at pass energies of 150 eV and 20 eV, respectively, with 3 scans for survey spectra and 20 scans for high-resolution spectra, using a 250 µm diameter X-ray spot. An electron flood gun was activated during analysis to prevent charging. Data were analyzed with Thermo Avantage software (Version 6.6.0).

5.2.4. Electrode manufacturing

The electrodes were produced *via* spray-coating of a water-based ink using an airbrush (Harder & Steenbeck Airbrush Evolution Silverline fPc, 0.4 mm nozzle and needle). The mixture for spray-coating contained 12 wt.% solids including Si/CX powders and xanthan gum (Sigma Aldrich) in a weight ratio of 88:12 in MilliQ water. The prepared mixture was magnetically stirred for 3 h prior to spraying. The prepared ink was sprayed onto pre-weighted stainless-steel discs (Type 304, 15.5 mm, MTI corp.) current collectors and the obtained samples were dried overnight at 60°C. The coated discs were then weighted and dried in an oven for 2 h under vacuum at 110°C before being introduced into the glovebox. The coin-cells were assembled using the Si/CX-based electrode as positive electrode, a metallic Li disc (PI-KEM) as counter and reference electrode, GF/D (glass microfiber) as separator and 100 µL of electrolyte (1 M $LiPF_6$ in an ethylene carbonate:diethyl carbonate:dimethylcarbonate – 1:1:1 mixture, Sigma Aldrich). The prepared half-cells were then used for electrochemical characterization.

5.2.5. Electrochemical characterization of the Si/CX composites

Si/CX half-cells were characterized using a BioLogic VMP3 multichannel potentiostat. First, cyclic voltammetry (CV) was conducted in order to understand the electrochemical reactions within the cell. CVs were recorded between 0.05 and 1.5 V *vs.* Li^+/Li with 1 mV s^{-1} scan rate. Following this, two sets of galvanostatic charge/discharge (GCPL) experiments were performed between 0.05 and 1.5 V *vs.* Li^+/Li. First experiments involved a long cycling sequence consisting of 30 cycles at a cycling rate of C/10 (*i.e.* 10 h to charge and 10 h to discharge) to observe the capacity retention of the cells in the long term. The second set of GCPL experiments aimed at understanding the rate capability of the cells. In this case, a sequence comprising 5 cycles at C/20, 5 cycles at C/10, 5 cycles at C/5 and finally 5 cycles at 1 C were performed. The currents were set according to the calculation of theoretical capacities[12][21], C_{theo}, by considering the mass percentages obtained by TGA (Equation 5.3):

$$C_{theo} = m_{Si\%}.(C_{theo,Si}) + m_{CX\%}.(C_{theo,graphite}) \qquad (5.3)$$

Theoretical capacities of Si ($C_{\text{theo, Si}}$ = 4200 mAh g^{-1}) and graphite ($C_{\text{theo, graphite}}$ = 372 mAh g^{-1}) are used for calculation of theoretical capacity of the Si/CX composite powders. Note that the use of graphite theoretical capacity is an arbitrary choice since the given powders do not involve graphite but a carbon xerogel. However, no theoretical value can be accurately defined for CXs given the absence of plateau in the insertion-deinsertion curves; in other words, the capacity strongly depends on (i) the CX morphology and (ii) on the measurement conditions (especially the maximum voltage for delithiation [11]). The obtained capacities of CXs reported in literature can thus vary from 145 mAh g^{-1}[13] to 330 mAh g^{-1}[22] and even up to 400 mAh g^{-1}[23]. Therefore, the theoretical capacity of graphite was selected for standardization.

5.3. Results and discussion

5.3.1. Physico-chemical characterization of the Si/CX powders

Firstly, powders were observed *via* SEM in order to determine the size of the Si particles deposited on the carbon xerogel as well as the Si particle size homogeneity. Figure 5.1 shows images of sample CXSi-EB, *i.e.* obtained with both Ar^+ etching and voltage bias. Particle sizes were observed to be approximately 15 nm and no aggregate formation can be seen. This particle size falls well below the aimed target (150 nm [6]); thus, one can expect to avoid pulverization of silicon during charge and discharge. In addition, the particles seem to be well dispersed on the carbon surface and homogenous in size. Clearly, the particles are located outside the carbon nodules, within the mesoporosity. The small particle size of Si makes it difficult to distinguish clearly within the possibility of the equipment and those particles could not be observed for other samples except CXSi-EB. However, since the coating procedure is rather similar, the resulting Si particles are expected to be similar. Note that attempts to observe the samples by transmission electron microscopy (TEM) were not conclusive: Si particles could not be clearly observed, possibly due to Si and C having similar electron densities.

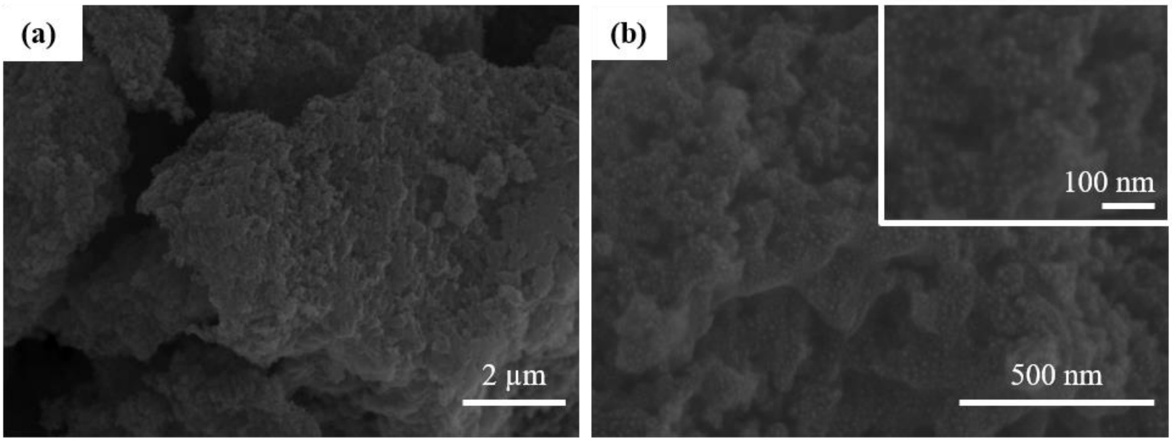

Figure 5.1. SEM images of sample CXSi-EB (a) at low magnification to observe the carbon xerogel structure and (b) at higher magnification to distinguish the silicon particles at the carbon xerogel surface. The insert in (b) is a close-up on silicon particles observed on the carbon surface.

Figure 5.2 shows the TGA curves of the different samples. It can be observed that the bare CX sample almost completely burned away, leaving only 0.2 wt.% at the end of the procedure. The Si/CX samples lost most of their mass, reaching as low as 5% of remaining mass when reaching ~600°C. Then, one observes a mass increase. The sharp decline can be associated with CX combustion; however, silicon oxidation also occurs up to 800°C, leading to a slight mass increase. Si content calculations were performed after stabilization of the TGA curves, *i.e.* after the 90 min rest at 800°C. From the remaining sample at the end of the experiment, the mass weight percentages of silicon were calculated *via* Equation 5.2: values of 3.2, 7.0, 9.3 and 9.4 wt.% Si were found for samples CXSi, CXSi-E, CXSi-B and CXSi-EB, respectively. The use of both pretreatment and bias led to increasing the amount of Si deposited onto the CX support. The bias however seems to have more impact, given that the highest Si contents were obtained for samples CXSi-B and CXSi-EB. Finally, considering the respective theoretical capacities of Si and CX as 4200 mAh g^{-1} and 372 mAh g^{-1}, the theoretical capacities of Si-containing samples were calculated equal to 497 mAh g^{-1}, 643 mAh g^{-1}, 727 mAh g^{-1} and 730 mAh g^{-1} for CXSi, CXSi-E, CXSi-B and CXSi-EB respectively. The current densities during electrochemical characterizations were set according to these calculated capacities.

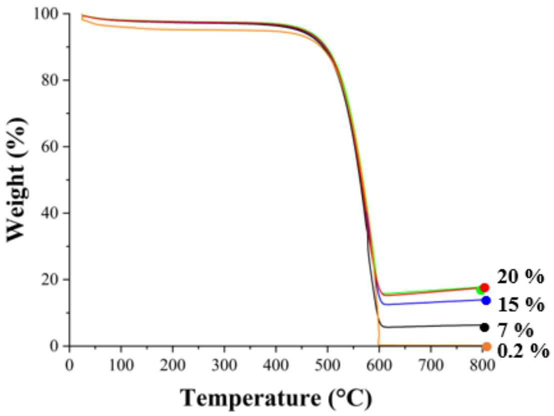

Figure 5.2. Thermogravimetric analysis under air, starting from room temperature to 800 °C with a temperature ramp of 10°C/min. (🟧) CX, (⬛) CXSi, (🟦) CXSi-E, (🟩) CXSi-B and (🟥) CXSi-EB.

X-ray diffractometry was used in order to observe the crystallinity of the powders (Figure 5.3). Very wide peaks around 2θ angles of 15º, 30º and 43º can be observed. Those can be associated with the carbon xerogel structure[24][25] and are very broad due to its amorphous nature. Additionally, for CXSi, CXSi-E, CXSi-B and CXSi-EB, the peaks observed at 2θ angles of 28º and 56º are ascribed to the diffraction peaks of Si (111) and Si (311) planes. Those peaks at 28º and 56º are much more intense for CXSi-B and CXSi-EB[24][26], which corroborates the higher Si content of these two samples. Meanwhile, two other diffraction peaks can be observed at 22º and 32º for all samples; those peaks can be associated with silica structure[24][26][27]. They are also more intense for CXSi-B and CXSi-EB. Therefore, there is a clear signature of silica within the powders although its amount cannot be determined. Experiments to accurately determine the respective silicon and silica contents could not be realized either because of lack of time or lack of sample.

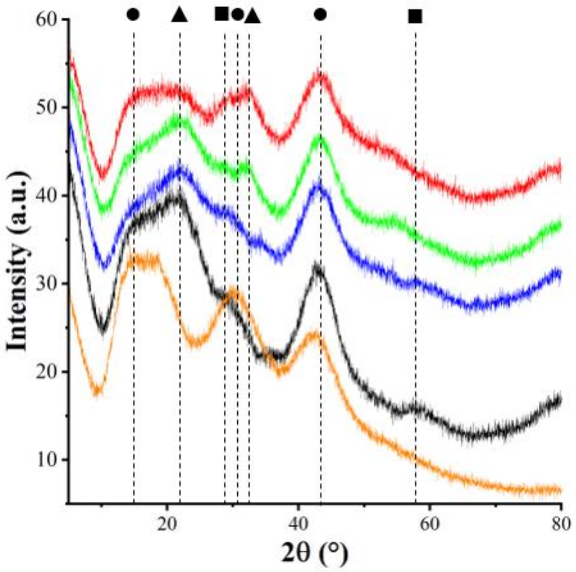

Figure 5.3. X-ray diffractometry patterns of (—) CX, (—) CXSi, (—) CXSi-E, (—) CXSi-B and (—) CXSi-EB with identification of (●) carbon xerogel, (▲) SiO_2 and (■) Si diffraction peaks.

XPS analysis was carried out in order to assess the surface chemistry of the powders and the oxidation state of the deposited silicon (Figure 5.4). XPS surveys (Figure 5.4a) show photoelectron peaks around binding energies of 530 eV, 285 eV, 150 eV and 100 eV; those peaks are associated with the detection of electrons coming from O1s, C1s, Si2s and Si2p orbitals, respectively. High resolution Si2p spectra (Figure 5.4b) clearly shows the presence of several chemical contributions, with two main components centred around 99.5 eV and 103.5 eV. The first peak at 99.5 eV is ascribed to metallic silicon, while the other peak around 103.5

eV can be associated with SiO_2.[28] Nevertheless, the broadness of the latter peak strongly suggests that different silicon oxidation states are present. Although all samples show the same peaks at the same positions, the intensity ratio of these peaks can be used to roughly estimate the extent of silicon oxidation[29]. Si/SiO_2 ratios at the sample surface were calculated as 0.30, 0.70, 0.76 and 0.93 for CXSi, CXSi-E, CXSi-B and CXSi-EB respectively, which shows that both pretreatment and bias voltage can prevent the silicon surface to be oxidized. Pretreatment can remove possible heteroatoms in carbon as well as contamination which would result in a decrease of oxygen at the end product. Also, bias voltage, which usually facilitates a denser coating, can reduce the oxidation of silicon.

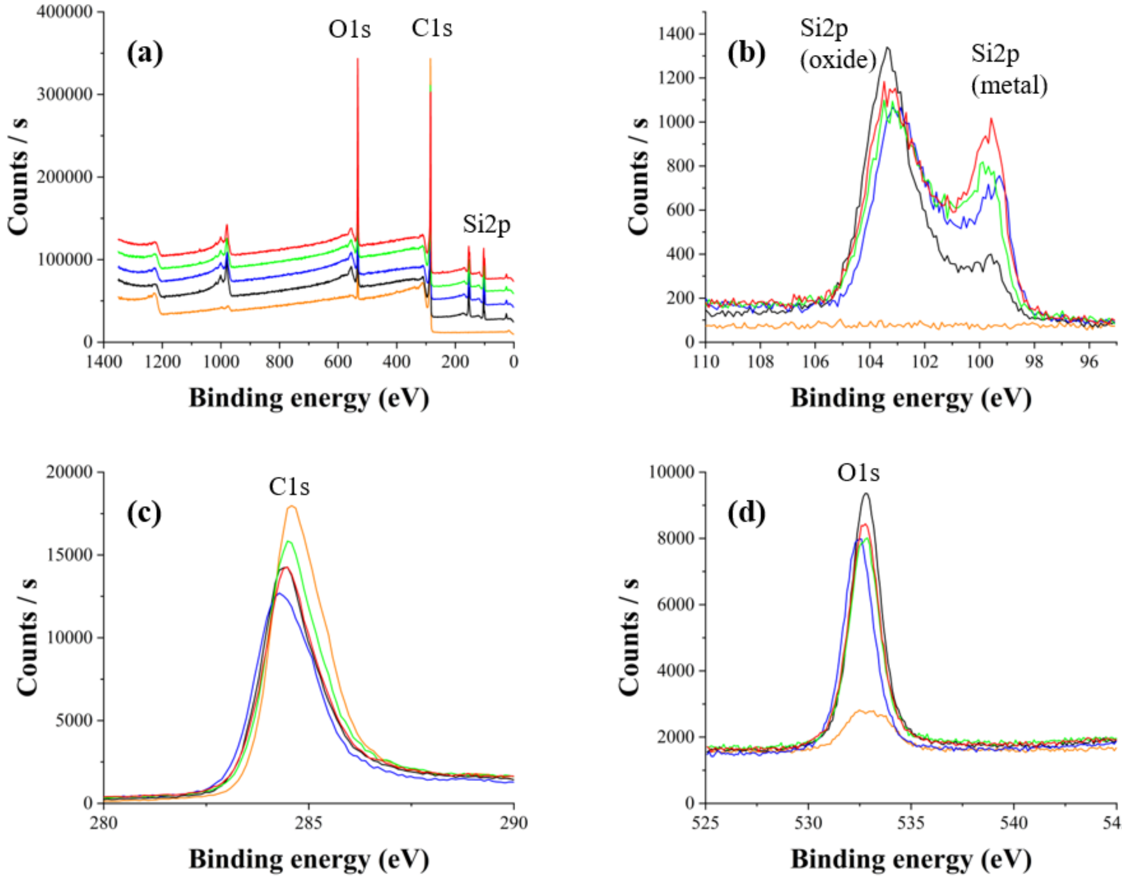

Figure 5.4. XPS measurements. (a) Complete XPS survey spectra, (b) Si 2p XPS spectra, (c) C 1s spectra and (d) O spectra of (🟧) CX, (⬛) CXSi, (🟦) CXSi-E, (🟩) CXSi-B and (🟥) CXSi-EB.

5.3.2. Electrochemical performances

First, cyclic voltammetry was performed on each electrode in order to observe the electrochemical characteristic differences. During the first discharge (Figure 5.5a), upon reduction, a peak around 0.55 V *vs.* Li^+/Li (Peak 1) can be observed; it is related with the SEI formation of CX[30][31]. This peak only exists in the first discharge (*i.e.* first lithiation) and completely disappears in the next cycle, which indicates that the SEI formation has been completed after the first lithiation (Figure 5.5.b). A significantly intense peak can be observed around 0.05 V *vs.* Li^+/Li (Peak 2). That peak is possibly related to the initial alloying of crystalline silicon with lithium and to SEI formation between Si and the electrolyte. Although it is challenging to distinguish between these two phenomena, several earlier studies proposed the same conclusions regarding the initial electrochemical silicon-lithium alloying peak[30][31]. For all samples, several oxidation peaks can be observed around 0.35 V (Peak 3) and 0.5 V (Peak 4) *vs.* Li^+/Li; the peak at 0.5 V *vs.* Li^+/Li (Peak 4) is higher in intensity than the one at 0.35 V *vs.* Li^+/Li (Peak 3). Those peaks can be attributed to delithiation processes of amorphous silicon. Indeed, the peak at 0.35 V *vs.* Li^+/Li corresponds to the delithiation of c-$Li_{15}Si_4$ (c = crystalline) to a-$Li_{\sim 2}Si$ (a = amorphous)[32], while the peak at 0.5 V *vs.* Li^+/Li is usually ascribed to the delithiation of a-Li_xSi to a-Si[33]. During the first reversible reduction (2nd lithiation, Figure 5.5b), another peak at around 0.15 V *vs.* Li^+/Li (Peak 5) is also observed and can be attributed to the lithiation of amorphous silicon [28][26][27]. These characteristic peaks are present for all 4 electrodes prepared from Si/CX composites. However, their relative intensities differ from sample to sample: CXSi-EB displays the highest peak intensity for the peaks 2, 3 and 4 while CXSi shows the lowest intensity. This conclusion can be expected as CXSi-EB has the highest Si content (9.4 wt.%) while CXSi has the lowest Si content (3.2 wt.%).

Cycling was continued for 10 cycles. At cycle 10 (Figure 5.5c), one observes that the ratio between the intensity of the peaks at 0.35 V and 0.5 V *vs.* Li^+/Li changed drastically. Indeed, the intensity of the peak at 0.35 *vs.* Li^+/Li is apparently higher than the intensity of the peak at 0.5 V *vs.* Li^+/Li (Figure 5.5c). This change in ratio of the intensity of the peaks which shows the formation of $Li_{15}Si_4$ has been observed in another study as well[32]. Firstly, it has been claimed that these two-phase boundaries ($Li_{15}Si_4$ and a-LiSi) cause additional particle damage due to difference in their volume changes during cycling. Also, formation of $Li_{15}Si_4$ is used as a sensitive indicator for weakly bound silicon regions which agrees with detachment of silicon particles that leads to capacity decay. It has been claimed that the cause lies in an insufficient connection between the Si particles; in that case, the Si particles suffer from incomplete lithiation or incomplete delithiation. This incomplete delithiation or lithiation is caused by higher contact and interfacial resistance during particle shrinkage[32].

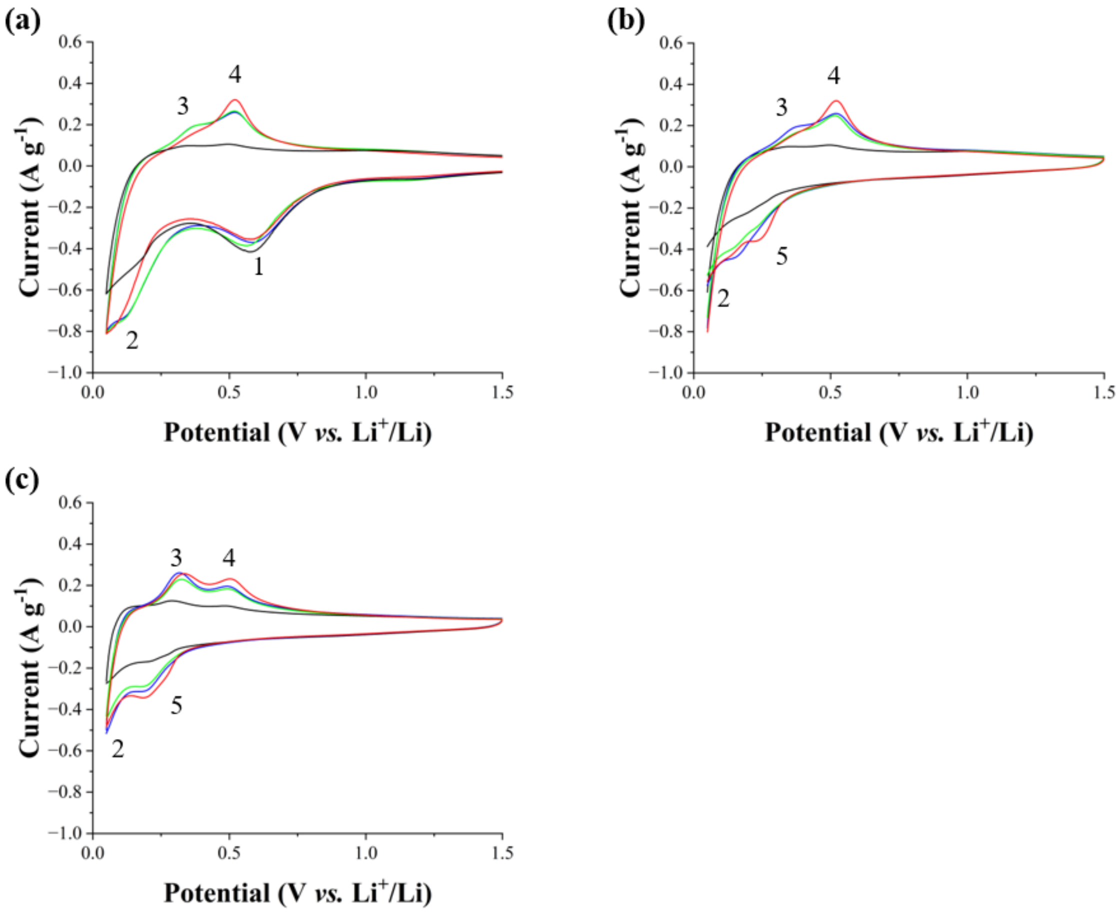

Figure 5.5. Cyclic voltammogram of (▬) CXSi, (▬) CXSi-E, (▬) CXSi-B and (▬) CXSi-EB. (a) Solid electrolyte interface formation cycle and first reversible cycle and (b) 2nd cycle and (c) 10th cycle between 0.05 V and 1.5 V *vs.* Li^{+}/Li in half-cell setup.

Table 5.2. Electrochemical performances of the Si/CX composites.

	$C_{\text{theo}}{}^{a}$ (mAh g^{-1})	$C_{\text{in}}{}^{b}$ (mAh g^{-1})	$C_{\text{rev}}{}^{b}$ (mAh g^{-1})	ICE^{b} (%)	$C_{\text{cap}}{}^{c}$ (%)	$C_{\text{ret}}{}^{b}$ (%)	$C_{\text{rev/theo}}{}^{a,b}$ (%)
CX	372	1210	304	26	56	72	91
CXSi	497	1130	364	32	54	70	73
CXSi-E	644	1247	520	41	41	62	81
CXSi-B	727	1274	526	41	39	62	72
CXSi-EB	730	1266	564	44	40	60	77

[a] Calculated by Equation 5.3.

[b] Determined from long-term cycling data.

[c] Determined from cycling at various C-rate data.

Following cyclic voltammetry, galvanostatic charge-discharge experiments were performed (Figure 5.5a). In Table 5.2, theoretical capacities (C_{theo}) are determined using Equation 5.3 and the performances of the cells are compared in terms of initial capacities (C_{in}), reversible capacity (C_{rev}), initial coulombic efficiency (ICE) and capacity at different C-rates (rate capability, C_{cap}) as well as long-term stability (capacity retention, C_{ret}). Reversible capacity, C_{rev}, is determined by the first reversible capacity, meaning the first lithiation after SEI formation. Capacity retention, C_{ret}, was calculated by subjecting the cells to 30 cycles at C/20 and comparing the average capacity of the first 3 lithiations with that of the last 3 lithiations of the series. In the meantime, the rate capability, C_{cap}, was calculated as the ratio of reversible capacity at C-rate over the reversible capacity obtained at C/20. Finally, the ratio between the reversible capacity and the theoretical capacity is reported in the last column of the table.

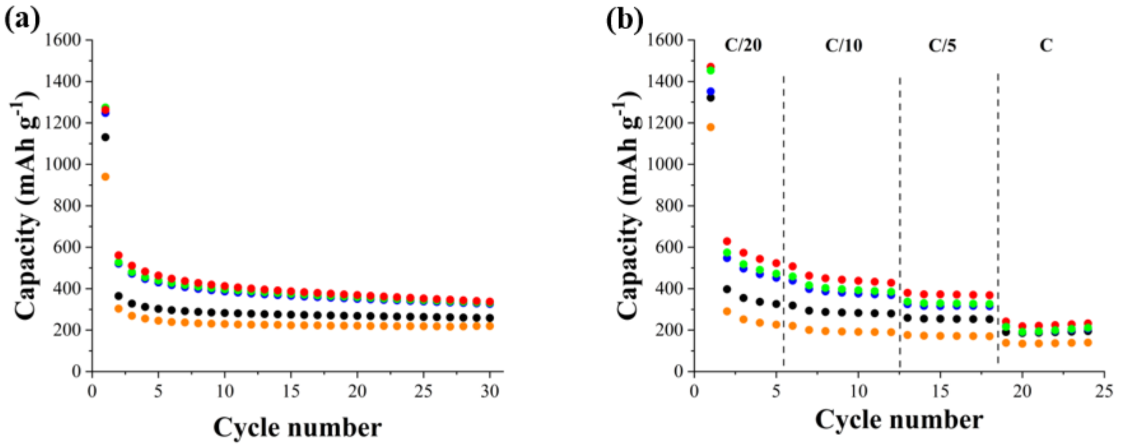

Figure 5.6. Galvanostatic charge-discharge measurements in half-cell setup. (a) Cycling at C/10 over 30 cycles between 0.05 V and 1.5 V *vs.* Li^+/Li. (b) Capacities observed at different C-rates for samples (●) CX, (●) CXSi, (●) CXSi-E, (●) CXSi-B and (●) CXSi-EB.

All samples show high initial capacities above 1000 mAh g^{-1} however their capacity quickly drops after the first lithiation: indeed, part of the initial capacity is due to SEI formation. CXSi-EB shows high initial capacity around 1250 mAh g^{-1} but it drops around 564 mAh g^{-1}, while CXSi-E and CXSiB reach about 520 mAh g^{-1}. The value is lower (364 mAh g^{-1}) for CXSi. When compared with bare CX (304 mAh g^{-1}), a significant increase in reversible capacity can be observed. Although those values are close to the theoretical ones, the samples prepared with pretreatment (Ar^+ etching, samples CXSi-E and CXSi-EB) show higher values of reversible capacity to theoretical capacity ratio (81% and 77%) than the samples prepared without pretreatment (CXSi and CXSi-B, 72 and 73%). In parallel, identical cells were submitted to long-term cycling with 30 cycles at a rate of C/10 (Figure 5.6a). Although the CXSi-EB sample starts with higher capacity than the other 3 Si/CX composites, the capacities are quite similar for all samples after the 10th cycle, except for CXSi. The values also become much more stable after that point. It was observed that cells made of samples CXSi-E, CXSi-B and CXSi-EB still can hold around 330 mAh g^{-1}. In the meantime, the reversible capacity of sample CXSi drops to 255 mAh g^{-1} after 30 cycles. These values correspond to capacity retentions, C_{ret}, of 70%, 62%, 62% and 60% for CXSi, CXSi-E, CXSi-B and CXSi-EB respectively, which shows that the cell degradation is not prevented. When compared to the bare CX (C_{ret} = 72%), one might argue that the decrease of the capacity can be coming from the carbon xerogel itself. However, the decrease of capacity of CX quickly stabilizes and barely moves after the 20th cycle while samples containing Si continue to lose their capacity. Thus, although relatively high reversible capacities are obtained, the degradation could not be prevented. Given that the particles with sizes below 15 nm should not crack upon lithiation-delithiation, degradation could be explained by the detachment of Si particles, resulting in overall capacity decay[32]. Additionally, another possible explanation is the continuous development of SEI by degradation of Si and its assimilation within the SEI layer, leading to the formation of a de-composite of Li_xSi and organic compounds produced by electrolyte decomposition[34].

Finally, GCPL tests were carried out in order to observe the rate capability of the samples (Figure 5.6b). Overall, moving from C-rate of C/20 to 1 C, samples CXSi-E, CXSi-B and CXSi-EB are able to hold around 200 mAh g^{-1}, which is more than 40% of their initial reversible capacity, while sample CXSi can deliver 54% of its initial capacity. The reason behind the better rate capability of CXSi might lie in its higher carbon content. Indeed, since it contains lower amounts of Si, the overall behavior is emphasizing that of the carbon xerogel material. Indeed, when CX is observed, it can be seen that the sample still possess 60% of its capacity at C compared to C/20. Thus, increased amount of carbon results in better capacity retention.

5.4. Conclusion

Silicon nanoparticles supported on a mesoporous carbon xerogel were produced *via* physical vapor deposition (PVD) in order to explore the possibility of using PVD to obtain Si/C composite materials to be used as Li-ion negative electrode material. It also aimed at determining the effects of the carbon surface pretreatment by Ar^+ etching and the use of bias voltage during Si coating procedure on the physico-chemical properties of the samples and on their performance as electrode material.

PVD process with different procedure steps, namely pretreatment by Ar^+ etching and/or use of bias voltage, were combined, resulting in four different samples that were compared to the naked carbon xerogel support. The four samples contained 3.2 wt.%, 7.0 wt.%, 9.3 wt.% and 9.4 wt.% Si when one used PVD procedures with (i) no bias and no Ar^+ etching pretreatment, (ii) only pretreatment, (ii) only bias and (iv) pretreatment and bias, respectively. This shows that both strategies increase the amount of silicon deposited on the carbon support, bias being however much more effective than Ar^+ etching. Additionally, XPS characterization showed that both Ar^+ etching and bias voltage application led to powders containing lower oxygen amounts. Well-dispersed silicon nanoparticles (~15 nm) were observed, which is far below the size limit (~150 nm) leading to Si particle cracking during cycling.

Regarding electrochemical performances, a high initial capacity around 1250 mAh g^{-1} could be reached for the sample produced with both etching and bias; it however dropped around 560 mAh g^{-1} at the second cycle. After 30 cycles, all cells dropped to around 60% of their initial reversible capacity, highlighting the degradation of the Si nanoparticles, despite their small size. Two degradation mechanisms can be proposed: detachment of silicon from the electrodes, causing incomplete delithiation/lithiation or continuous de-composite SEI formation by degradation of Si and incorporation within the SEI. Finally, capacities around 200 mAh g^{-1} could be observed for all samples at relatively high C-rate (1 C); this corresponds to 40% of their capacity observed at C/20.

Further studies could focus on protecting the Si nanoparticles from the electrolyte and preventing the continuous degradation observed, either by particle detachment or incorporation within the SEI. One possible strategy could consist in applying an additional carbon coating on top of the silicon particles, either by Chemical Vapor Deposition, or by PVD. Additionally, the applied carbon coating could facilitate electron transfer and further improve the electrode performance. Those strategies will be explored in the near future.

5.5. References

[1] R. Borah, F.R. Hughson, J. Johnston, T. Nann, Mater Today Adv 2020, 6.

[2] B. Liang, Y. Liu, Y. Xu, *J Power Sources* **2014**, 267, 469.

[3] D. Ma, Z. Cao, A. Hu, *Nanomicro Lett* **2014**, 6, 347.

[4] N. Dimov, S. Kugino, M. Yoshio, *Electrochim Acta* - **2003**, 48, 1579.

[5] M.T. McDowell, S.W. Lee, J.T. Harris, B.A. Korgel, C. Wang, W.D. Nix, Y. Cui, *Nano Lett* **2013**, 13, 758.

[6] X.H. Liu, L. Zhong, S. Huang, S.X. Mao, T. Zhu, J.Y. Huang, *ACS Nano* **2012**, 6, 1522.

[7] S. Chae, S.-H. Choi, N. Kim, J. Sung, J. Cho, Angew. *Chem. Int. Ed.* **2020**, 59, 110.

[8] M. Hu, H. Wu, G.J. Zhang, *Chem Phys Lett* **2023**, 833, 140917.

[9] Z. Yan, S. Yi, X. Li, J. Jiang, D. Yang, N. Du, *Mater Today Energy* **2023**, 31, 101225.

[10] N. Job, R. Pirard, J. Marien, J.P. Pirard, *Carbon* **2004**, 42, 619.

[11] M.L.C. Piedboeuf, A.F. Léonard, G. Reichenauer, C. Balzer, N. Job, *Micropor Mesopor Mat* **2019**, 275, 278.

[12] M.L.C. Piedboeuf, A.F. Léonard, F.L. Deschamps, N. Job, *J Mater Sci* **2016**, 51, 4358.

[13] X. Yuan, Y.J. Chao, Z.F. Ma, X. Deng, *Electrochem Commun* **2007**, *9*, 2591.

[14] L. dos Santos-Gómez, N. Cuesta, I. Cameán, S. García-Granda, A.B. García, A. Arenillas, *Electrochim Acta* **2022**, *426*, 140790.

[15] X. Li, H. Shi, L. Zhang, J. Chen, P. Lü, *Chin J Chem Eng* **2020**, *28*, 579.

[16] H.C. Barshilia, A. Ananth, J. Khan, G. Srinivas, *Vacuum* **2012**, 86, 1165.

[17] G. Skordaris, K.-D. Bouzakis, P. Charalampous, T. Kotsanis, E. Bouzakis, R. Bejjani, *Wear* **2018**, 404–405, 50.

[18] W. Dai, Y. Shi, *Coatings* **2021**, 11, 911.

[19] N. Bensalah, F.Z. Kamand, M. Zaghou, H.D. Dawoud, T. Al Tahtamouni, *Thin Solid Films* **2019**, 690, 137516.

[20] K.S. Lee, Y.N. Lee, Y.S. Yoon, *Electrochim Acta* **2014**, *147*, 232.

[21] M.R. Kaiser, Z. Han, J. Liang, S.X. Dou, J. Wang, *Energy Storage Mater* **2019**, 19, 1.

[22] H. Zhang, H. Xu, C. Zhao, *Mater Chem Phys* **2012**, 133, 429.

[23] M. Kakunuri, S. Vennamalla, C.S. Sharma, *RSC Adv* **2015**, 5, 4747.

[24] J. Carabetta, S.P.N. Job, B. Heinrichs, N. Job, *Carbon Xerogels Doped with Silicon or Tin Oxide for Lithium-Ion Battery Anodes*, **2021**.

[25] B. Kartick, S.K. Srivastava, I. Srivastava, *J Nanosci Nanotechnol* **2013**, *13*, 4320.

[26] J.M. Westra, V. Vavruňková, P. Šutta, R.A.C.M.M. Van Swaaij, M. Zeman, in *Energy Procedia*, **2010**, *2*, 235.

[27] N. Noor Aien Mohamed Abdul Ghani, M. Alam Saeed, I. Hazwani Hashim, *Mal. J. Fund. Appl. Sci.* **2017**, *13*, 178.

[28] B. Philippe, R. Dedryvère, J. Allouche, F. Lindgren, M. Gorgoi, H. Rensmo, D. Gonbeau, K. Edström, *Chem. Mater.* **2012**, *24*, 1107.

[29] A. Rezqita, H. Vasilchina, R. Hamid, M. Sauer, A. Foelske, C. Täubert, H. Kronberger, *Batteries* **2019**, *5*, 11.

[30] E.N. Attia, F.M. Hassan, M. Li, R. Batmaz, A. Elkamel, Z. Chen, *J Mater Chem A Mater* **2017**, *5*, 24159.

[31] F.M. Hassan, R. Batmaz, J. Li, X. Wang, X. Xiao, A. Yu, Z. Chen, Nat Commun **2015**, 6, 8597.

[32] M. Wetjen, D. Pritzl, R. Jung, S. Solchenbach, R. Ghadimi, H.A. Gasteiger, *J Electrochem Soc* **2017**, *164*, A2840.

[33] D. Wang, R. Wang, K. Huang, M. Lei, H. Tang, *Adv Compos Hybrid Mater* **2022**, *5*, 1362.

[34] L.B. Hubrechtsen, L.L. De Taeye, P.M. Vereecken, *Small Methods* **2024**, *8*, 2300857.

Conclusions and Outlook

The general goal of the present thesis was to develop new concepts and approaches aiming at producing more environmental-friendly battery designs. The strategy was threefold:

1- Instead of using toxic PVDF/NMP combination as a binder for electrodes, **water-based electrode processing** previously studied at the NCE laboratory **was pushed further to expand the overall proof of concept**. The manufacturing process uses xanthan gum as binder to replace PVDF. It is an organic, water-soluble sugar-type binder which not only eliminates the toxic PVDF: it also eliminates NMP, which is toxic, carcinogenic and has a much higher normal boiling temperature than water. The method was used to manufacture (i) $LiFePO_4$ (LFP) positive electrodes with various designs, (ii) Si/carbon xerogel negative electrodes for Li-ion batteries and (iii) carbon xerogel negative electrodes for Na-ion batteries. The procedure was successful in all cases, which enables to generalize the process. Other electrode chemistries such as NMCs could be attempted in the future.

2- A second approach, which led to one of the biggest efforts, was to **optimize the design of batteries by a combination of modelling and data acquisition**. Indeed, modelling of batteries comes in front when attempting to improve the device design without considering endless number of experiments, but models still need data for identification and validation. Modelling of the battery was the task of the ULB team involved in the global project, while efforts at ULiège were dedicated to the design of electrochemical characterization procedures and data collection. Finally, the effect of particle size and material loading to the performance of Li-ion battery electrodes was studied in order to gain experimental knowledge and to optimize the design of Li-ion battery positive electrodes made from different LFP powders.

3- In parallel to optimization studies, **different materials were developed in order to decrease the amount of critical raw materials used in current batteries**. First, since one of the biggest problems of LIBs is the abundance of Li as well as other critical materials such as Co or Cu, **other types of devices such as Na-ion batteries are considered as an alternative**. In the present work, we focused on negative electrode materials: hard carbons. Those carbons have larger interlayer distance than graphite, making it possible to host Na^+ ions in-between. Carbon xerogels (CXs) are one type of hard carbons that can be envisaged, but their large specific surface area heavily contributes to the Solid-Electrolyte-Interface formation. The present work aimed at improving the Initial Coulombic Efficiency of such carbons by (i) modifying the carbon morphology (especially its nodule size) and (ii) modifying its surface properties. In the latter approach, the CXs were post-treated either by chemical vapor deposition (CVD) of a secondary carbon layer and/or by CO_2 activation in order to increase the amount of micropores suitable for Na^+ insertion. Second, one can consider **limiting the amount of graphite at the negative electrode of Li-ion batteries**. To that aim, one can add an alloying material with high capacity such as (4200 mAh g^{-1}) to a carbon scaffold, which acts both as electron-conductive material and volume expansion buffer. In the present work, Si/carbon xerogel composites were prepared by Physical Vapor Deposition and characterized as negative electrodes of Li-ion batteries.

The first strategy was applied throughout the whole thesis. The study of the design of batteries from known materials was developed in Chapters 1 and 2. Finally, new materials corresponding to the third axis were developed in Chapters 3 to 5. The specific general conclusions of each chapter are regrouped in the next paragraphs and are followed by suggestions of further prospects to continue the research.

Standardization of experimental conditions for modelling of $LiFePO_4$ cells

In Chapter 1, the combined efforts of ULB and ULiège to develop and validate a physical model were described. The final aim of the model, developed by ULB, was to be used as a tool to design batteries with the best properties. In the study presented, the objective function was the maximisation of the battery specific (gravimetric) energy density. The task of ULiège was to provide data to verify and identify a model of dSPMe type (dimensionless single particle model with electrolyte). In that ambit, a standardization of experimental conditions was realized and the obtained experimental data were used for model identification and verification. In order to ensure the results reproducibility, the experimental conditions of various techniques, *i.e.* galvanostatic charge and discharge (GCPL), electrochemical impedance spectroscopy (EIS) and galvanostatic intermittent titration technique (GITT), were studied in details. For EIS, parameters such as the resting duration before the procedure, the State Of Charge (SOC) at which EIS takes place and the calculation of the SOC were studied and standardized.

Additionally, an alternative way to classical GITT was developed. Indeed, the normal GITT procedure is known to last for weeks, or even months, which makes it very impractical at best for research on batteries. The alternative GITT method developed included two distinct procedures: (i) one GITT procedure that has few current pulsations and after very long resting periods (referred to as “long GITT”) and (ii) numerous pulsations and short resting periods (referred to as “short GITT”). For the long GITT, it consists of fewer measurement points on the charging/discharging profile but would include a long rest until the cell is as close to equilibrium state as possible. The short GITT includes numerous pulsations and much shorter resting periods. This would give many points on the charging/discharging profile but very short resting periods that would not let cell to completely be in equilibrium. The aim is to use long relaxation time data points from long GITT as a pattern to fit the data points obtained by the short GITT. By this way, the time required for GITT could be lessened to 2 weeks compared to months.

After the data acquisition standardization, the model developed by ULB was used to maximize the specific energy density of a lithium-ion battery ($LiFePO_4$ in half-cell configuration). The model was based on a reduced-order model, which is a derivation of Doyle-Fuller-Newman (DFN) model. For this, the DFN model was simplified with the assumption that the electrode consists of a dimensionless single particle in contact with the electrolyte; this model is related to as “dimensionless single particle model with electrolyte” (dSPMe) in the literature. The model was first used in a sensitivity analysis to determine the most relevant design parameters for energy density; those were found to be (i) the LFP particle radius, (ii) the electrode thickness and (iii) the electrode cross-sectional area. Also, an adaptive particle swarm optimization was used to solve the optimal design problem. Finally, the optimal electrode design was found to be a thickness of 310 µm, 10 nm particle radius (corresponding to the lower physical limit imposed to the model) and 2×10^{-4} m^2 electrode cross-sectional area. Following the model, that design would result in 250 Wh kg^{-1}. This result corresponds to an increase of 61 Wh kg^{-1} from an initial design defined from literature.

Water-based processing of $LiFePO_4$ positive electrodes with various particle size and active material loading

In Chapter 2, series of experiments were conducted in order to understand the effect of particle size and active material loading on the performance of $LiFePO_4$ (LFP) electrodes. For this, the electrodes were prepared with water-based manufacturing process using xanthan gum, with various active material loadings (from 3 to 12 mg active material on 1.88 cm^2 current collector) by using 2 LFP powders with different particle sizes (0.24 µm and 0.84 µm). The water-based process successfully coated both LFP powders with desired material loadings without any problems. The goal was to show that both electrode design parameters can affect the electrochemical performance, and were interdependent. To that aim, the electrode capacity was measured at various cycling rates, for several electrode thicknesses, with both LFP powders. Results show that, although at lower C-rates (*e.g.* C/5) the capacities were similar for electrodes with various thicknesses, differences started to appear once the C rate was increased. The capacity drops almost by half at 2C compared to C/5 when the particle size is large while it decreases about 30% for the electrodes made with smaller particles. Indeed, the electrode group with smaller LFP particle size performs better at higher C-rates, even when the active material loading is increased. The better rate capability of smaller LFP particles is explained by electrochemical impedance spectroscopy as a significant difference in terms of charge transfer resistance is observed by EIS.

The cells were also studied in terms of stability. Both groups of electrodes were submitted to 100 cycles at C rate. Low material loadings (3 mg), regardless of the particle size, got affected much less as both electrode groups can still hold around 96% of their capacity after 100 cycles. Again, regardless of the particle size, the cells got affected much harsher when the material loading is increased to 12 mg: indeed, the capacity retention decreases significantly (down to 36% for the small LFP particles and as low as 32%, in the case of the large LFP particles). When the two different particle size groups are compared, the electrodes with smaller LFP particle are less degraded by long term cycling. In terms of electrochemical properties, one can observe both internal and charge transfer resistance increase for both groups of electrodes. However, in the case of small LFP particle electrodes, increase of these resistances are much less pronounced.

Post-treatments of carbon xerogels used as negative electrodes of Na-ion batteries produced by water-based processing

In Chapters 3 and 4, carbon xerogels (CXs) were used as negative electrode material for Na-ion batteries. Those materials are hard carbons (*i.e.* non-graphitizable) made of interconnected microporous nodules of various size, depending on the synthesis conditions. In principle, one would expect that their high specific surface area (~600 m²/g) would lead to low Initial Coulombic Efficiencies due to massive Solid Electrolyte Interface formation; therefore, it was attempted to coat the initial carbons with a secondary carbon layer *via* Chemical Vapor Deposition (CVD) in order to mask the micropores accessible to the electrolyte and boost the ICE. Both the impact of the nodule size and the presence of the secondary carbon layer on the electrochemical performance were studied in Chapter 4. Both studies were performed in collaboration with the LRCS laboratory in Amiens and the ENSTIB/IJL in Epinal.

All electrodes were again successfully processed using the water-based method. It was first observed that the nodule size of CXs has a drastic impact on the ICE of the electrodes, while all CXs displayed similar total specific surface areas, measured by N_2 adsorption (*e.g.* A_{BET}, derived from the Brunauer-Emmett-Teller equation). Indeed, ICE values increased from 29% to 80% when the nodule size was increased from 50 nm to 2 µm. This result clearly shows that ICE values are not directly related to the powder specific surface area, while ICE values are quite often discussed on the basis of A_{BET} in the literature. One can also note that 298 mAh/g and 80% ICE were obtained for the CX with 2 µm nodules, which is the highest value obtained at pyrolysis temperature below 1000°C (800°C in this case). CVD coating allowed to reduce the specific surface areas in all samples by totally masking the micropores; in most cases, the A_{BET} values corresponded to the external surface of the nodules. The secondary carbon layer led to an improvement of the electrochemical properties of the CXs in all cases. In particular, for the largest nodules, the specific surface area dropped from 600 m^2 g^{-1} to 2 m^2 g^{-1}, leading to an ICE of 84%. Again, this clearly shows that the specific surface area is not the key indicator to high ICE values. Additionally, CVD treatment enabled lengthening the plateau zones ascribed to the filling of small micropores by Na^+. That lengthening of plateau zone resulted in higher capacity values, up to 298 mAh g^{-1}, for the sample with the largest nodule size.

Given the importance of closed micropores to the performance of hard carbons, as observed both in literature and in Chapter 3, an additional modification was introduced in Chapter 4. Prior to CVD coating, a CX with large nodule size (~2 µm) was activated by CO_2 in order to increase the micropore volume; this also resulted in a significant increase of specific surface area. Without any coating, the electrochemical performances were spectacularly degraded: the reversible capacity dropped from 248 mAh g^{-1} to 62 mAh g^{-1}, and the ICE from 80% to 18%. This was expected given that high surface areas are supposed to lead to higher SEI formation, thus lower ICEs; however, the ICE drop was not at all proportional to the total surface increase, questioning again the relationship between A_{BET} and the ICE usually mentioned in the literature. Measurements in capacitor configuration showed indeed that the electrode surface accessible to the electrolyte does not correspond to the total specific surface area: the electrolyte does not enter most of the micropores volume, which explains why surface areas measured by gas adsorption are not a good indicator of the final electrode performances. It also explains the excellent results obtained with the pristine CX: much probably, only the outer nodule surface (~2 m²/g, calculated geometrically) is accessible to the electrolyte. Finally, combination of CO_2 activation and CVD carbon layer was performed in an attempt to obtain an increased amount of closed micropores. A record ICE value of 88% and a capacity of 298 mAh g^{-1} were obtained, which is again an excellent result for carbons processed below 1000°C. More importantly, the sample that underwent activation followed by coating displayed better rate capability and increased stability over long cycling.

All in all, the studies in Chapters 3 and 4 were conducted following strategies 1 and 3. Firstly, it was shown that xanthan gum can be used to produce carbon xerogels electrodes for Na-ion battery negative electrodes. The coatings were done successfully and electrodes worked without noticeable problem due to electrode assembly. Regarding strategy 3, it was shown that carbon xerogels are suitable as Na-ion battery negative electrodes. The main issue of carbon xerogels, which was the initial coulombic efficiency, was improved greatly as values up to 88% could be achieved. Additionally, more in-depth information regarding the relationship between the surface area of the carbon materials and the initial coulombic efficiency was retrieved.

Si nanoparticles deposited on carbon xerogels *via* Physical Vapor Deposition

In Chapter 5, silicon nanoparticles were deposited onto a mesoporous carbon *via* Physical Vapor Deposition (PVD) in order to produce Si/C composite materials to be used in Li-ion negative electrodes. The strategy was to select a suitable carbon scaffold that could act both as an electron conductive support and as a buffer for Si particle growth upon lithiation. The impact of different procedures such as surface pre-treatment by Ar^+ etching and application of a bias voltage during coating was explored. The produced materials were then characterized in terms of physico-chemical properties and performance as electrode materials.

Well-dispersed silicon nanoparticles (~15 nm) were obtained; this is far below the minimum reported for avoiding Si nanoparticles cracking and pulverization during cycling. Both Ar^+ etching pretreatment and bias voltage have an impact on the amount of Si deposited on the carbon support. Indeed, the composite sample contained 3.2 wt.%, 7.0 wt.%, 9.3 wt.% and 9.4

wt.% Si when PVD procedures with (i) no bias and no pretreatment, (ii) only pretreatment, (ii) only bias and (iv) pretreatment and bias are applied, respectively. This result indicates that both bias and pretreatment enable increasing the amount of Si deposited. Additionally, both procedures seem to decrease the amount of oxygen in the final powder.

A high initial capacity around 1250 mAh g^{-1} can be observed for the sample with the highest Si content, *i.e.* the Si/CX composite produced using both Ar^+ etching pretreatment and bias application during coating. This value is close to the theoretical one, when considering the carbon and Si capacities as well as the sample composition. However, the capacity dropped around 560 mAh g^{-1} at the second cycle. The same phenomenon was observed for all produced samples. After 30 cycles at C/10, all capacities dropped to around 60% of their initial values due to degradation, despite the small size of silicon nanoparticles. This clearly indicates that the control of the size of the Si nanoparticles is not sufficient to avoid their degradation, probably due to direct contact with the electrolyte.

Outlook

Modelling is a very useful tool in order to optimize the design of batteries without doing exhaustive amount of experiments. To this aim, a dimensionless single particle model with electrolyte has been developed by the researchers of Université Libre de Bruxelles (ULB). In the present work, standardization of various experimental methods such as GITT, EIS and GCPL have been conducted at the laboratory in order to obtain reproducible data to be used to verify/identify the model. Some of these experiments have not been used in the model yet. Therefore, future work could include GITT and galvanostatic charge-discharge experiments in order to identify the parameters and develop the model further. Additionally, once validated with LFP electrodes, the model could be easily extended to other chemistries. Ultimately, the model should serve as a design tool to help the experimenters finding the best parameter combination for the manufacturing of half- and full-cells with various geometries. This is a work in progress between ULB and ULiège.

For the second chapter, $LiFePO_4$ powders with different particle sizes and electrodes with various active material loadings were used in order to understand the effect of these two parameters on the performance of the cells: this choice was guided by the parameter sensitivity analysis performed in Chapter 1. Similar studies could be performed with other materials (for example LTO, graphite or NMC) using the same procedure after checking that particle size and electrode thickness remain the key parameters to electrode design as in Chapter 1. This would help understanding the general impact of those design parameters under various circumstances and shed light on the differences between two different active materials. Additionally, only half-cells were used in the present study. Extending the method to full cells could possibly be done, considering the electrode balancing in an appropriate way. In many battery designs, the positive electrode is slightly overloaded compared to the negative one in order to provide an excess of Li^+. Further studies of the same kind (coupling Chapters 1 and 2) could help reaching the best possible full-cell design.

Regarding new materials for batteries with less environmental impact, the work concerning hard carbons for Na-ion batteries can be continued in many directions. Indeed, carbon xerogels can be modified in many different ways and it is much probable that the optimal material for Na-ion batteries has not been found yet. In this thesis, carbon xerogels with various nodule sizes have been produced by pyrolysis of resorcinol-formaldehyde gels at 800°C. The resulting best powder in terms of ICE and capacity was the one with the largest nodule size (~2 µm). Further works could attempt to produce and characterize materials with larger nodule sizes to find the limit, and check how this increase further modify the rate capability, which seems to decrease with increasing nodule size. Possibly, the best possible material will depend on the final application (high capacity or high power). The study of the impact of the pyrolysis temperature should be carried out as well. Indeed, from literature, it is clear that increasing the pyrolysis temperature improves the ICE. Since the carbon xerogels used in the present thesis were produced at the lowest possible temperature to reach carbonization (800°C), an increase of temperature might prove beneficial on both the xerogel (even though it is not graphitizable). Post-treatments up to at least 1500°C should be performed to check what temperature is optimal, keeping in mind that, from an industrial viewpoint, the lowest would be the best.

As for carbon xerogels coated using Chemical Vapor Deposition (CVD), a systematic study is necessary to understand better the impact of the secondary carbon layer on the material performances. The approach would aim at optimizing the secondary carbon layer in terms of thickness, crystallographic structure and chemical properties. Numerous parameters can be modified during the process, and post-treatments are possible. Quite obviously, the temperature of the CVD treatment, its duration and the temperature of the final heat treatment can be modified. Presumably, this study would also include the modification of CVD parameters as a function of the carbon xerogel to be coated. Since the mass uptake changes greatly with the difference of available surface area, which in turn depends on the CX morphology and pore texture, all the processing parameters must be adapted to the different nodule sizes. One primary goal could be to define the parameters leading to the same coating thickness, whatever the nodule size, as a function of the available nodule surface area to be coated.

In parallel, the CO_2 activation procedure should be optimized as well with regard to the final properties. In particular, the impact of the amount of closed micropores on the electrochemical performances should be studied in more details, using CXs with various activation degrees. The optimal activation degree remains to be determined. The current work also showed that activation led to higher oxygen content. The exact impact of oxygen is also to be understood properly, maybe by using CXs with controlled oxygen surface groups type and content. Those oxygen surface groups can be modified by selected oxidation procedures.

Also, it remains to elucidate how the combination of CO_2 activation and CVD carbon deposition modifies the inner structure of the carbon xerogels. It is certain that CO_2 activation leads to the appearance of new micropores and there are several indirect proofs of the existence of closed pores in CVD-coated xerogels; however, direct observation could not be performed in this thesis. In order to confirm the existence and development of the closed micropores, small angle X-ray scattering (SAXS) measurements can be performed. It would enable understanding if the carbon layer deposited by CVD closes or fills the micropores and could provide information on the structure of the newly introduced pores by CO_2 activation. Also, *in situ* experiments such as SAXS, Raman or X-ray diffraction (XRD) during galvanostatic charge-discharge can be used to fully understand how and where the Na^+ ions are stored in the carbon nodules of the xerogels, especially when the nodule size is large and after coating by CVD. The combination of those studies, based on model carbon materials, could help understanding better the relationship between the physico-chemical properties of the carbon and its final properties as active material for Na-ion negative electrode. It could then help selecting other promising carbon materials prepared from renewable sources, such as bio-based raw precursors. Those subjects are currently under investigation between ULiège, the LRCS laboratory in Amiens and the ENSTIB/IJL in Epinal.

Finally, in Chapter 5, silicon nanoparticles (~15 nm) were successfully deposited on a carbon xerogel scaffold via Physical Vapor Deposition. The Si amount was relatively low (max 9.3 wt.%) while current researches in Si/C composites try to reach 20-30 wt.%. A further study could consist in checking (i) if the amount of Si deposited can be increased and (ii) if the nanoparticle size remains small enough (< 100-150 nm) in that case. The impact of the carbon xerogel nodule size and pore texture could also be checked. In addition, the electrodes prepared from the Si/CX composites were unstable upon cycling, probably because the Si nanoparticles remained in direct contact with the electrolyte. To tackle this issue, another layer of carbon could be coated on top of the Si nanoparticles, either by PVD (directly after the Si deposition) or by CVD; this would reduce (or even suppress) the direct Si-electrolyte contact. Stated otherwise, this carbon layer could behave like a barrier to avoid continuous Solid Electrolyte Interface formation. But the question is the accessibility of Si to Li^+ in that case. This approach will be studied by the research groups involved (ULiège, UNamur and ICS) in the near future.